THE UNIVERSITY *of* EDINBURGH

Evolution of Emission Line Properties and Metallicities of Star-Forming Galaxies up to $z \sim 3$

Fergus Cullen

Doctor of Philosophy
The University of Edinburgh
April 2015

Lay Summary

The work presented in this thesis explores the properties of galaxies which existed when the Universe was roughly 20% of its current age, approximately 10.5 billion years ago. We are able to look into the past in this way because the speed of light is finite, and so as we look deeper into the Universe at more distant objects, we are actually looking backwards in time. In fact, with modern space-based observatories like the *Hubble Space Telescope (HST)*, it is possible to see galaxies back to within the first 1 billion years of the Universe's history. In essence, when we look at these distant galaxies we are seeing what our own galaxy, the Milky Way, was like all that time ago.

The galaxies which existed 10.5 billion years ago are particularly interesting because, from what we can tell, at this time galaxies in the Universe were undergoing the most active stage of their evolution. Specifically, the stars within galaxies were being formed at a more rapid rate than ever before or since. We call this era the 'peak of cosmic star-formation history'. To put it into some perspective, galaxies in the present day Universe form, on average, one star every three years, whereas at this epoch galaxies were forming tens to hundreds of stars per year. Determining the properties of these galaxies in this crucial epoch will ultimately help us understand the evolution history of the galaxies we see around us today.

The specific focus of my research has been to study a sample of these galaxies taken from new state-of-the-art *HST* data, and to measure their physical properties. In particular I focus primarily on measuring the oxygen abundance which, in this context, means the amount of oxygen present in a galaxy relative to the amount of hydrogen. In recent years, with the development of new improved spectrographs, it has become possible to directly measure the emission from oxygen in these galaxies, as well as hydrogen and nitrogen, and hence infer their relative abundances.

Measuring the oxygen abundance is interesting because it tells us how the elements were built up across cosmic time. Before the first stars were formed, the Universe contained mostly hydrogen and helium with a very small fraction of other light elements (e.g. lithium, beryllium etc). Only in stars can the other heavier elements be synthesised. Therefore, as more stars form the Universe becomes more enriched with these heavy elements, such as oxygen, carbon, nitrogen etc. If this is the case, then as we look back into the past galaxies should have, for example, less oxygen relative to hydrogen than galaxies we see today. I show in Chapter 3 that, indeed, the oxygen abundance of the galaxies 10.5 billion years ago is lower than that observed today. However, my measurements are not consistent with other authors who make the same measurement using a slightly different method.

Therefore, in Chapter 4, I explore the cause of this inconsistency by investigating how the environments in which stars form may change with time. Since stars are forming much more rapidly in these galaxies, then perhaps the environmental conditions within which they form are different in some way? By comparing to a set of new theoretical models for star-formation, I conclude that the conditions in star-forming regions is more intense in these early galaxies than in galaxies today: the gas clouds which surround them are denser, and the stars themselves emit stronger ultra-violet light. This result can neatly explain the inconsistencies in Chapter 3, and points towards a more robust way of making measurements of oxygen abundance.

To conclude, in Chapter 5, I revisit the oxygen abundance measurements that I made in Chapter 2 and, with this new information on the evolution of star forming regions, I am able to bring the previously inconsistent data into good agreement. My research shows that stars 10.5 billion years ago did not form in similar environments to the stars that we see in the local Universe, and that this effect must be carefully corrected for when measuring element abundances. When this evolution is properly accounted for, my research suggests that galaxies, 10.5 billion years ago, contain roughly half as much oxygen as present-day galaxies like our own Milky Way.

Abstract

Until recently, obtaining rest-frame optical spectra of galaxies at $z > 1$ was a time consuming and challenging observation due to the difficult nature of near-infrared (near-IR) spectroscopy. However, with the advent of second generation ground-based near-IR spectrographs (e.g. KMOS, MOSFIRE), and the new low resolution near-IR grisms on the *Hubble Space Telescope (HST)*, we have entered a new era in the study of high redshift galaxies. This thesis explores the physical properties of star-forming galaxies in the redshift range $1 < z < 3$ by utilising a custom reduction of the 3D-*HST* near-IR grism spectroscopic survey.

One of the most important observational constraints on the evolution of galaxies is the mass-metallicity relation (MZR), which is sensitive to both the star-formation history and various inflow/outflow processes. I use the 3D-*HST* spectra to provide a new constraint on the MZR at $2.0 < z < 2.3$, and moreover measure the O/H abundance directly from the oxygen and hydrogen emission lines ([OII], [OIII] and Hβ) as opposed to the more common method at high redshift of inferring O/H from the N/H ratio (via [NII] and Hα). I show that the traditional form of the MZR is recovered from the 3D-*HST* data, with metallicity increasing with the stellar mass of a galaxy. However, the absolute metallicity values I derive are inconsistent with previous N/H-based measurements of metallicity at these redshifts. Moreover, I show that the 3D-*HST* data is inconsistent with the 'fundamental metallicity relation' (FMR), and that, contrary to previous claims, this local Universe relation may not hold out to $z \gtrsim 2$.

To investigate this metallicity discrepancy further, I measure the evolution of the [OIII]/Hβ nebular emission line ratio in the 3D-*HST* spectra over the redshift range $1.3 < z < 2.3$. I compare this observed line ratio evolution with state-of-the-art theoretical models which take into account the independent evolution of the ionization parameter, electron density and metallicity of star-forming regions with redshift. The homogeneous 3D-*HST* dataset allows me to perform

a consistent analysis of this evolution which takes into account line luminosity selection effects. I show that, according to models, the observed [OIII]/Hβ evolution cannot be accounted for by pure metallicity evolution. Instead I am able to infer that the line ratio evolution is more consistent with, at the very least, an evolution to stronger ionizing conditions at high redshift, and perhaps even denser star-forming regions. I explore how this result can also explain the observed discrepancy between high redshift metallicity measurements.

In light of this finding, I revisit the MZR at $z \gtrsim 2$ and employ a purely theoretical approach to inferring metallicities from nebular lines, which is able to account for an evolution in ionization conditions. I then use a selection of galaxies from the local Universe, which mimic the properties of high redshift galaxies, to derive a more robust ionization sensitive, conversion, between N/H and O/H. With this new conversion which I am able to bring the previous inconsistent metallicity measurements at $z \gtrsim 2$ back into agreement. Finally, I am able to show that, in this new formalism, the metallicity evolution between $z = 2$ and $z = 3$ is perhaps not as large as previously reported.

To conclude I discuss ongoing work as part of the KMOS Deep Survey (KDS) being undertaken with the near near-IR Multi-Object Spectrograph KMOS on the VLT. I describe the observations and data reduction that has been completed to date and describe how this instrument will allow me to extend the work presented in this thesis to $z > 3$. I also introduce FIGS, a new *HST* near-IR grism survey seeking to spectroscopically identify galaxies at $5.5 < z < 8.5$ and work I have begun in exploring this dataset.

Declaration

I declare that this thesis was composed by myself, that the work contained herein is my own except where explicitly stated otherwise in the text, and that this work has not been submitted for any other degree or professional qualification except as specified.

Parts of this work have been published in Cullen et al. (2014).

(*Fergus Cullen, April 2015*)

To Mum, Dad, Emily and Hannah

Acknowledgements

First and foremost I'd like to thank Michele for his excellent supervision, guidance and unwavering high spirits throughout the course of these four years. Thank you for giving me the freedom to explore my own ideas and helping me pursue the ones which actually made sense. Thank you also for initiating me to the trials and tribulations of observational astronomy out at Paranal. I still remember pouring over photographs of those telescopes when I was younger, when any thought of ever going there was just an improbable fantasy.

Thank you to Ross and Jim for all your level-headed criticism, and constructive advice, in the face of an onslaught of haphazard theories and bad grammar. And to Jim for giving me the opportunity to continue my research for another year. Thanks to Lisa Kewley, for giving your time and for everything I have been able to learn from you.

Thank you to my various officemates and the fellow students/post-docs - too many to name - who have become valued friends throughout my time at the ROE. More generally, thank you to the whole community up at the observatory who make it such an enjoyable and friendly place to work. Thank you to Elliot and Lizzie for being great flatmates and friends.

Thank you to my family: Mum, Dad, Emily and Hannah, for your constant support and encouragement. I will have truly achieved a lifetime ambition if this thesis can become the most incomprehensible, and poorly written, addition to the family bookshelf. Now that the dust has settled I hope I will have more time to visit you all. Thank you to Ali for supporting me and putting up with me, especially during the final months.

On the whole, I would just like to express my sincere thanks to everyone who has helped me over the years. As I write this I can't help thinking of the hours spent staring up at the night sky in Kilbrien, wondering what it all was, and how I have been the grateful recipient of a generous amount of good fortune since then.

List of Acronyms

A useful reference list of acronyms use throughout this thesis.

AGN: Active Galactic Nuclei.

BBNS: Big Bang Nucleosynthesis.

BPT: [OIII]/Hβ versus [NII]/Hα Plane.

CMB: Cosmic Microwave Background.

EUV: Extreme Ultraviolet

FMR: Fundamental Metallicity Relation.

FOV: Field of View

HST: Hubble Space Telescope

IFU: Integral Field Unit

IGM: Intergalactic Median.

IMF: Initial Mass Function.

ISM: Interstellar Medium.

MZR: Mass-metallicity Relation.

SDSS Sloan Digital Sky Survey.

SED: Spectral Energy Distribution.

SFH: Star-formation History.

SFR: Star-formation Rate.

SFRD: Star-formation Rate Density.

SMD: Stellar Mass Density.

WCS: World Coordinate System

Contents

List of Figures

List of Tables

Chapter 1

Introduction

Galaxies are believed to form and evolve within dark matter halos seeded from initial density perturbations in the early Universe (e.g. Benson, 2010). These perturbations are predicted by the ΛCDM cosmological model, which is currently favoured as the most likely description of the global content and time evolution of the Universe as a whole, with strong constraints placed on the model parameters by the recent Planck satellite data (Collaboration et al., 2015). According to this model we live in a spatially flat Universe, $\sim$ 13.8 Gyr old, in which the energy density is shared between three constituents: dark energy, dark matter and baryonic matter.

However, while cosmological data has become so extensive that future observations are perhaps better thought of as precision tests of a well specified theoretical framework, no such strong constraints are placed currently on our understanding of the formation and evolution of galaxies. Though numerous models and public codes exist, using both smoothed particle hydrodynamics (e.g. GADGET Springel (2005b), AREPO Springel (2010)) and semi analytic methods (e.g. GALFORM Cole et al. (2002), Somerville et al. (2008)) the observations currently available cannot sufficiently constrain all the model parameters, and as such the study of galaxies and their evolution is still a topic driven by observations. In this introduction I will give an overview of the latest galaxy formation models as well and the key observational constraints currently placed on these models. Towards the end of the introduction I will place specific emphasis on the properties of star-forming galaxies across cosmic time, the study of which will form the bulk of the remainder of this thesis.

1.1 Theoretical Model of Galaxy Formation

1.1.1 ΛCDM Cosmology

The modern theory of galaxy formation and evolution is set within the context of the Λ-Cold-Dark-Matter (ΛCDM) cosmology. This cosmological model has its origins in Einstein's theory of gravitation and the observation of the expanding Universe made early in the 20th century (e.g. Hubble, 1929; Slipher, 1916). In this model the Universe formed in the Big Bang (Lemaître, 1932) and has evolved over the last $\sim$ 13.8 Gyr into the Universe we observe today, with an energy density made up of $\sim$ 68% dark energy ($\Omega_\Lambda = 0.68$), $\sim$ 27% dark matter and $\sim$ 5% baryonic matter ($\Omega_M = 0.32$) (Collaboration et al., 2015).

Our understanding is that after the Big Bang a rapid period of inflation set the initial conditions for cosmic structure formation (Guth, 1981). During the first $\sim 10^3$ seconds the temperature and density were large enough for nuclear reactions to take place, laying the foundation of the chemical elements. Until $\sim 10^5$ years after the Big Bang radiation and matter were coupled because the photon energy was sufficiently large to ionize any proton-electron pairs that formed. However, as the Universe expanded it cooled, until eventually the radiation and matter decoupled ($\sim$380,000 years after the Big Bang or $z \sim 1000$), protons and electrons combined, and the photons could 'free-stream'. This epoch is commonly referred to as the surface of last scattering.

The thermal radiation from the surface of last scattering is a near perfect black body, and the temperature of the photons at the point of decoupling was predicted by Gamow (1946), before being first detected by Penzias & Wilson (1965). Known as the Cosmic Microwave Background (CMB), it is isotropic across the sky to one part in 10^5 and represents the earliest snapshot of the Universe after the Big Bang and before the formation of the first stars and galaxies. The temperature fluctuations visible within the CMB (Fig. 1.1) are regions of over-densities and under-densities seeded by the small perturbations in the density field in the early Universe after inflation. The regions of over-density represent areas where the dark and baryonic matter (now decoupled from the radiation field) can collapse gravitationally to form the first stars and galaxies in the Universe (e.g. Peebles, 1965). In this way, the theory of the Big Bang and ΛCDM cosmology sets the initial conditions for the formation of galaxies in the Universe.

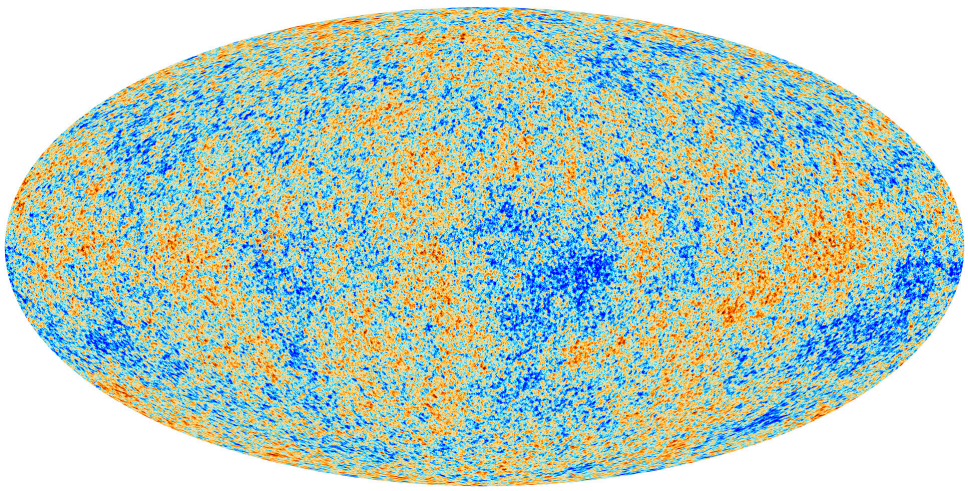

Figure 1.1 *CMB temperature map from the Planck mission (Collaboration et al., 2015) showing the variations in temperature across the sky. The temperature of the CMB is* $\sim 2.74K$ *with the fluctuations visible in the map of the order* $\sim 10^{-5}K$.

Though the existence of the CMB in itself provides compelling evidence in favour of the current cosmological model, it is worth briefly reviewing some of the other observational evidence for ΛCDM before moving on to discussing galaxies specifically:

Primordial Element Abundance: ΛCDM provides a framework with which to predict the primordial abundance of the chemical elements. As the Universe expanded and cooled after the Big Bang, nuclear reactions were able to take place in which protons and neutrons could combine to form atomic nuclei, a process referred to as Big Bang Nuclear Synthesis (BBNS). This process would continue until the Universe was sufficiently cool that no further nuclear reactions could take place. ΛCDM predicts the chemical element abundance after BBNS to be $\sim 75\%$ Hydrogen, $\sim 25\%$ Helium and a non-zero but negligibly small percentage of the heavier elements (Gamow, 1946). To-date all observations of the primordial element abundances are consistent with these values, though there is still some dispute with regard to the heavier elements (e.g. lithium) (see e.g. Cooke et al., 2014; Izotov & Thuan, 2010).

Large-Scale Structure: The large-scale structure and clustering of galaxies is another observable prediction of ΛCDM cosmology. Fig. 1.2 shows the structure of galaxies on the sky out to $z \sim 0.25$ taken from Peacock et al. (2001) using the 2dF Galaxy Redshift Survey (Colless et al., 2001). The overall structure of galaxies measured by the two-point correlation function (Peebles, 1980) can be

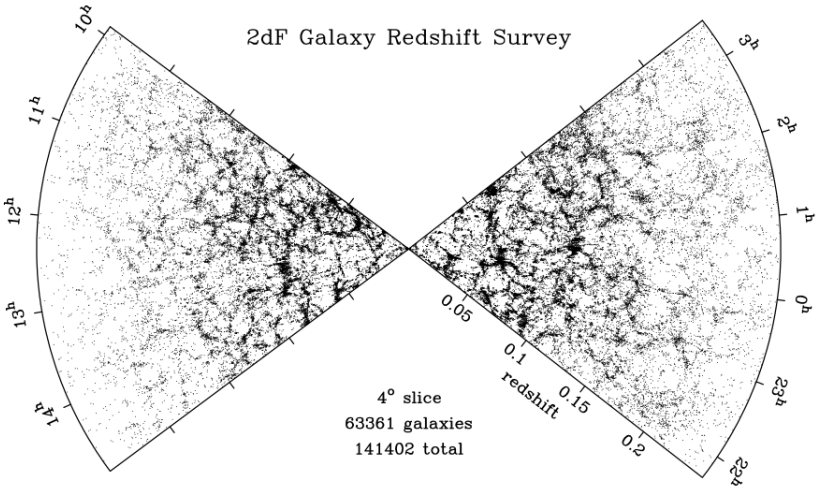

Figure 1.2 *Large-scale structure of galaxies measured from the 2dFGRS survey (Colless et al., 2001). The 'spider-web' structure, including mixture of galaxy over-densities, large voids, and filamentary structures, is a prediction of the ΛCDM model. Figure taken from Peacock et al. (2001).*

well reproduced by ΛCDM models with $\Omega_M \sim 0.3$ (e.g. White & Frenk, 1991). The prediction of an excess clustering at $\sim$ 100Mpc from cluster cores, known as the Baryon Acoustic Oscillation (BAO), is also a commonly observed prediction of the model (e.g. Anderson et al., 2014; Eisenstein et al., 2005).

Accelerating Expansion: Finally, Riess et al. (1998) and Perlmutter et al. (1999) used the observed brightness of Type Ia supernovae out to $z \sim 1$ to show that the expansion of the Universe is accelerating. Type Ia supernovae are a specific type of supernova explosion thought to have a characteristic peak luminosity, in this way they act as standard candles in the Universe. The observed luminosity of a standard candle at a given redshift places strong constraints on the way the Universe is expanding. The observed accelerated expansion is only possible in a model containing a dark-energy term Ω_Λ in the overall energy density of the Universe. Fig. 1.3 shows the difference between observed and intrinsic magnitude of these supernovae as a function of redshift compared with the expected values for different cosmologies.

Of course there are still many outstanding issues with the ΛCDM cosmology. For example the nature of dark-matter and dark-energy are still unknown, and they remain substances whose existence and properties we infer from our observations rather than have detected directly. However, as this thesis is based on the

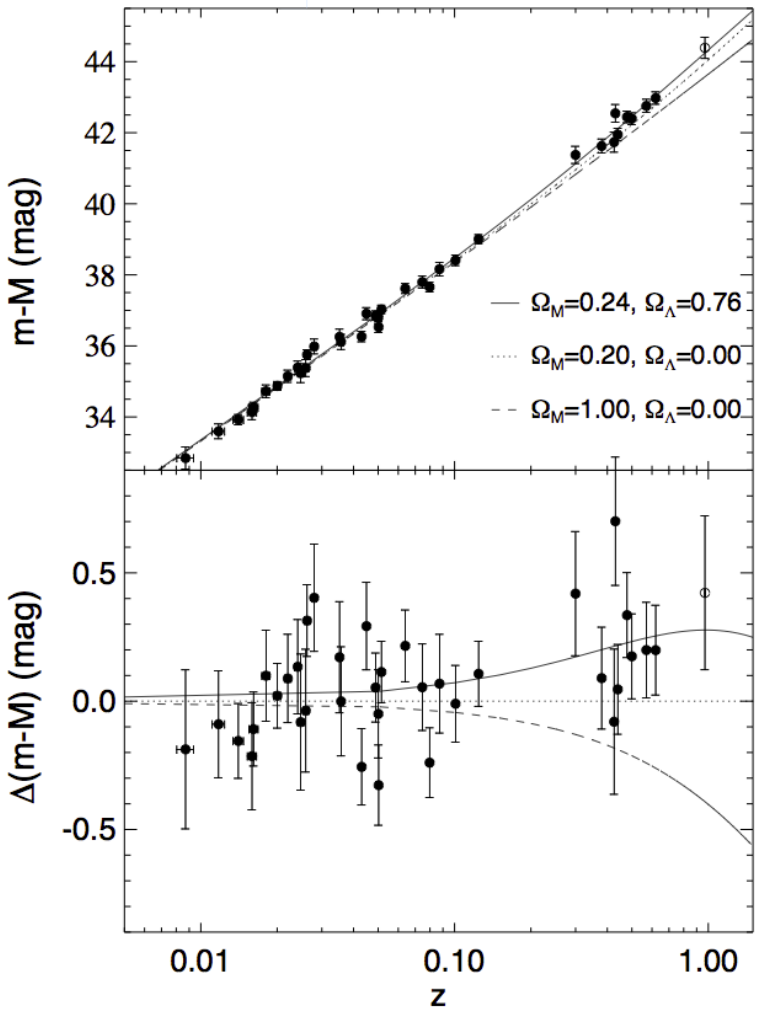

Figure 1.3 *Difference between observed and intrinsic magnitude for Type Ia supernovae out to $z \sim 1$ taken from Riess et al. (1998). The data are compared to three different cosmologies and favour model with a non-zero value of Ω_Λ*

properties of galaxies and not cosmology, it is enough for my purposes to accept ΛCDM as the current best model available for the descriptions of the Universe as a whole, and as the basis for our understanding of galaxy formation and evolution.

1.1.2 Formation and Evolution of Galaxies

To summarize the above discussion, the initial conditions for galaxy formation, specified by the ΛCDM cosmological model, is an isotropic distribution of neutral gas (75% H, 25% He) and dark matter seeded with density perturbations originating shortly after the Big Bang. The puzzle of galaxy formation is discovering how these perturbations grow with time, and how the baryonic gas is eventually turned into the stars, and by extension galaxies, we observe throughout the Universe.

Formation of Dark Matter Halos

Since dark-matter only interacts gravitationally, the formation of the large-scale dark matter structure in the Universe is can be accurately modeled. The current idea is that the dark matter particles will collapse under gravity within the initial density perturbations. This collapse quickly becomes a non-linear process but can be accurately simulated with modern N-body gravitational codes (e.g. Springel et al., 2005a). Eventually the collapsing dark matter will be supported against further gravitational collapse by the random motions of the constituent particles, and at this point a dark matter halo has formed (Benson, 2010).

The first halos will form from the smallest-scale density perturbations, and subsequent halos will be built up via the merging of these first halos, a scenario known as hierarchical structure formation (Kauffmann et al., 1993). The mass distribution of the dark matter halos at a given time since the Big Bang was first proposed by Press & Schechter (1974), and this work was subsequently built upon to calculate the distribution of halo progenitor mass for a given halo, at a given redshift (Lacey & Cole, 1993). These analytical estimates of the halo mass distribution and merger history have since been verified and refined by large N-body simulations (e.g. Springel et al., 2005a).

The result of the whole process is a network of dense regions containing large dark matter halos interspersed with large voids and filamentary structures similar to

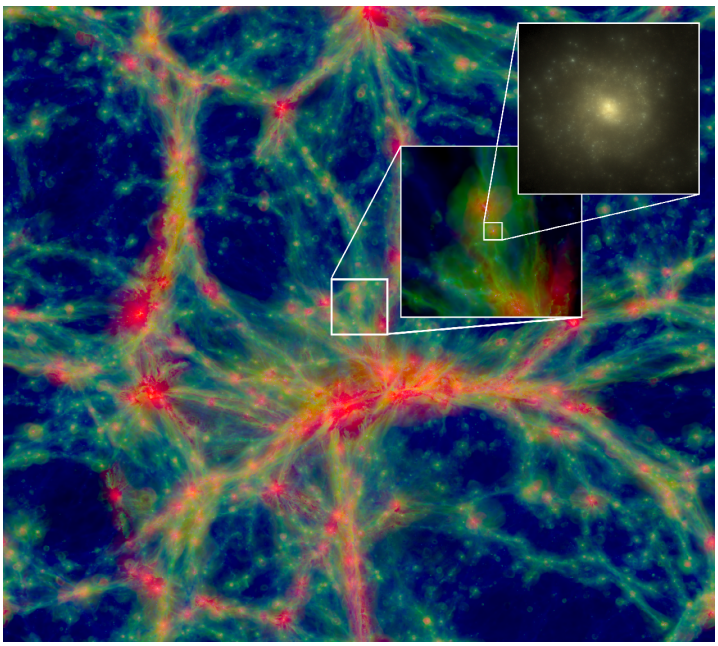

Figure 1.4 *A slice through the EAGLE N-body simulation (Schaye et al., 2015) showing the gas distribution in a* 100x100 *co-moving Mpc slice of the Universe at* $z = 0$*. The colour of the gas indicates the temperature with red hottest and blue coldest. The insets show two zoomed in regions of* 60x60 *and* 10x10 *co-moving kpc respectively with the final inset showing the simulated image of a galaxy formed within the gas.*

that seen with large spectroscopic surveys (see Fig. 1.2). However, these surveys trace the baryonic mass (since it is a distribution of galaxies on sky), therefore it seems apparent that the baryonic mass distribution traces the dark matter distribution. Understanding this process, and how the baryons cool and condense to form stars is the final step in understanding the formation of galaxies.

Gas Cooling and Formation of Galaxies

It is expected that the baryonic mass (i.e. gas) will, to first order, follow the distribution of dark matter as the baryons fall into the potential wells of the dark matter halos, since dark matter dominates the total matter budget of the Universe. As the gas falls into the halo it must cool in order to condense to the necessary densities for star-formation. In the case of the first stars, the primordial gas cannot cool radiatively because the thermal temperature of the gas is too low to excite the atoms present, therefore the gas must cool via the trace amounts of molecular hydrogen (Bromm et al., 2009). Once the first generation of stars has enriched the halo with metal and heated the gas, further cooling of the gas will be

dominated by atomic processes such as recombination and collisional excitation (Benson, 2010).

In the simplest picture, eventually enough gas will cool sufficiently over time and condense at the centre of the dark matter halo, stars will form within this dense, cool gas forming the first proto-galaxies. The proto-galaxy will then grow by accumulating more cold gas from the extended halo, and the stellar mass of the galaxy will increase with time as more and more stars are formed. However, in reality, the situation is more complex than this and accurate models of the physics of galaxy formation must take into account effects such as the merging of galaxies, the growth of black holes, formation of spheroids and disks, feedback from AGN and supernova on the halo gas, the chemical enrichment of the inter-galactic medium (IGM) and growth of dust grains.

Such modeling requires highly non-linear physics and advanced numerical techniques. The two main methods are N-body hydrodynamical simulations which attempt to solve the numerical equations directly via computer simulation (e.g. Schaye et al., 2015; Springel, 2005b, 2010), and 'semi-analytic' models which attempt to approximate some of physical processes analytically in order to save computational time (e.g. Cole et al., 2002; Guo et al., 2013; Somerville & Primack, 1999; White & Frenk, 1991). As can be seen in Fig. 1.4 modern N-body hydrodynamical simulations can reach exceptional levels of detail, however computational limitations require a compromise between simulation resolution and scale. Semi-analytic models also suffer from the same issues and the fact that the analytic approximations will at some point break-down, especially at smaller scales.

1.2 Observed Properties of Galaxies Through Cosmic Time

Observations of the main physical, chemical and dynamical properties of galaxies over cosmic time is key to our understanding of the processes that shape galaxy formation and evolution and provide vital constraints to the theoretical models. However, tracing in detail the formation of the different types of galaxies and galaxy structures we observe in the local Universe is a complex question. One has to answer, for example, how star-formation is initiated, how

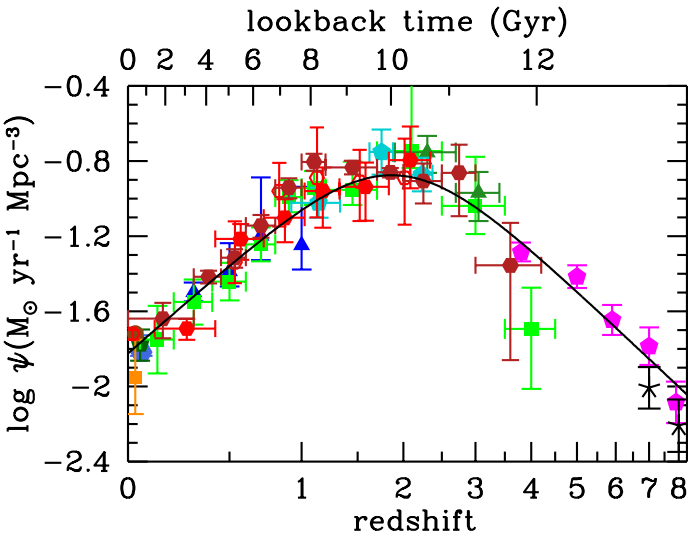

Figure 1.5 *History of cosmic star formation taken from Madau & Dickinson (2014). The data points are a compilation of data with star formation estimates from FUV and IR measurements.*

the disk/spheroid structures of a galaxy form, how different feedback processes from AGN/supernovae affect any subsequent star-formation, what effect different environments have on a galaxies evolution? In this section I will review these global properties to build up a broad picture of the history of galaxy evolution in the Universe; for example the rate at which stars have been forming in galaxies, the build up of stellar mass and the heavy elements, and the fraction of red dead and blue star-forming galaxies across the whole Universe as a function of time.

1.2.1 Cosmic Star Formation History

A key way to investigate how galaxies form and evolve in the Universe is to measure the global star formation rate density (SFRD) at a given epoch. Tracing the cosmic star formation history through the SFRD continues to be one of the main observational goals of extragalactic astronomy. Its use is two-fold since, as well as giving the star formation rate at any given redshift, the integral should return the assembled stellar mass in the Universe at that redshift, which can be independently measured. In practice the SFRD is obtained by first measuring the luminosity function at a given redshift and wavelength, which gives the number of galaxies per unit luminosity per unit volume; integrating the luminosity function gives the total luminosity density at that redshift which can then be converted into a SFRD following the Kennicutt (1998) or Kennicutt & Evans

(2012) prescriptions.

Indeed, much work has gone into measuring the cosmic star formation history over the past couple of decades, using a variety of different SFR indicators (e.g. FUV, IR, nebular emission lines), and at present the data stretches out into the re-ionization epoch at $z \sim 8 - 9$ (e.g. McLure et al., 2013). Recently Madau & Dickinson (2014) have compiled data from a variety of literature sources with star formation densities measured from either the UV and/or IR in the redshift range $0 < z < 8$ (representing ~ 12.8 Gyr of cosmic time, or 95% of the history of the Universe). Their SFRD plot, shown in Fig. 1.5, is in agreement with the general picture which has been emerging for the past ~ 20 years: a trend of increasing SFRD from early times until $z \sim 2$, after which there is a subsequent decline by an order of magnitude up to the present day ($z = 0$) (see e.g. Hopkins & Beacom, 2006; Lilly et al., 1996; Madau et al., 1998). The trend between $0 < z < 2$ has also been corroborated by pure emission line studies where SFR is traced via the Hα line (e.g. Sobral et al., 2013).

Perhaps unsurprisingly, the peak in the SFRD at $z \sim 2$ also coincides with the observed peak in the AGN activity in the Universe (e.g. Hopkins et al., 2007). Overall, a consistent picture is emerging whereby galaxy star formation and AGN activity peaks at $1 < z < 3$, which begs the question were the conditions in the Universe at this time different to the present day, and what is the cause of the quenching of this activity between then and $z = 0$? Clearly, this picture of SFRD evolution provides a key observational constraint on any theoretical models of galaxy formation and evolution.

1.2.2 Deriving Global Galaxies Properties from SED's

Due to the expense and difficulty of spectroscopic observations at high redshift, much of our understanding of galaxy formation and evolution is based on photometric techniques. The most common method of deriving galaxy properties from broad-band photometry is referred to as spectral energy distribution (SED) fitting. The concept of SED fitting is to take a library of synthetic stellar population models (e.g. Bruzual & Charlot, 2003) (BC03), which have been derived using either theoretical stellar evolution models, real stellar spectra, or a mixture of both (see Conroy, 2013, for a comprehensive review). These stellar population models are then used to generate models for the broad-band stellar continuum of a galaxy as a function of various physical properties including the

star-formation history (SFH), stellar initial mass function (IMF), total mass in stars, stellar metallicity, stellar population age and dust attenuation. To fit an SED, all these physical parameters are varied until the best-fitting solution to the photometry is achieved, most often using a χ^2 minimization technique. Typically an IMF is assumed and all other parameters free to vary. Often, however, the redshift of the galaxy is unknown and is therefore added as an extra free parameter in SED modeling. Galaxy redshifts determined in this way are referred to as photometric redshifts and constitute the majority of redshift estimates in the $z > 1$ Universe.

Fig. 1.6 shows a basic illustration of the technique by comparing the SED of a solar-metallicity BC03 starburst template as a function of age in the UV+optical wavelength regime. The mock photometric measurements demonstrate how broad-band photometry can constrain important features of the global SED, for example the rise at UV wavelengths for young ages ($\sim$ 100 Myr) and the strong Balmer continuum break at intermediate ages ($\sim$ 300Myr). In theory, once the best-fitting SED is found for a given galaxy, the main physical parameters of that galaxy are known (e.g. SFR, mass A_v, age etc). However, it has been well established that many degeneracies exist in fitting broad-band SED's. Fig. 1.7 shows an example of one degeneracy between age and dust at UV wavelengths: two models are compared with different ages and dust extinctions, both models look very similar in the wavelength regime shown and would be difficult to distinguish using only UV photometry. Another important example is the age-metallicity degeneracy first comprehensively investigated in Worthey (1994) who found that a factor 3 change in age is almost completely degenerate with a factor 2 change in metallicity when attempting to fit stellar population models to optical and near-IR photometry. Other issues exist related to the modeling of stellar spectra at different evolutionary stages, most notably the contribution of thermally-pulsating asymptotic giant branch stars at near-IR wavelengths (e.g. Maraston, 2005). For a comprehensive review of SED fitting techniques and the current outstanding problems see the review of Conroy (2013).

Traditionally, SED fitting techniques were restricted to the UV - NIR wavelength regime however modern SED fitting codes have begun to incorporate IR-FIR wavelengths to cater for the increasing data quality at these wavelengths, which has become available through space telescopes such as the *Herschel Space Observatory* (Pilbratt et al., 2010). Fig. 1.8 shows a full UV-FIR SED template fit to three local Universe galaxies from da Cunha et al. (2008). Extension of the SED

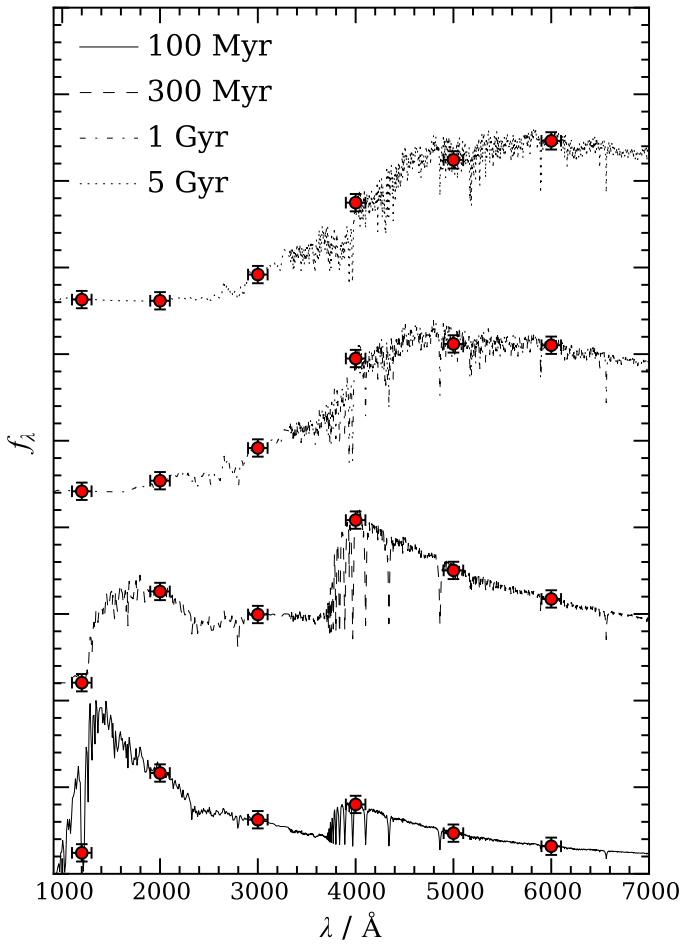

Figure 1.6 *Showing a starburst galaxy BC03 SED as a function of age. The red-points represent typical photometric measurements with which a given SED is fit to. Key features of the SED which can be picked up by photometry include the strong spectra break at* ~ 4000Å *for older populations*

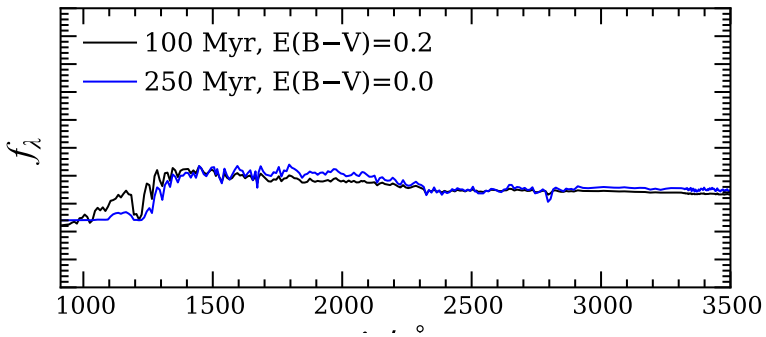

Figure 1.7 *Illustrating the age-dust degeneracy in the UV spectrum of a starburst galaxy. The black SED shows a 100 Myr starburst with E(B-V) = 0.2, whilst the blue SED shows a 250 Myr starburst with zero dust attenuation.*

to FIR wavelengths can provide important constraints on the dust attenuation at UV/optical wavelengths since energy conservation implies that the energy lost in the UV/optical must be re-emitted by dust in the FIR. This is illustrated in Fig. 1.8 where the cyan curves show the underlying stellar continuum and the black curve shows how the light attenuated in the UV/optical is re-emitted by dust in the IR.

In summary, fitting theoretical galaxy templates to observed photometry is a very powerful tool in helping to constrain the properties of galaxies, especially at high redshift where detailed spectroscopic measurements are challenging. However, it is also important to realise where potential degeneracies and systematic biases in these measurements may exist due to either a lack of sufficient high-quality data or gaps in our theoretical understanding (e.g. certain stages of stellar evolution, dust physics).

1.2.3 Stellar Mass Assembly

In an analogous manner to the star formation rate density, the history of stellar mass assembly can be traced through the stellar mass density (SMD) as a function of redshift by integrating the measured stellar mass function (SMF). As mentioned above, this independent measurement can be directly compared for consistency with SFRD measurements, since the integral of SFRD should be equal to the SMD. It is worth noting that unlike star formation, which can be well calibrated against single photometric measurements such as UV flux, and emission line signatures such as Hα, stellar mass measurements must also trace

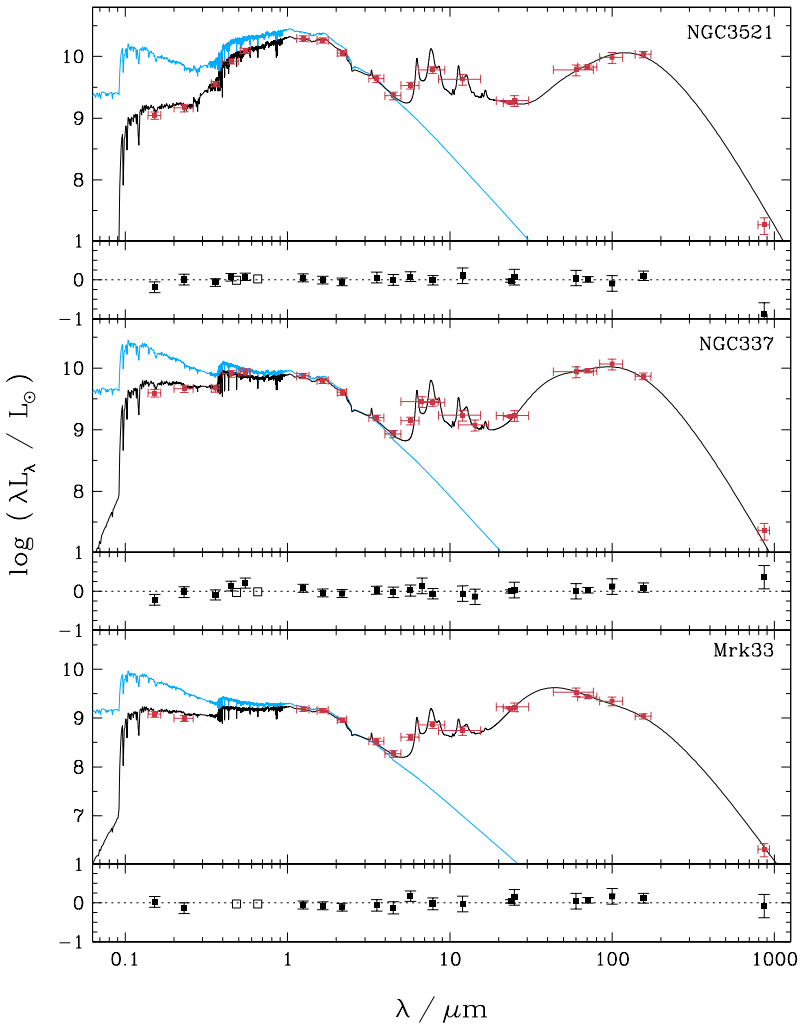

Figure 1.8 *From da Cunha et al. (2008) showing model fits (black) to observed photometry (red) from th UV-FIR for three galaxies in the local Universe: NGC 3521 (top), NGC 3521 (middle) and Mrk 33 (bottom). In each plot the blue line shows the unattenuated stellar continuum to illustrates how the energy lost in the UV/optical is re-emitted by dust at IR wavelengths ($\gtrsim 5\mu$m). The smaller intermediate panels show the offsets between model and photometry for each of the fits.*

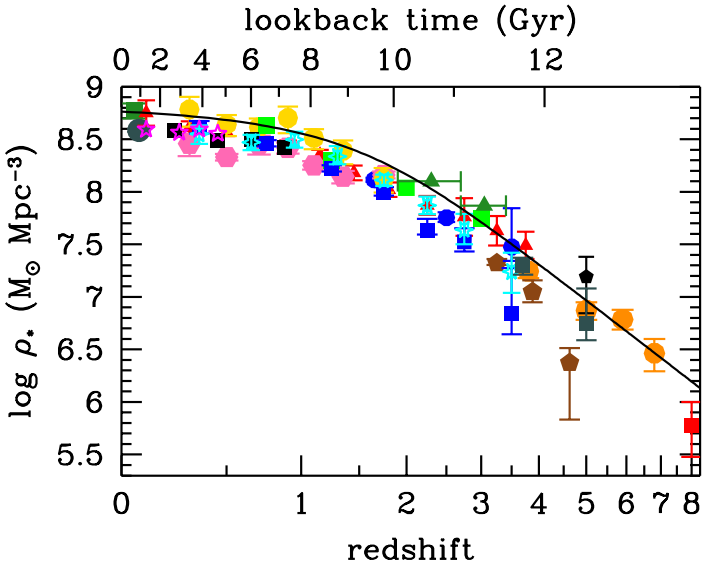

Figure 1.9 *Evolution of the stellar mass density from $z = 8$ to $z = 0$ taken from Madau & Dickinson (2014). The plot shows a compilation of many different surveys and datasets which all show reasonable agreement within the errors. The black line shows the stellar mass density evolution obtained by integrating the best fitting line to the cosmic star formation rate density shown in Fig. 1.5.*

the old evolved stellar population, and therefore rely on large sets of good quality multi wavelength photometry.

Figure 1.9 shows a recent compilation of stellar mass density evolution data from Madau & Dickinson (2014) covering the redshift range $0 < z < 8$. The compiled data covers a range of different redshift baselines (e.g. Ilbert et al., 2010a; Marchesini et al., 2009; Moustakas et al., 2013; Muzzin et al., 2013, and many more), and reassuringly all show good agreement within the errors, generally to within a factor 2. As can be seen from the figure there is a steady build up of stellar mass between $z = 8$ to $z = 1$, after which the data flattens out to a roughly constant SMD between $z = 1$ and $z = 0$, coinciding with the truncation of global star formation from Fig. 1.5.

The solid line in Fig. 1.9 shows the inferred SMD obtained by integrating the best fitting SFRD function from Fig. 1.5, assuming that 27 % of the mass in stars is returned to the ISM (this 'return fraction' assumes a Salpeter IMF). This model is higher than most of the data by ~ 0.2 dex (factor ~ 1.4), though some data is in excellent agreement. Reassuringly, the shape of the curve is in excellent agreement and the inconsistencies appear to be an issue with the normalization

(i.e. systematically overestimated star-formation rates and/or underestimated stellar masses). Furthermore, there are many reasons to suspect such systematic issues do exist in the measurements, for example SFRs may by overestimated due to over-correcting for dust, and there are uncertainties inherent in extrapolating the luminosity function beyond current observational limits in both the UV and IR. Alternatively stellar masses may be underestimated when using simplified star formation histories (e.g. Pforr et al., 2012).

Overall, however, there is now good general agreement between measurements of the SFRD and SMD which corroborate a picture of a rapid build up of stellar mass in the Universe up to $z \sim 2$, after which there is a rapid decline in the rate at which galaxies form new stars. Nevertheless, systematic issues still persist in these measurement which remain to be fully understood.

1.2.4 Bi-Modal Galaxy Population

The shutting down of star formation from $z \sim 1$ has by extension led to a build up in passively evolving red 'dead' galaxies since that time. Indeed, large surveys of the local Universe such as the Sloan Digital Sky Survey (SDSS) have identified the existence of a distinct bi-modality in the galaxy population, backed for the first time by extremely robust statistics (e.g. Baldry et al., 2004; Blanton, 2006). The observations suggest the existence of a so called 'red sequence' and 'blue cloud' between which the galaxy population is split. Galaxies in the red sequence are red in colour and typically seen to be quiescent elliptical early-type galaxies with old stellar populations and little evidence for on going star formation, whilst galaxies in the blue cloud are blue in colour and mainly seen to be late-type spiral galaxies with typically younger stellar populations showing evidence of current star formation. A key question that has been sought to be addressed in the past decade is how the stellar mass densities of the populations evolve, and whether they contribute equally, or unequally, to the global evolution of the stellar mass density. At high redshift it is still possible to identify and select these two populations by using color-color diagrams (e.g BzK at $1.4 < z < 2.5$; Daddi et al. (2004)) or using rest-frame colors (e.g. UVJ; Williams et al. (2009)). Using these techniques a population of red sequence galaxies have been found to much higher redshift but at significantly decreased number densities compared to the local Universe (e.g. Brammer et al., 2009; Muzzin et al., 2013).

In a recent study, Muzzin et al. (2013) derived the stellar mass functions of

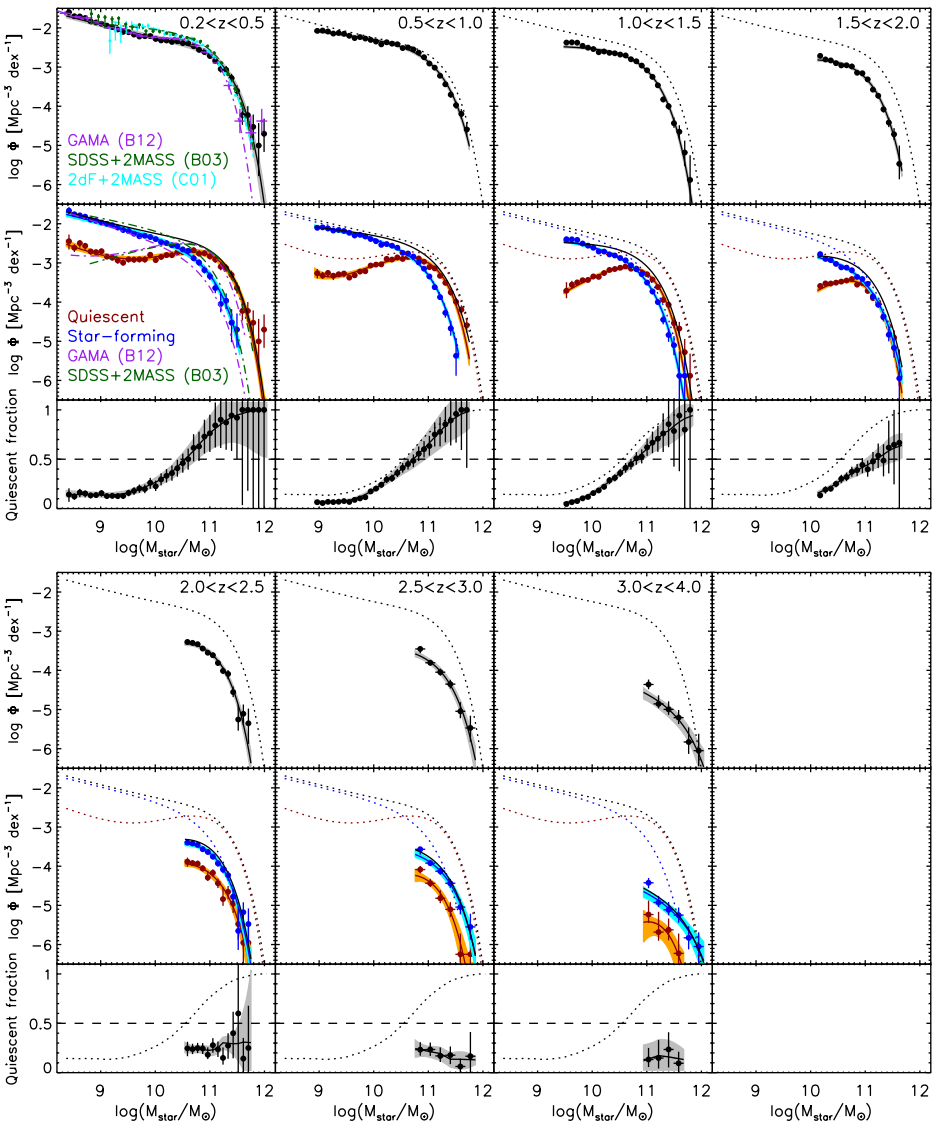

Figure 1.10 *The top panels show the stellar mass functions of the total galaxy population in 7 bins from $z = 0$ to $z = 4$ from Muzzin et al. (2013). The middle panels show the stellar mass functions split into the quiescent (red) and star-forming (blue) populations. The bottom panels show the fraction of quiescent galaxies as a function of stellar mass. The dotted lines show the total, star-forming and passive stellar mass functions in the $0.2 < z < 0.5$ bin.*

quiescent and star-forming galaxies separately between $z = 0$ and $z = 4$. The results are shown in Fig. 1.10 where is can be seen that, at lower stellar masses, star-forming galaxies dominate the mass fraction at all redshifts, while at the largest stellar masses, star-forming galaxies only dominate from $z = 4$ to $z \sim 1$, after which most high-mass galaxies become quiescent systems. Many other studies have also come to similar conclusions (e.g. Brammer et al., 2011; Cirasuolo et al., 2007; Ilbert et al., 2010b).

It can also be seen from Fig. 1.10 that the SMF for star-forming galaxies remains approximately constant across the full redshift range, whereas there is a rapid evolution in the quiescent galaxy mass function towards a higher fraction of mass in quiescent galaxies across the full range of stellar masses. The overall picture is somewhat counter intuitive since mass density is building up in galaxies which are not forming stars, whilst remaining constant among the population that would naively be expected to be increasing its stellar mass by star formation. Such a scenario can be achieved if massive star forming galaxies are somehow having their star formation quenched and migrating from the blue cloud to the red sequence. The question then becomes what physical process can shut down star formation in galaxies so effectively, and why is this happening more efficiently in the highest mass star-forming galaxies? The more rapid evolution onto the 'red-sequence' of more massive galaxies is often referred to as 'downsizing' (e.g. Cowie et al., 1996).

Overall a coherent picture has begun to emerge over the past decade of a bimodal galaxy population extending out to $z \sim 4$, which is mostly formed of star-forming galaxies at $1 < z < 4$, with passive galaxies dominating at $z < 1$.

1.2.5 Evolution of the Metals

Another important global property of galaxies is the metal content in the ISM and stars. Tracing the build up of the heavy elements, which form in stars and are distributed to the ISM and IGM by stellar winds and supernova explosions, tells us about the history of past star formation in galaxies, as well as the inflow and outflow of material driven by galactic scale winds. Unlike star formation rates and stellar masses, measurements of the metal content of gas and stars requires spectroscopic observations and can be achieved in a number of different ways. For example, stellar metallicities are measured through absorption lines in stellar spectra; the metallicity of neutral gas in the IGM can be probed using absorption lines imprinted on the spectrum of distant quasars; and the metallicity of the gas

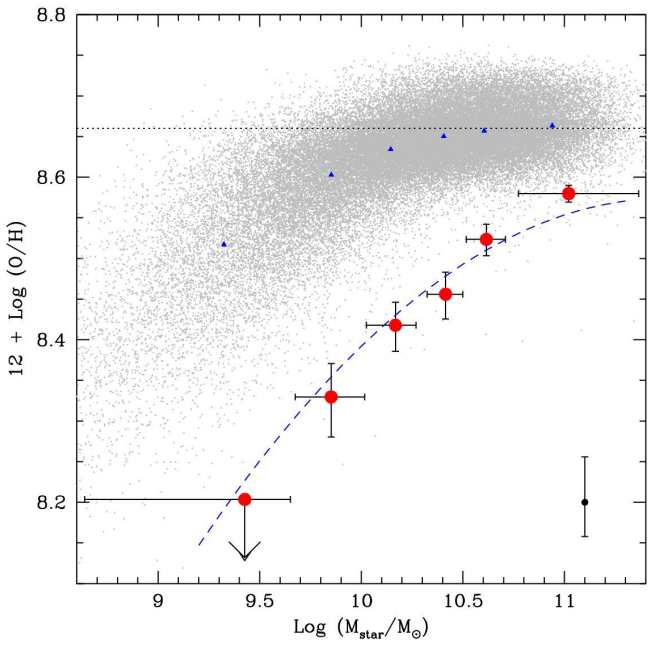

Figure 1.11 *The mass-metallicity relationship from Erb et al. (2006b) at $z \sim 2$ (red) compared to the $z = 0$ measurements from Tremonti et al. (2004) (grey). The horizontal dotted line shows the solar oxygen abundance. The error bar in the bottom corner shows the systematic uncertainty associated with the specific metallicity calibration used. The blue dashed line shows the best fit $z = 0$ MZR of Tremonti et al. (2004) shifted downward by 0.56 dex.*

within a galaxy can be estimated from the nebular emission lines emanating from star-forming regions.

At high redshift, obtaining stellar metallicities is extremely difficult and has only been achieved for a small number of galaxies (e.g. Pettini et al., 2000; Sommariva et al., 2012), and absorption lines studies trace mainly the metal content of the IGM (e.g. Aguirre et al., 2008; Simcoe, 2011). Most commonly, when referring to the metallicity of galaxies as a function of time, especially at high redshift, one is referring to nebular emission line metallicities (e.g. Erb et al., 2006b; Maiolino et al., 2008; Tremonti et al., 2004). These gas-phase metallicities are quoted in terms of the oxygen abundance and are expressed in the form 12+log(O/H), which gives the logarithm of the number of oxygen atoms for every 10^{12} hydrogen atoms. A detailed review of the way these nebular line metallicities are measured is given in Section 1.3.6. Here I will review insights that have been made over the past decade in measuring metallicities with this technique throughout the Universe's history.

Unlike with stellar masses and star-formation rates, there is not a 1:1 relation

between the metallicity of galaxies and the global metallicity content of the Universe. This is because metals in a galaxy can be expelled from the ISM through winds driven by stars and supernovae (see e.g. Finlator & Davé, 2008, for descriptions of various wind models), and the metallicity can be diluted by the infall of metal-poor gas from the IGM (e.g. Dekel et al., 2009). Most commonly the metallicity of a galaxy is traced as function of stellar mass to construct the mass-metallicity relationship (MZR), and more recently as a function of both stellar mass and star-formation rate to construct the so called fundamental metallicity relation (FMR). Observations of the MZR and FMR at different redshifts allow us to track the evolution of the metals in galaxies with time.

The Mass-Metallicity Relation

Initial studies into the relationship between mass and metallicity dates back to the work of Lequeux et al. (1979), where, before sophisticated SED modeling had been introduced, galaxy luminosity was used as a proxy for stellar mass. With the advent of the SDSS Tremonti et al. (2004) conducted the first statistically comprehensive study of the MZR in the local Universe with a sample of $\sim$ 53,000 galaxies, finding a metallicity increase with increasing stellar mass (see Fig. 1.11). Since then the MZR has been studied out to $\sim 3-4$ (see Chapter 3 and e.g. Cullen et al., 2014; Erb et al., 2006b; Maiolino et al., 2008; Savaglio et al., 2005; Shapley et al., 2015; Steidel et al., 2014; Troncoso et al., 2014; Zahid et al., 2014a, for a thorough, but by no mean comprehensive compilation of MZR's across cosmic time).

The general consensus of these studies is that a MZR is observed at all redshiftS, with a shape similar to the one observed at $z = 0$, but with a decreasing normalization. This is illustrated in Fig. 1.11 where the $z \sim 2$ study of Erb et al. (2006b) is compared to the Tremonti et al. (2004) data. The shape of the MZR has been speculated to arise from a number of physical effects including decreasing outflow efficiency with stellar mass (Finlator & Davé, 2008; Kobayashi et al., 2007), increased star-formation efficiency at larger stellar mass (Calura et al., 2009), possible mass-dependent variations in the IMF (Koppen et al., 2007), or mass dependent gas inflow rates regulating the gas-to-stellar mass ratio (Zahid et al., 2014b). However, there still remain inconsistencies in the measured slope of the MZR, especially at high redshift, and therefore a more solid theoretical footing needs to be established before any theoretical conclusions can be drawn.

For example the recent $z \sim 2$ study of Steidel et al. (2014) find a much shallower MZR slope at this redshift than the Erb et al. (2006b) relation shown in Fig. 1.11.

Consistently however, at increasing redshift, galaxies of a given stellar mass are found to have lower gas-phase metallicities. Interestingly, this evolution is relatively slow when considering the time scales involved: a factor ~ 2 increase in metallicity over ~ 10 Gyr. The evolution can be naively interpreted as a build up in the global metallicity content of the Universe however again the inconsistencies and biases in observations must be fully understood before this can be firmly established, for example the inconsistencies between different line indicators at high redshift and the systematic offsets between different metallicity diagnostics (Cullen et al., 2014; Kewley & Ellison, 2008; Steidel et al., 2014), the possible biases introduced by selection effects at high redshift (Juneau et al., 2014) and the possible star formation rate dependence on metallicity which will be discussed below (Lara-Lopez et al., 2010; Mannucci et al., 2010).

The Fundamental Metallicity Relation

The FMR introduces star formation rate as a third parameter in the MZR to explain both the scatter observed in the SDSS relation and the redshift evolution of the relation up to $z \sim 2$. The concept was first introduced by Mannucci et al. (2010) and Lara-Lopez et al. (2010) though the SFR dependence of the MZR had first been noted by Ellison et al. (2008). In their original paper, Mannucci et al. (2010) proposed a FMR which defines a surface in the three dimensional mass-metallicity-SFR space, and in Mannucci et al. (2011) this original FMR was extended to lower masses. The nature of the FMR is illustrated in Fig. 1.12, from the original Mannucci et al. (2010) paper, which shows how the scatter in the SDSS MZR is simply related to the scatter in the SFR of the sample. The nature of the SFR dependence is such that high SFR galaxies, at fixed stellar mass, will have lower gas phase metallicities.

In Mannucci et al. (2010) local SDSS galaxies lie on the FMR surface with a residual dispersion of ~ 0.05 dex in metallicity. Many other studies have since investigated the SFR dependence of the MZR in the SDSS dataset, with some variations seen depending on the methodology adopted, e.g. the turnover in SFR dependence at high stellar mass in Yates et al. (2012) or the stronger SFR dependence measured using different metallicity calibrations in Andrews

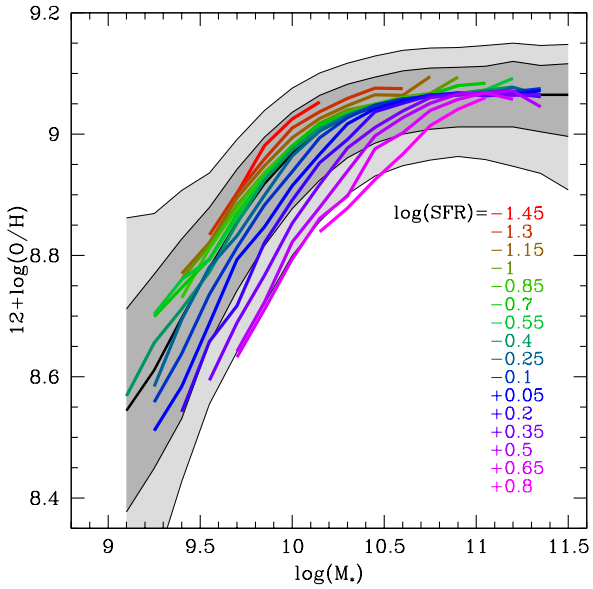

Figure 1.12 *Showing the mass metallicity relation of SDSS galaxies split into bins of star formation rate. The grey shaded areas contain, respectively 64% and 90% of all SDSS galaxies with the thick black line showing the median MZR relation. The coloured lines show the median MZR for different bins of star formation rate, showing how the spread in metallicities in the SDSS sample is a strong function of star formation rate.*

& Martini (2013). However, overall, the existence of some form of FMR in the SDSS dataset has now become well established observationally. Many theoretical interpretations of the FMR also exist in the literature, for example Dayal et al. (2013) re-create the local FMR with an analytical model in which, at higher SFR, galaxies can generate stronger outflows to eject the metal-enriched ISM gas, with this effect becoming more pronounced at lower stellar masses.

Intriguingly, the FMR defined locally was also found, using the data from Erb et al. (2006b), to extend out to $z \sim 2.5$ in Mannucci et al. (2010), above this redshift, however, a strong deviation was observed in the $z \sim 3-4$ data of Maiolino et al. (2008) and Mannucci et al. (2009). These observations suggested that the process of star-formation and gas is recycling into and out of the IGM had been constant over the past ~ 10 Gyr of cosmic time, before which some fundamentally different process governed the build up of stars and metals in galaxies.

However, the redshift evolution of the FMR still remains a much debated topic. Many subsequent studies between $z = 0$ and $z = 2$ have appeared to confirm

the initial observation of Mannucci et al. (2010), (e.g. Belli et al., 2013; Cresci et al., 2012; Henry et al., 2013b), whereas other studies either find little or no SFR dependence at high redshifts (Steidel et al., 2014; Zahid et al., 2014a), or a different degree of evolution in the FMR up $z \sim 2$ (Sanders et al., 2015; Wuyts et al., 2014). As will be discussed in Chapter 3 of this thesis, and as argued in Cullen et al. (2014), systematic effects in the use of locally calibrated metallicity indicators may also be biasing our measurements of the FMR at high redshift.

1.3 Optical Emission Lines in Star-Forming Galaxies

Much of the remainder of this thesis is concerned with measuring galaxy properties from optical emission lines in their spectra. Therefore, to finish the introduction, it is worth reviewing what we can learn about a galaxy from these emission lines. Optical emission lines reveal detailed physical information about a galaxy such as the rate of star-formation, the chemical abundance of the ISM and the number of ionizing photons in star-forming regions (commonly referred to as HII regions). They also allow us to identify galaxies undergoing an Active Galactic Nuclei phase (AGN) in their evolution. Though the rest-frame optical is not the only wavelength regime in which detailed spectroscopic measurements can provide estimates of these quantities (e.g. Lyα studies in the UV and CO studies in the infra-red), the optical window is, for obvious reasons, the most studied and well-understood region of a galaxies spectrum. In this section I will give an overview of the properties of emission-line galaxies at optical wavelengths across cosmic time, comparing observations in the redshift range ($0 < z < 4$) with the state-of-the-art photo-ionization models which comprise our current theoretical understanding of optical emission from galaxies and AGN.

1.3.1 Physics of Nebular Emission Lines

First, I will give a brief overview the physics of nebular emission from gas in galaxies. The basic astrophysical situation is illustrated in Fig. 1.13 (taken from De Marchi et al., 2011)), a young cluster of new stars form within a gas cloud and the high energy ultra-violet radiation from the stars excites elements within the gas and heats it. The excitation occurs either via photo-excitation or through

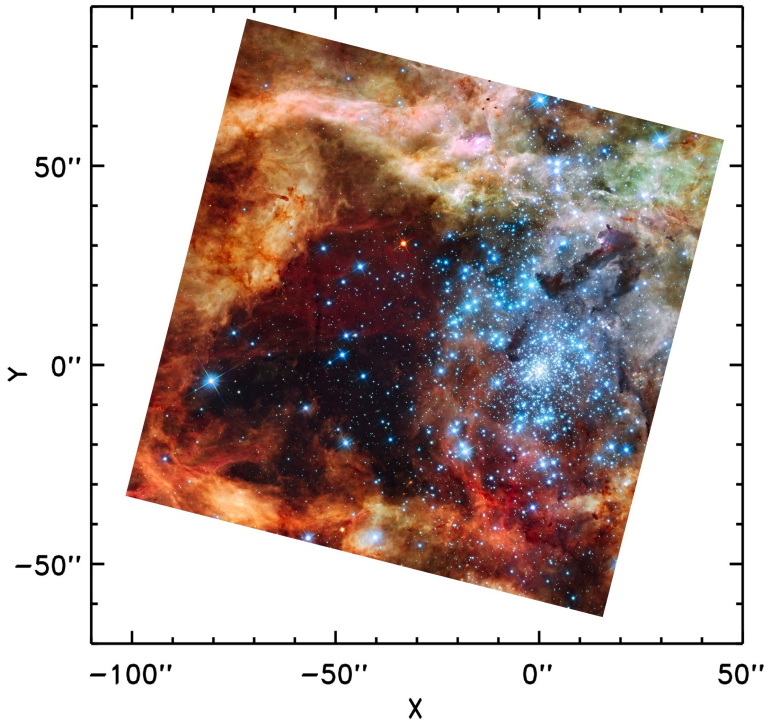

Figure 1.13 *A color composite image of the 30 Doradus star-forming region (or Tarantula Nebula) in the Large Magellanic Cloud (LMC) taken from De Marchi et al. (2011). A large cluster of bright young stars is visible surrounded by the remnants of the gas cloud from which they formed.*

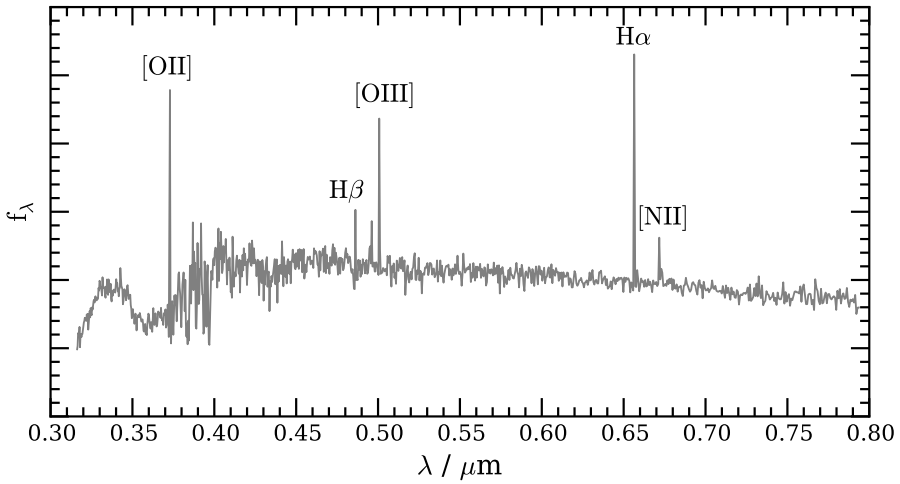

Figure 1.14 *Example SDSS spectrum showing the most prominent optical emission features of a star-forming galaxy.*

collisions, and the excited elements then emit radiation as they fall back to the ground state. The optical radiation from the star-forming region is then observed as a continuum (from the capture of thermal electrons in the gas) plus emission lines from these excited elements. Fig. 1.13 shows the star-forming region 30 Doradus in the Large Magellanic Cloud (LMC) in which both the young blue stars and the diffuse gas surrounding them are visible. Another scenario can also occur in which the gas is not heated predominantly by ionizing radiation from stars, but by ionizing radiation from an AGN. Therefore, an important point to note is that, when studying optical emission line spectra, we are probing the physical conditions of the gas surrounding newly born stars (from which they were presumably formed), or likewise the gas around AGN at the centres of galaxies.

1.3.2 Theoretical Modeling of HII Regions

Before observations can be understood we first require a theoretical framework within which to interpret them. Fig. 1.14 shows a typical star-forming galaxy spectrum in the wavelength range $0.3 - 0.8\mu$m, labeled in the figure are the most prominent optical emission line features: [OII], Hβ, [OIII], Hα, [NII]. In this section I will explore how using these emission lines we are able to come to an understanding of the physical processes acting in star-forming regions in galaxies across cosmic time. In other words, we wish to understand under what physical conditions do a cluster of young stars, embedded in a gas cloud, produce the

spectrum observed in Fig. 1.14.

1.3.3 AGN - Star-Forming Separation

The first question to address is what is the source of ionizing radiation producing the optical spectrum? Much of the pioneering work into this issue was conducted in the 1980's, for example Baldwin et al. (1981) showed theoretically how the position of galaxies in the [OIII]/Hβ vs. [NII]/Hα emission-line ratio plane (hereafter BPT diagram) could be used to separate star-forming galaxies from AGN. Using the BPT diagram, galaxies in which the dominant form of nebular excitation was produced by starlight could be distinguished from those in which an AGN dominated the nebular excitation. This distinction is of vital importance because, before anything can be said about the physical properties of the gas, the source of ionizing radiation illuminating it must first be known. The general physical principle underlying the BPT diagram is that the harder extreme ultraviolet (EUV) radiation from AGN would produce more photons capable of ionizing metallic species such as oxygen and nitrogen, thus producing larger [OIII]/Hβ and [NII]/Hα ratios.

This fundamental AGN/star-formation difference is illustrated in Figure 1.15 where I compare the EUV spectrum of a young star-forming galaxy to three power-law spectra typical of AGN (all normalized to the flux at 1000Å). The star-forming galaxy spectrum, generated using the `STARBURST99` spectrophotometric modeling code (Leitherer et al., 2014, 2010, 1999), represents the EUV output of a 10^4 year old starburst. At this age main sequence O-type stars (lifetime $\sim 10^6$ years) are still burning therefore the spectrum represents a snapshot of a star-forming galaxy at the peak output in the EUV. The three AGN spectra are power laws of the form $f_\nu \propto \nu^\alpha$ (with α in the range -1.5< α <-2.0) transformed into f_λ. These power law spectra are consistent with the most recent observations of AGN at $0 < z < 1.44$ (e.g. Shull et al., 2012) and are commonly used in modern photoionization models (e.g. Kewley et al., 2013a). Fig. 1.15 illustrates how the fraction of EUV photons above 1000Å is elevated for power-law AGN spectra relative to the EUV generated by starburst galaxies for these typical α values. The effect is also illustrated in Fig. 1.16, taken from Steidel et al. (2014), where the ionizing photon density is shown as a function of photon energy for different models of the EUV spectra. Again, for the power law model representative of AGN, the photon density at energies equivalent to the ionization potential for

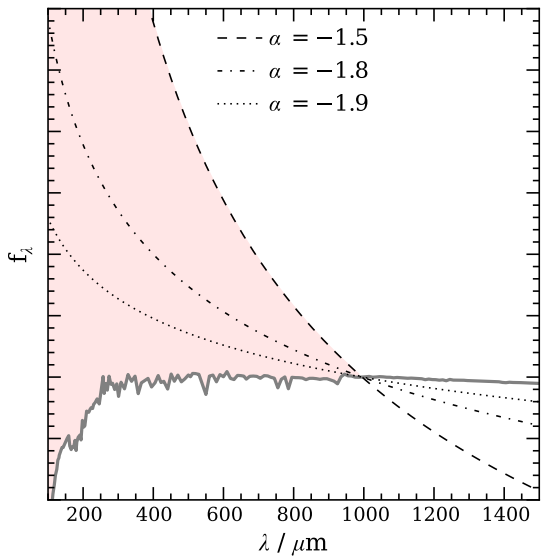

Figure 1.15 *Tick solid grey line shows the EUV spectrum of a* 10^4 *year old instantaneous burst from the STARBURTS99 models. The dashed, dot-dashed and dotted line show power-law EUV spectra typical of AGN with* α *= -1.9, -1.8, -1.5 respectively. All spectra are normalized to the flux at 1000*Å*. The filled red region illustrates the excess of EUV photons in the AGN spectra.*

the OII-OIII and NI-NII transitions are elevated with respect to the star-forming models. The result of the harder EUV radiation on the optical emission is show in Fig. 1.17 where the star-forming galaxy spectrum from Fig. 1.14 is compared to a characteristic AGN optical spectrum (Seyfert-II type). Notable in the Seyfert-II spectrum is the elevated emission strength of the high-ionization [OIII] and [NII] emission lines as a result of the harder EUV field.

These physical ideas have since been verified by numerous observations. The first semi-empirical separation of star-forming galaxies and AGN in the BPT diagram was carried out by Osterbrock & Pogge (1985) and Veilleux & Osterbrock (1987) using a combination of observations and photoionization models. This early work was subsequently built upon using improved stellar evolution and photoionization models by Dopita et al. (2000) and Kewley et al. (2001). Kewley et al. (2001) (K01) provide a classification line giving the upper limit of the [OIII]/Hβ ratio at a given [NII]/Hα for 'extreme' starburst galaxies assuming the case of continuous star-formation within a galaxy. With the advent of the SDSS survey (York et al., 2000), which provided a wealth of optical spectra for nearby galaxies, the classification schemes were put to the test for the first

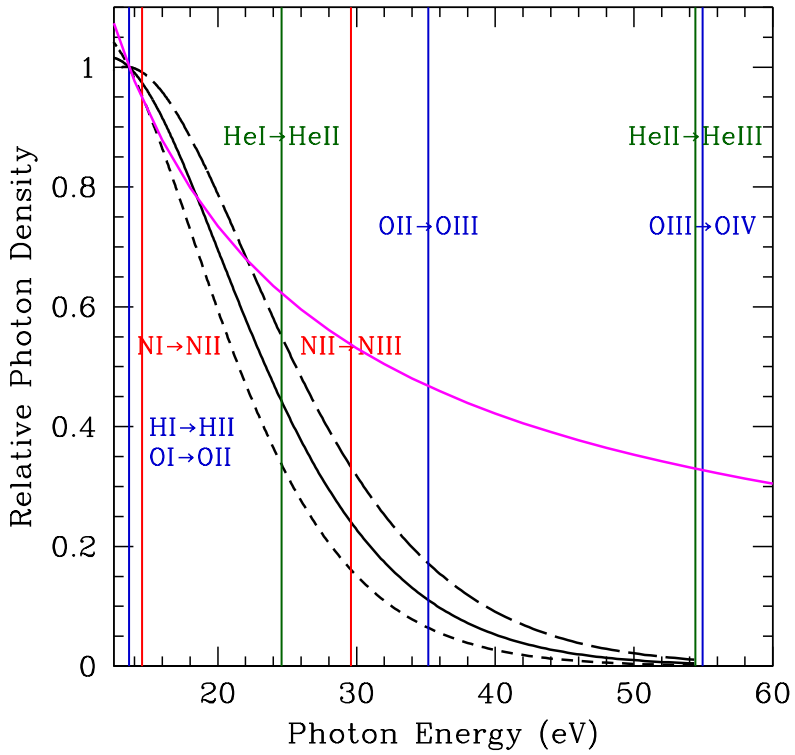

Figure 1.16 *Showing the relative intensity of ionizing photons for various models of the EUV spectra of star-forming galaxies taken from Steidel et al. (2014). The vertical lines show the ionization potentials of relevant elements. The short-dashed, solid and long-dashed black lines show models for black-body spectra with effective temperatures 45000, 50000 and 55000K respectively. The magenta line is a power law spectrum of the form $f_\nu \propto \nu^\alpha$ with $\alpha = -0.8$, slightly steeper than those shown in Fig. 1.15.*

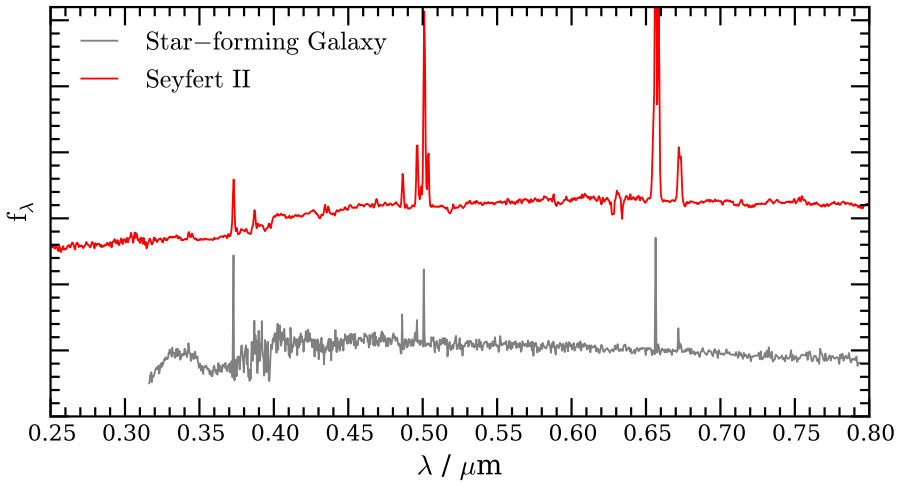

Figure 1.17 *Grey line shows the SDSS star-forming galaxy spectrum as in Fig. 1.14, the red line shows for comparison a Seyfert-II type spectrum. The y-axis is curtailed for clarity of comparison.*

time with a large statistical sample of galaxies. Kauffmann et al. (2003a) (K03) investigated the positions of 122,808 SDSS galaxies at $0.02 < z < 0.3$ in the BPT diagram, finding most SDSS galaxies fell well below the K01 demarcation line. They provided a new, purely empirical, demarcation line based on their data.

Fig. 1.18 shows the BPT diagram for SDSS galaxies (line ratios taken from the JHU/MPA DR7 catalogues[1]) along with the K01 and K03 demarcations lines. From Fig. 1.18 three populations of galaxies can be discerned: the tight sequence of purely star-forming galaxies below and to the left of the K03 line, the purely AGN-ionized galaxies above and to the right of the K01 line, and the composite galaxies (mix of star-formation and AGN) in between the K03 and K01 lines.

Also marked in Fig. 1.18 is the position of the 'abundance' sequence of star-forming galaxies (red curve). Understanding how this sequence is formed provides key insights into the physical conditions in star-forming regions, and since this thesis is primarily concerned with the properties of purely star-forming galaxies, for the remainder of this section I will limit the discussion to the optical emission line properties of these galaxies, neglecting a discussion of pure AGN or composite galaxies.

[1]http://www.mpa-garching.mpg.de/SDSS/DR7/

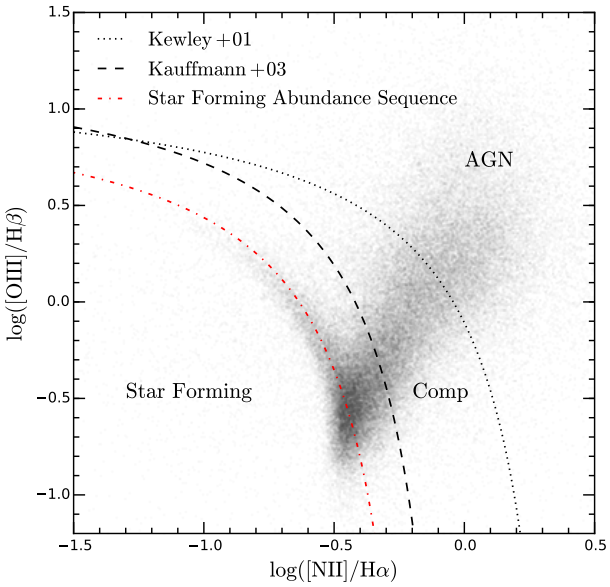

Figure 1.18 *Showing the position of SDSS galaxies in the BPT diagram, also shown are the Kewley et al. (2001) and Kauffmann et al. (2003a) demarcation lines. The red dot-dashed line shows the position of the star-forming abundance sequence taken from Kewley et al. (2013a).*

1.3.4 Star-Forming Abundance Sequence

The tight correlation of star-forming galaxies in the BPT diagram contains a wealth of physical information. There are five main factors which determine the value of the [OIII]/Hβ and [NII]/Hα ratio in galaxies: (i) the shape/strength of the EUV field illuminating the gas, (ii) the metallicity of the gas, (iii) the density/pressure of electrons within the gas, (iv) geometrical distribution of the gas and (v) shocks from supernovae/stellar winds (Kewley et al., 2013a). The fact that SDSS star-forming galaxies form such a tight-sequence in the BPT diagram tells us a lot about the distribution of these parameters in star forming galaxies in the local Universe. Below I will briefly discuss each of the above factors.

(i) Shape of EUV field: As discussed above (and illustrated in Figs. 1.15 and 1.16) the shape of the EUV field incident on gas in a HII regions affects the relative photon density of higher energy photons capable of overcoming larger ionization potentials. Thus a harder EUV spectrum will result in more [OIII] and [NII] ions and hence stronger [OIII] and [NII] emission.

(ii) Metallicity of the gas: Metallicity affects the absolute amount of oxygen

and nitrogen relative to hydrogen in the gas phase. Therefore to first order an increase in the metallicity will cause an increase in the [OIII]/Hβ and [NII]/Hα ratios. However, as will be discussed in later sections, the situation is in reality more subtle. As metallicity increases the nebula cools more efficiently, there are less high-energy electrons to collisionally excite [OIII] and [NII], and so the ratios decrease. Thus the metallicity dependence is not simply monotonic. In practice the metallicity determines the position along the abundance sequence in the BPT diagram (see e.g. Kewley & Dopita, 2002; Kewley et al., 2013a; Maiolino et al., 2008).

(iii) Electron density: The electron density determines the rate of collisional excitations capable for exiting [OIII] and [NII] ions. It is governed by the ISM pressure and electron temperature via $n_e = \frac{P}{T_e k}$ (Kewley et al., 2013a). A higher electron density results in larger [OIII]/Hβ and [NII]/Hα ratios. It is worth noting here that the effects of the hardness of the EUV field and electron density is often encapsulated in the term known as the ionization parameter, which is defined as the ratio of the density of ionizing photons to the density of free electrons (Osterbrock, 1989). The ionization parameter can be measured by taking the ratio of two ionization states of the same element. For example the line ratio [OIII]/[OII] can be used, and since both are strong emission lines the ionization parameter can be estimated out to high redshift more easily than electron density or ionizing photon density alone.

(iv) Geometrical distribution of gas: A clumpy, non-uniform, gas distribution within an HII region may affect line ratios by allowing ionizing photons to escape. The effect is to reduce the density of [OIII] and [NII] ions. Yeh & Matzner (2012) show that in the case of a porous or clumpy HII region the ionization parameter is effectively lowered with respect to a uniform gas cloud.

(v) Shocks: Radiative shocks can be produced in star-forming galaxies from outflows driven by stellar winds or supernovae (e.g. Ho et al., 2014; Rich et al., 2010). Shock excitation produces strong emission lines at longer wavelengths (Kewley et al., 2013a) and the [NII]/Hα ratio is particularly shock sensitive. Detailed photoionization modeling indicates that galaxies in which shock excitation dominates over stellar excitation will move towards higher [NII]/Hα ratios and into the composite or AGN region of the BPT diagram (Allen et al., 2008; Rich et al., 2010). However, the tight star-forming abundance sequence observed in local galaxies suggests that the prevalence of shocks, averaged over the whole population, is low.

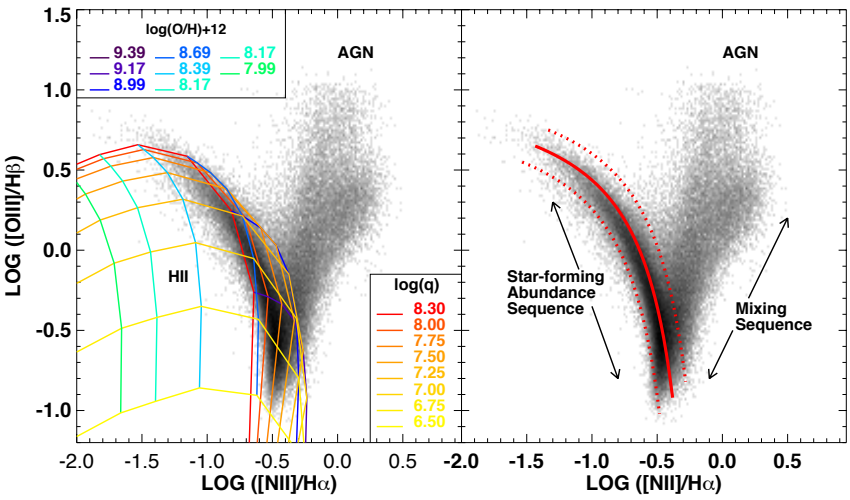

Figure 1.19 *Theoretical stellar population synthesis and photoionization model grids for star-forming galaxies in the BPT diagram taken from Kewley et al. (2013a). Left panel: Showing the model grid predictions for various values of the metallicity and ionization parameter with the different values indicated. Right panel: The mean position of the SDSS star-forming sequence.*

The culmination of these physical ideas is illustrated in Fig. 1.19 which shows an example of photoionization modeling of star-forming abundance sequence in the BPT diagram from Kewley et al. (2013a). The left panel of the figure shows the position in the BPT diagram as a function of metallicity and ionization parameter (neglecting the effects of geometry or shock excitation). The figure demonstrates how the shape of the star-forming abundance sequence of SDSS galaxies can be well understood accounting for the strength of the ionizing radiation field, electron density and metallicity in an HII region.

1.3.5 Open Questions: Evolution of the Abundance Sequence?

One of the current questions emerging from the study of high redshift star-forming galaxies is whether this abundance sequence evolves with redshift. Or equivalently, are the physical conditions in star-forming regions at early cosmic times significantly different to those observed locally? For the past decade, observations have hinted at an offset from the BPT abundance sequence for galaxies at $z > 1$ (e.g. Erb et al., 2006b; Liu et al., 2008; Shapley et al., 2005), but

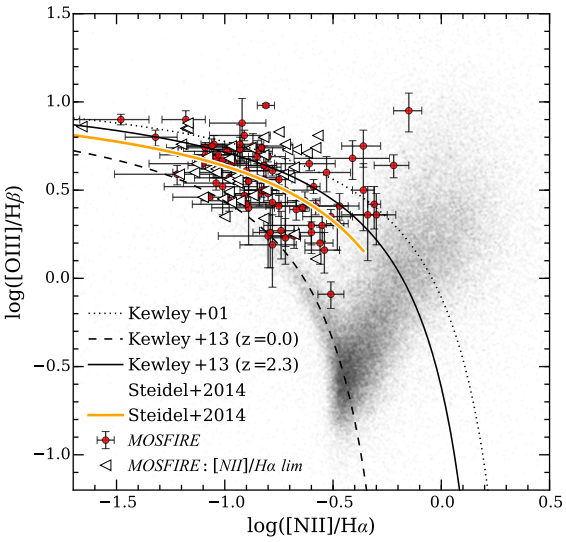

Figure 1.20 *The BPT diagram for 126 star-forming galaxies from Steidel et al. (2014). The red points show galaxies from the Steidel et al. (2014) dataset with measurements in all required emission lines, the open triangles show galaxies with only an upper limit on the [NII]/Hα ratio. The solid orange line shows the best-fitting relationship for the Steidel et al. (2014) data, the other black lines show various theoretical derivations from the literature.*

only in the past year have instruments become available, for example MOSFIRE (McLean et al., 2012) and KMOS (Sharples et al., 2013), to allow a systematic study of the full suite of rest-frame optical emission lines at these redshifts.

Recently, Steidel et al. (2014) have shown for a sample of 126 UV-selected galaxies at $2.0 \leq z \leq 2.6$ that these galaxies form a similarly tight, yet clearly offset, sequence in the BPT plane. Fig. 1.20 shows the galaxies from Steidel et al. (2014) in the BPT diagram where this offset is clearly evident. A similar effect has also been observed by Shapley et al. (2015) using rest-frame optically selected galaxies at $z \sim 2.3$; the offset is not as significant as the one reported by Steidel et al. (2014), but this is most likely a reflection of different selection biases when comparing UV to optically selected galaxies, since the offset is fundamentally correlated with the physical properties of the galaxies, not simply redshift.

Indeed, when studying the physical properties of galaxies via the rest-frame optical emission lines at high redshift one must be extremely careful with regard to selection effects. This issue has been recently highlighted in detail by Juneau et al. (2014) who try to mimic high redshift selection effects in the SDSS galaxy

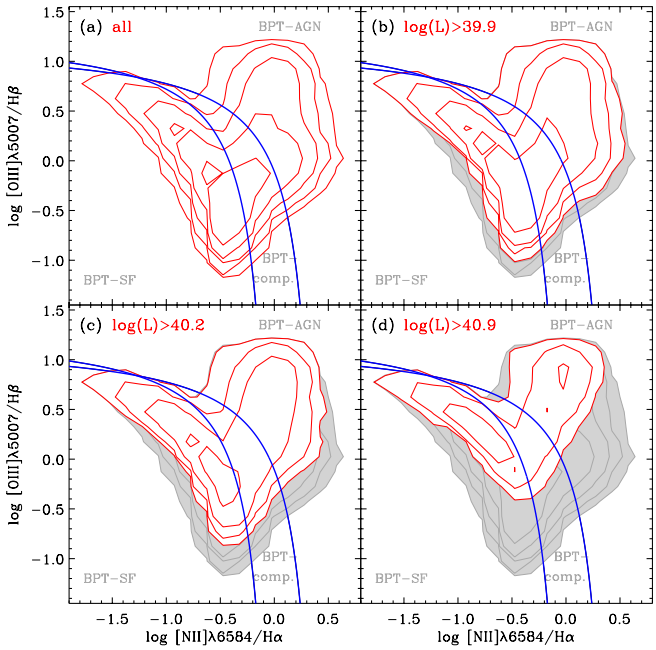

Figure 1.21 *The position of [OIII]+ Hα luminosity-selected subsets of SDSS galaxies in the BPT diagram from Juneau et al. (2014). As the minimum line luminosity is increased, mimicking selection effects in high redshift samples, the observed offset of galaxies in the BPT plane is reproduced.*

sample by imposing increasing line luminosity limits to the two strongest optical emission lines: Hα and [OIII]. They show that as the line luminosity limit is increased to values typical of observed high redshift galaxies the BPT diagram offset is reproduced, albeit with a significantly reduced SDSS sample size (see Fig. 1.21). This selection bias is, crudely, not very surprising in the sense that such high luminosities in themselves imply extreme physical conditions i.e. increased star-formation rate. However their correlation with line ratios (e.g. [OIII]/Hβ and [NII]/Hα), which are sensitive to all the factors outlined in section 1.3.4, is not entirely obvious. Nevertheless, the work of Juneau et al. (2014) raises an important issue which has yet to be fully addressed. Their results imply that $z \sim 2$ galaxy analogues can be found within the local SDSS sample, however they represent a very small fraction of the overall local star-forming population, the key question is whether these extreme galaxies represent a greater proportion of the overall population at high redshifts?

If the BPT offset of high redshift galaxies is found to hold, on average, across the whole population, the cause of this offset remains an open question. This issue has been explored preliminarily in recent works such as Kewley et al. (2013a,b),

Steidel et al. (2014) and Shapley et al. (2015) but at present observations are not sufficient to unequivocally distinguish between all possibilities. Briefly, the evolution of the abundance sequence may be a manifestation of more extreme ISM conditions at high redshift where these extreme conditions take the form of an either increased ionization parameter, electron density, a harder UV radiation field (i.e. more O^+-ionizing photons relative to H-ionizing photons), or a combination of all these factors (Kewley et al., 2013b). Alternatively some authors have suggested that variations of the N/O abundance ratio, at a fixed O/H abundance, can account for some of the observations (e.g. Masters et al., 2014; Shapley et al., 2015; Steidel et al., 2014). Steidel et al. (2014) appeal to an increasing importance of binary star systems and rapidly rotating stars at high redshift which can increase the main sequence lifetimes of massive main sequence stars (thereby enhancing the amount of hard-UV radiation incident on the ISM), as well as elevating N production relative to O (see e.g. Eldridge & Stanway, 2012).

1.3.6 Gas-Phase Metallicities

Finally, one of the main uses of the strong optical emission lines in the integrated spectra of high redshift galaxies is to measure the gas-phase oxygen abundance in the ISM (hereafter referred to as the galaxy metallicity). Most commonly, a given optical line ratio (e.g. [OIII]/Hβ, [NII]/Hα) is mapped to value of O/H by calibrating the relationship in some way, either empirically or purely theoretically. However, as mentioned above, such line ratios are not simply sensitive to metallicity, therefore, as will be discussed further below, a possible evolution in the star-forming abundance sequence can have profound implications for these metallicity measurements.

There are two main methods for calibrating a given line ratio to a metallicity: (i) empirical calibrations based on temperate measurements of the ISM, and (ii) theoretical calibrations based on photoionization modeling of HII regions, however it is worth noting that there are also calibrations which are mixture of both empirical and photoionization techniques. Below I will give a brief summary of these techniques.

(i) Empirical Calibrations: Empirical calibrations fit the relationship between HII region line ratios and 'direct' estimates of metallicity. Most commonly the direct method (or T_e method) involves taking the ratio the [OIII]λ4363 auroral

line and the [OIII]λ5007 forbidden line. This ratio gives an estimate of the HII region temperature which can be converted to a metallicity after correcting for unseen ionizations stages (see e.g. Osterbrock, 1989). Examples of this type of calibration include the Pettini & Pagel (2004) (PP04) calibrations of the N2 ($\equiv$ log[[NII]/Hα]) and O3N2 ($\equiv$ log[[OIII]/Hβ/[NII]/Hα]) line ratios, Fig. 1.22 shows as an example of the PP04 N2 calibration. Many other examples of empirical calibrations exist e.g. Pilyugin & Thuan (2005), Liang et al. (2007).

Despite the fact that the empirical method is based a direct measurement of the metallicity, estimated using the electron temperature of the gas, there are certain drawbacks to this method. Firstly, the [OIII]λ4363 line is generally very weak, even in low-metallicity environments, and requires either high S/N spectra or spectral stacking in order to be observed (e.g. Andrews & Martini, 2013). Indeed, this is the reason why strong line calibrations are needed at high redshift, as it is not feasible to measure auroral lines in spectra at these distances, although hopefully this situation will improve over the coming decade (Steidel et al., 2014). Secondly, even when the [OIII]λ4363 can be observed, the derived electron temperature may not be representative of the HII region as a whole. This is because, in the presence of temperature gradients/fluctuations in a nebula, [OIII]λ4363 will be emitted pre-dominantly from high temperature regions and consequently the measured metallicity will be biased low with respect to the average across the whole HII region (e.g. Esteban et al., 2004; Stasinska, 2005). In this case, calibrations based on electron temperature methods may be underestimating the overall metallicity by 0.2 - 0.3 dex (e.g. Moustakas et al., 2010).

Finally, as pointed out by Moustakas et al. (2010), among others, any empirical calibration is only strictly applicable to the type of galaxies from which the calibration is made, in terms of the physical conditions of the ISM. For example, the PP04 calibration should only be applied to galaxies covering the same range of ionization conditions, ISM pressure and metallicities as the 137 galaxies used in their sample.

(ii) Photoionization Modeling: Due to the difficulty in measuring metallicities using the T_e method, over the past $\sim$ 20 years strong-line ratios have been calibrated against metallicity using photoionization modeling of HII regions. The two most commonly used photoionization model codes in the literature are `MAPPINGS` (Allen et al., 2008; Groves et al., 2004; Sutherland & Dopita, 1993) and `CLOUDY` (Ferland et al., 1998). In these models the ionization

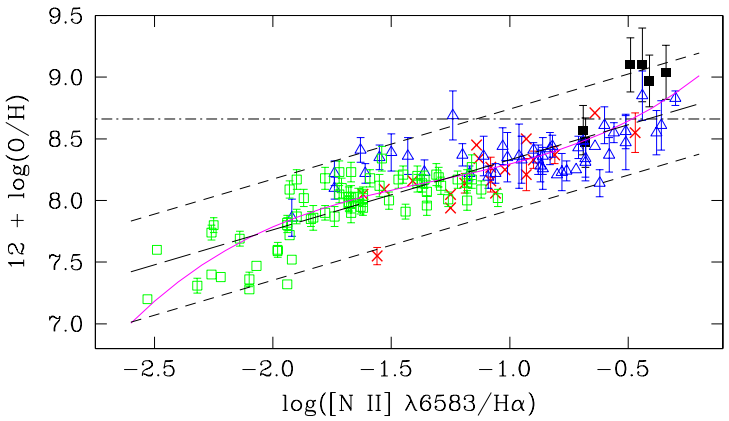

Figure 1.22 *Showing the empirical [NII]/Hα metallicity calibration from Pettini & Pagel (2004). The data points (barring the filled black squares) represent individual* HII *regions, or integrated galaxy spectra, which have a T_e-estimated metallicity (see text for details). The black filled squares show metallicity estimates from photoionization models. Because N=133/137 of the data points are T_e based metallicities this is thought of as an empirical metallicity calibration.*

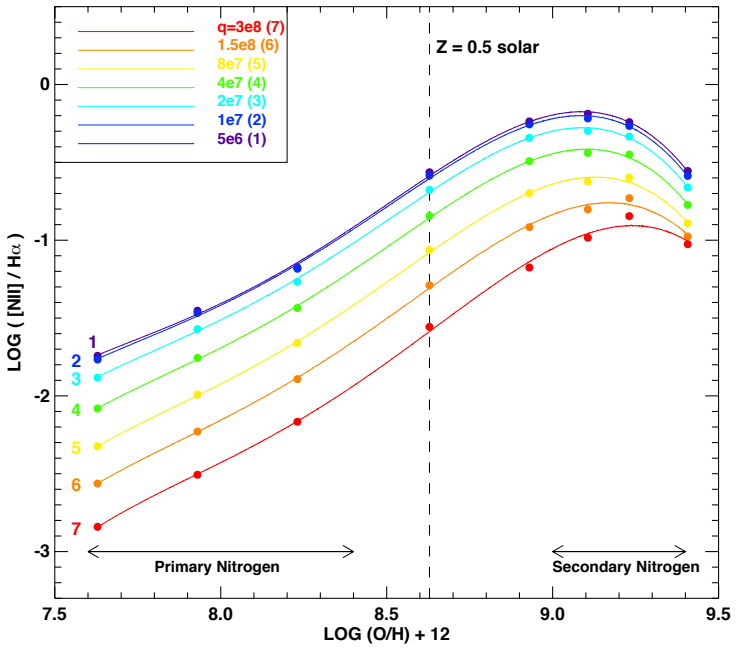

Figure 1.23 *Showing the theoretical [NII]/Hα metallicity calibration from Kewley & Dopita (2002). The different coloured curves show the calibration for different values of the ionization parameters, highlighting the strong ionization dependence of the [NII]/Hα ratio.*

radiation field is calculated from stellar population synthesis models such as STARBURST99 (Leitherer et al., 1999) using either an instantaneous burst or continuous star-formation history (Kewley & Dopita, 2002). This radiation field is then propagated through a plane parallel or spherical HII region of a given metallicity, ionization parameter, ISM pressure and dust content and the resulting emission line intensities calculated. In this way line ratios can be calibrated as a function of metallicity taking into account all other dependencies.

The major advantage of these theoretical calibrations is that they can be made to span a wide range of ionization conditions and metallicities and therefore do not suffer from the selection biases inherent in empirical calibrations. An example of the [NII]/Hα calibration from Kewley & Dopita (2002) is shown in Fig. 1.23. As can be seen from the figure, this calibration covers $\sim$ 2 dex in ionization parameter and metallicity and a strong ionization parameter dependence is apparent. Therefore, according to Fig. 1.23, it would be incorrect to convert an [NII]/Hα line ratio into a metallicity (as in PP04 for example) without taking into account the ionization parameter.

However, photoionization models also suffer from a number of uncertainties. For example the use of simplified HII region geometries (plane-parallel or spherical), unknown metal depletion onto dust grains, varying star-formation histories and also the form of the input stellar ionizing spectrum (e.g. unknown effects of binaries and rotation). Recently, Nicholls et al. (2012) have showed that even the assumption of a Maxwell-Boltzmann electron energy distribution in HII regions may be incorrect, and that electrons instead follow a κ-distribution. Such uncertainties will most likely result in systematic offsets in the theoretical metallicity scale which must be improved by a combination of more sophisticated codes and better theoretical knowledge of the physics of HII regions.

(ii) Combined Methods: Finally, there also exist metallicity calibration which use a combination of T_e-based metallicities and photoionization-based metallicities to calibrate the strong emission line ratios (e.g. Diaz & Pérez-Montero, 2000; Maiolino et al., 2008; Nagao et al., 2006). Of these, the most commonly applied is the Maiolino et al. (2008) calibration (M08) which is illustrated in Fig. 1.24. As can be seen in the figure, at low metallicities (12+log(O/H) $\lesssim$ 8.2) the calibration is based on a sample of 259 galaxies with T_e-estimated metallicities, whereas at high metallicities a sample of $\sim 23,000$ SDSS galaxies is used, with metallicities estimated from photoionization modeling.

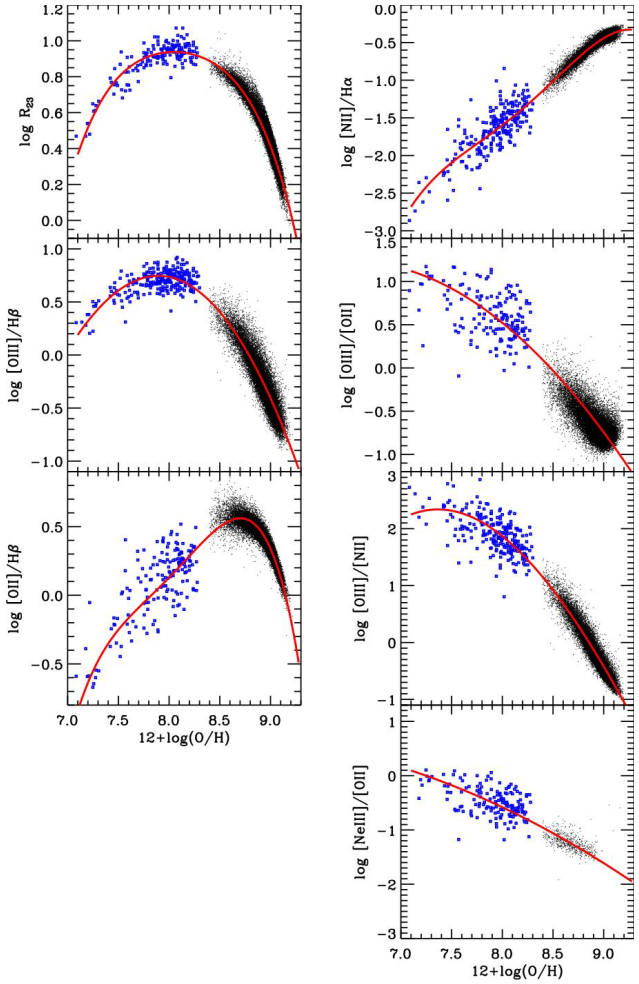

Figure 1.24 *Showing the calibrations of emission line ratios with metallicity from Maiolino et al. (2008). The blue squares show low metallicity galaxies with metallicities estimated using the T_e method and the black points show SDSS galaxies which metallicities estimated from photoionization modeling. The red line shows the (up to) 4th order polynomial fits which define the conversion between line ratio and metallicity.*

M08 also suffers from the fact that, though photoionization modeling is used, no ionization parameter dependence is incorporated into the calibration. The calibrations are fits through the bulk of these low redshift galaxies (see Fig. 1.24) and therefore when applying M08 one must assume that the ionization conditions, ISM pressure, etc. are consistent with the average of these parameters in the local population. This is the same bias one encounters when applying purely empirical calibrations.

In summary, there remains great debate and uncertainty regarding the use and reliability of metallicity measurements using strong line ratio calibrations. Perhaps the most stark example of this is investigated in Kewley & Ellison (2008), who apply 10 different metallicity calibrations (a mixture of empirical, theoretical and combined) to an SDSS galaxy sample and find systematic offsets of up to ~ 0.7 dex in the derived metallicity scale. Given that the strong line ratios are for now the only feasible method of determining metallicity at high redshift, understanding these systematic difference is an imperative goal of future work as is investigating how metallicities at high redshift may be biased by all the effects discussed above.

1.4 Surveys/Data

Throughout this thesis I utilize many different public datasets from various spectroscopic surveys carried out by different collaborations across the world. Therefore, in this section I will give a brief overview of each dataset and the selection methods they employ. Some of the information presented here will be reiterated when a given dataset is introduced in the results chapters, but this list will provide a more general synopsis which can be referred back to as a reference. To conclude, I will discuss the various sample biases that results from the various selection methods mentioned. The list below is in a rough redshift/occurrence order.

SDSS: The sample I use throughout this thesis is from the seventh data-release (DR7) of SDSS (York et al., 2000). SDSS DR7 provides imaging and spectroscopy across one quarter of the entire sky and is 95% complete down to optical r-band apparent magnitude of 22.2 $\mathrm{mag_{AB}}$[2] (AB). I use the MPH-JHU emission line

[2] classic.sdss.org/dr7/

analysis catalogue[3] which provides spectroscopic measurements for a sample of $\sim$ 900,000 galaxies from the DR7 release for galaxies at $z < 0.7$. In each of the relevant chapters, I will describe in detail how I apply further constraints to select subsets of galaxies from the MPA-JHU catalogues.

DEEP2: The Deep Extragalactic Evolutionary Probe 2 (DEEP2) survey consists of spectra of $> 50,000$ galaxies at $z > 0.7$, taken using the DEIMOS spectrograph on Keck (Newman et al., 2013a). DEEP2 was taken over four survey fields (Groth Survey Strip South, Zone of very low extinction, 2x SDSS deep strips) covering an area of 2.8deg^2. The survey observes down to a limiting r-band apparent magnitude of 24.1 mag$_{\rm AB}$ across the spectral wavelength range 0.65 - 0.91μm.

3D-*HST*: The 3D-*HST* survey (Brammer et al., 2012) is the main spectroscopic survey utilized in this thesis, for which I have written a custom data reduction and analysis pipeline. Chapter 2 is dedicated to a detailed description of the pipeline, data analysis and sample selection, I will only mention here that the 3D-*HST* sample is selected using rest-frame optical emission lines in the redshift range $1.30 \lesssim z \lesssim 2.30$.

Erb et. al. 2006: The Erb et al. (2006b) sample consists of Hα spectra 114 galaxies at $z \gtrsim 2$ selected by their rest-frame UV colors (see Steidel et al., 2004). The sample was slightly biased towards higher masses than a pure UV selected sample because some galaxies were selected based on bright rest-frame optical magnitudes (see discussion below).

KBSS/MOSFIRE: The KBSS/MOSFIRE sample I use in Chapters 4 and 5 is taken from the publicly available data published in Steidel et al. (2014). The selection is predominantly via the rest-UV, however additional UV/optical information was used to reduce the bias against heavily reddened galaxies. The final spectroscopic sample consists of 251 galaxies in the redshift range $1.95 \lesssim z \lesssim 2.65$. Galaxies were included in the sample if [OIII]λ5007 and Hα were detected at $> 5\sigma$ significance, and Hβ and [NII] at $> 2\sigma$.

MOSDEF: The MOSFIRE Deep Evolution Field (MOSDEF) survey will consist of rest-frame optical spectra for $\sim$ 1500 galaxies at $1.37 \leq z \leq 3.80$ down to a minimum H-band magnitude of 25.0 mag$_{\rm AB}$ Kriek et al. (2015). The MOSDEF sample used in Chapter 5 is taken from Sanders et al. (2015) and consists of 87 galaxies at $2.08 \leq z \leq 2.61$ with $\geq 3\sigma$ detections in Hα and Hβ.

[3]http://www.mpa-garching.mpg.de/SDSS/DR7/

Wuyts et al. 2014: The sample of 222 galaxies at $0.7 < z < 2.6$ published in Wuyts et al. (2014), and utilised in Chapter 5, is taken from a mixture of the LUCI/SINS/zC-SINF/KMOS^{3D} surveys. As a result the selection procedure is not uniform across the full dataset. The KMOS^{3D} selection is based on rest-optical spectroscopic redshifts for galaxies down to a H-band magnitude of 24 $\mathrm{mag_{AB}}$, the LUCI selection is based on galaxies in GOODS-N with a measured spectroscopic redshift and the SINS/zC-SINF galaxies were selected based on various rest-UV/optical magnitudes or colors (Förster Schreiber et al., 2009).

AMAZE/LSD: The AMAZE/LSD sample (Maiolino et al., 2008; Mannucci et al., 2009; Troncoso et al., 2014) consists of integral field spectroscopy of 40 star-forming galaxies at $3 < z < 5$. The spectroscopic sample is drawn from the rest-UV selected samples of Steidel et al. (2003) and Vanzella et al. (2006). In addition five lensed galaxies are included in the sample in order to probe to intrinsically lower rest-UV luminosity and SFRs.

Holden et al. 2014: The Holden et al. (2014) sample consists of 24 galaxies at $3.2 < z < 3.7$ taken from a sample spectroscopically confirmed, rest-UV selected galaxies published in Vanzella et al. (2008) and Balestra et al. (2010). The galaxies are bright in the UV with i-band magnitudes typically < 25 $\mathrm{mag_{AB}}$.

1.4.1 Biases due to sample selection

Different methods of selecting a galaxy sample result different biases, which make that sample incomplete in terms of the global physical properties of the total population, such as stellar mass, SFR etc. Below I give a description of the biases affecting the three main selection techniques employed in the surveys used in this paper.

Rest-Frame Optical Emission Lines: As demonstrated in Fig. 1.25, selections based on the rest-frame optical emission lines will be biased towards galaxies with low stellar mass and high SFRs. This figure shows the distribution of stellar masses and SFRs for a sample of SDSS star-forming galaxies as an increasing line flux limit on [OIII]λ5007 is imposed. As the [OIII]λ5007 flux limit increases the sample properties shift to lower mass and higher SFR, implying that emission line selections will select galaxies with elevated specific star-formation rates (sSFRs) relative to the underlying population. Additionally, emission line samples will be biased towards galaxies with lower levels of dust reddening. Since

dust reddening is know to correlate with stellar mass (e.g. Garn & Best, 2010), this accounts in part for the bias against higher masses. Finally optical emission line selection can result in metallicity biases, for example metal-rich galaxies will produce low [OIII] fluxes as the collisional excitations rate decreases with decreasing HII region temperature; in addition, selecting based on [NII] will bias against low metallicity galaxies as the [NII] line flux decreases with decreasing metallicity (e.g. Mannucci et al., 2010).

Rest-Frame UV: The rest-frame UV selects for galaxies with ongoing star-formation since the UV emission is dominated by massive, short-lived O and B type stars. This means UV selections are useful for selecting low mass galaxies, undergoing a recent burst of star-formation, which may be missed by rest-frame optical selections. On the other hand, UV selections are strongly biased against passive galaxies. Furthermore, UV light is the extremely sensitive to dust reddening (e.g. Calzetti et al., 2000) and UV selections are insensitive to heavily dust-obscured galaxies, introducing a bias against massive dusty star-forming galaxies . However, this mass bias is balanced by the fact that massive galaxies have on average higher SFRs (e.g. Daddi et al., 2007; Whitaker et al., 2012), and hence larger intrinsic UV luminosities.

Rest-Frame Optical: In contrast to the rest-frame UV, the light in the rest-frame optical is also sensitive to evolved populations of longer lived stars (e.g. A-type). Therefore, rest-frame optical selection is not necessarily dominated by galaxies with on-going star formation and is not biased against passively galaxies. Optical light is less sensitive to dust reddening than UV and so optically selected galaxies are less biased against dusty galaxies. However, because optical emission is less sensitive than UV to light emitted from O and B stars, rest-frame optical selection is less efficient at selecting low mass galaxies.

1.5 Thesis Outline

As hinted at by the overall emphasis of this introduction, the remainder of this thesis will concentrate on measuring the physical properties of high redshift star-forming galaxies using strong nebular emission lines. In Chapter 2 I will describe how the sample of $1 < z < 3$ star-forming galaxy spectra was selected from a custom reduction the *HST* near-IR spectroscopic survey 3D-*HST*. At the start of my PhD 3D-*HST* was a new survey for which there were no public data products,

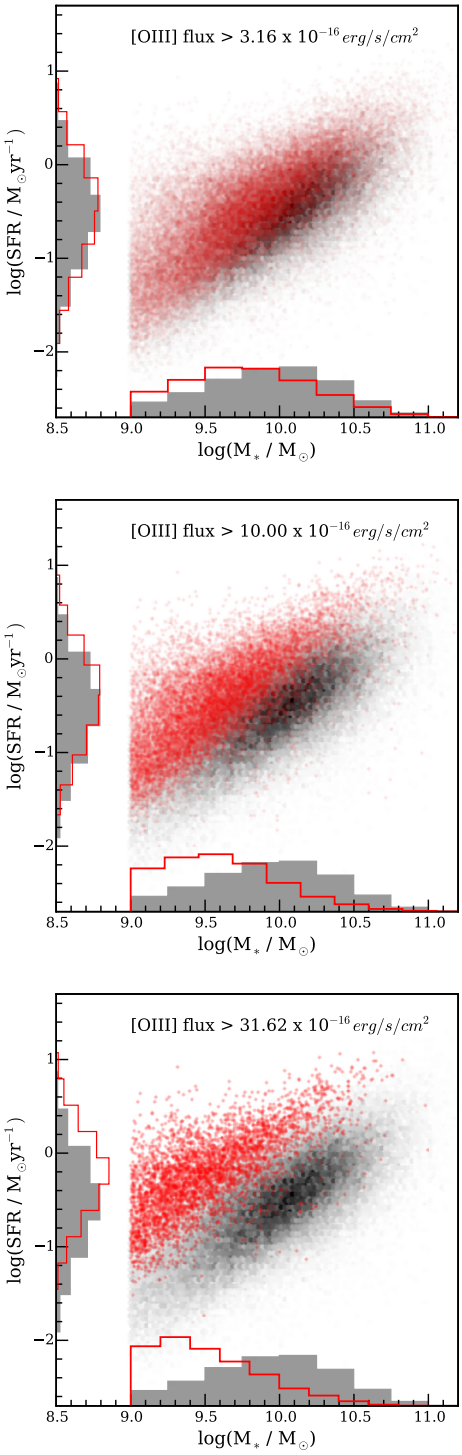

Figure 1.25 *Showing the mass-SFR plane for different cuts in [OIII]λ5007 flux for a sample of SDSS star-forming galaxies. In each panel the grey scale and grey histograms shows the distribution of the full sample, while the red points and red histograms represent the distributions for the quoted flux limit.*

and therefore I developed a full data reduction and analysis pipeline. In Chapter 2 I will also describe how line and continuum fluxes were measured from the reduced 3D-*HST* spectra, and how stellar masses, dust extinctions and star-formation rates were estimated from the accompanying CANDELS photometry. Chapter 3 details how I use the 3D-*HST* spectra in the redshift range $2 \leq z \leq 2.3$ to provide a new measurement of the $z \gtrsim 2$ mass-metallicity relation, and conduct the first detailed investigation of the fundamental metallicity relation at these redshifts. The majority of the work from this chapter has been previously published in Cullen et al. (2014). In Chapter 4, in an attempt to investigate further some of the results presented in Chapter 3, I explore the evolution of metallicity, ionization parameter and ISM pressure in star-forming galaxies over a larger redshift range ($1.3 \leq z \leq 2.3$), by comparing the 3D-*HST* spectra to new state-of-the-art theoretical models. My inference, based on the results of these two chapters, is that metallicity measurements at high redshift are being biased by an evolution in the ionization conditions of HII regions with redshift. Therefore, in Chapter 5 I revisit the mass-metallicity relationship at $2 \leq z \leq 2.3$ with an alternative method, collating all current $z \sim 2$ emission line measurements available in the literature. Finally, in Chapter 6 I detail how the near-IR data reduction expertise I have gained through this PhD will allow me to perform future studies with the new ground-based near-IR multi-object spectrograph KMOS, and also allow me take advantage of new public *HST* surveys.

Throughout this thesis I assume a cosmology with $\Omega_m = 0.3$, $\Omega_\Lambda = 0.7$ and $H_0 = 70$ km s^{-1} Mpc^{-1}.

Chapter 2

3D-*HST* Survey

The majority of the work in this thesis is based upon the 3D-*HST* near-IR grism spectroscopic survey (Brammer et al., 2012) taken with the WFC3 on board *HST*. In this chapter I will briefly discuss the principles of grism spectroscopy with *HST* in Sec. 2.1, describe the 3D-*HST* survey in Sec. 2.2 and give an in-depth description of the data reduction pipeline in Sec. 2.3.

2.1 Introduction: *HST* Grism Spectroscopy

Grism spectroscopy involves using a combination of a diffraction grating and prism to disperse all the light falling within an instruments field-of-view (FoV). The WFC3 grisms on-board *HST* are placed in the instrument where normally a conventional filter would be situated, thus the light for every object in the WFC3 FoV is dispersed onto the WFC3 detector creating a spectral image of the field in the wavelength range defined by the grisms. There are two near-IR grisms on WFC3, the shorter wavelength G102 grism (0.8 - 1.15 μm) and the longer wavelength G141 grism (1.1 - 1.7 μm). Fig. 2.1 shows an example of a G141 grism image with its corresponding direct image in the F140W filter. In Fig. 2.1 each spectrum in the G141 image corresponds to an object seen in the direct image. The majority of this thesis will focus on work done using the G141 grism however the same principles apply to both grisms, the only difference being their wavelength coverage.

The position of the spectrum on the detector is purely governed by the position

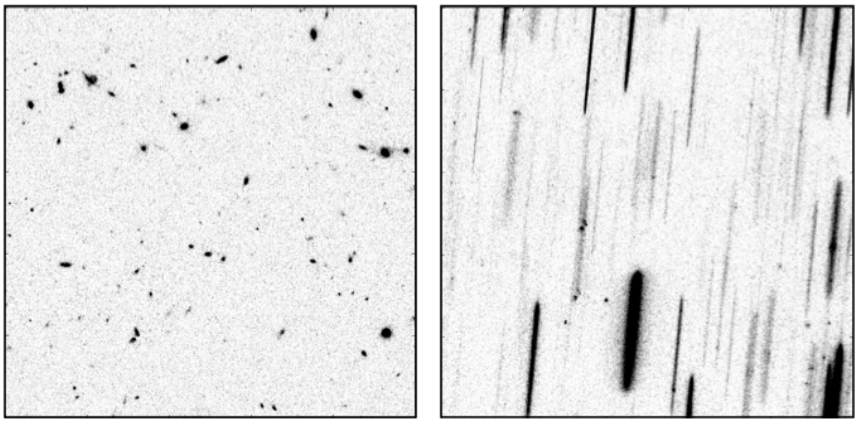

Figure 2.1 *Showing an example from a WFC3 G141 grism image (right-hand panel) and corresponding direct image in the F140W filter (left panel).*

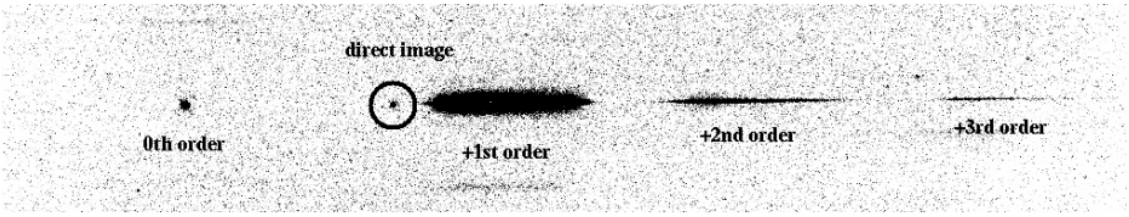

Figure 2.2 *Showing the multiple dispersion orders for a dispersed G141 spectrum (taken from Kuntschner et al. (2013)). The superimposed direct image of the object is shown and circled for reference. The sensitivity of each dispersion order as a function of wavelength (normalized to the 1st order) is shown in Fig. 2.3.*

of the object (star/galaxy) in the FoV. This differs from the conventional 'slit' method used in ground-based spectroscopy where a mask/fibre is placed over the object of interest and only the light within the mask/fibre is dispersed onto the detector. The nature of slit-based spectroscopy allows an unambiguous conversion between detector pixel and wavelength for the dispersed spectrum, however in slitless spectroscopy an objects position on the detector defines it's wavelength solution for the grism exposure. As in all grating spectroscopy multiple dispersion orders of a given spectrum are dispersed onto the detector as illustrated in Fig. 2.2. The sensitivity of the various orders is shown in Fig. 2.3, as can be seen the instrument is at least an order of magnitude more sensitive in the 1st order spectrum across the full wavelength range.

The lack of a slit or fibre mask is both the main advantage and dis-advantage of grism spectroscopy. Firstly it allows spectra of all galaxies within a large field of view to be observed simultaneously compared to one object at a time in a traditional single slit spectrograph. Although this situation is steadily improving with the new generation of near-IR multi-object spectrographs (e.g. KMOS, MOSFIRE), it still cannot compete with the number of available objects in a grism FoV. However, the lack of a slit mask also means that spectra within a given FoV can overlap one another and thus there is a certain amount of extra modeling which must be done to reliably extract spectra increasing the complexity of the data reduction. All this will be described in greater detail in Section 2.3.

2.2 3D-*HST* Survey Description

The spectroscopic data used in this thesis are part of the 3D-*HST* observations described in Brammer et al. (2012).[1] At the start of my PhD only the raw data products were publicly available from the *HST* data archive. The 3D-*HST* survey provides low resolution (R $\sim$ 130) spatially resolved near-IR grism spectra over the wavelength range 1.1 - 1.68μm taken with the WFC3 G141 grism on *HST*. In this wavelength range important rest-frame optical features of galaxies are covered in the redshift range $0.8 < z < 3.5$ such as the Hα, Hβ, [OII] and [OIII] nebular emission lines. The 4000Å break in passive non-star-forming galaxies is also covered at $1.8 < z < 3.2$. These optical features and the redshift ranges in which they are observable with the G141 grism are illustrated in Fig.

[1]These observations were taken by a survey team headed by Yale University (P.I. Dr Pieter Van Dokkum).

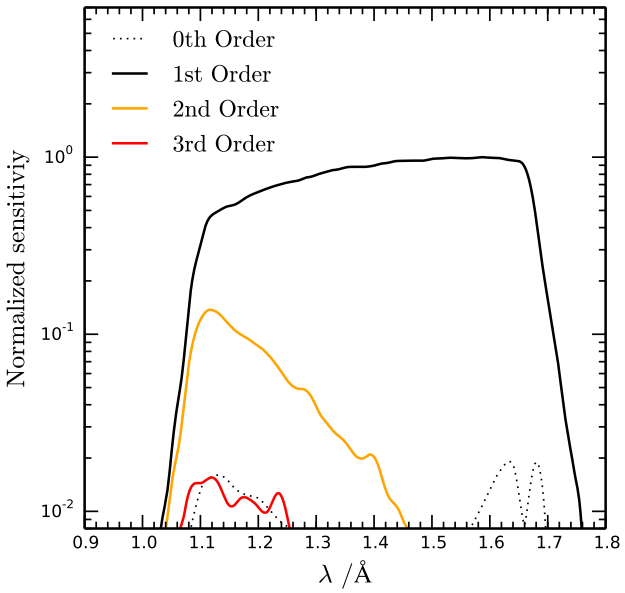

Figure 2.3 *Showing relative sensitivity (normalized to the peak of the 1st order sensitivity) of the multiple dispersion orders for a dispersed G141 spectrum as a function of wavelength.*

2.4.

The survey covers a total area of 675 arcmin^2, providing spectroscopic follow-up of three quarters of the deep near-IR CANDELS imaging survey (Grogin et al., 2011; Koekemoer et al., 2011) in four fields: AEGIS, COSMOS, GOODS-S, and UDS. In addition, the G141 grism survey of the GOODS-N field from program GO-11600 (PI: B. Weiner) is incorporated into the 3D-*HST* survey since the observing strategy is almost identical. Each field is covered by a mosaic of G141 pointings (hereafter tiles) and each tile is made up of four separate G141 exposures with total exposure times ranging from 4111 - 5111s; the four separate exposures are dithered for reasons which will be explained Sec. 2.3. Accompanying the grism exposures are four direct images taken with the F140W filter with a total exposure time of 812s; the direct images are also dithered with the same pattern as the G141 exposures. The reason for these accompanying direct images will also be explained below. An example of the tiling pattern for one of the five 3D-*HST* fields (GOODS-S) is show in Fig. 2.5.

Over the total survey area of 3D-*HST* it is estimated that it will be possible to obtain $\sim$ 7000 galaxy spectra at $z > 1$ (see Brammer et al., 2012). 3D-*HST* therefore represents the largest sample of galaxies with near-IR spectroscopy at

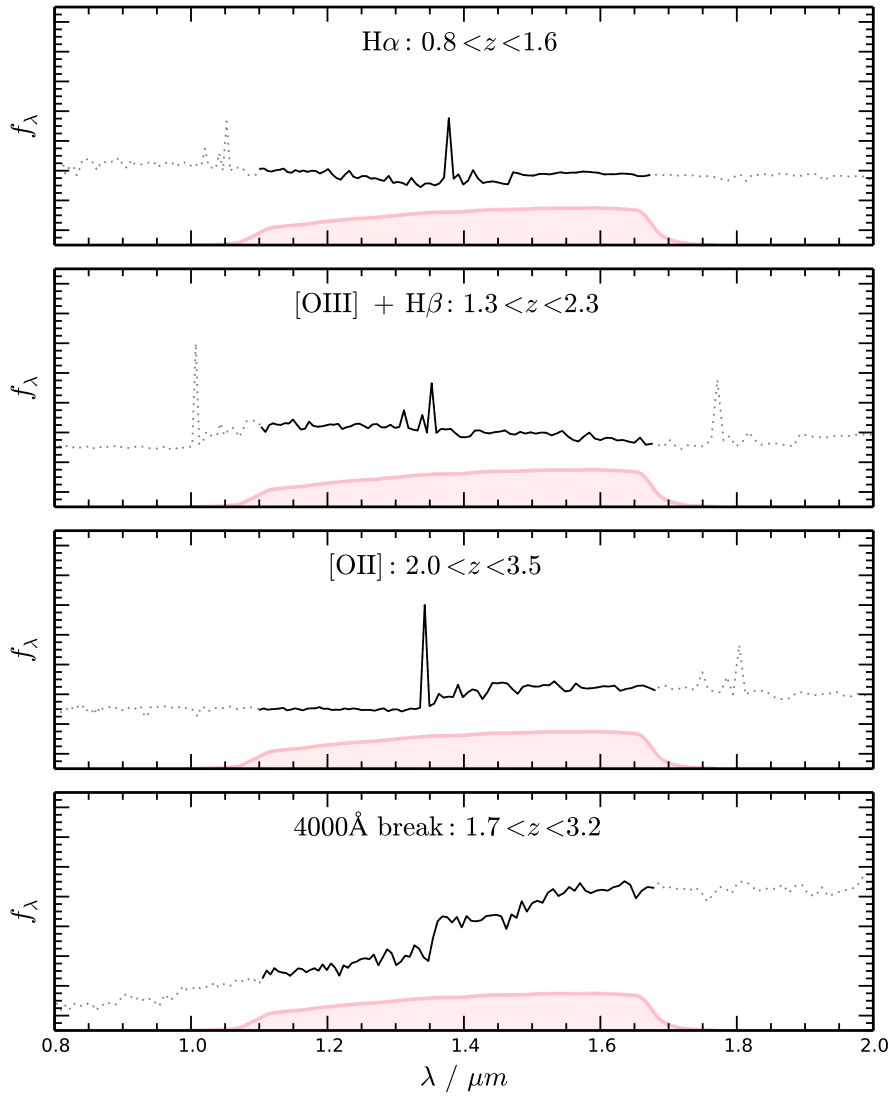

Figure 2.4 *Showing the rest-frame optical features of galaxy spectra accessible with 3D-HST. From top to bottom the figure shows: Hα available at* $0.8 < z < 1.5$*, [OIII] and Hβ available at* $1.3 < z < 2.3$*, [OII] available at* $2.0 < z < 3.5$ *and the* 4000Å *break available at* $1.7. < z < 3.2$*. The flux in the y-axis of each panel is in arbitrary units so no scale is shown. The region where the spectra are solid black lines shows the G141 grism wavelength coverage. THe G141 filter response cruve is shown in red to illustrate the variation of response with wavelength. The template spectra are taken from the K20 survey (Mignoli et al., 2005) and are at higher resolution* ($R \sim 300 - 500$) *than the actual grism spectra* ($R \sim 130$)*.*

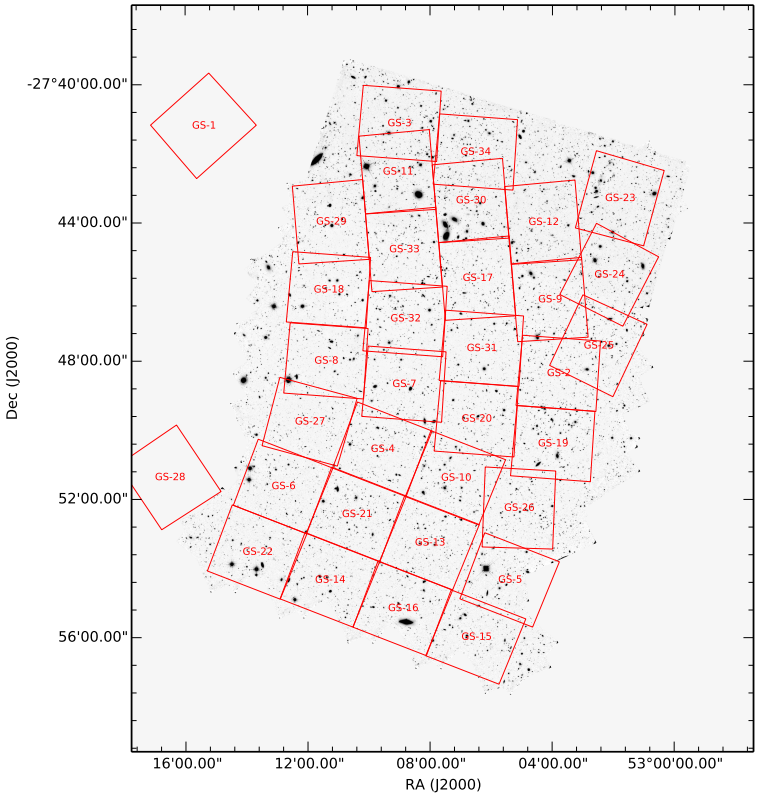

Figure 2.5 *The 3D-HST pointing layout for the GOODS-S field. The underlying image is a CANDELS image mosaic of the GOODS-S field.*

these redshifts currently available and a precursor for future generation of ground-based near-IR surveys with KMOS, MOSFIRE and MOONS.

2.3 3D-*HST* Data-Reduction Pipeline

As mentioned above the raw data products for 3D-*HST* consist of four pairs of G141 grism images and F140W direct images for each tile. These four pairs are dithered such that each WFC3 pixel is sampled at half-pixel intervals allowing interpolation to sub-pixel grids when combining with `multidrizzle` (see Sec. 2.3.4 for details). Examples of the four raw G141 and F140W images for one of the 3D-*HST* tiles in shown in Fig. 2.6. These raw images, provided by *HST* through the MAST archive[2], are not completely raw, but they have been pre-processed with the `calwf3` reduction pipeline to perform a bad pixel rejection, bias subtraction, cosmic ray rejection and correction for detector gain and flat field structure for all G141 and F140W exposures. This a standard procedure for all HST data products and the `calwf3` pipeline is described in details in Koekemoer et al. (2011). However, to fully reduce these raw data products and to extract the spectra a full reduction pipeline is needed. Below I describe the various steps, procedures and software packages I used for the data reduction. The full pipeline comprises the dedicated *HST* grism software package `aXe` (Kümmel et al., 2009), various `iraf` packages (including `multidrizzle`), as well as scripts and routines I wrote in python.

2.3.1 Correcting for Guide Star Errors

First the four input direct images must be corrected for residual shifts between *HST* exposures. These residual shifts can arise because the WCS information of a given *HST* exposure is based on the position of the guide star used during the observation, therefore uncertainties in guide star position will translate to residual WCS shifts between the individual exposures. These uncertainties may arise, for example, owing to slight offsets introduced when re-acquiring a guide star during observations. I use the `iraf` routine `tweakshifts` to calculate the shifts and write the new WCS information to the image headers. The `tweakshifts` routine can correct for sub-pixel x-y shifts and rotation between images by using the position

[2]https://archive.stsci.edu/hst/

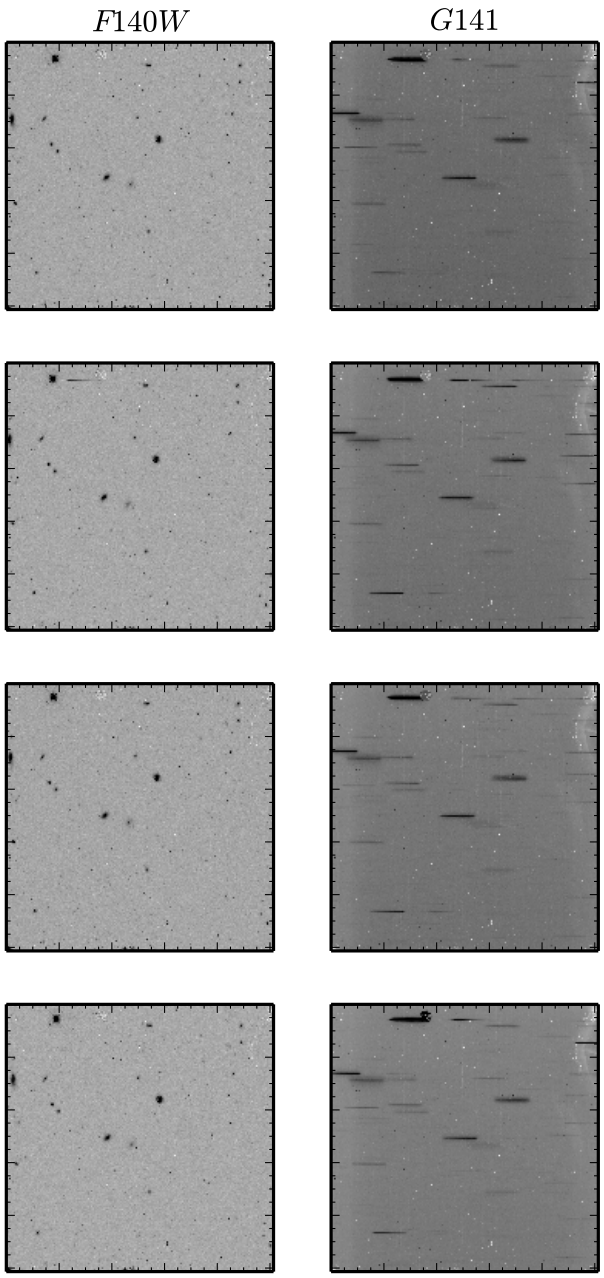

Figure 2.6 *Showing an example of the four raw F14OW (left column) and G141 (right column) exposures for a single 3D-HST tile.*

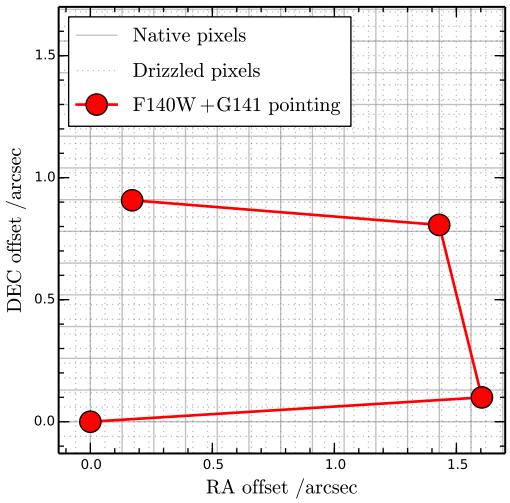

Figure 2.7 *The 3D-HST dither pattern for a single pointing.*

of stars common to all images to compute the geometric transformation relative to a reference image. The `tweakshifts` routine produces an output file containing the shift and rotation respect to the reference image, which can be input to the `multidrizzle` image combination routine (see Sec. 2.3.2) which then takes the relative shifts into account when combining. Which one of the four direct images is chosen as the reference is arbitrary. I find the effect of rotation to be negligible for the 3D-*HST* exposures and therefore it can be ignored.

2.3.2 Cosmic Ray Removal

Once the residual shifts have been calculated I can proceed to combine the four direct dithered exposures using the `iraf` task `multidrizzle` (Fruchter & Hook, 2002). The final goal of this process is to produce a drizzled image which can be aligned to a reference CANDELS mosaic (see Sec. 2.3.3). However, the native pixel size of the WFC3/IR detector is $\sim$ 0.13" whereas the CANDELS mosaics have a 0.06"/pixel sampling. Also, despite having passed through the `calwf3` pipeline, the raw F140W images may still have hot-pixel artifacts such as cosmic rays which need to be removed. To facilitate an optimal alignment with the CANDELS mosaic, I first remove cosmic rays before drizzling the dither exposures to half-pixel sampling, this is achieved with the `iraf` task `multidrizzle` as described below.

The aim of `multidrizzle` is to combine dithered images at integer-pixel or sub-

pixel offsets, correcting for the geometric distortion of the WFC3 detector. It requires observations to have been 'dithered'. Dithering is a popular technique used in astronomical observations which involves spatially offsetting observations by shifts smaller than the size of the detector pixels. This means that a given target in an image (e.g. a galaxy or star) is sampled by a number of different points on the detector and therefore dithered observations can be combined with improved spatial sampling relative a single pointing. 3D-*HST* employs a dithering strategy as shown in Fig. 2.7. Each of the four exposures are offset in both x and y direction by $\sim 1 - 1.5$" (corresponding to an ~ 10 pixel offset). This dither pattern is chosen to ensure that each pixel in the WFC3 exposure is sampled at half pixel intervals (Brammer et al., 2012). Thus, the spatial resolution of the final combined image can be improved by up to a factor 2 relative to the native pixel resolution of WFC3.

However, before the direct images are combined at half pixel sampling, I first run `multidrizzle` at native pixel sampling to flag cosmic rays (multidrizzle parameter `pixfrac` = 1). This is safer than performing cosmic ray rejection at half pixel sampling as the interpolation process used in sub-pixel drizzling can cause errors in the cosmic-ray detection algorithm. To make a cosmic ray mask for each exposure `multidrizzle` first combines the four exposure to create a median image using the 'minmed' algorithm: the value for each pixel in the combined image is taken as the median value of the four corresponding pixels in each input image, for the case where < 4 images contribute to a given pixel (i.e. on the edge of the image) the minimum is used instead of the median if one of the pixels exceeds the others by $> 4\sigma$.

This median combined image is then transformed back to each individual direct frame so that each pixel in an input frame ($I_{\rm in}$) can be directly compared to the combined median value of that pixel ($I_{\rm med}$). The pixel is then flagged as a cosmic ray in the input frame if the following relation is satisfied:

$$|I_{\rm in} - I_{\rm med}| > \alpha\Delta_{\rm med} + \beta\sqrt{\sigma^2_{\rm read} + |I_{\rm med} - B|}, \tag{2.1}$$

where α and β are scaling factors provided to the `multidrizzle` algorithm (parameters `drz_cr_scale` and `drz_cr_sn` respectively) for which we adopt the same values used by the CANDELS team (Koekemoer et al., 2011), B is a background sky value estimated for the exposure and $\Delta_{\rm med}$ is defined as the steepest gradient between the pixel and each of its surrounding pixels in the

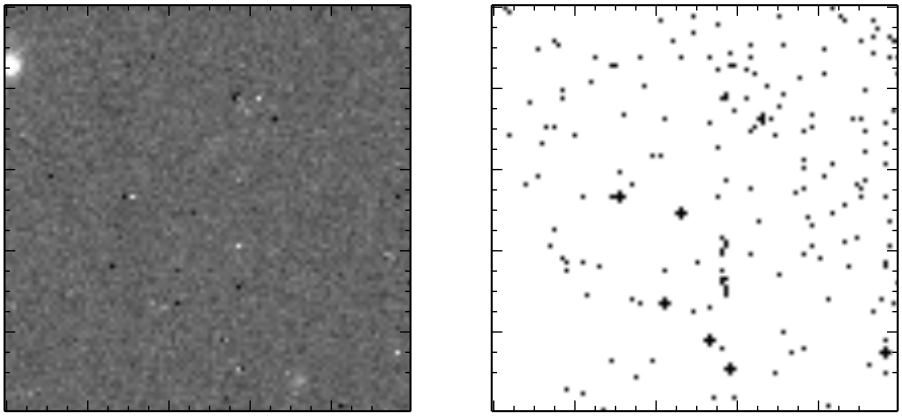

Figure 2.8 *An example 3D-HST cosmic ray mask. The left panel shows the image of a portion of a 3D-HST direct image and the right panel shows the cosmic ray mask (identified cosmic rays shown in black).*

median image. Fig. 2.8 shows an example cosmic ray mask for a typical 3D-*HST* direct exposure. In practice $\sim 1-2\%$ of pixels in a typical grism exposure are flagged as cosmic rays via this method. The image is then cleaned of cosmic rays by setting the value of each flagged pixel to the median value of its surrounding pixels.

2.3.3 Alignment to Reference Image

After cosmic-rays and bad pixels have been masked as described, the next step is to align the 3D-*HST* images with a mosaic from the CANDELS survey (Koekemoer et al., 2011). This is necessary because, by matching each grism spectrum with the deep photometry from the CANDELS catalogues, I can use this ancillary photometric information to help derive properties of the galaxies such as the redshift, mass or star-formation rate. Indeed, the availability of such a deep photometric dataset to compliment 3D-*HST* spectra is one of the unique aspects of the 3D-*HST* grism survey with respect to other *HST* grism surveys for example WISP (Atek et al., 2010). The importance of this ancillary data will be described in more detail throughout the remainder of this thesis.

For the WCS of the 3D-*HST* frames to be aligned to a CANDELS mosaic the images must first be converted to the same pixel sampling. Therefore, I re-run

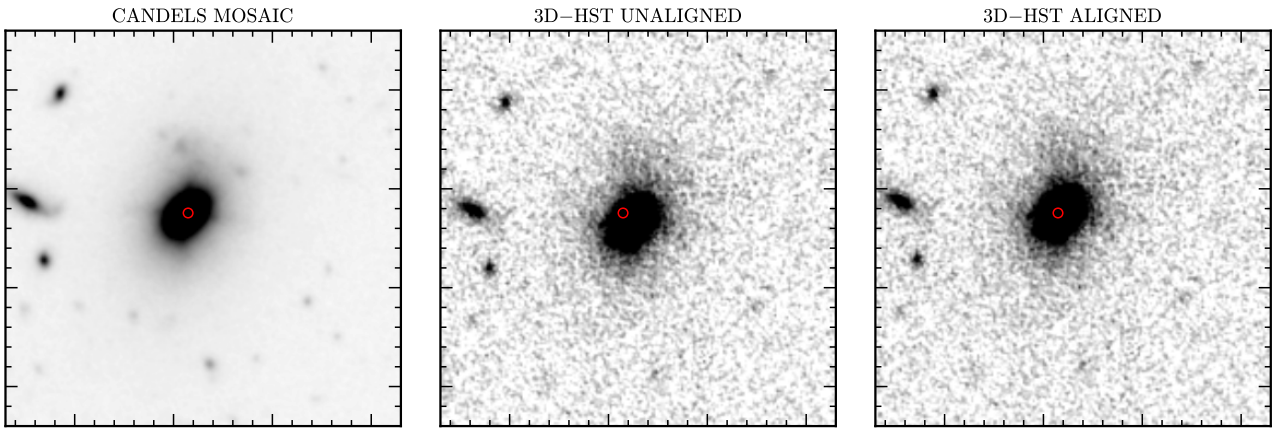

Figure 2.9 *Showing an example of the offset of one galaxy in a typical 3D-HST tile (GOODS-S-36) with respect the CANDELS mosaic. The red circle in each image represents the centroid of the galaxy as measured in the CANDELS mosaic.*

multidrizzle on the cosmic-ray corrected input frames and drizzle to half-pixel sampling (0.06") to match the sampling of the CANDELS mosaics.

I now run the `iraf` routine `sregister` to cut-out a section of the CANDELS mosaic which overlaps the 3D-*HST* pointing. Although the WCS of each image is not aligned at this stage, they will not be significantly different with respect to the WFC3 FoV, therefore there is bound to be some overlap such that there are enough objects common to both images with which I can perform a full alignment. This is not a completely necessary step but saves a lot of processing time because later, when running object detection software, it is much quicker to do on a small section of the CANDELS mosaic than the full image.

I then run `SExtractor` (Bertin & Arnouts, 1996) on both the CANDELS mosaic and 3D-*HST* pointing with a high detection threshold (`DETECT_THRESH` = 50) to select the brightest objects in the image (typically > 10 objects are needed for a good fit). I then use the two resulting catalogues with the `iraf` tasks `xyxymatch` and `geomap` to compute the relative shifts. `xyxymatch` finds the x and y positions of corresponding objects in the CANDELS and 3D-*HST* images and writes the matched co-ordinates to an output file. The matched objects file is then passed to `geomap` which computes the required transformation to align the two co-ordinate lists. The `xyxymatch`, `geomap` procedure is repeated iteratively until a solution is found. Finally, the shift solution is written to a shift file to be used when the

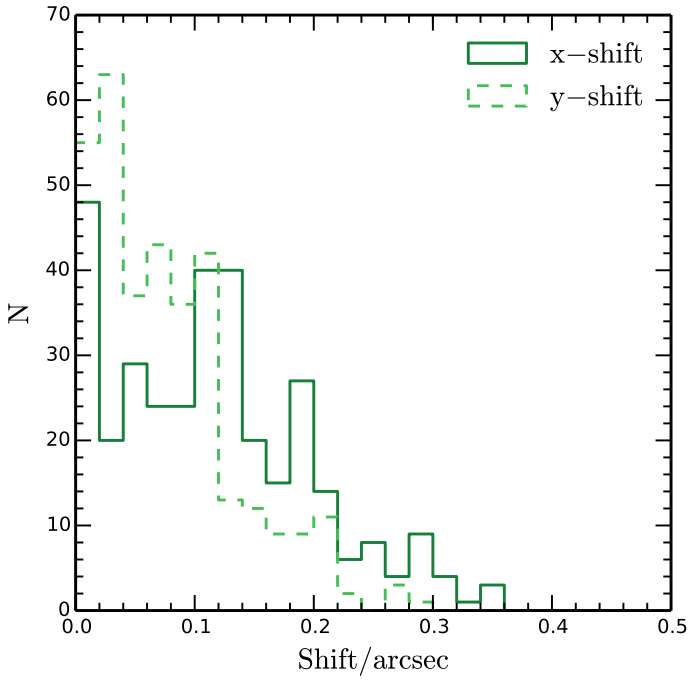

Figure 2.10 *Shifts of the GOODS-S, UDS and COSMOS 3D-HST pointings with respect to the corresponding CANDELS mosaic. The median shift (across both x and y directions) is 0.08".*

raw images are combined a final time.

Figure 2.9 shows the results of the alignment procedure. The left-hand panel shows the CANDELS mosaic with the objects selected for matching, the centre panel shows the 3D-*HST* image before alignment and the right-hand panel shows the 3D-*HST* image after alignment. Generally the shifts are very small relative to the size of the WFC3 detector. Figure 2.10 shows the distribution of x and y shifts across all the reduced 3D-*HST* tiles, the median shift in both direction is 0.08" which corresponds to 1.3 pixels at the final sampling, however some shifts are as much at $\sim$ 5-6 pixels. One final point to note is that though 3D-*HST* direct images are taken with the F140W filter, the lack of a deep CANDELS pointing in this filter means I must perform the alignment using either the F125W or F160W CANDELS image. However, this does not have any significant detrimental affect on image alignment.

2.3.4 F140W Background Subtraction and Combination

To subtract the background in the direct F140W image I follow a procedure similar to the one outlined in Koekemoer et al. (2011) for CANDELS images. First I mask objects in the F140W images using `SExtractor` with an aggressive detection threshold (`DETECT_THRESH` = 1.5) to ensure accurate determination of source-free pixels. The `SExtractor` parameter `DETECT_THRESH` defines the number of sigma above the `SExtractor` estimated background level above which a pixel is considered a source and so determines how aggressively potential sources in the exposure are masked. After some experimentation I found that a value of 1.5 provides a optimal fit for aggressively masking sources whilst at the same time leaving enough free pixels for a good statistical determination of the background level. This leaves only pixels representing the sky distribution, an example segmentation image for a typical 3D-*HST* exposure is shown in Fig. 2.11. An iterative sigma-clipping procedure is then performed on the resulting sky-pixels whereby $> 3\sigma$ outliers are rejected at each iteration. This step ensures as many of the remaining pixels containing actual sources are removed from the sky pixels distribution. I then take the median of the remaining sky pixels and assume a flat background at this level, this flat background is then subtracted from the image. Fig. 2.12 shows the results of this procedure for a typical exposure, the filled grey histogram shows the distribution of the final sky pixel sample with a median value of 0.65 e^{-}/s, the open black histogram shows the final sky pixel distribution after subtracting off this median value across the image.

2.3.5 G141 Background Subtraction

The previous section described the background subtraction for the direct F140W image. Here I describe the process of background subtraction for the grism G141 images, which is a critical step in the reduction process. There is significant background structure in the grism images due to overlapping grism orders at all positions across the image. Also, not all parts of the detector are exposed to all grism orders and the background levels in these areas are significantly reduced (e.g. see dark bands in left-hand edge of detector in Fig. 2.13). There are two default options for grism background subtraction when running the `aXe` software: (i) use a 'master' grism sky background provided with the `aXe` package which is scaled and subtracted from each input grism image; (ii) perform a local

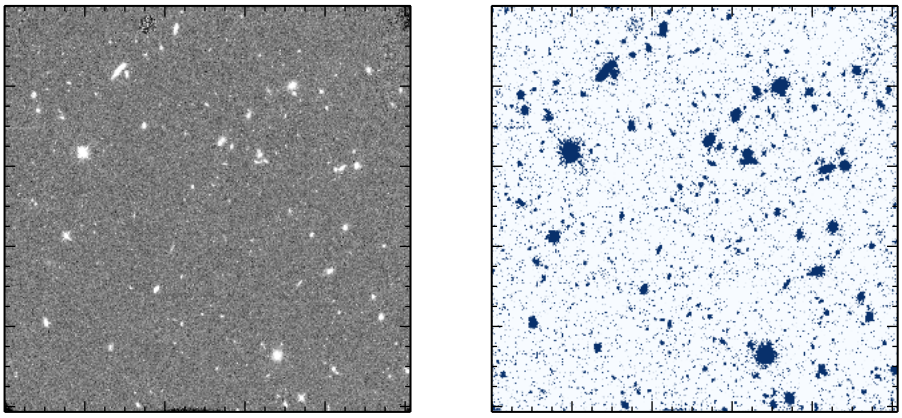

Figure 2.11 Left panel: *Showing an example F140W image.* Right panel: *Showing the segmentation map produced with SExtractor for this exposure, all the white pixels in this image are pixels used for estimating the background.*

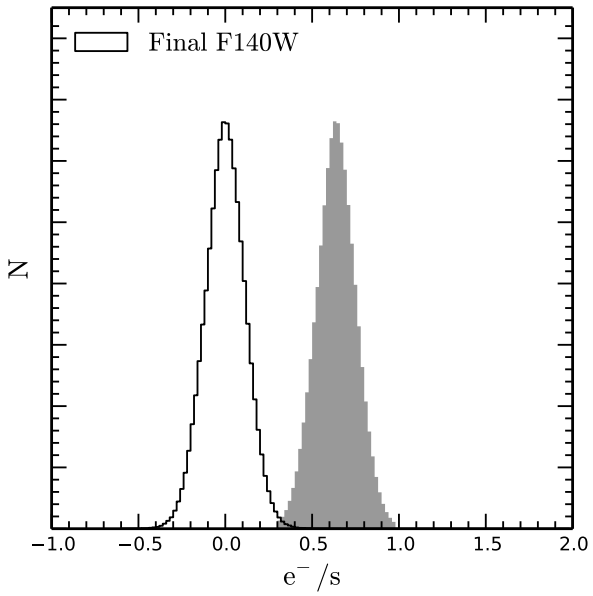

Figure 2.12 *Showing the pixel distribution between the original F140W image (gray histogram) compared to the background-subtracted one (open black histogram).*

background subtraction around each grism spectrum individually. The latter option is not preferred for deep grism images of faint sources as the vicinity of any given grism spectrum is often dominated by spectra of other objects in the grism pointing. Therefore, the immediate vicinity of a given spectrum is not necessarily representative of the background level across the image.

Brammer et al. (2012) have also found that using one 'master' sky image is not optimal for 3D-*HST* exposures because the survey spans a wide range of celestial co-ordinates and therefore different exposures are subject to varying levels of zodiacal and Earth glow background light. Therefore these authors provide four representative master background images for optimal background subtraction. These master images, shown in Fig. 2.13, are median combinations of subsets of the 3D-*HST* exposures with similar background structure grouped together by eye. As can be seen in Fig. 2.13, while being broadly similar, the images have distinctly different structure in the x-pixel direction. I have implemented a background subtraction routine using these four master sky images, choosing not to use one of the default `aXe` methods. Below I described this process for one typical 3D-*HST* pointing (`GOODS-S-32`).

First, spectra in the grism exposures are masked by creating a segmentation map with `SExtractor` (Bertin & Arnouts, 1996) to locate areas of minimal source contamination for estimating the sky background level. An example of a segmentation map for one exposure in the `GOODS-S-32` pointing is shown in Fig. 2.14.

Once the segmentation map is created I match the background level in the pointing to one of the four master images. The background level in each x-pixel in the G141/master image is estimated by taking the median of the source-free pixels along the y-axis. This creates a background profile across the image (see Fig. 2.15). The profile in each of the master images is scaled to the profile in the G141 exposure and that profile is compared using a χ^2 test. The master sky images with the lowest χ^2 is selected as the best representation of the background in the G141 exposure. Fig. 2.15 shows the background profile for one exposure in the `GOODS-S-32` pointing compared to the four master sky images, in this particular case the `sky_cosmos.fits` master sky image returns the best-fitting background profile.

Once the best-fitting master sky background is chosen I loop through each column in the G141 image and sky image and scale the sky image to the G141 image

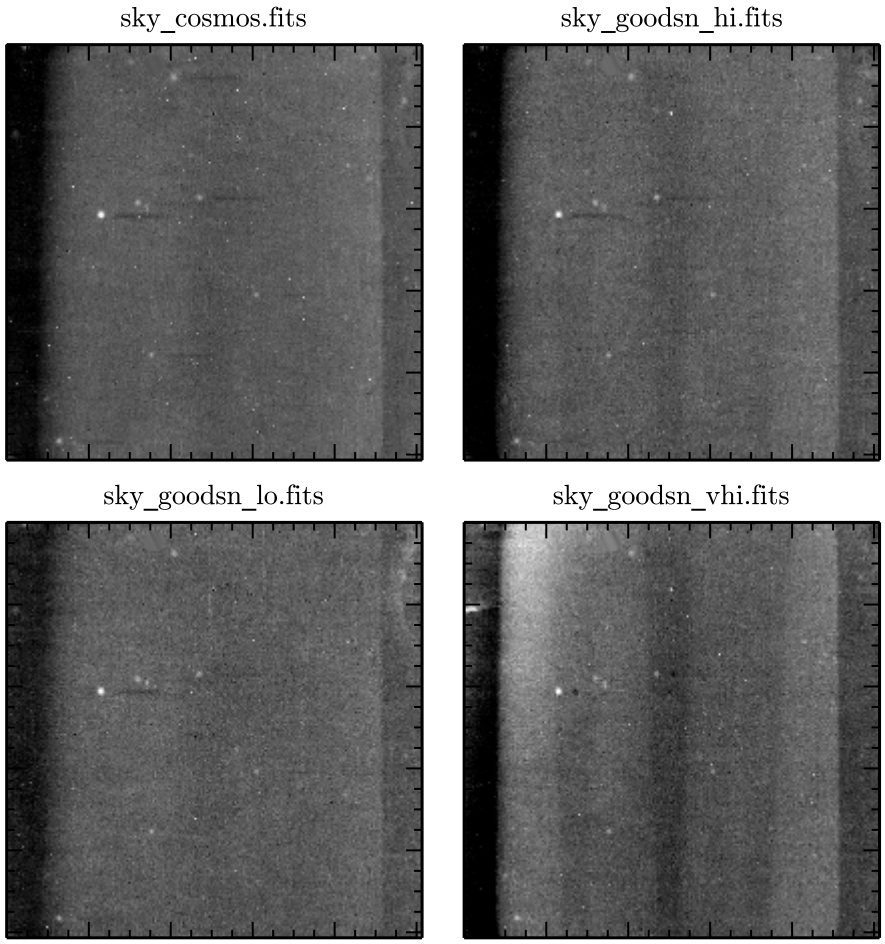

Figure 2.13 *Showing the four G141 master sky images for the 3D-HST survey. These images are median combinations of subsets of 3D-HST pointings with a similar background structure which have been grouped together by eye (Brammer et al., 2012). While being broadly similar, each sky image shows unique structure in the level of the background in the x-pixel direction.*

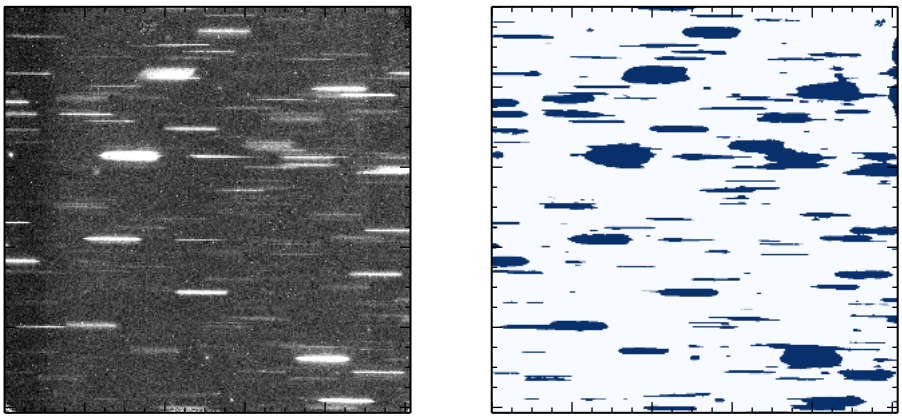

Figure 2.14 Left panel: *Showing an example G141 exposure divided by the F140W flat-field.* Right panel: *Showing the segmentation map produced with SExtractor for this exposure, all the white pixels in this image are pixels used for estimating the background.*

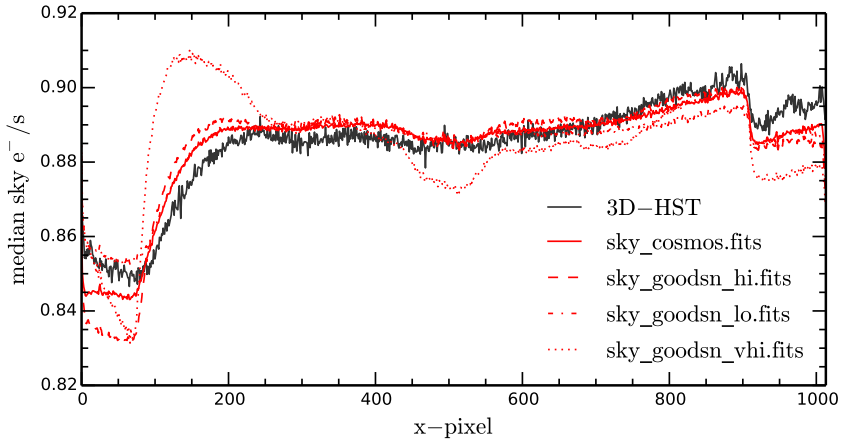

Figure 2.15 *Illustrating the procedure for selecting the best-fitting master sky background for a G141 3D-HST exposure. The black line shows the background profile of the G141 image calculated by taking the median value of sky-free pixels along the y-axis. This is compared to the profiles of each sky image (red lines), the best-fitting sky image is determined by a χ^2 comparison of the background profiles.*

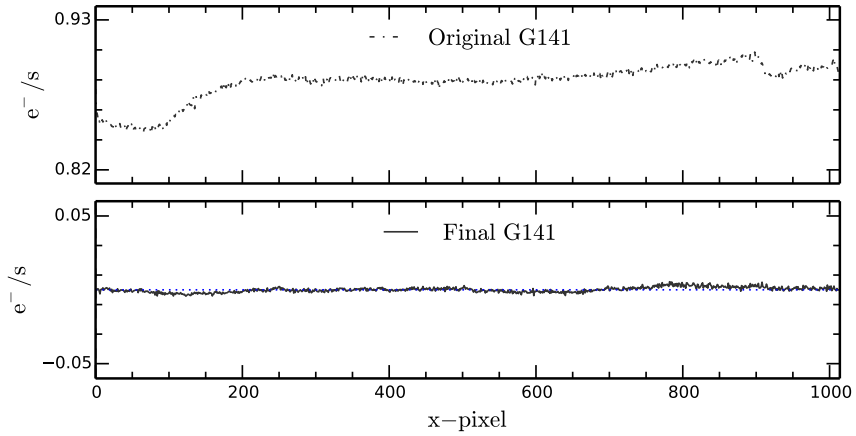

Figure 2.16 *A comparison of the sky-subtracted G141 column profile (bottom panel) and the original column profile (top panel). The figure illustrates how the background subtraction removes both the background structure and overall level from the G141 image.*

using the median pixel value along that column (where the median is taken for the sky free pixel in the G141 image). In this way I subtract the scaled sky columns from the G141 image columns across the entire image. Finally I subtract the median value of sky free pixels along each column in the sky-subtracted G141 image to removed any residual structure that is not accounted for in the master sky backgrounds (Brammer et al., 2012).

The results of the total process are shown in Figs. 2.16 and 2.17. Fig. 2.16 shows the median pixel value along columns, in the original G141 image (top panel) and the final sky-subtracted image (bottom panel), where it can be seen that both the overall background level and the background structure have been removed leaving a smooth background across the full image. This is further illustrated in Fig. 2.17 which shows the pixel value distribution in all sky free pixels for the original and sky-subtracted G141 images. The sky-subtracted G141 image is consistent with a zero mean background level. Finally, in Fig. 2.18 I show the normalized distributions of the sky subtracted pixel values across all the 3D-*HST* fields used in this thesis (GOODS-S, COSMOS, UDS). The standard deviation of the distribution, calculated across all fields, is 0.05 e^-/s, with extremely small field-to-field differences (~ 0.008 e^-/s), highlighting the stability and accuracy of the background subtraction routine.

At this stage in the pipeline the G141 grism image and F140W direct image have both been corrected for intrinsic shifts due to guide star errors, been aligned

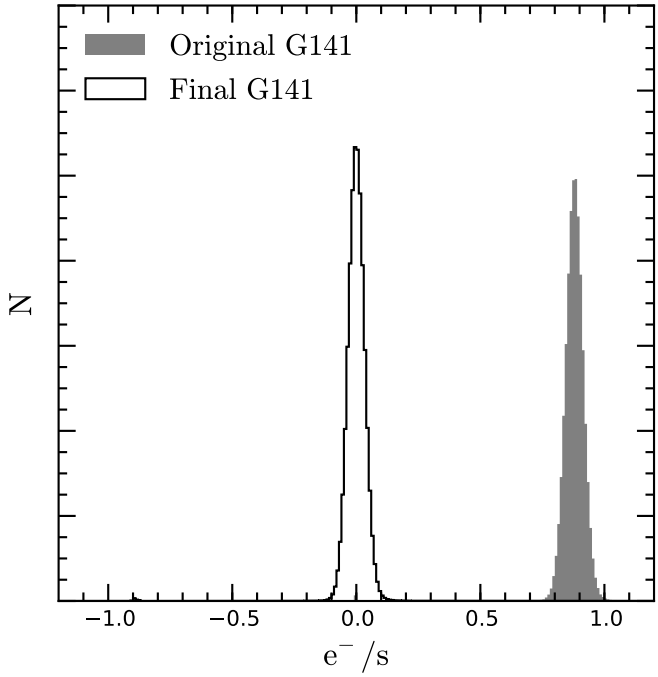

Figure 2.17 *Background pixel value distribution for the background-subtracted G141 exposure (open histogram) compared to the original (filled histogram).*

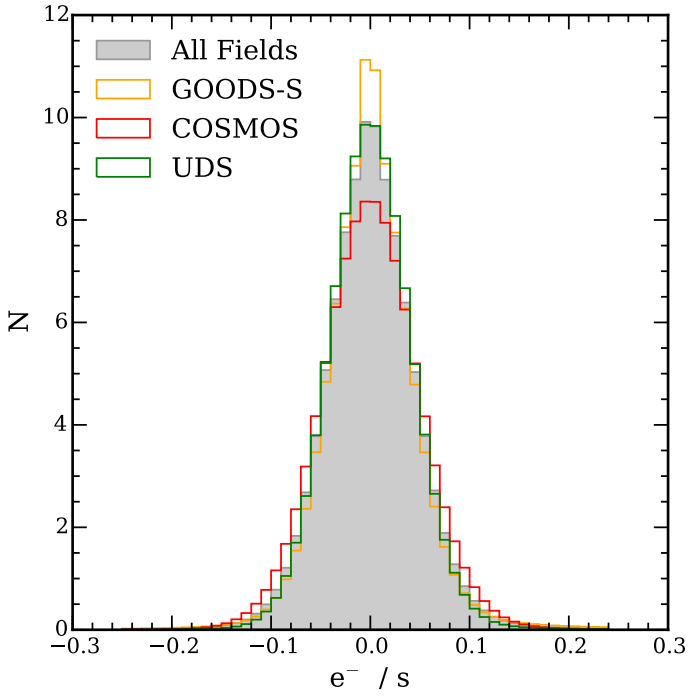

Figure 2.18 *Showing the normalized background pixel distibutions for GOODS-S (open orange histogram), COSMOS (open red histogram), UDS (open green histogram) and the three fields combined (filled grey histogram). A guassian fit to the combined data has a standard deviation of 0.05 e^{-}/s.*

to the reference CANDELS image mosaic, and had cosmic rays and the overall background removed. The data are now fully prepared and ready to use with the `aXe` spectral extraction software. However, before the spectral extraction is run a few more preparation steps are required, including generating an object list for extraction and preparing a model grism image for estimating spectral overlap and contamination.

2.3.6 Object Catalogue creation with SExtractor

To run the `aXe` spectral extraction software an object list must be supplied specifying the x, y and world co-ordinates of the objects of interest. I generate this catalog by running `SExtractor` (Bertin & Arnouts, 1996) on the F160W (H-band) CANDELS mosaic. As well as generating the positions of all objects in the image `SExtractor` can also produce a segmentation map to be used for making the model grism image as described in Section 2.3.7.

An important consideration when making the object catalogue is estimating contamination in the grism image. To maximize the accuracy of the model grism image I run `SExtractor` with an aggressive detection threshold (`DETECT_THRESH` = 2.0) to ensure all objects in the image are accounted for. The source detection is performed on the CANDELS F160W mosaic because it is much deeper compared to the F140W direct imaging from 3D-*HST* and therefore ensures an accurate and reliable source detection.

2.3.7 Contamination Estimation: Making a Model Grism Image

The estimation of contamination is one of the most prominent challenges in the reduction grism spectra. Because no masks are applied in grism spectroscopy there is the potential for contamination of a given spectra by both nearby sources in the cross-spectral direction and more distant sources in the spectral direction. This is especially true for the 3D-*HST* survey (or any grism survey of distant galaxies) where multiple targets occupy a single WFC3 pointing.

One method often employed in grism spectroscopy is to take spectra of a given pointing at multiple position angles in the hope that, for at least one position angle, a given spectrum will be free from spectral contamination (e.g. Pirzkal et al., 2013). However this is not the case for the 3D-*HST* survey which, because of the large survey area, only utilizes one position angle per pointing. Fortunately the 3D-*HST* survey covers the CANDELS fields and therefore is supported by a wealth of ancillary photometric information which can be used to construct model grism images to give a quantitative estimation of the contamination of each spectrum.

The basic situation is illustrated in Fig. 2.19. A set of images in different bands (possibly covering the same wavelength range of the grism spectra) are supplied to the `aXe` task `fcubeprep` to generate a model grism image. For 3D-*HST* I use the F105W, F125W and F160W mosaics from CANDELS which combined span the wavelength range $\sim 0.9 - 1.7\mu$m. This ensures complete photometric coverage of the spectral range of the G141 filter. `fcubeprep` then constructs a model spectral energy distribution (SED) for each object in the master catalogue, created as described in Section 2.3.6, using a cubic spline interpolation between the flux in each band. This photometric information is then combined with an

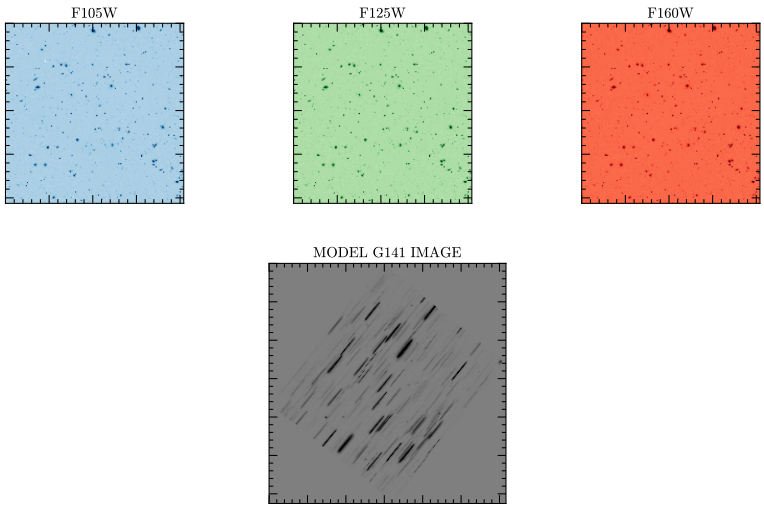

Figure 2.19 *Illustrating the process by which the model grism image is created. Individual images in different filters are combined to get the spatial and flux information across a large spectral range, this information is used to create a model grism image as described in the text.*

objects morphological information derived from the segmentation map to create a model grism image of the exposure. To summarise, this procedure generates a simulated grism image, where for every object the continuum spectrum and its normalisation is derived from the broad-band photometry provided by the CANDELS images(F105W, F125W and F160W). It is worth noting that fcubeprep provides only the continuum and the normalisation, but no information on possible emission lines. This simulated images (or 'contamination model') is then used to evaluate the level of contamination for each extracted spectrum from the real data.

Accounting for Objects Outside the F140W FOV

`aXe` also allows for objects outside the F140W field of view (FoV), whose spectra have been dispersed onto the G141 image, to be extracted in the final reduction. The dispersion of spectra from outside the WFC3 FoV onto the grism detector can be clearly seen in the example grism exposure shown in Fig. 2.14. Also, Fig. 2.2 shows how the 1^{st} order spectrum is shifted with respect to the position in the direct image. To account for these objects one must simply include these objects in the input object catalogue. To achieve this I add an artificial 500 pixel border to the F140W exposure and run the `sregister` task in `iraf` to cut out an

enlarged section of the CANDELS detection image. This procedure is possible since the F140W image has been previously aligned to the CANDELS WCS (see Section. 2.3.3). I then use this enlarged CANDELS detection image to create the object catalogue as described in Section 2.3.6.

2.3.8 Final Spectra Extraction with aXe

At this stage the data has been sufficiently prepared for spectral extraction with the dedicated grism reduction software `aXe` (Kümmel et al., 2009). To briefly recap, the following procedures have been preformed up to this point:

- Correct WFC3 exposures for guide star errors and cosmic rays.
- Align WFC3 exposers to CANDELS reference images to correct WCS information.
- Custom background subtraction of both F140W and G141 exposures.
- Create master catalogue for reduction using CANDELS detection image.
- Creation of simulated grism images to evaluate contamination.

In this section I will give a detailed description of the subsequent `aXe` reduction, breaking it down into each of the individual procedures:

`aXe.axeprep:` The main purpose of this task is to perform the default master sky background subtraction of the grism exposures. This master background is scaled to each exposure separately by first masking the brightest spectral traces (in a very similar way to that described in Section 2.3.5). However, in the event of using a custom background subtraction, as I do, this step can be switched off.

`aXe.axecore:` The main bulk of the spectral extraction is performed by the `axecore` task. First, using the measured size and position of an object from the input master catalogue, the region on the grism exposure containing the spectral trace for that object is determined (referred to as the 'BEAM')[3]. The length of the beam is determined from the WFC3 G141 configuration files and the width of the beam is set by the size of the object and the input extraction width parameter.

[3]The combination of all beams (i.e. the dispersion orders) for an object is referred to as the object's APERTURE.

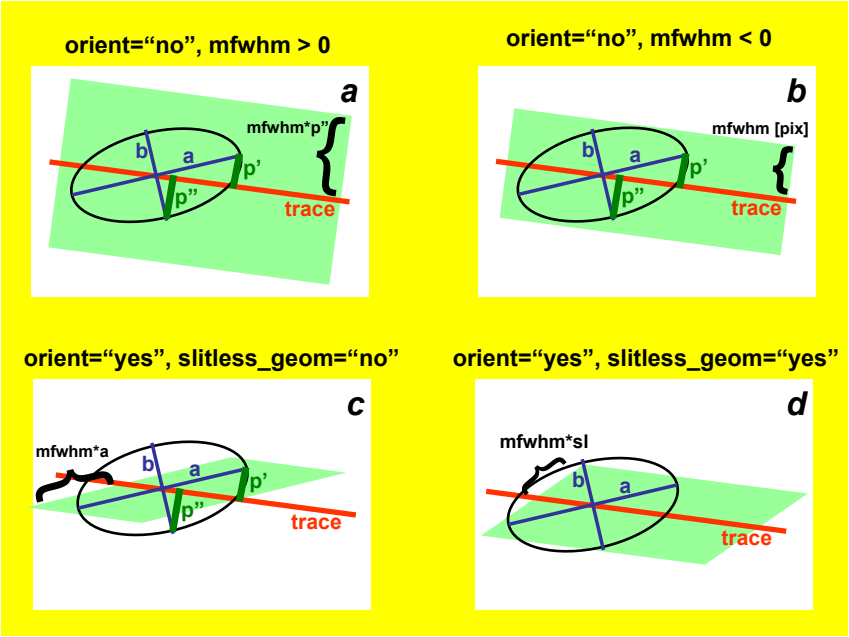

Figure 2.20 *Showing the different scenarios for setting the extraction width and direction in the* `aXe` *reduction, the details of each scenario are described in the text below.*

It is worth reviewing here the different ways in which this extraction width can be defined since the ability to extract spectra with arbitrary slit widths is one of the major advantages of grism spectroscopy. In conventional slit spectroscopy, where the slit is determined by the physical size of the mask, one has to often correct for signal lost because the slit does not encompass the whole light of the galaxy. However, since the grism slit can be arbitrarily defined, the issue does not arise.

For the simple case in which the spectrum is extracted at 90° with respect to the trace, the extraction width is determined by projecting the semi-major and semi-minor axes of the object (`A_IMAGE`, `B_IMAGE`) onto the trace, taking the maximum value and multiplying by the input `extrfwhm` parameter (set to 4 by default by the `aXe` software). This procedure is illustrated by panel (a) of Fig. 2.20 (taken from the `aXe` user manual[4]), panel (b) shows a similar case in which the value of `extrfwhm` is taken as a fixed extraction width and the objects size is ignored.

It is also possible to extract the final 1D spectra at an arbitrary angle with respect to the spectral trace. This technique allows one to effectively increase the resolution of the final spectrum because slitless spectroscopy is spatially resolved. For example an emission line, in the case of perpendicular extraction, may be

[4]http://axe.stsci.edu/axesim/manual/aXeSIM1.4_manual/index.html

artificially blurred by the width of the galaxy in the trace direction, however an extraction direction may be chosen in which this morphological blurring is reduced. Panel (c) shows an example scenario in which the extraction direction is taken as the direction of the major axis multiplied by `extrfwhm`, in this case the width of the object in the trace direction is reduced. Panel (d) shows the final option whereby the optimal extraction direction is determined from the geometrical properties of the object (`A_IMAGE`, `B_IMAGE`, `THETA_IMAGE`).

The choice between all these options is controlled through the input parameters `orient` and `slitless_geom` as illustrated in Fig. 2.20. In the 3D-*HST* reductions I chose to extract always perpendicular to the trace with a variable width (i.e. scenario in panel (a)), this was motivated by the fact that the morphological distortion of high redshift galaxies will be minimal due to their small size on the detector, and the fact that any extreme distortions to emission line profiles could, if necessary, be handled separately using custom de-convolution routines.

`axecore` then uses the contamination model derived as described in Section 2.3.7 to create a 'contamination BEAM' for the object. Essentially the same BEAM region used for the real spectral extraction is also extracted from the model grism image giving a model 2D spectrum, or contamination BEAM. The model 2D trace of the object of interest is then subtracted from the contamination BEAM leaving only the modeled contribution of other sources whose spectra contaminate the real extracted BEAM. For every 2D object spectrum `aXe` provides a quantitative 2D model of the contamination in that spectrum from other objects in the FoV.

At this stage each object has four wavelength-calibrated 2D spectra (one from each of the four G141 exposures) and the wavelength-dependent flat field response of the G141 detector can be applied. The flat field must be wavelength dependent since, in principle, each pixel on the G141 detector can collect light from any given wavelength, which will vary from object to object.

`aXe.axedrizzle:` The next step involves drizzling together the four separate 2D spectra from each G141 exposure to create the final 2D spectrum. This final drizzled spectrum will then be used to extract the 1D spectrum as described below. The drizzling process is essentially the same as the one described above in Section 2.3.2, and the purpose is similar: to flag any additional cosmic rays in the images which have not already been filtered out, increase the signal-to-noise in each pixel and to optionally re-grid the data to higher spatial and spectral sampling.

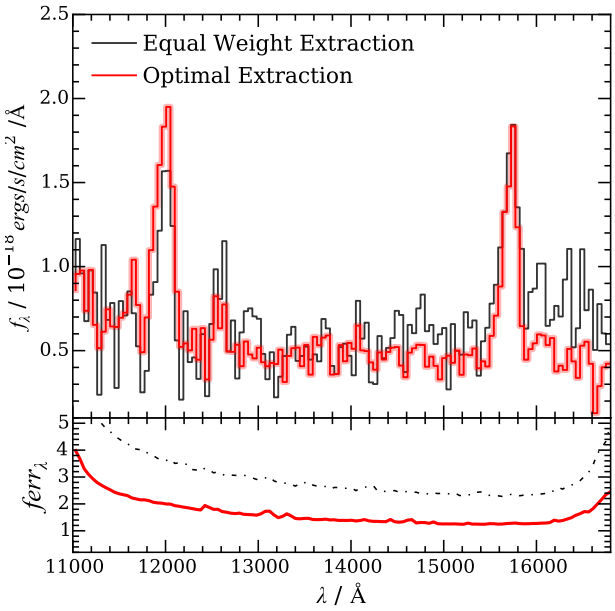

Figure 2.21 *Illustrating the difference between an extraction assuming equal weights in all pixels (black) to an optimal extraction technique (red). The top panel shows extracted 1D spectrum and the bottom panel shows the corresponding 1D error spectrum. See text for details on the different extraction methods.*

I choose to drizzle to 0.06" sampling in the spatial (cross-dispersion) direction and 46.5Å/pixel in the wavelength direction. In theory the wavelength direction can also be drizzled to half-pixel sampling (i.e. 22Å/pixel), however I chose not to implement this since at the native 46.5Å/pixel the [OII], Hβ and [OIII] emission lines are all resolved and to achieve further emission line resolution (i.e. de-blend the Hα and [NII] lines) would require ∼10Å/pixel. Therefore, at the risk of spurious effects arising from interpolating between pixels, drizzling to 22Å/pixel does not carry any significant benefits.

Extracting a 1D Spectrum

The final 1D grism spectrum can now be extracted from the 2D drizzled spectrum. In the simplest case the 2D spectrum can just be summed along each wavelength pixel however this is not in general the optimal solution for achieving the best possible signal-to-noise ratio. Instead the sum can be weighted such that pixels further from the spectral trace, containing less object flux and therefore at lower signal-to-noise, are given a lower weighting.

Developed initially by Horne (1986) and subsequently by Rodríguez-Pascual et al. (1999), the equation for optimal extraction is:

$$f(\lambda) = \frac{\Sigma_x [f(x,\lambda) - b(x,\lambda)] \frac{p(x,\lambda)}{\sigma(x,\lambda)^2}}{\Sigma_x \frac{p(x,\lambda)^2}{\sigma(x,\lambda)^2}}, \tag{2.2}$$

where λ is the wavelength co-ordinate, $f(x,\lambda)$ is the flux value at pixel (x,λ), $b(x,\lambda)$ is the background value (which in this case has already been subtracted), $\sigma(x,\lambda)$ is the noise value and $p(x,\lambda)$ is the spatial profile of the object. $p(x,\lambda)$ is estimated from the 2D model spectrum of the object at each wavelength value. $\sigma(x,\lambda)$ also makes use of the 2D beam model and is estimated using the equation:

$$\sigma(x,\lambda) = \sqrt{f_{\mathrm{model}}(x,\lambda) + b(x,\lambda) + \mathrm{rdnoise}^2}, \tag{2.3}$$

where rdnoise is the detector readout noise value. In this way a 1D spectrum from the object is produced and this represents the final product of the spectral extraction. Fig. 2.21 shows the difference between an optimal extraction and an equal-weight extraction for an example grism spectrum, it can clearly be seen that, though there is a small change in the final extracted spectrum, the error in the optimally-extracted spectrum is significantly reduced.

The electron counts measured by the detector are converted into flux units using standard G141 sensitivity curves derived from measurements of standard stars. Similarly, a 1D contamination model is produced. In the next chapter I will described how I implemented a routine for estimating redshifts for the emission-line grism spectra using these 1D spectra, as well as how continuum and line flux emission was estimated.

2.4 3D-*HST* Spectral Analysis

2.4.1 Redshift Estimation

Before continuum and line fluxes can be fit to the spectra the redshift must be known. Initially all galaxies that have been processed through the pipeline are fed through a separate analysis procedure to estimate redshifts. Since 3D-*HST* boasts extensive photometric coverage from the CANDELS survey it is possible to combine spectral template fitting with photometric redshifts estimated

from the broad-band photometry; the combination of the redshift probability distributions resulting from the two techniques, as described below, gives an accurate estimation of the redshift of emission line galaxies.

χ^2 Spectral Template Fitting

The first technique I employ is a χ^2 spectral template fitting procedure. Using the composite spectral template of star-forming galaxies from the K20 survey (Mignoli et al., 2005), smoothed to the wavelength resolution of the grism spectra, I produce $\chi^2(z)$ plot by estimating the χ^2 statistic at each redshift via the following equation:

$$\chi^2 = \sum_{i=1}^{n} \frac{(bm_i - d_i)^2}{\sigma_i^2}, \tag{2.4}$$

where the sum is over each spectral pixel and m_i, d_i and σ_i are, respectively, the template value, data value and data error value in that pixel. b is the overall normalization of template spectrum to the grism spectrum found be solving $\frac{\partial \chi^2}{\partial b} = 0$ which gives:

$$b = \frac{\sum_{i=1}^{n} \frac{m_i d_i}{\sigma_i^2}}{\sum_{i=1}^{n} \frac{m_i^2}{\sigma_i^2}}. \tag{2.5}$$

The best redshift estimate is then given by the minimum of the resulting $\chi^2(z)$ function. This can be seen from considering the posterior probability distribution $\mathrm{P}(m|d)$ for the redshift variable which, from Bayes' theorem, is proportional to the likelihood function $\mathrm{P}(d|m)$:

$$\mathrm{P}(m|d) \propto \mathrm{P}(d|m), \tag{2.6}$$

where again m is the model, which is a function of the variable of interest (i.e. redshift), and d is the data. In the case of a variable with an assumed Gaussian error distribution, the likelihood function is given by the normal distribution:

$$\mathrm{P}(d|m) \propto \exp[-\tfrac{(m-d)^2}{2\sigma^2}], \tag{2.7}$$

or

$$\mathrm{P}(d|m) \propto \exp[-\tfrac{\chi^2}{2}]. \tag{2.8}$$

Therefore, finding the maximum of the likelihood function (or maximum probability) is equivalent to finding the minimum of the χ^2 function. Equations 2.7 and 2.8 above also illustrates how to turn a $\chi^2(z)$ function into a $p(z)$ function. This in turn provides a convenient way to combine probability functions from independent redshift estimates, as will be discussed in more detail below.

An example of the χ^2 technique is shown in Fig. 2.22 where I plot an example grism spectrum along with the K20 template spectrum at the best-fitting redshift. It can be seen from the figure that the template fitting has correctly identified the [OIII], Hβ and Hα emission lines in the grism spectrum. The inset panel to Fig. 2.22 shows the $\chi^2(z)$ function derived as described above, and the clear minimum at $z \sim 1.4$ indicates the best-fitting redshift. This illustrates an example where, thanks to multiple emission lines being visible in the grism spectrum, a redshift solution can be unambiguously distinguished using this technique.

However, a robust redshift solution cannot always be found using this technique alone. Fig. 2.23 shows an example where only one prominent emission line is visible in the grism spectrum, and from the inset $\chi^2(z)$ function it is clear two redshift solutions are identified ($z = 1.055$ and $z = 1.690$). These solutions correspond, respectively, to Hα and [OIII] being responsible for the visible emission line and both spectral fits are illustrated in the plot (green and orange lines). Clearly, in this example the χ^2 technique is not able to accurately identify a robust redshift solution and therefore alternative redshift estimates are required. Thankfully, due to the deep multi-wavelength photometric coverage of the 3D-*HST* fields it is possible to estimate accurate photometric redshifts for these galaxies. This independent redshift measurement, based purely on the galaxy photometry (but over a much longer wavelength baseline from UV to infrared), will then in theory help us to distinguish between the solutions illustrated in Fig. 2.23.

Photometric Redshifts with EAZY

I estimate photometric redshifts using the publicly available code `EAZY` (Brammer et al., 2008). The concept for determining redshifts with EAZY is very similar to the above χ^2 template fitting technique: a set of SED templates are compared to

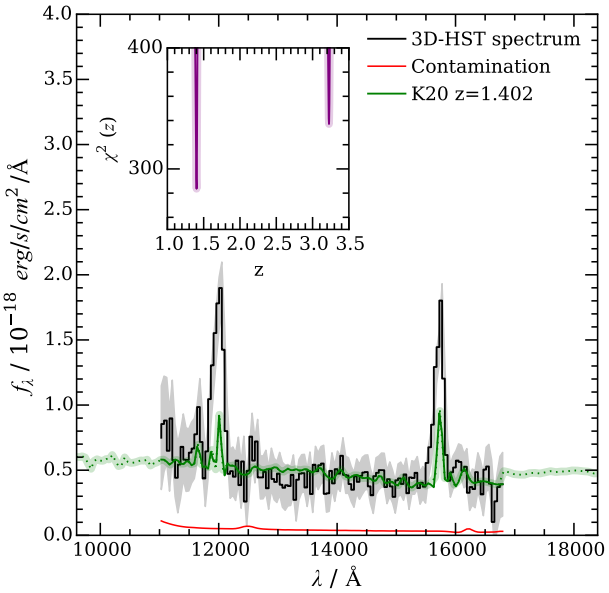

Figure 2.22 *Showing an example of the χ^2 spectral template fitting technique used to estimate redshift from an emission line grism spectrum (GOODS-S-4-8527). The black line shows a 3D-HST grism spectrum and the green line shows the K20 template interpolated to the same wavelength resolution. The red line at the bottom of the figure shows the spectral contamination. The inset panel shows the $\chi^2(z)$ function obtained by the method described in the text, with a clear mimimum at $z \sim 1.4$. The second minimum at $z \sim 3.3$ occurs when the [OII] template emission line overlaps with the Hα emission line, however this solution is clearly dis-favoured with a significantly higher χ^2 and is therefore rejected. This is an example of a 3D-HST spectrum with a clear, unambiguous redshift solution.*

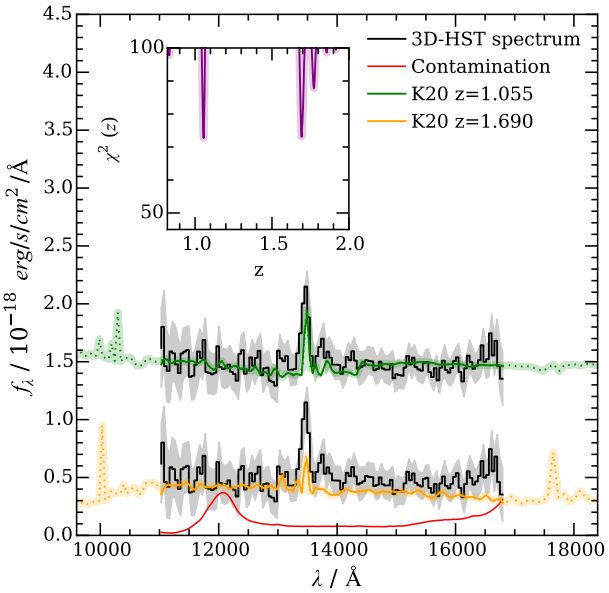

Figure 2.23 *Showing another example of the χ^2 spectral template fitting technique used to estimate redshift from an emission line grism spectrum (GOODS-S-4-9060). All lines and symbols are the same as for Fig. 2.22 with the exception that here two versions of the grism spectra have been plotted (one offset from the other for clarity). The two spectra compare the K20 templates at the two different redshift solutions, visible in the inset $\chi^2(z)$ plot, $z = 1.055$ and $z = 1.690$, fitting Hα and [OII] respectively. This shows an example where, due to the low resolution and wavelength coverage of the grism spectra multiple solutions cannot be distinguished when only one emission line is seen in the spectrum.*

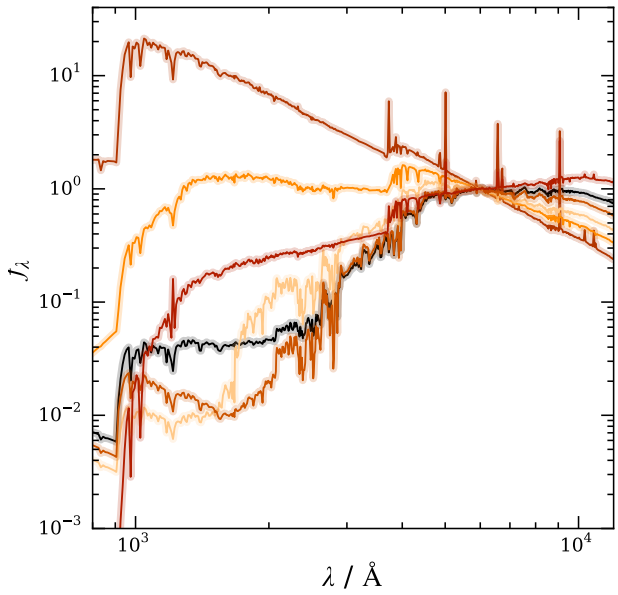

Figure 2.24 *Showing the six input spectral templates used for deriving photometric redshifts with EAZY (see text for details). All templates are normalized at 6000Å. Figure adapted from Brammer et al. (2008).*

the observed photometry across a range of redshifts, and the best-fitting redshift determined where the χ^2 is minimized.

The templates used in `EAZY` are produced by fitting a set of synthetic galaxy spectra from the `PEGASE` library (Fioc & Rocca-Volmerange, 1997), to a set of mock-photometry of 10^4 galaxies, in the redshift range $0 < z < 4$, generated from the semi-analytic models of De Lucia & Blaizot (2007). This method of producing galaxy templates from semi-analytic models is particularly appropriate for fitting high redshift galaxies since in other codes, where the template set is produced by fitting the photometry of observed galaxies in the local Universe, the resulting templates may not be representative of the SEDs of the high redshift population. Additionally, De Lucia & Blaizot (2007) show the synthetic photometry produced in their models is a realistic representation of observed photometry out to high redshift.

From the 10^4 resulting SED templates, a set of six 'basis' templates are produced using a 'non-negative matrix factorization' algorithm from Blanton & Roweis (2007). The resulting six templates can be thought of as the 'principal components' of the input SEDs, which can be linearly combined to reproduce

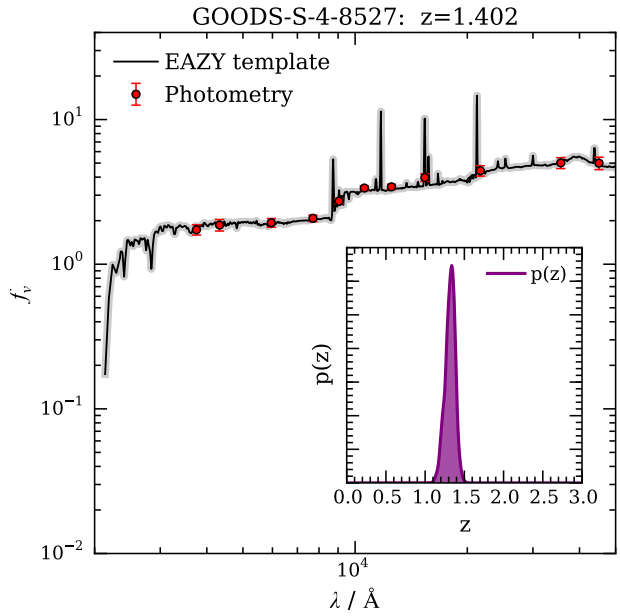

Figure 2.25 *Example of an SED-derived photometric redshift using EAZY. The black curve shows the best-fitting template SED with the observed photometry shown in red. The inset plot shows the normalized p(z) distribution derived from the χ^2 analysis.*

any given input SED. The six `EAZY` templates are illustrated in Fig. 2.24, and can be seen to cover the range of young star-forming galaxies to old evolved passive galaxies, including nebular emission lines as appropriate. When fitting redshifts, `EAZY` allows linear combinations of these basis templates to provide the best match to the shape of the observed photometry.

This has the advantage of being able to reproduce complex star-forming histories, for example, in the case of an old passive galaxy which has undergone a recent burst of star formation, this method can account for the presence of both populations.

Figs. 2.25 and 2.26 show the best-fitting `EAZY` template and redshift probability distributions (inset axis) for the 3D-*HST* spectra from Figs. 2.22 and 2.23 respectively. From an inspection of these figures it can be seen how `EAZY` can handle a variety of different SED shapes and also attempt to account for the presence of emission lines in the galaxy photometry. The output probability distributions provide an independent measure of the galaxies redshift which can be combined with the spectral template fitting described above to determine redshifts in ambiguous cases.

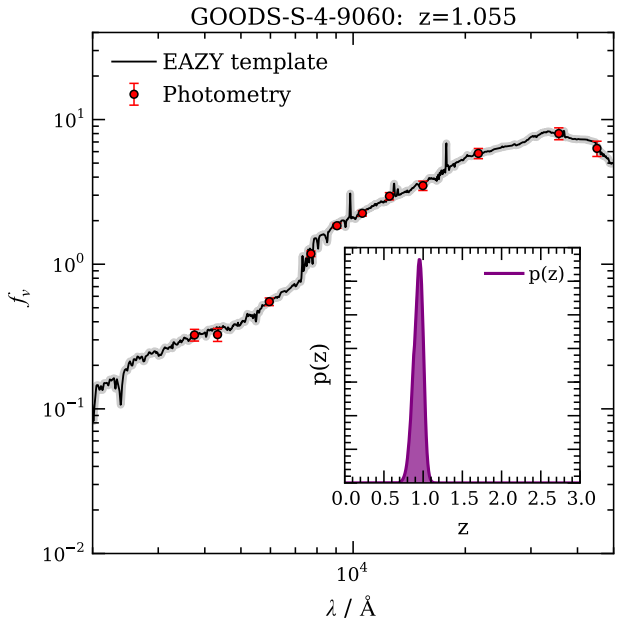

Figure 2.26 *Example of an SED-derived photometric redshift using EAZY. The black curve shows the best-fitting template SED with the observed photometry shown in red. The inset plot shows the normalized p(z) distribution derived from the χ^2 analysis.*

Combining $p(z)$ Distributions

The combination of the χ^2 spectral fitting and photometric redshift probability distributions is illustrated in Figs. 2.27 and 2.28. In essence the photometric $p(z)$ acts as a prior for spectral $p(z)$ and the final $p(z)$ distribution is the product of the two, i.e.

$$p(z)_{\rm final} = p(z)_{\rm spec} \cdot p(z)_{\rm photom}. \tag{2.9}$$

Fig. 2.27 shows the results of this process for the galaxy shown in Figs. 2.22 and 2.25. In this case, a clear redshift solution is obtained from the spectral χ^2 fitting (orange curve), and this is corroborated by a photometric solution which peaks at a similar redshift (purple curve). Combining the two $p(z)$ solutions essentially returns the same $p(z)$ from the spectral χ^2 fitting (black curve) as this distribution is more strongly peaked (i.e. it places a stronger constraint on the redshift than the photometric template fitting).

Fig. 2.28 illustrates the importance of the photometric redshifts for the majority

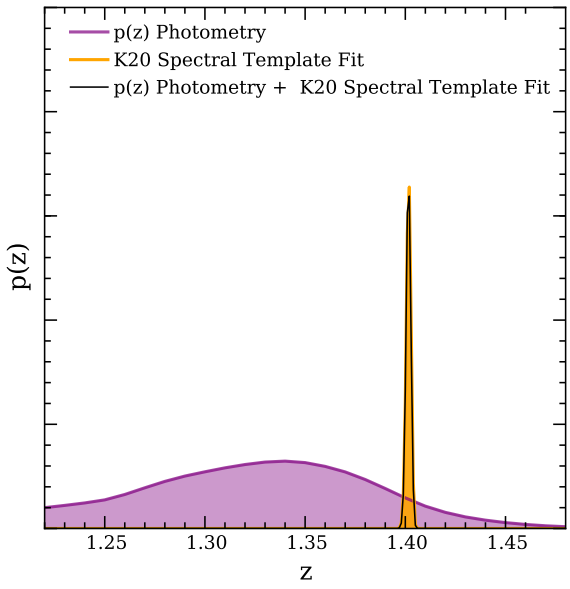

Figure 2.27 *Showing the $p(z)$ distributions obtained from χ^2 spectral fitting (orange curve) and photometric SED fitting (purple curve) for the 3D-HST whose spectra is illustrated in Fig. 2.22 and SED illustrated in Fig. 2.25. The black curve shows the combined $p(z)$ distribution.*

of 3D-*HST* galaxies a with single line detection, this figure corresponds to the galaxy from Fig. 2.23 and 2.26. Here there are two possible redshifts solutions returned from the spectral χ^2 fitting (orange curves) ($z = 1.055$ and $z = 1.690$), however the photometric fitting strongly favours the lower of the two solutions (purple curve).

Now, when the two $p(z)$ solutions are combined (black curve) the resulting probability is strongly peaked around $z = 1.055$, indicating that the emission line observed in the spectrum is Hα as opposed to [OIII]. This case illustrates that, even though the χ^2 spectral fitting is able to place tighter constraints on the final redshift, through a more strongly peaked $p(z)$ distributions, the less tightly constrained photometric redshifts are often required for distinguishing the between degeneracies when only one emission line is present in the 3D-*HST* spectrum.

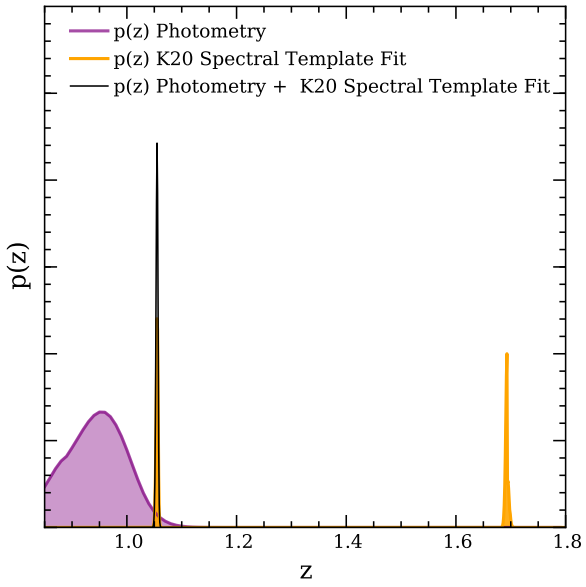

Figure 2.28 *Showing the $p(z)$ distributions obtained from χ^2 spectral fitting (orange curve) and photometric SED fitting (purple curve) for the 3D-HST whose spectra is illustrated in Fig. 2.23 and SED illustrated in Fig. 2.26. The black curve shows the combined $p(z)$ distribution.*

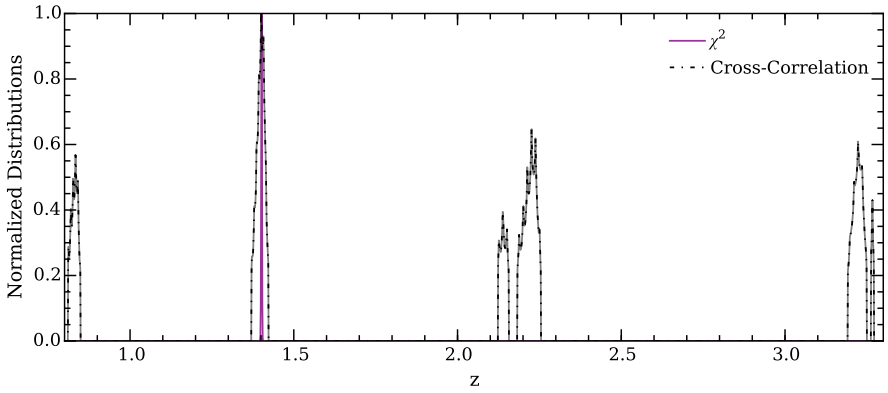

Figure 2.29 *Showing an example of the cross-correlation technique used to help assess the quality redshift estimates as described in the text. The purple line shows the combined $p(z)$ distribution from the photometric and spectral template fitting procedures described above and the black dashed line shows the results of preforming the cross-correlation analysis. Both distributions are normalized to their maximum value. This figure corresponds to the galaxy featured in Figs. 2.22, 2.25 and 2.27.*

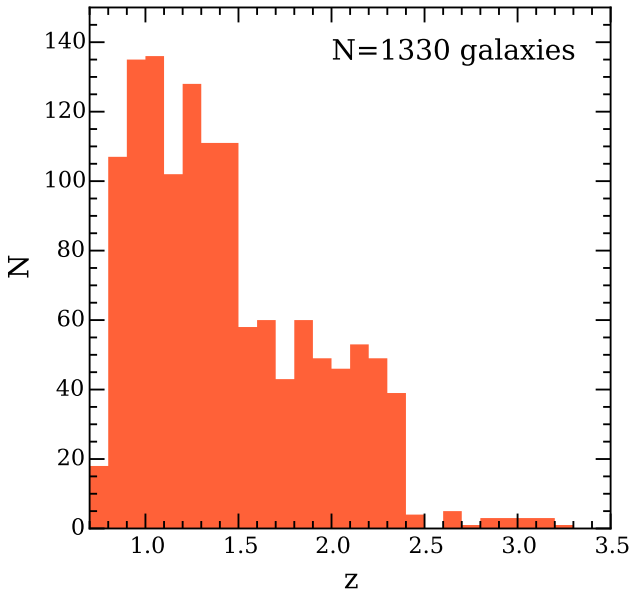

Figure 2.30 *The redshift distribution of all 1330 emission line galaxies in the final catalogue.*

Cross-correlation Fitting

Finally, I use a cross-correlation technique to provide further verification of the final redshift solution, though the resulting cross-correlation function is not incorporated into the final $p(z)$ distribution. Cross-correlation is a way of determining the similarity of two spectra as a function of some variable, in this case redshift. At each redshift value I multiply the grism spectrum by the normalized K20 spectrum, producing a cross-correlation signal which peaks at the redshift where the spectra are most similar. An example of this is shown in Fig. 2.29 which shows the cross-correlation function (normalized to its maximum value) for the grism spectrum featured in Figs. 2.22, 2.25 and 2.27. As can be seen, the function peaks at the same redshift where the combined probability distribution peaks. This spike in the cross-correlation function provides as further support for the redshift solution identified using the spectral template fitting and photometric techniques.

Final Redshift Catalogue

In summary, all 1D grism spectra are passed through a redshift analysis pipeline which calculates the redshift probability distribution derived from χ^2 template

fitting to both the spectrum and the ancillary photometry. In addition, the redshift cross-correlation function is calculated to provide an additional independent estimate of the redshift. However, due to the low signal to noise and low-resolution of some spectra it is not safe to simply assume this automatic procedure has correctly identified the redshift for all emission line galaxies. Therefore, to produce the final redshift catalogue I first visually inspected all reduced spectra and assigned each a redshift quality flag (0, 1, 2, 3 or 4) as described below:

Quality Flag 0: Multiple emission lines visible in the spectrum. Robust redshift solution based purely on the χ^2 spectral template fitting (e.g. Fig. 2.22).

Quality Flag 1: Single high S/N emission line in grism spectrum which can either be identified do to asymmetry in the line profile (e.g [OIII]λ4958,5007 line) or which has a strong photometric redshift solution (e.g. Fig. 2.23).

Quality Flag 2: Single low S/N emission line for which the redshift solution relies mostly on the photometry.

Quality Flag 3: Spectra contains what appears to be an emission line but the spectra contains defect (e.g. overlaps the WFC3 death star, on the edge of the detector) or is strongly contaminated and for which the contamination model has not worked (e.g. strange continuum shape, defects left in spectrum).

Quality Flag 4: No emission lines visible in spectrum (i.e. signal to noise too low).

Quality flags 0, 1 and 2 are retained for science purposes leaving a final catalogue of 1330 emission line galaxies in the redshift range $0.73 < z < 3.48$. The redshift distribution of this catalogue is shown in Fig. 2.30. Fig. 2.31 compares 169 of these 3D-*HST* redshifts in the GOODS-S field to other redshifts published in the literature (taken mainly from Le Fèvre et al., 2005; Mignoli et al., 2005; Vanzella et al., 2008), where it can be seen that the vast majority (N=165/169) show excellent agreement with previously published results.

2.4.2 Continuum and Emission Line Fitting

Once the final emission line catalogue was established I next proceeded to measure the emission line fluxes for each galaxy. These line fluxes and ratios between

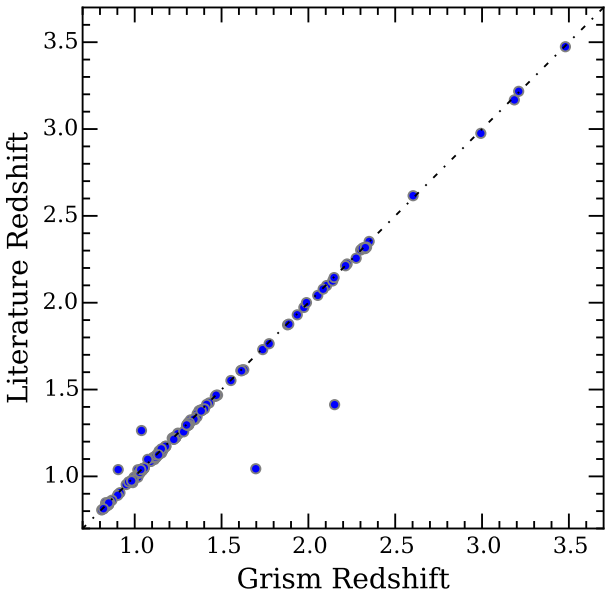

Figure 2.31 *Showing a comparison between the 3D-HST derived redshifts and various literature spectroscopic redshifts for 169 sources in GOODS-S.*

different lines will form a key part in much of the work through the remainder of this thesis. However, before emission line fluxes can be measured one has to first subtract the stellar continuum from the galaxy spectrum, and to do this I used the SED fitting code `LePhare` (Ilbert et al., 2006).

Brief overview of LePhare

`LePhare` works in essentially the same way as `EAZY` with the added benefit that it can estimate stellar masses, star formation rates, ages and dust attenuations as well as a redshift from the galaxy photometry. Since the redshift has been estimated as described above, this parameter can be fixed when running `LePhare`, and the program can be used solely for the purpose of deriving purely physical parameters.

To run `LePhare` I employ the Bruzual & Charlot (2003) stellar evolution models (hereinafter BC03), considering solar metallicity models ($Z_{\odot}$) with exponentially declining star formation histories with characteristic timescales in the range 0.3 Gyr $< \tau <$ 30 Gyr. The Calzetti et al. (2000) attenuation law is employed to account for dust reddening of the SEDs, in the range $0 < E(B-V) < 0.6$. The

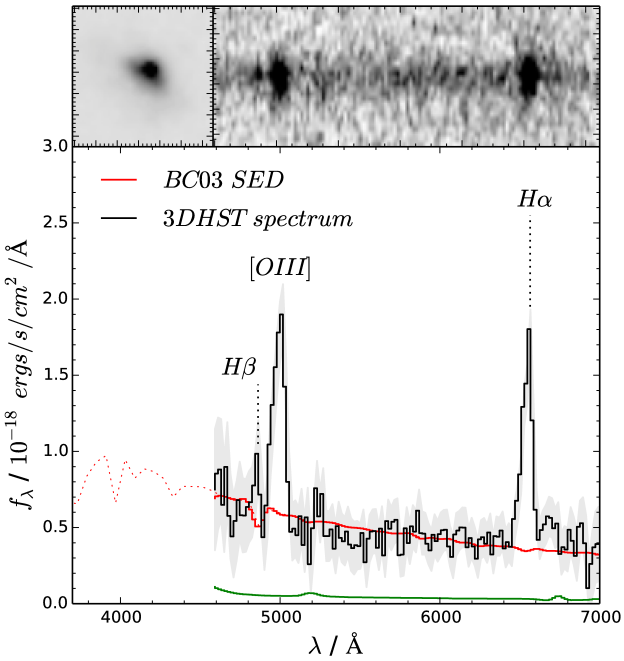

Figure 2.32 *Showing an example of a continuum fit to a 3D-HST grism spectrum. The main panel shows the grism spectrum (black) with the BC03 stellar continuum fit with* `LePhare` *overlaid in red. A key feature to notice in the continuum is the stellar absorption of the Hβ and Hα lines which would not be accounted for with a simple polynomial fit. The green line shows the contamination of this spectrum. The upper left panel shows a thumbnail image of the galaxy from the HST F160W filter. The upper right panel shows the 2D spectrum for the galaxy in which the emission lines are clearly visible.*

age of each SED is allowed to vary between 50 Myr and the age of the Universe at the redshift of the galaxy, and a Chabrier (2003) IMF is assumed. To estimate the physical parameters of a galaxy, `LePhare` produces a library of SEDs covering the full range of parameters described above, the best-fitting template is found by comparing the measured CANDELS photometry in 15 bands to each SED and minimizing the χ^2 statistic as described in detail above.

Continuum Fitting

The resulting best-fitting BC03 SED is then taken as the stellar continuum of each galaxy and subtracted off in the following way. First the SED in the grism wavelength range ($1.1 < \lambda/\mu m < 1.68$) is interpolated to the same wavelength resolution as the grism spectrum. Then, the SED is normalized to the level of the

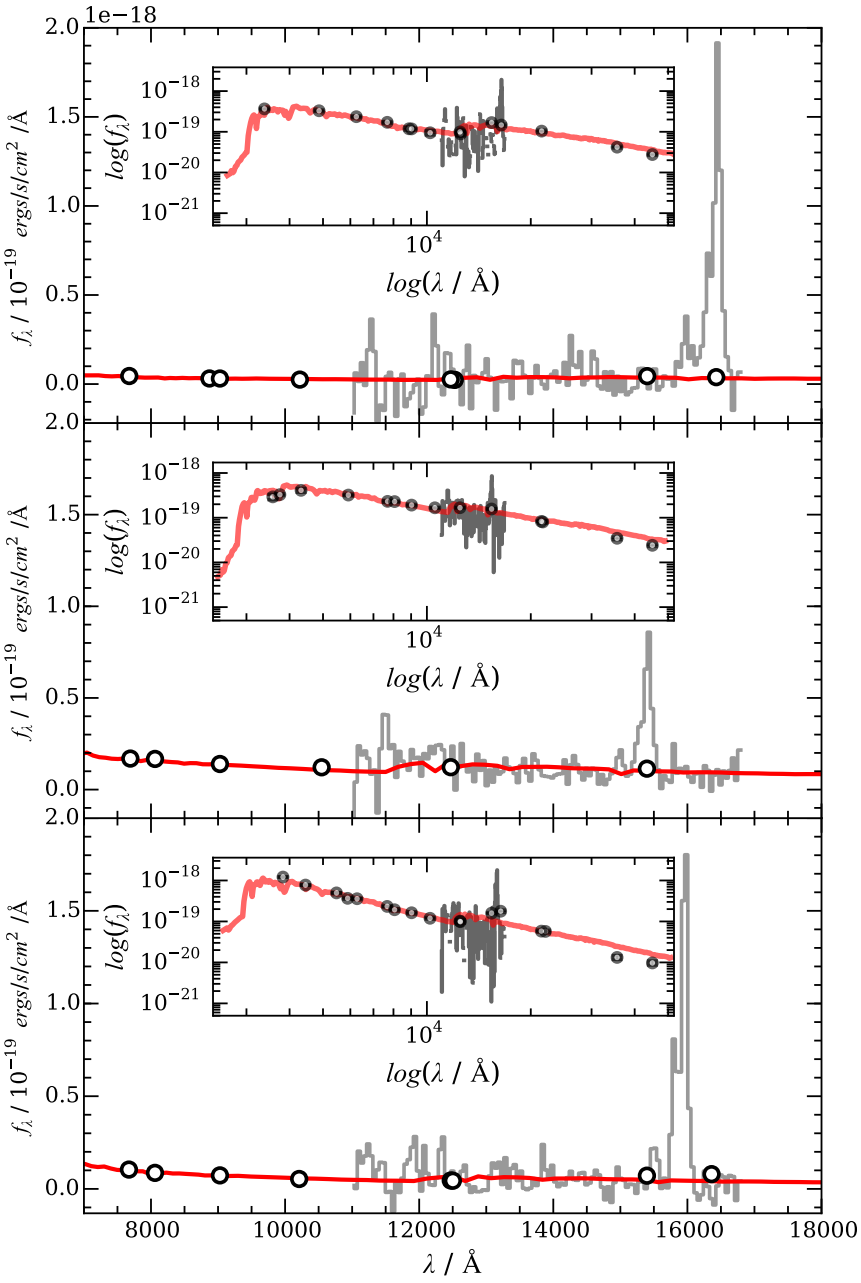

Figure 2.33 *Showing example continuum fits to three galaxies in the final sample. Each panel shows a grism spectra in the rest frame with the continuum fit from the SED plotted in red and the photometry points plotted as black empty circles. Inset in each panel shows the full best-fitting SED of the galaxy derived using* `LePhare` *as described in the text, with the photometry and grism spectra over-plotted.*

observed continuum in the grism spectrum, which can be offset, most likely due to the emission lines present in these galaxies. `LePhare` accounts for emission lines in the overall SED by calculating the SFR based on the UV flux and converting this SFR into a [OII] flux using the Kennicutt (1998) prescriptions, the remaining emission line fluxes are then calculated by assuming flux ratios with respect to [OII] based on local Universe galaxies (Ilbert et al., 2008). However these line ratios are not representative of the observed line ratios at high redshift (e.g. Cullen et al., 2014; Steidel et al., 2014) and therefore their presence will still cause systematic offsets in the estimated continuum level for SED fitting. Therefore, normalization is performed by masking the emission lines in the grism spectrum and, using the emission free pixels, performing a least-squares minimization to estimate the normalization factor. At this point the continuum can be subtracted from the grism spectrum to leave a pure emission line spectrum.

Fig. 2.32 and 2.33 show examples of the continuum fitting described above. Fig 2.32 in particular shows how the shape of the BC03 SED is a good fit to the shape of the 3D-*HST* spectrum and also illustrates one of the main advantages of using the stellar continuum: correction for underlying absorption of the hydrogen Balmer transitions. These absorption features are caused by Hydrogen in the atmosphere of stars and crucially the strength of the absorption depends on the age of the stellar population. Fitting the continuum with a simple low-order polynomial would not account for this underlying absorption, and therefore would systematically underestimate the intrinsic line flux of the Hα and Hβ emission lines. Additionally, due to the age dependence of the absorption factor it is not possible to apply a uniform correction to all galaxies. Fig. 2.33 shows the SED and continuum fits to three galaxies at $z > 2$ and illustrates how this technique also accounts for the 4000Å Balmer break crossing the [OII] emission line which also cannot be accounted for with a simple polynomial fit.

Emission Line Fitting

Once the stellar continuum has been fit and subtracted as described above it is possible to measure the emission lines in the galaxy spectra. All lines are fit in the rest-frame by correcting the wavelength axis for the galaxies measured redshift via:

$$\lambda_{\rm rest} = \frac{\lambda_{\rm obs}}{1+z}. \tag{2.10}$$

Due to the sensitivity and wavelength resolution of the grism spectra only the [OII], [OIII]λ4958,5007, Hβ and Hα+[NII] (fully blended) lines are available to measure, and weaker emission lines such as Hγ, Hδ or [OIII]λ4363 are for the vast majority of spectra not visible. The Hα+[NII] and [OII] lines are both well represented by single gaussian line profile whereas [OIII]λ4958,5007 and Hβ can often be partially blended and it is often best to fit these line simultaneously. Below I will give a short description of each process:

[OII] and Hα+[NII]: These line are fit using the least-squares minimization Python package `lmfit`[5] with the line profile assumed to be a single Gaussian of the form:

$$f(\lambda; A, \mu, \sigma) = A\exp[-\frac{(\lambda-\mu)^2}{2\sigma^2}], \tag{2.11}$$

where A is the normalisation, μ is the line centre and σ is the line width. All three parameters are allowed to vary in the fit with the line centre estimated at the rest-frame vacuum wavelength[6], and the line width restricted to be within one wavelength-resolution pixel in the rest-frame. Once the lines have been fit in this way the flux in the line is derived by integrating over the gaussian profile with the derived parameters.

[OIII]λ4958,5007 and Hβ: Due to their small wavelength separation these lines are partially blended and therefore a different approach must be adopted when fitting. Again `lmfit` is used but now this emission line complex is modeled as a sum of three separate gaussians each with its own height, width and centroid parameters:

$$f(\lambda; A_i, \mu_i, \sigma_i) = \sum_{i=1}^{3} A_i\exp[-\frac{(\lambda-\mu_i)^2}{2\sigma_i^2}]. \tag{2.12}$$

Here, because the [OIII]λ5007 line is always at the highest S/N, I use this line to estimate the line width and fix the width of the [OIII]λ4958 and Hβ lines to this value. The centroids of each line are estimated at their rest-frame wavelength but allowed to vary, as is the height of each line. An example of such a line fit is shown in Fig. 2.34 where it can be seen how the [OIII] doublet is severely blended (though the asymmetric shape of the line is clearly visible).

Due to the blended nature of the [OIII]λ4958,5007 lines, I use two methods to estimate the individual fluxes. Firstly I use the best-fitting gaussian parameters for each line directly from the fit as described above, and secondly I sum the two gaussians from the triple Gaussian and take the [OIII]λ5007 flux to be 3/4 of the

[5]http://lmfit.github.io/lmfit-py/intro.html
[6]from http://www.sdss2.org/dr2/algorithms/linestable.html

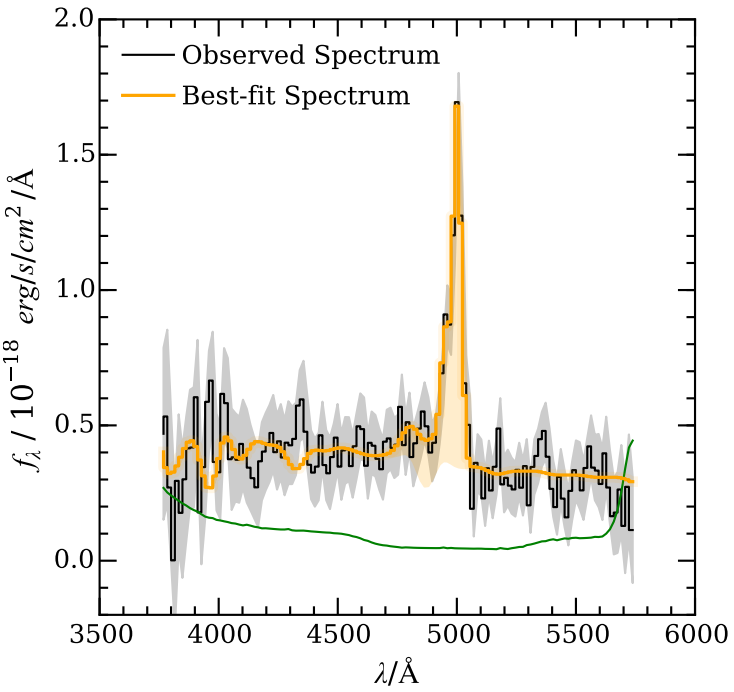

Figure 2.34 *Showing an example of the line fit to the [OIII] and Hβ emission lines. The observed spectrum is shown in black with the grey shaded areas representing the 1σ error spectrum. The yellow curve shows the best-fitting spectrum and the green curve shows the contamination.*

total (Storey & Zeippen, 2000), this follows previous methods for measuring the [OIII] line fluxes from grism spectra (Trump et al., 2013). I have checked that both methods are fully consistent with one another.

To estimate errors on line measurements each spectrum is perturbed using the equation $f = f_0 + \sigma R$, where f_0 is the input grism spectrum, σ is its error spectrum, and R is a random number drawn from a normal distribution with a mean of 0 and a standard deviation of 1 (in the interval $-\infty$ to ∞) (Lenz & Ayres, 1992). The continuum and line fits described above are then performed on the perturbed spectrum. This process is repeated 1000 times and the line flux error is taken as the standard deviation the final distribution.

Chapter 3

The Mass-Metallicity-Star Formation Rate Relation at $z \gtrsim 2$

The contents of this chapter have been published in Cullen et al. (2014)

3.1 Background

As discussed in the thesis introduction, over recent years evidence has been accumulating for the existence of a tight relationship between mass, gas-phase metallicity (hereafter metallicity) and star-formation rate (SFR) in galaxies out to z $\sim$ 2.5. This so called 'fundamental metallicity relation' (FMR) was first proposed by Mannucci et al. (2010) and Lara-Lopez et al. (2010), though the SFR dependence of the mass-metallicity relation (MZR) had been initially noted earlier by Ellison et al. (2008). The existence of an FMR has since been supported by other studies (e.g. Belli et al., 2013; Cresci et al., 2012; Henry et al., 2013a,b; Lara-López et al., 2013; Mannucci et al., 2011; Niino, 2012; Richard et al., 2011; Stott et al., 2013), though the exact form of the FMR has been shown to be dependent on the methodology adopted (e.g. Andrews & Martini, 2013; Yates et al., 2012). In their original paper, Mannucci et al. (2010) proposed a FMR which defines a surface in the three dimensional mass-metallicity-SFR space, and in Mannucci et al. (2011) this original FMR was extended to lower masses. Local galaxies from the Sloan Digital Sky Survey (SDSS) lie on the FMR surface with a residual dispersion of $\sim$ 0.05 dex in metallicity and this local relation seems to

hold unchanged up to $z \sim 2.5$ (Mannucci et al., 2010).

This suggests that the physical processes acting on star-forming galaxies have been consistent over the past $\sim$ 10 Gyr of cosmic time. Interestingly, however, Mannucci et al. (2010) observed an evolution of $\sim$ 0.6 dex away from the FMR for galaxies at z $>$ 2.5 using galaxies at $3 < z < 5$ from the AMAZE/LSD surveys (Maiolino et al., 2008; Mannucci et al., 2009), suggesting some change in the processes acting in star-forming galaxies at this epoch. This observation has recently been corroborated by Troncoso et al. (2014) with an increased sample size at these redshifts.

The original motivation for investigating the relationship between mass, metallicity and SFR was an attempt to explain some of the features of the more extensively studied mass-metallicity relation. The MZR has been established across a large range in redshift from the local Universe (Kewley & Ellison, 2008; Liu et al., 2008; Panter et al., 2008; Tremonti et al., 2004), to z $\sim$ 1 (Cowie & Barger, 2008; Rodrigues et al., 2008; Roseboom et al., 2012; Savaglio et al., 2005; Shapley et al., 2005; Zahid et al., 2014a, 2011), z $\sim$ 2 (Erb et al., 2006b; Henry et al., 2013b; Kulas et al., 2013; Sanders et al., 2015; Steidel et al., 2014; Wuyts et al., 2014), and out to z $\sim$ 3 (Maiolino et al., 2008; Mannucci et al., 2009; Troncoso et al., 2014). A consistent picture has emerged from these studies that galaxies at high redshifts follow a MZR with a similar shape compared to galaxies in the local Universe, but with a different normalisation. In fact, at a given redshift, galaxies with lower stellar mass are found to have lower metallicities and at a given stellar mass, galaxies at higher redshift are found to have lower metallicities. In the context of the FMR, the evolution of the MZR with redshift is explained due to the fact that metallicity anti-correlates with SFR, and at higher redshifts galaxies of a given mass have higher SFRs (e.g. Daddi et al., 2007).

As discussed in the introduction (Chapter 1; Section 1.4.6), one outstanding issue with the observational measurements of metallicities at high redshifts is that the only feasible method relies on measuring strong nebular emission lines. These lines are not direct tracers of metallicity and therefore have to be calibrated in some way. One method that has been adopted is to empirically calibrate these emission line ratios in the local Universe using a combination of direct metallicity tracers and photoionization modeling. At low metallicities the line ratios are calibrated using direct metallicity tracers such as the weak [OIII]λ4363 auroral line, whereas at high metallicities, the auroral line becomes too weak

and instead local galaxy spectra are fit with photo-ionization models of star-forming regions to calibrate the line ratios (see e.g. Maiolino et al., 2008; Nagao et al., 2006). Using these local empirical calibrations at high redshift assumes that the calibrations sufficiently account for the change in physical conditions of star-forming galaxies with redshift. However, from data currently available there is evidence to suggest that conditions in star-forming regions are evolving with redshift (e.g. Brinchmann et al., 2008; Hainline et al., 2009; Kewley et al., 2013a,b; Nakajima & Ouchi, 2014; Shirazi et al., 2014b; Steidel et al., 2014), and if this is the case using empirical metallicity calibrations at high redshifts may not be reliable. It is important to note that purely theoretical metallicity calibrations (e.g. Kewley & Dopita, 2002) are in principal not subject to the potential bias introduced by using local Universe galaxies to calibrate emission line ratios, as theoretical models can explore a large range in ionization conditions which may not be sampled in local galaxies (e.g. Kewley & Dopita, 2002). However, because the original FMR is built upon the local empirical metallicity calibration of Maiolino et al. (2008), I will use this calibration throughout this chapter.

As shown in the introduction, star-forming galaxies in the local Universe form a tight sequence in the BPT diagram (e.g. Kauffmann et al., 2003a), however an evolution away from this sequence is observed at high redshifts towards higher [OIII]/Hβ and [NII]/Hα ratios (e.g. Erb et al., 2006b; Hainline et al., 2009; Shapley et al., 2005; Yabe et al., 2012). At the same time there seems to be an evolution in the ionization parameter of galaxies, which is a measure of the degree of excitation of HII regions, with high redshift galaxies having higher ionization parameters (e.g. Hainline et al., 2009; Lilly et al., 2003; Nakajima & Ouchi, 2014; Richard et al., 2011). This evolution towards higher ionization parameters has been used to explain the offset of high redshift star-forming galaxies from the local Universe relation in the BPT diagram (e.g. Brinchmann et al., 2008; Kewley et al., 2013a,b), and has most recently been suggested as a possible reason for the apparent evolution of galaxies away from the FMR at z $\sim$ 3 (Nakajima & Ouchi, 2014). Interestingly, using a sample of low-redshift galaxies with elevated ionization parameters - supposed analogues of observed high redshift star-forming galaxies - Ly et al. (2014) observe an offset from the FMR of the order of 0.1 - 0.2 dex similar to that observed at $z \sim 3$. These observations beg the question: is the observed evolution in the MZR and FMR really metallicity evolution or are the measurements been biased by the changing physical conditions, in particular an increasing ionization parameter, at high redshift?

In this chapter, I will provide additional observational constraints on the MZR and FMR at $z \gtrsim 2$, using a sample of 93 star-forming galaxies with a mean redshift $\langle z \rangle = 2.16$ selected from the 3D-*HST* catalogue described in Chapter 2. 3D-*HST* provides an ideal data set for obtaining a large sample of $z \gtrsim 2$ galaxies with which metallicities can be measured as the [OII], Hβ and [OIII] nebular emission lines fall into the grism spectra in the redshift range $2 < z < 2.3$. At the time of publication I had generated a sample of galaxies similar in size to the current largest dataset of $z \gtrsim 2$ galaxies with measured metallicities studied by Erb et al. (2006b) ($\langle z \rangle = 2.26$), though this has since been superseded by the work of Steidel et al. (2014), which contains ~ 250 galaxies in a similar redshift range. The Steidel et al. (2014) data agree well with the Erb et al. (2006b) data for $\log(M_*/M_\odot) \gtrsim 9.8$, while implying higher values of metallicity below this mass limit. Since the Erb et al. (2006b) study was based on a sample of ultraviolet (UV) selected star-forming galaxies observed from the ground, our line-flux limited sample taken with the HST allows us to probe lower SFRs than the Erb et al. (2006b) data. Finally, since Erb et al. (2006b) measure metallicities with the Hα and [NII] nebular lines, I am able to use an independent method with the [OII], Hβ and [OIII] lines. These are the same nebular emission lines as used for measuring metallicities in the z $\sim$ 3 studies (Maiolino et al., 2008; Mannucci et al., 2009), and therefore this data provide useful insight into the observed shift of the FMR between z $\sim$ 2 and z $\sim$ 3.

3.2 $z \gtrsim 2$ Spectroscopic Data

In this section I describe the spectroscopic dataset derived from the 3D-*HST* survey (see Chapter 2) that I will use to determine the mass-metallicity-SFR relation at $z \gtrsim 2$.

3.2.1 Sample selection

From the 3D-*HST* data, it not possible to deblend Hα and [NII] to measure metallicities, due to the low spectral resolving power. However, the redshift range $2.0 \leq z \leq 2.3$ represents a sweet-spot where it is possible to simultaneously measure the [OII], Hβ and [OIII] emission lines, which can be used for estimating SFRs and metallicities (e.g. Kobulnicky & Kewley, 2004; Maiolino et al., 2008).

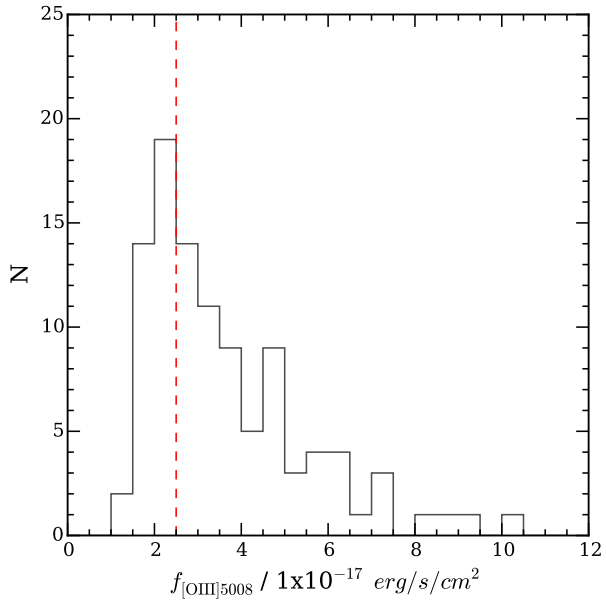

Figure 3.1 *Distribution of [OIII]λ5007 fluxes for the final galaxy sample. The formal 3-σ line flux limit is shown by the red dashed line.*

Restricting the 3D-*HST* sample described in Chapter 2 to sources in the redshift range $2.0 \leq z \leq 2.3$, leaves 103 galaxies with a 3σ flux limit in [OIII]λ5007 of $\sim$ 2.5 x 10^{-17} ergs/cm^2/s. This value is consistent with the flux limit derived in Brammer et al. (2012) for compact, low sky-background, sources. A histogram of the observed [OIII]λ5007 fluxes is given in Fig. 4.2 with the 3σ limit shown. It is clear that many galaxies are included in the sample below the formal 3σ limit, however the sample is based on visual identification of spectral features rater than on line signal-to-noise ratio criteria. This is necessary so as to not bias the sample against high metallicity galaxies with low [OIII] fluxes due to efficient cooling of the HII regions, as well as galaxies with high levels of dust extinction. Moreover, all spectra must be visually inspected to make sure the subtraction of the contamination model has not left any residuals, at present visual inspection is the most reliable method of quality control for grism spectra. As will be described below, I overcome the low SNR of a large portion of galaxies by stacking the individual spectra.

AGN removal

The theoretical models for [OIII]/Hβ evolution explored in this chapter assume the ionizing radiation responsible for the nebular emission has stellar origin.

Therefore, to facilitate and accurate comparison between models and data, care must be taken to account for the effect of AGN contamination in all samples. Unfortunately the wavelength coverage, sensitivity, and resolution of the 3D-*HST* spectra do not allow us to detect simultaneously enough emission lines to use classical AGN diagnostic diagrams (e.g. the BPT diagram).

The most reliable method for AGN removal applicable to our sample is X-ray detection. I remove possible active galactic nuclei (AGN) for the sample by first cross-matching with the *Chandra* 4 MS X-ray catalogue in GOODS-S (Xue et al., 2011) and *Chandra* 1.8 Ms X-ray catalogue in COSMOS (Civano et al., 2012). Three galaxies were identified and removed based on the X-ray data in this way. Strong X-rays emission is observed from AGN which originates from inverse scattering of photons by hot electrons in the surrounding hot corona. However, due to the varying depths of the observations this techniques will most likely pick up only the most active AGN. In addition the UDS does not have good X-ray coverage, therefore I also attempted to use optical AGN diagnostics.

I followed the method of Henry et al. (2013b) in using the Mass-Excitation (MEx) diagram (Juneau et al., 2011) to separate star-forming galaxies and AGN based on their [OIII]/Hβ ratio and mass (see Fig. 3.2). In this method, the SDSS MZR is employed to use stellar mass as a proxy for the [NII]/Hα ratio. We follow Henry et al. (2013b) in shifting the Juneau et al. (2011) relation by + 1.0 dex in mass to account for the observed mass-metallicity evolution at high redshift, we also shift by + 0.2 dex in [OIII]/Hβ to account for the evolution of the [OIII]/Hβ ratio in star-forming galaxies at $z \sim 2$ due to evolving ionization conditions (see Kewley et al. (2013a) and Chapter 4 of this thesis). Across the range of [NII]/Hα occupied by the majority of observed $z > 2$ galaxies, +0.2 dex is the average shift in the [OIII]/Hβ ratio between $z \sim 0$ and $z \sim 2$ based on the Kewley et al. (2013b) models (see Fig. 3.3). Hβ is not detected in all individual galaxies and in this case I can only put a lower limit on the [OIII]/Hβ ratio, however I do not exclude galaxies with lower limits which fall below the AGN separation line. Using this modified MEx diagram approach I remove a further six galaxies from the sample, leaving a total of 9/103 galaxies (9%) identified as AGN. This AGN fraction is consistent with other studies at slightly lower redshift (z $\sim$ 1.5) (e.g. Stott et al., 2013; Zahid et al., 2014a).

Finally I exclude one further galaxy from the following analysis as it has a measured mass of ($\log(M_*/M_o) = 8.63$ - see Section 3.3), which is offset by 0.66 dex from the next lowest mass galaxy in the sample. As part of the analysis

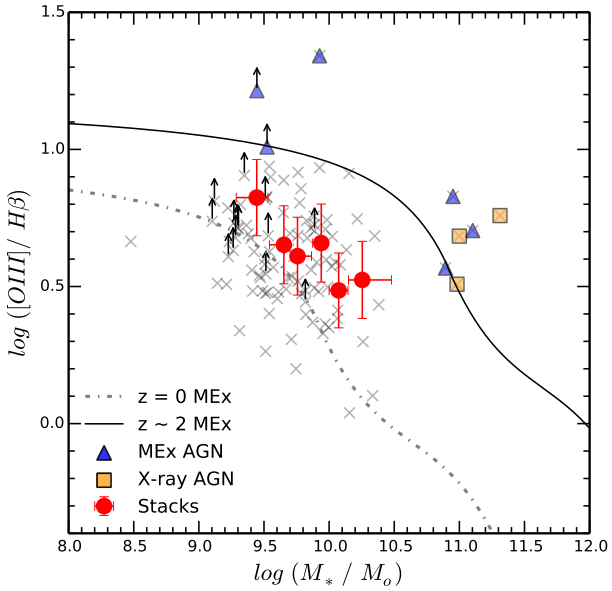

Figure 3.2 *A modified version of the MEx diagram (Juneau et al., 2011) used for selecting AGN in the 3D-HST sample.. The original form of the separation line given in Juneau et al. (2011) at $z = 0$ is given by the grey dot-dashed line and the black solid line shows the modified version of this line used for our $z \gtrsim 2$ sample (see Section 3.2 for details). The grey crosses show individual galaxies in the sample which are not classified as AGN. The yellow squares show AGN identified from X-ray counterparts and the blue triangles show MEx classified AGN. The black arrows represent individual galaxies with only an upper limit on the [OIII]/Hβ ratio. The red circles with error bars show the position in the MEx diagram of the final stacked spectra.*

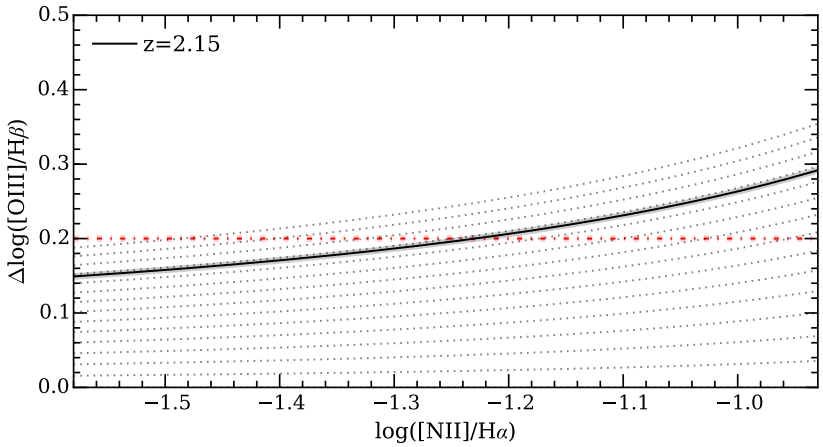

Figure 3.3 *Showing the offset of the [OIII]/Hβ at fixed [NII]/Hα ratio assuming the evolution of the BPT abundance sequence from Kewley et al. (2013a). The offset is relative to the value at $z = 0$. The dotted lines show the evolution from $0 < z < 3$ in redshift intervals of $\Delta z = 0.1$. The black solid line shows the offset at $z = 2.15$, the average redshift of the sample used in this chapter. The average value of the offset across the plotted range of [NII]/Hα values is 0.2 dex.*

involves stacking the 3D-*HST* spectra in bins of stellar mass, this galaxy would skew the stellar mass distribution of the stack at in the lowest mass bin. In summary, this leaves a final sample of 93 galaxies, which still represents one of the largest samples of galaxies at z$\gtrsim$ 2 for which it is possible to derive accurate metallicity measurements.

3.2.2 Galaxy stacking method

As described in Chapter 2, I measure line fluxes for all the individual galaxies in the sample, and therefore can derive individual physical properties such as the SFR and metallicity. However, to reduce the uncertainty in the measured line ratios due to the lower signal-to-noise of the weaker lines (e.g. Hβ), I also stacked the spectra in bins of stellar mass, following the method of Erb et al. (2006b). These stacks will be utilized for the majority of the measurements in this chapter. The mass bins were chosen such that each bin contained a similar number of galaxies and contained enough galaxies ($N \sim 15$) to get good S/N spectra. A detailed description of how masses were measured is given below in Section 3.3. Within each mass bin the rest-frame continuum-subtracted 3D-*HST* spectra were interpolated to a common wavelength grid and I determined

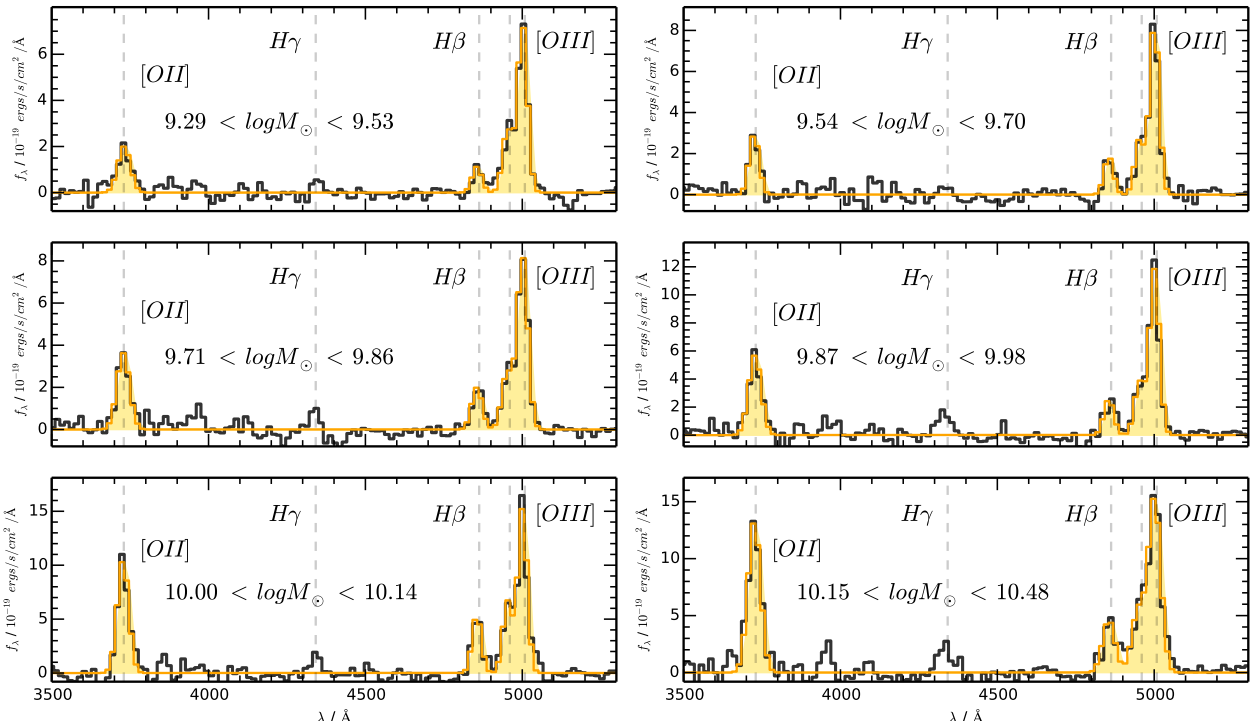

Figure 3.4 *The rest-frame stacked spectra of galaxies in our sample split into six bins of increasing stellar mass. Each panel is labeled with the range of stellar mass in each bin and the [OII], Hγ, Hβ and blended [OIII] emission lines are marked by dashed lines. The stacked spectra are shown in black with the fit to the emission lines overlaid in orange.*

the median flux within each wavelength pixel. The final stacked galaxy spectra are shown in Fig. 3.4. I also checked that the final stacked spectra and the results presented here are not affected by the way in which the continuum is subtracted. Indeed, removing the continuum from each galaxy before stacking is consistent with stacking first the original spectra and then subtracting the continuum determined by the stacked SEDs models.

It is important to consider that, as previously noted by other authors, stacking the intrinsic fluxes of each galaxy may be biasing our measurements towards the brightest emission lines galaxies in the stack (e.g. Domínguez et al., 2013; Henry et al., 2013b). However, taking the median flux in each wavelength bin, as opposed to an average, should mitigate this effect. To investigate the potential effect I checked that the line ratios measured from stacks where each individual spectrum is normalized by its [OIII]λ5007 flux are consistent with the line ratios measured from a non-normalized stack. Therefore, I find that the measured metallicities of these normalized stacks are fully consistent with those measured without normalizing. I choose to use the intrinsic stacked spectra in the remainder of this paper as this has the added benefit that I can also measure the SFR directly from the spectra (which would not be possible with normalized spectra).

3.3 CANDELS Photometry and Stellar Mass Measurements

The photometric data for galaxies in the 3D-*HST* sample are taken from three separate catalogues for the GOODS-S, UDS and COSMOS fields. All photometry covers the rest-frame UV to mid-IR (*Spitzer*/IRAC 3.6 and 4.5μm). In both GOODS-S and UDS we take the photometry from existing CANDELS catalogues described in Guo et al. (2013) and Galametz et al. (2013) respectively. For COSMOS I use a new catalogue produced by first convolving all the available ground-based and space-based optical and near-IR imaging (see Bowler et al. (2012) for details) to a common PSF (0.8″) and then performing aperture photometry using the smoothed F160W image as the detection band. The *Spitzer*/IRAC 3.6 and 4.5μm photometry was included by de-confusing the IRAC images using the UltraVISTA Ks-band imaging (McCracken et al., 2012).

Table 3.1 *Measured line flux data for the galaxy stacks in our sample.*

ID	Mass Range	N_{gal}[b]	$\langle z \rangle$[c]	$f_{[OIII]5008}$[d]	$f_{H\beta}$[d]	$f_{[OII]}$[d]
1	9.29 - 9.54	15	2.22	2.9 ± 0.3	0.5 ± 0.1	1.0 ± 0.1
2	9.54 - 9.70	15	2.11	3.1 ± 0.3	0.7 ± 0.1	1.2 ± 0.2
3	9.70 - 9.86	16	2.15	3.5 ± 0.4	0.9 ± 0.1	1.8 ± 0.2
4	9.86 - 9.98	16	2.14	4.6 ± 0.5	1.1 ± 0.1	2.9 ± 0.3
5	9.98 - 10.14	16	2.17	6.1 ± 0.6	2.0 ± 0.3	4.8 ± 0.5
6	10.14 - 10.48	15	2.20	7.7 ± 0.8	2.3 ± 0.3	6.7 ± 0.7

[a] Range of stellar masses in the stack in units of $\log(M/M_\odot)$.
[b] Number of individual galaxies in the stack.
[c] Average redshift of the stack.
[d] Dust corrected flux in units of 10^{-17} erg/s/cm^2

3.3.1 Stellar masses and SFRs from SED fitting

Stellar masses and SFRs for individual galaxies are measured as described in Chapter 2 using the publicly available code LEPHARE (Ilbert et al., 2006). The normalization factor required to scale the best-fitting template to the observed magnitudes in each band gives the stellar mass. In order to compare directly with previous $z \gtrsim 2$ data of Erb et al. (2006b), I correct the default LEPHARE output of instantaneous stellar mass to the total mass of stars formed using the standard conversions in the BC03 templates. The median increase in mass when applying this correction is + 0.18 dex. I use this definition of stellar mass to all data presented in this chapter, applying the above conversion where necessary. The SED fitting also provides an estimate of the SFR by converting the rest-frame UV flux (corrected by the best fit dust extinction) using the Kennicutt (1998) prescriptions. This SFR derived by the SED fitting can be compared with SFR derived from Hβ line fluxes (see next section).

3.4 Metallicities and SFRs from 3D-*HST* Spectra

Complementary to the CANDELS photometric data, the 3D-*HST* spectra allow us to measure line fluxes, which are used derive star-formation rates and gas metallicities. The line fluxes are measured from the continuum-subtracted grism spectra as described in Chapter 2. Similarly, the line fluxes for the stacked spectra are measured in the same way and the values for the various lines in the six mass bins are given in Table 1.

Star-formation rates

I measure SFRs from the Hβ line flux, first converting it to luminosity and then using the common conversion factor Hα/Hβ = 2.86 (Kennicutt, 1998). I then scale down by a factor 1.7 to convert to a Chabrier (2003) IMF. Use of the Hα/Hβ conversion factor relies on the assumption that the galaxies in the stacks have $E(B-V) = 0$ after the de-reddening of individual spectra, therefore a good estimate of the extinction suffered by emission lines in the galaxy is required. There has been much debate in the literature as to whether the extinction returned from SED fitting, which corresponds to the extinction in the stellar continuum, is the same as the extinction suffered by emission lines, since emission lines emanate from dusty star-forming regions and therefore could potentially suffer larger extinction than stars.

The extra extinction of nebular emission lines is parametrized by a factor f where $E(B-V)_{\rm stars}$=$fE(B-V)_{\rm gas}$. Calzetti et al. (2000) find that $f = 0.44 \pm 0.03$ for local starburst galaxies and similar corrections have been reported for galaxies out to z $\sim$ 2 (e.g. Cresci et al., 2012; Förster Schreiber et al., 2009; Yabe et al., 2012). However at intermediate redshifts (z $\sim$ 1.5) there is some evidence for an evolution towards larger f values (e.g. Kashino et al., 2013; Price et al., 2014), and at z $\sim$ 2 some studies find an apparent evolution to $f \sim 1$ (e.g. Erb et al., 2006a; Hainline et al., 2009).

The method of de-reddening spectra described in Chapter 2 assumes no extra reddening in nebular regions (i.e. $\mathrm{E(B\text{-}V)_{stars}} \sim \mathrm{E(B\text{-}V)_{gas}}$), so to get a sense as to whether I am making sensible dust corrections we can compare our best-fitting SFR from SED fitting to that derived from the de-reddened line flux. The comparison is shown in Fig. 3.5. The figure shows that the two independent measures of SFR are in good agreement for the galaxy stacks, for the Hβ and SED methods respectively the median and median absolute deviation (MAD) of the SFRs of the whole galaxy sample are 17.2 ± 8.8 and 13.0 ± 12.3 $\mathrm{M_{\odot}yr^{-1}}$. Given the good agreement between the SFRs, in this chapter I adopt the $E(B-V)$ values returned by SED fitting for correcting the emission lines and therefore follow the previous studies at z $\sim$ 2 in assuming that $\mathrm{E(B\text{-}V)_{stars}} \sim \mathrm{E(B\text{-}V)_{gas}}$.

Nonetheless it is useful to quantify by how much the SFRs derived from Hβ may be underestimated if there is indeed still extra attenuation in HII regions in $z \sim 2$ galaxies. To do this, I adopt the prescription of extra nebular extinction proposed by Wuyts et al. (2013), who compare Hα based SFRs for a sample of

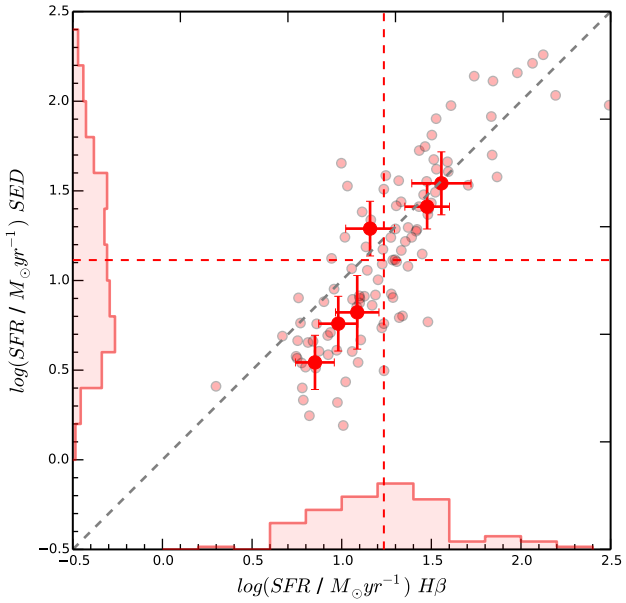

Figure 3.5 *A comparison of SFR measured from the Hβ line with SFR as derived from SED fitting. The galaxy stacks are shown as the large red points with error bars. The SED SFRs for the stacks are taken as the median of the SED-derived SFRs of individual galaxies within the stack with measured Hβ. The small red points represent the individual galaxies. On both axes histograms of the values for the individual galaxies are plotted and the dotted red lines show the median values for each distribution. Respectively, the median and median absolute deviation (MAD) of the SFRs of the whole galaxy sample are 17.2 ± 8.8 $M_{\odot}yr^{-1}$ and 13.0 ± 12.3 $M_{\odot}yr^{-1}$*

.

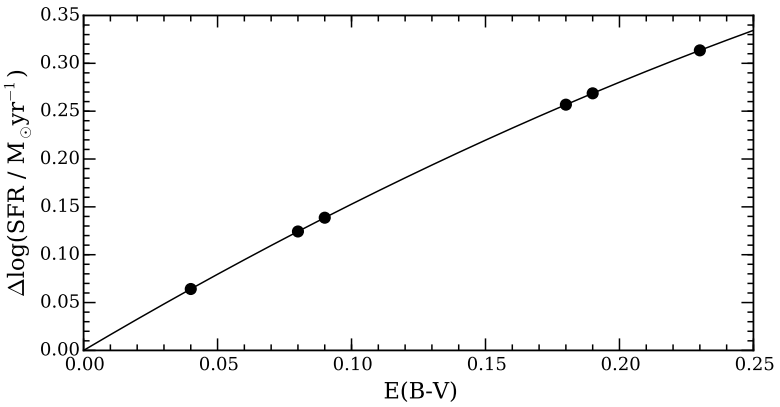

Figure 3.6 *Showing how the Hβ derived SFRs will vary as a function of E(B-V) using the Wuyts et al. (2013) extra attenuation prescription. The black points represent the mean E(B-V) of the galaxy stacks as presented in Table 1.2.*

.

473 3D-*HST* galaxies to the ladder of SFR indicators introduced in Wuyts et al. (2011), which is based on UV+IR emission, or SED modeling where no IR data is available. Wuyts et al. (2013) parameterize the extra attenuation as:

$$A_{\rm extra} = 0.9A_{\rm cont} - 0.19A_{\rm cont}^2 \tag{3.1}$$

implying a saturation of $A_{\rm extra}$ with increasing $A_{\rm cont}$. Using this prescription I have calculated how the Hβ SFR changes as a function of $E(B-V)$. Fig. 3.6 shows how, at the highest levels of attenuation measured in the stacks, the SFR may be underestimated by up to ~ 0.3 dex. Where appropriate, I will return to how these SFRs offset may affect the results presented in the relevant sections.

3.4.1 Gas phase metallicity

As discussed in the introduction, the metallicity of a galaxy is a measure of the abundance of metals relative to hydrogen in the interstellar medium and is most commonly quoted in terms of the oxygen abundance ratio 12 + log(O/H). Measuring the metallicity at high redshifts relies on using ratios of various strong, optical emission lines emanating from HII regions. These line ratios are a combination of strong hydrogen recombination lines such as Hα and Hβ, and collisionally excited forbidden transitions in metals such as [NII], [OII] and [OIII]. Unfortunately the ratios of the strengths of these lines do not depend solely on the element abundances but have other dependences (e.g. gas density,

hardness of ionizing radiation, etc.), and therefore must be calibrated against direct metallicity tracers. In this chapter I use the local empirical calibrations described in Maiolino et al. (2008) as this calibration was used in the original investigation of the FMR (Mannucci et al., 2010). As described previously, Maiolino et al. (2008) calibrations are derived from a sample for low metallicity galaxies for which metallicities can be measured directly using the T_e method, and a sample of SDSS spectra at higher metallicity for which metallicities are derived from photoionization modeling.

I measure metallicities using the [OII], [OIII]λ4958, [OIII]λ5007 and Hβ emissions lines via a method similar to that used for the z $\sim$ 3 galaxies in the AMAZE and LSD surveys (Maiolino et al., 2008; Mannucci et al., 2009). However, in a slight departure from their method, I do not fit to metallicity and extinction simultaneously across all line ratios. However, both Maiolino et al. (2008) and Mannucci et al. (2009) note that their fit, whilst constraining the metallicity, does not simultaneously provide good constraints on the dust extinction, implying that the derived metallicity is weakly dependent on the value of dust extinction adopted. I measure all line ratios available which have metallicity calibrations given in Maiolino et al. (2008) (fig. 5 in their paper). Specifically the line ratios are R_{23} (=[OII] + [OIII]λ4958 + [OIII]λ5007/Hβ), [OIII]λ5007/Hβ, [OIII]λ5007/[OII] and [OII]/Hβ. The line ratios and calibration curves are shown in Fig. 3.7.

To measure the metallicity of a galaxy stack I first calculate the observed line ratio in each of the four diagrams. At each value of metallicity, within a large range ($7 < \log(O/H) + 12 < 9.5$), I calculate, for each calibration curve, a χ^2 statistic from the difference between the observed line ratio and calibration line ratio at that metallicity. Thus for all four calibration curves I construct a χ^2 versus $\log(O/H) + 12$. I combine the χ^2 values from each of the four diagrams to construct an overall χ^2 versus $\log(O/H) + 12$. I take the metallicity at the minimum of the combined χ^2 as the best-fitting metallicity as shown in Fig. 3.8. I take the 1σ confidence intervals to be within $\Delta\chi^2 = 1$ of the best-fitting value. The metallicities of the stacked spectra along with all other derived properties are given in Table 3.2.

To check for consistency I apply this method to the galaxies in the AMAZE/LSD program Maiolino et al. (2008); Mannucci et al. (2009). I take the measured line ratios from the Maiolino et al. (2008) and Mannucci et al. (2009) papers, de-redden via the best-fitting extinctions quoted, and measure the metallicities

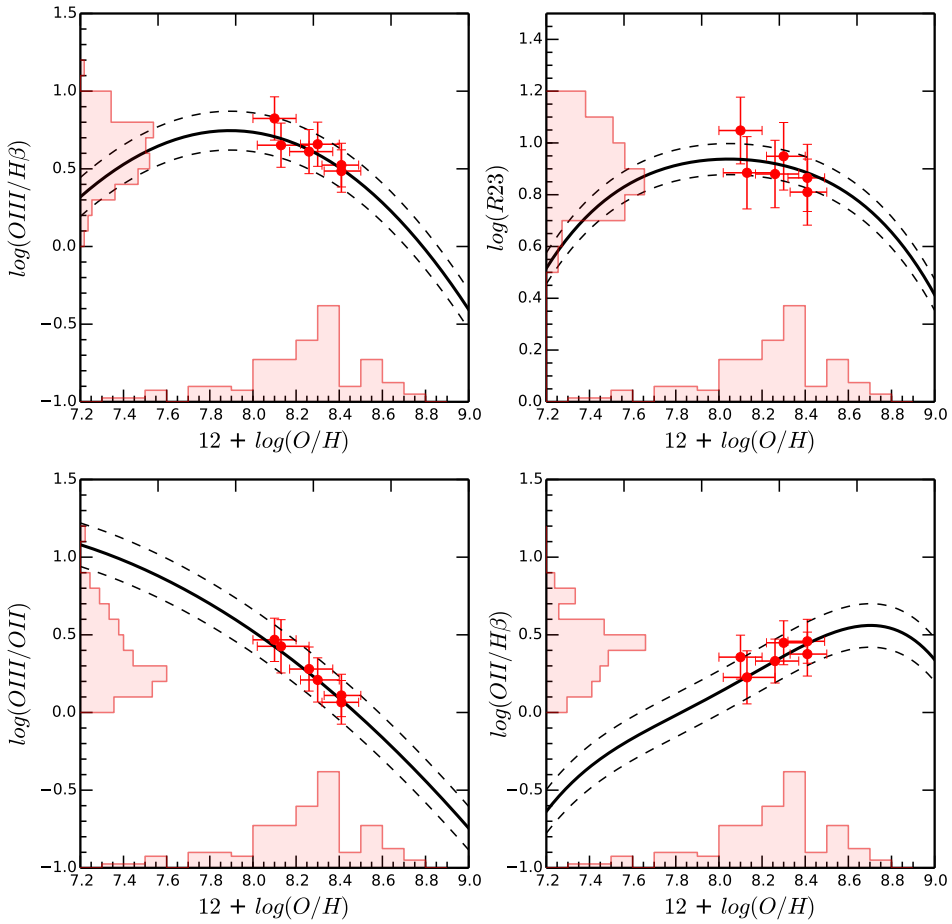

Figure 3.7 *Relationship between line ratio and derived metallicity values for each of the four metallicity calibrations used to determine galaxy metallicities in this paper. The calibration curves are taken from Maiolino et al. (2008). Shown as red solid circles are the metallicities derived using a combination of all four line ratios as described in Section 3.4.1. The red histograms represent the distributions of individual galaxies in the sample with detections in the appropriate emission lines.*

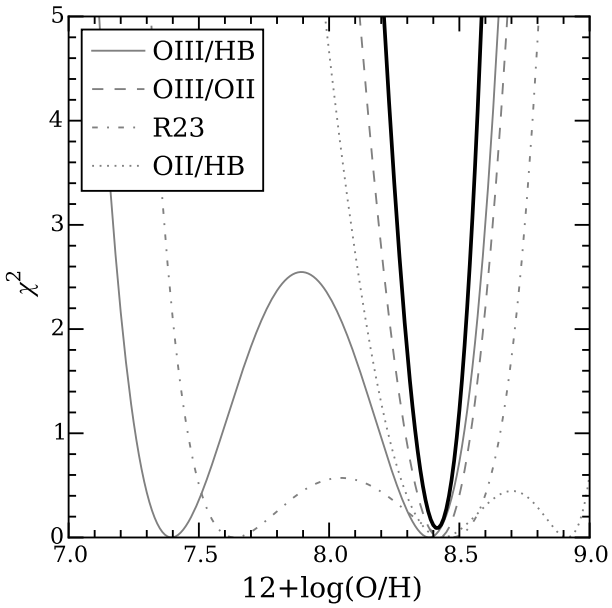

Figure 3.8 *Showing an example of the χ^2 technique for estimating metallicity described in the text. The grey lines show the χ^2 vs 12+log(O/H) curve for each individual line ratio and the thick black line shows shows the combined probability of all these curves. The minimum of this black line gives the best-fitting metallicity solution.*

in the same way as described above. I compare these measured metallicities to the metallicities quoted in those papers. Fig. 3.9 shows the results of this test; the method I adopt agrees very well across the all 15 data points with median and average difference of 0.004 and 0.013 dex respectively.

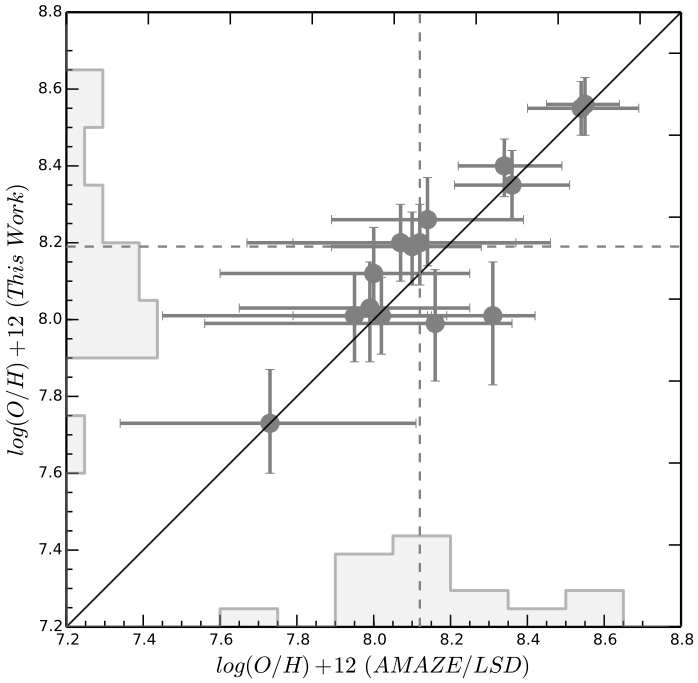

Figure 3.9 *A comparison of my measurement of metallicity for the $z \sim 3$ galaxies in Maiolino et al. (2008) and Mannucci et al. (2009) compared to the metallicities quoted in those papers. The mean and median offset of the measured metallicities are 0.013 and 0.004 dex respectively. On each axis the histograms represent the distribution of the individual points and the dashed lines represent the median of those distributions.*

Table 3.2 *Derived data for the galaxy stacks in the sample.*

ID	$\log(M/M_{\odot})^a$	$12 + \log(O/H)^b$	$\log(SFR_{H\beta}$ / $M_{\odot}$ $yr^{-1})^c$	$\log(SFR_{SED}$ / $M_{\odot}$ $yr^{-1})^d$	$E(B-V)^e$
1	$9.44^{+0.09}_{-0.16}$	$8.10^{+0.10}_{-0.11}$	0.86 ± 0.16	0.57 ± 0.15	0.04 ± 0.04
2	$9.65^{+0.05}_{-0.11}$	$8.13^{+0.13}_{-0.12}$	0.97 ± 0.17	0.78 ± 0.22	0.09 ± 0.04
3	$9.75^{+0.11}_{-0.05}$	$8.26^{+0.11}_{-0.09}$	1.09 ± 0.12	0.81 ± 0.36	0.08 ± 0.07
4	$9.94^{+0.04}_{-0.07}$	$8.30^{+0.09}_{-0.09}$	1.17 ± 0.14	1.28 ± 0.31	0.19 ± 0.09
5	$10.07^{+0.07}_{-0.07}$	$8.41^{+0.09}_{-0.09}$	1.47 ± 0.16	1.37 ± 0.28	0.18 ± 0.07
6	$10.25^{+0.22}_{-0.11}$	$8.41^{+0.09}_{-0.08}$	1.56 ± 0.17	1.62 ± 0.43	0.23 ± 0.13

[a] Median mass of the stack, error bars represent the range of stellar masses in each bin.

[b] Metallicities of the stacks derived from the Maiolino et al. (2008) calibrations.

[c] The SFR of the stacks measured from the Hβ flux corrected for dust extinction.

[d] Mean and standard deviation of SED SFR of the individual galaxies in the stack.

[e] Mean and standard deviation of $E(B-V)$ of the individual galaxies in the stack.

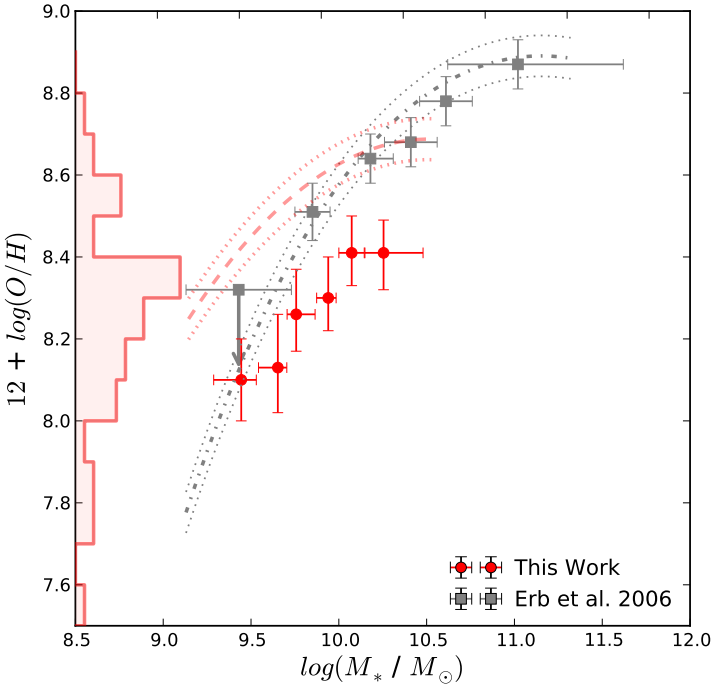

Figure 3.10 *The MZR for the $z \gtrsim 2$ galaxies in the 3D-HST sample. The red circles represent the galaxy stacks presented in this chapter with metallicities derived from the [OII], [OIII] and Hβ nebular emission lines. The red histogram shows the distribution of metallicities for the individual galaxies in the stacks with a measured metallicity. The grey squares represent the $z \gtrsim 2$ MZR from Erb et al. (2006b) with metallicities derived from [NII] and Hα. The red dashed line (my sample) and the grey dot-dashed line (Erb et al., 2006b) show the predicted positions of the two data sets in the M-Z plane derived using the FMR (see Section 5.7).*

3.5 Mass-Metallicity Relation

I now present the results of our study of the MZR and FMR, exploring the position of the 3D-*HST* z$\gtrsim$2 emission line galaxies in the MZR plane and on the FMR surface. Throughout I compare to the previous z $\gtrsim$ 2 sample of Erb et al. (2006b). I also compare in Section 5.7 to the complimentary study of Henry et al. (2013b) at lower redshift (z $\sim$ 1.8) with metallicities measured from stacked grism spectra using the same nebular emission lines.

Fig. 3.10 shows the MZR for our data compared to the MZR from Erb et al. (2006b). Erb et al. (2006b) measured metallicities from the [NII]/Hα ratio using the calibration of Pettini & Pagel (2004), so I convert their data to the Maiolino

et al. (2008) calibration to keep the metallicity scales consistent. As previously mentioned, it is important that strong line metallicity diagnostics are compared using the same calibration since it has been noted that mismatches between different calibration scales can cause systematic offsets in derived metallicities (e.g. Kewley & Ellison, 2008). Erb et al. (2006b) used a Chabrier IMF to derive stellar masses so that no mass conversion is necessary for consistency with my analysis. As a cross-check, I have run the photometric data from their paper through LEPHARE and confirmed that I derive similar stellar masses.

The 3D-*HST* data support the existence of the MZR at z $\sim$ 2. It can be seen from Fig. 3.10 that I find, in agreement with many other studies of the MZR, a decrease in metallicity with decreasing stellar mass. Across the range of stellar mass 9.3 $<$ log(M/M$_\odot$) $<$ 10.5 I observe a decrease of $\sim$ 0.3 dex in metallicity. The data extends the Erb et al. (2006b) study as I probe masses below log(M/M$_\odot$) $\sim$ 10.0 where their data could only place an upper limit on the metallicity. However, at a given value of stellar mass I measure lower metallicities than Erb et al. (2006b). This discrepancy is of the order of $\sim$ 0.2 - 0.3 dex in the highest mass bins. This offset is large considering the similar redshifts of the two samples, in Section 5.7 I explore a possible explanation for this offset given by the FMR.

3.6 Fundamental Metallicity Relation

To investigate the FMR the SFR of the galaxy stacks were measured from the Hβ line flux as described in Section 3.4. I use the original FMR equation given in Mannucci et al. (2010) as opposed to its extension in Mannucci et al. (2011) as I find that the Mannucci et al. (2010) FMR was derived using a sample that best matches the mass-SFR parameter space of our sample and the Erb et al. (2006b) sample. The Mannucci et al. (2011) FMR extension was derived by adding low-mass (log(M / M$_\odot$) $<$ 9.2), low-SFR galaxies which are not representative of the galaxies in our data set. I find that the using Mannucci et al. (2011) FMR parametrization produces discontinuities in the M-Z relation at the high masses and high SFRs of our sample (Fig. 3.12). However, we note that adopting the Mannucci et al. (2011) FMR parametrization does not significantly change the results discussed below.

According to the FMR, measuring lower metallicity in a given stellar mass bin should indicate that the average SFR in that bin is higher. Therefore, given that

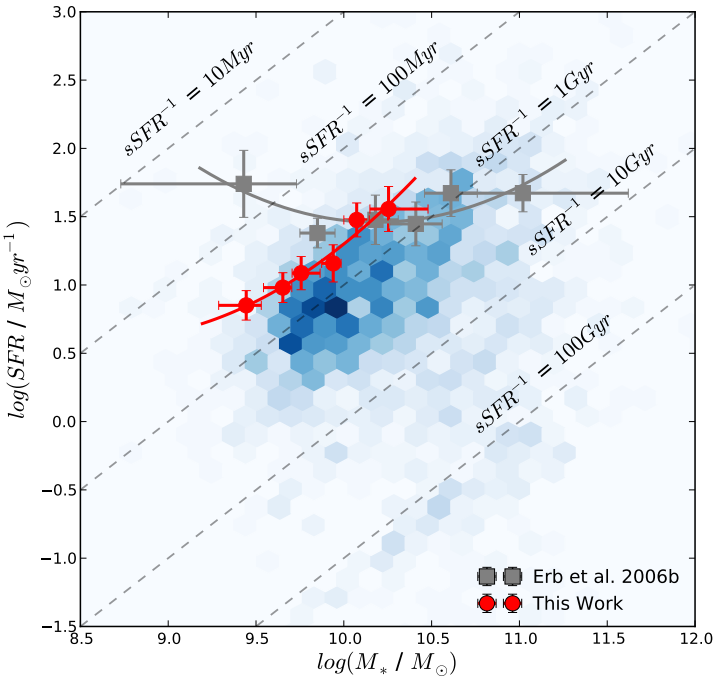

Figure 3.11 *The position of galaxies in the 3D-HST sample in the M_*-SFR plane. Red circles represent SFRs for the stacked galaxies presented in this chapter with SFR measured from the Hβ flux of the stacked spectra, converted to Hα via the common conversion factor Hα/Hβ = 2.86 (Kennicutt, 1998). The grey squares represent SFRs for the stacked galaxies from Erb et al. (2006b) (grey squares) with SFR measured directly from Hα. The points are overlaid on a 2D histogram (in blue) of ∼ 3000 galaxies at $2 < z < 2.5$ from Whitaker et al. (2012) to provide a visual reference for the region of the M_*-SFR plane I am sampling. Polynomial fits to the Erb et al. (2006b) data (grey line) and the data presented here (red line) are indicated on the plot, these lines represent two slices along the FMR surface.*

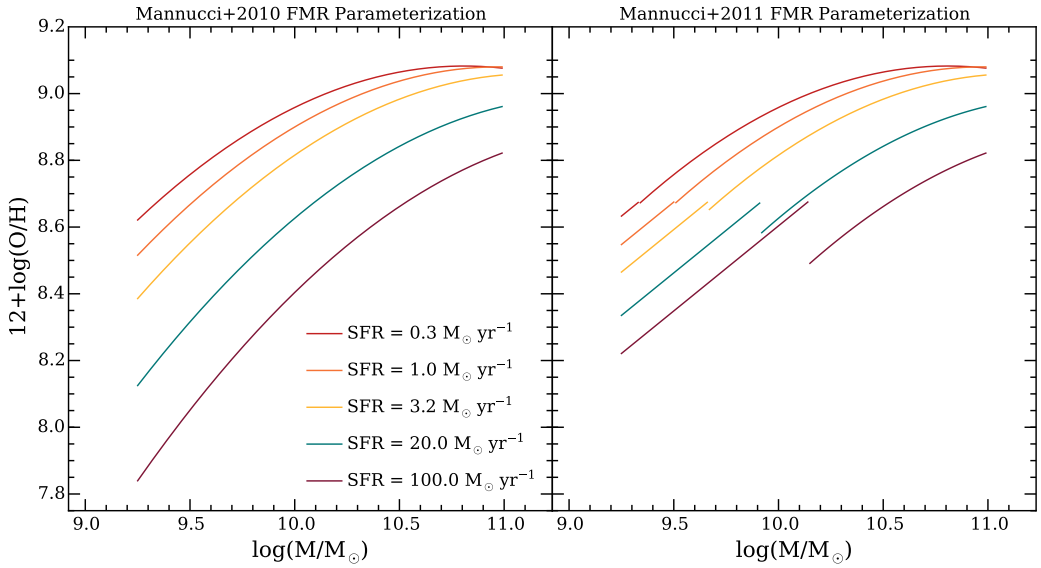

Figure 3.12 *The mass-metallicity plane as a function of SFR for the Mannucci et al. (2010) (M10) and Mannucci et al. (2011) (M11) FMR parameterizations. Left panel: Solid lines show the M10 FMR in the mass-metallicity plane along lines of constant SFR ranging from 0 - 100 $M_\odot$ yr^{-1}. Right panel: showing the same for the M11 FMR, discontinuities are apparent at the high SFRs and low masses of the 3D-HST sample.*

I measure lower metallicities than Erb et al. (2006b) across our stellar mass bins (Fig. 3.10), we should also observe elevated average SFRs in those bins. However as illustrated in Fig. 3.11 the average SFR within our stellar mass bins is lower than the Erb et al. (2006b) data, converging to similar values towards the higher mass bins in our sample ($\sim 10^{10} M_{\odot}$). This implies at least one of these data sets is in contradiction to the FMR. The problem is not alleviated by taking our SFRs from SED fitting as these are on average slightly lower than the Hβ derived SFRs as discussed in Section 3.4.

The FMR offset of various samples is illustrated in Fig. 3.13. This figure shows the difference between the metallicity observed and the metallicity predicted from the FMR given the Hβ derived SFR and the median values of stellar mass for each galaxy stack. It can be seen that the galaxies presented in this chapter lie offset from the FMR by an average of ~ 0.3 dex (dashed red line) whilst the Erb et al. (2006b) data are consistent with the FMR. This is also illustrated in Fig. 3.10 where the predicted positions of the two samples, based on the FMR, are shown in the MZ plane. I investigate how the potential underestimation of SFRs discussed in Section 3.4 would affect this measurement. Fig. 3.14 shows how the FMR offset would change by correcting the SFR of the stacks by the values shown in Fig. 3.6. In general, an increase to higher SFRs results in a slight decrease in the offset which is more pronounced at higher masses (due to larger dust corrections), but which are nevertheless still significantly offset from the FMR predictions, and within the 1σ errors of the original measurements.

Also shown in Fig. 3.13 is the ~ 0.5 dex offset of the AMAZE/LSD galaxies (Maiolino et al., 2008; Mannucci et al., 2009) at z ~ 3. The offset was calculated by taking the median values of mass, metallicity, and SFR of the individual galaxies quoted in those papers. We convert the stellar mass from Maiolino et al. (2008) to be consistent with the Chabrier IMF used in this analysis. This offset of the z ~ 3 galaxies was also noted in Mannucci et al. (2010). As discussed in Section 3.4.1 I use the same calibration and the same set of emission lines to measure metallicities as the AMAZE/LSD surveys. Furthermore, my method of metallicity measurement is shown to return consistent results (see Fig. 3.9).

The fact that the z $\gtrsim 2$ galaxies presented here are offset from the FMR, as are the z ~ 3 galaxies from AMAZE/LSD, whilst the z $\gtrsim 2$ galaxies of Erb et al. (2006b) are in agreement, suggests that the choice of metallicity indicator may be affecting the measured metallicities. At first sight it appears that this should not be the case, since all line ratios are calibrated to the same metallicity scale.

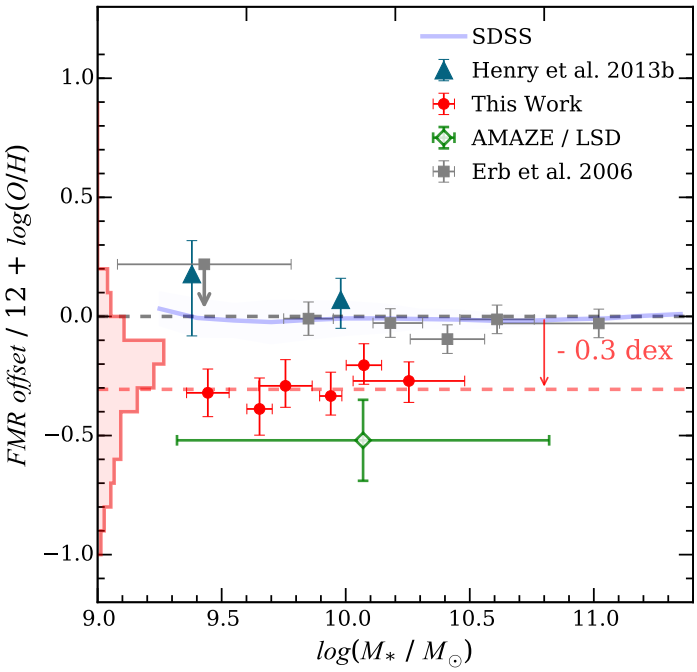

Figure 3.13 *The difference in the observed values of metallicity from those predicted by the FMR as a function of stellar mass for various samples. The blue line is the original SDSS sample of Mannucci et al. (2010) with the blue shaded region representing the 1σ dispersion. The filled red circles represent the galaxy stacks presented in this chapter. The green diamond shows a combination of $z \sim 3$ galaxies from the AMAZE/LSD surveys (Maiolino et al., 2008; Mannucci et al., 2009) and the grey squares show the Erb et al. (2006b) galaxies. The navy blue triangles show data from Henry et al. (2013b) for the mass bins in their data which overlap with our sample. My results, within the error bars, are not consistent with the FMR derived in the local Universe persisting out to $z \gtrsim 2$, and yield a average offset of ~ 0.3 dex.*

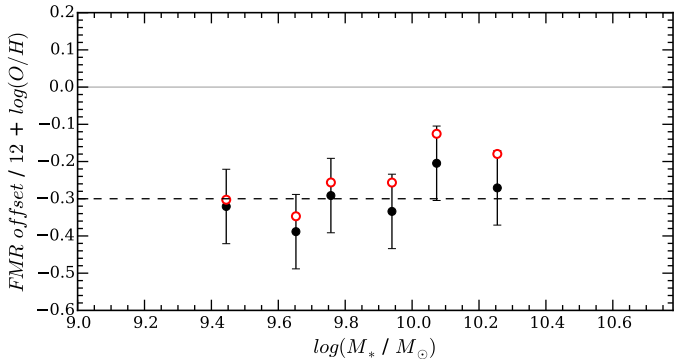

Figure 3.14 *Illustrating how correcting the Hβ measured SFRs of the 3D-HST stacks, using the extra attenuation prescription of Wuyts et al. (2013), affects the measured FMR offset. The black circles show the original measurements shown presented in Fig. 3.13, and the red open circles show the corrected measurements.*

However, these calibrations were made using local Universe star-forming galaxies which may not be representative of typical star-forming galaxies at high redshift. In Chapter 4 I investigate in detail whether a change in the ionization conditions of HII regions at high redshifts affects the consistency of metallicity measurements using different sets of line ratios.

I also compare our results with data from Henry et al. (2013b) in Fig. 3.13 (blue triangles). The Henry et al. (2013b) sample consists of 83 grism spectra in the redshift range $1.3 < z < 2.3$, the spectra are stacked in four bins of stellar mass and metallicities are measured from the oxygen and Hβ lines using the Maiolino et al. (2008) calibrations. In this respect my data and methods are very similar. The main difference between our data sets is that their sample spans a much wider redshift range resulting in a lower median redshift ($z = 1.76$), and the Henry et al. (2013b) sample probes to lower stellar masses ($\log(M/M_{\odot}) < 10^{9.2}$). In Fig. 3.13 we only include the mass bins which overlap with our sample. Despite using the same line diagnostics, the data from Henry et al. (2013b) lie on the FMR relation, in disagreement with our results. Again, an evolution in ionization conditions, as explored in the next chapter, may explain this inconsistency.

Newman et al. (2013b) data

To further investigate the discrepancy between line indicators, I took a sample of 11 $z \sim 2$ galaxies from Newman et al. (2013b) which have flux measurements in the [NII], Hα, [OIII]λ5007 and Hβ lines, and have measured masses and SFRs.

The masses were derived using a Chabrier IMF, so no conversion was necessary for comparison with the results presented here. However, I have increased the stellar masses by the median value of + 0.18 dex derived in Section 3.3.1 for converting instantaneous stellar mass to the total mass of stars formed, for consistency with the 3D-*HST* and Erb et al. (2006b) data. Metallicities were derived from the [NII]/Hα and [OIII]/Hβ line ratios individually and the offset from the predicted FMR value computed as described in Section 5.7.

Note that the full set of oxygen and Hβ calibrations used on the 3D-*HST* data could not be used on the Newman et al. (2013b) data so oxygen and Hβ metallicities were derived from the [OIII]/Hβ ratio alone. When used independently the [OIII]/Hβ metallicity calibration is double-valued (see Maiolino et al. (2008) and Fig. 3.7), so to derive a metallicity from the [OIII]/Hβ ratio solely it is necessary to choose between the upper and lower solutions. For each galaxy in the Newman et al. (2013b) sample the upper solution was taken, as it was in agreement with the high metallicities implied from the [NII]/Hα solution. Nevertheless, even when taking the upper solution for [OIII]/Hβ, the [NII]/Hα ratio returns systematically higher values of metallicity in better agreement with the FMR. This is illustrated in Fig. 3.15. The median and MAD for the [NII]/Hα ratio and [OIII]/Hβ ratio respectively are -0.10 $\pm$ 0.09 dex and -0.44 $\pm$ 0.22 dex. It is also interesting to note that the Newman et al. (2013b) data probe a higher-mass regime, similar to the Erb et al. (2006b) sample, indicating this effect is seen across a wide range in mass $\sim 9.5 < \log(M/M_{\odot}) < 11.5$.

3.7 Summary and Conclusions

I have selected a sample of 93 galaxies in the redshift range $2.0 < z < 2.3$ from an independent reduction of the 3D-*HST* spectroscopic grism survey. In this redshift range the [OII], [OIII] and Hβ emission lines fall within the wavelength range of the grism spectra. My aim is to use those emission lines to measure the metallicities of galaxies and measure their masses from the ancillary CANDELS photometry available in the 3D-*HST* survey fields. I stack the galaxies in bins of stellar mass and construct a mass-metallicity relationship for this sample, which we can directly compare with the previous $z \gtrsim 2$ study of Erb et al. (2006b). I then measure the SFR from the Hβ line and use this to investigate the FMR at these redshifts. Below is a summary of the results.

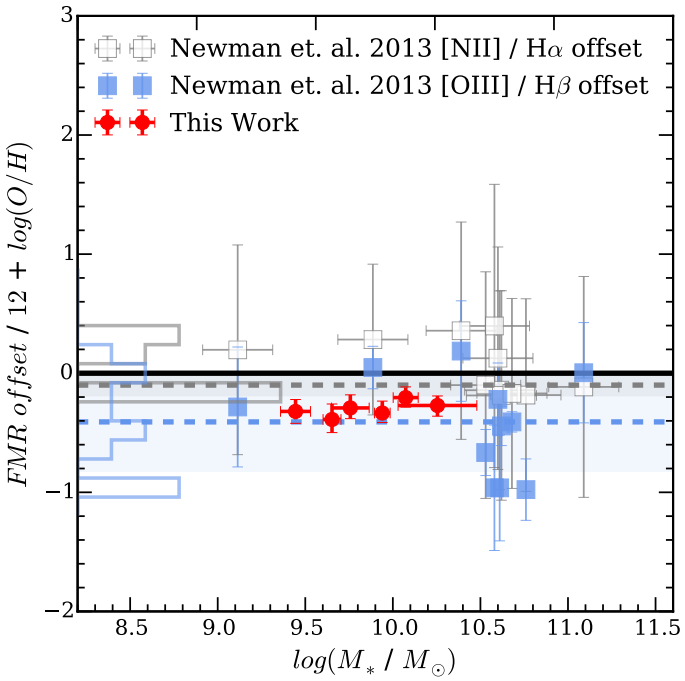

Figure 3.15 *The FMR offset for a sample of $z \sim 2$ star-forming galaxies taken from Newman et al. (2013b). Open grey squares show the metallicities derived from the [NII]/Hα ratio and the filled blue squares show the metallicities derived from the [OIII]/Hβ ratio. On the y axis the grey and blue histograms show the distribution of the individual points with the horizontal dashed lines representing the median values of the distributions. The median and MAD for the [NII]/Hα ratio and [OIII]/Hβ ratio respectively are -0.10 ± 0.09 dex and -0.44 ± 0.22 dex., the MAD is shown by the shaded region around the median line. For reference the galaxies presented in this chapter are plotted as filled red circles as in Fig. 3.13.*

- I measure the metallicities of the 3D-*HST* galaxies from the [OII], Hβ and [OIII] emission lines via the calibrations of Maiolino et al. (2008). I find a MZR in the galaxy sample consistent with the MZR reported elsewhere in the literature (e.g. Erb et al., 2006b; Mannucci et al., 2009; Yuan et al., 2013) in that observe a decrease in metallicity with a decrease in mass of the galaxy stacks (Fig. 3.10). However this MZR is offset to lower metallicities at a given stellar mass from the z $\gtrsim$ 2 MZR of Erb et al. (2006b).

- I investigate this metallicity offset using the FMR proposed by Mannucci et al. (2010) which incorporates mass, metallicity and SFR in an attempt to explain the scatter and redshift evolution of the MZR. However I find the data are apparently inconsistent with the FMR. I measure metallicities lower by $\sim$ 0.3 dex from those predicted from the FMR given the measured masses and SFRs (Fig. 3.13). The previous z $\gtrsim$ 2 data of Erb et al. (2006b) are consistent with the FMR as discussed in Mannucci et al. (2010), therefore there is a discrepancy between the current z $\gtrsim$ 2 data. One difference between the Erb et al. (2006b) study and the one presented here is the metallicity indicator used. Erb et al. (2006b) use the [NII]/Hα ratio whereas the 3D-*HST* metallicities are based on the oxygen and Hβ lines. Interestingly my adopted method for metallicity measurement follows previous z $\sim$ 3 MZR studies (Maiolino et al., 2008; Mannucci et al., 2009) who find a similar offset from the FMR using the same set of emission lines.

- For further investigation I also take a sample of 11 z $\sim$ 2 galaxies with measured [NII], Hα, [OIII]λ5007 and Hβ fluxes from Newman et al. (2013b) and confirm that the metallicities derived using the Maiolino et al. (2008) calibrations are systematically higher than when using the [NII]/Hα ratio (Fig. 3.15). This suggests that metallicities derived from the oxygen and Hβ lines are not equivalent to those derived using [NII]/Hα at high redshift.

In the next chapter I will investigate, using a sample of galaxies over a much larger redshift range, how evolving ionization conditions in star-forming galaxies with redshift may be biasing measurements of metallicities at high redshift using local Universe calibrations. Finally, in Chapter 5, I will return to the $z \gtrsim 2$ mass-metallicity relation to attempt to properly account for the offset between the 3D-*HST* and Erb et al. (2006b) datasets, extending the $z \gtrsim 2$ sample with more recent measurements from surveys with KMOS and MOSFIRE.

Chapter 4

Changing of Physical Conditions in HII Regions: Evolution of the [OIII]/Hβ Ratio

A small portion of this chapter has been published in Cullen et al. (2014)

4.1 Introduction

In this chapter, following on from the results of chapter 3 (i.e. Cullen et al., 2014), I use the [OIII]/Hβ nebular emission line ratio to investigate the evolution of the metallicity, ionization parameter, and ISM pressure in star-forming galaxies in the redshift range $0 < z < 4$.

In the local Universe the relations between the strong emission lines have been extensively studied. Thanks to the large statistical galaxy sample provided by the Sloan Digital Sky Survey (SDSS), key properties of the population such as the mass-metallicity relationship have been investigated for $\sim 10^4$ galaxies (e.g. Tremonti et al., 2004). Similarly, the position of the star-forming 'abundance sequence', and AGN locus, of local galaxies on the [OIII]/Hβ vs [NII]/Hα diagram (Baldwin et al., 1981, BPT) has become well established (e.g. Kauffmann et al., 2003a; Kewley et al., 2006) This abundance sequence, which is dependent upon the global gas-phase metallicity distribution, the stellar ionizing radiation field and various properties of the ISM within galaxies (such as the geometrical

distribution of gas and electron density), is observed to evolve with redshift (Kewley et al., 2013a,b).

Specifically, from the growing sample of galaxies at $z > 1$, an evolution away from the local abundance sequence toward higher values of the [OIII]/Hβ and [NII]/Hα ratios is observed (see e.g. Erb et al., 2006b; Hainline et al., 2009; Kewley et al., 2013b; Shapley et al., 2005, 2015; Steidel et al., 2014; Yabe et al., 2012). It has also been reported that the [OIII]/Hβ ratios are consistently elevated from the average value for star-forming galaxies in the local Universe (e.g. Cullen et al., 2014; Holden et al., 2014; Kewley et al., 2013b; Troncoso et al., 2014). Recently, Steidel et al. (2014) have definitively confirmed this trend with a sample of 179 star-forming galaxies at $z \sim 2.3$, finding that these galaxies form a distinct, yet similarly tight, locus in the BPT plane compared to SDSS galaxies. Such an evolution toward more extreme conditions in the overall star-forming population is perhaps also hinted at by the observed increase of the star-formation rate of galaxies at a given mass out to $z \gtrsim 2$ (e.g. Pannella et al., 2014; Salmon et al., 2015; Whitaker et al., 2012).

Kewley et al. (2013a) have investigated theoretically how a change in the physical conditions in galaxies at high redshift will cause the local star-forming galaxy abundance sequence to evolve. They suggest more extreme ISM condition in high redshift HII regions will result in the abundance sequence at a given redshift being offset from the one defined locally. However, the precise nature of these 'extreme conditions' is still a matter of debate. Brinchmann et al. (2008) argue that a higher ionization parameter at high redshift could account for elevated line ratios, and an increase in ionization parameter is indeed observed for galaxies at $z > 1$ (e.g. Cullen et al., 2014; Hainline et al., 2009; Nakajima & Ouchi, 2014). The commonly cited example of this is an increase of the [OIII]/[OII] ratio (O32) at fixed R23 ratio in high redshift galaxies; which, since O32 is primarily ionization parameter sensitive and R23 primarily metallicity sensitive, is said to be indicative of an increase in ionization parameter at fixed metallicity (e.g. Nakajima & Ouchi, 2014; Shapley et al., 2015). I illustrate this in Fig. 4.1 by showing the position of a number of galaxy samples (including the 3D-*HST* sample from Chapter 3) in the O32 versus R23 plane. Other observational studies have also found that the elevated line ratios may be the result of higher electron densities and gas pressures in star-forming regions at high redshift (e.g. Lehnert et al., 2009; Shirazi et al., 2014b,a). However, it has as yet been unclear whether either one of these effects is dominant, or if both play an equal role in the evolution.

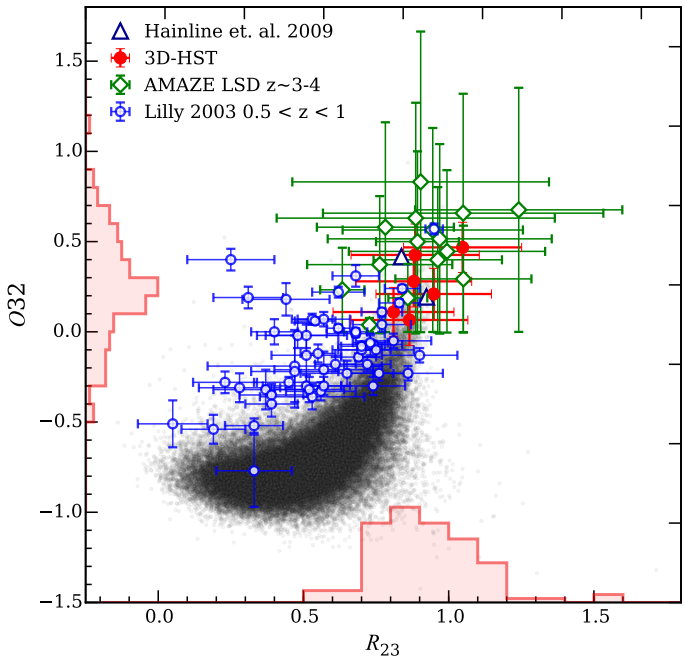

Figure 4.1 *The O32 versus R_{23} diagnostic diagram used to differentiate change in ionization conditions from a change in metallicity of galaxies (Hainline et al., 2009; Lilly et al., 2003; Nakajima & Ouchi, 2014). The stacked galaxies from the 3D-HST sample used in Chapter 3 are represented by filled red circles and the distribution of the individual galaxies are shown as histograms on each axis. The open blue circles represent a sample of $0.5 < z < 1$ galaxies taken from Lilly et al. (2003), the open green diamonds are the AMAZE/LSD sample of $z \sim 3$ -4 galaxies from Maiolino et al. (2008) and Mannucci et al. (2009).*

In this chapter I investigate the redshift evolution of [OIII]/Hβ nebular emission line ratio between $z = 1.3$ and $z = 2.3$ with the 3D-*HST* dataset. 3D-*HST* has the distinct advantage of allowing one to account for any selection effects resulting to redshift dependent line luminosity thresholds. The importance of accounting for such selection biases has been recently highlighted by Juneau et al. (2014) who find that, using a sample of SDSS galaxies, it is possible to re-create the abundance sequence offset at high redshift by applying increasing [OIII] and Hα luminosity cuts to the sample. I address the issue of completeness and selection biases in the 3D-*HST* sample in Section 4.3. Once accounting for possible selection biases, I can then compare the evolution of the [OIII]/Hβ ratio between the SDSS and 3D-*HST* samples, across ~ 10.7 Gyr of cosmic time, to the theoretical models introduced in Kewley et al. (2013a). I will describe how these models are applied in the context of the present work in Section 4.4. These models allow one to distinguish between different scenarios for the physical evolution of the star-forming regions with redshift. I also supplement our SDSS and 3D-*HST* data with $z \sim 3.5$ data from the AMAZE/LSD surveys and a sample of galaxies from Holden et al. (2014). The results are presented in Section 4.5.

In Section 4.6 I examine the scatter about the [OIII]/Hβ vs. redshift relation to assess which physical parameters are responsible for the [OIII]/Hβ distribution at a given redshift, and whether these are the same as the parameters driving the redshift evolution. For this Section I additionally utilize a DEEP2 dataset at $z \sim 0.8$. Finally in Section 4.7 I discuss the practical implication of the results with respect to accurately measuring the gas-phase metallicity of galaxies at high redshift and explore various theoretical interpretations.

4.2 Data and Sample Selection

The data analysed in this chapter are drawn from a variety of separate star-forming galaxy catalogues across the redshift range $0 < z < 4$. The objective behind this selection is to sample the [OIII]/Hβ vs. redshift relation across the widest redshift baseline possible. Below I will describe the separate samples. All datasets are cut to only include galaxies with $\log(M/M_*) > 9.0$ for consistent comparison with the theoretical models described in Section 4.4.

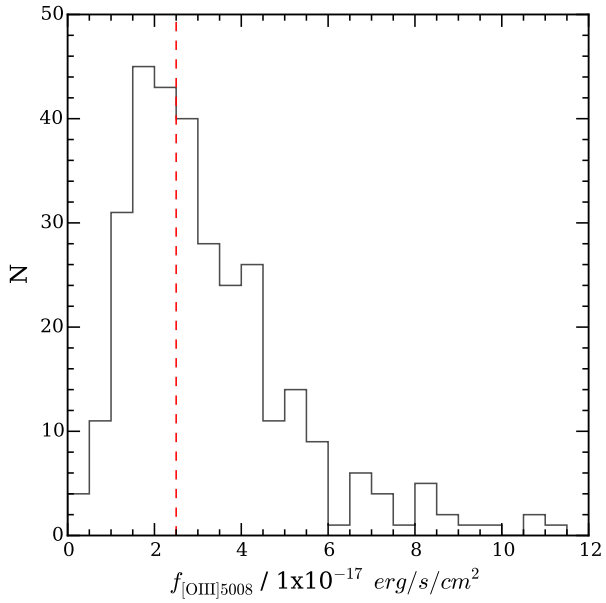

Figure 4.2 *Distribution of [OIII]λ5007 fluxes for the final galaxy sample. The formal 3-σ line flux limit is shown by the red dashed line.*

4.2.1 3D-*HST*

Given the wavelength coverage of the 3D-*HST* spectra it is possible to measure the [OIII]/Hβ ratio in the redshift range $1.3 < z < 2.3$. Therefore, we extended the sample presented in Chapter 3 to include all galaxies in this redshift range from 3 CANDELS fields: COSMOS, GOODS-S and UDS. The individual line fluxes and continuum fits are performed as described in Chapter 2. This initial sample is then checked for AGN contaminants as described below, once the AGN have been removed the sample contains 313 galaxies with a 3-σ flux limit in [OIII]λ5007 of 2.5 x 10^{-17} ergs/cm^2/s. The distribution of [OIII]λ5007 fluxes is shown in Fig. 4.2. As in Chapter 3, most results in this chapter are derived by stacking the individual spectra to overcome the problem of a high proportion of low SNR galaxies.

AGN Removal

Using the same method described in Chapter 3, I cross-match galaxies with X-ray sources in the GOODS-S (Xue et al., 2011) and COSMOS (Civano et al., 2012) fields to remove 17 X-ray selected AGN from the initial sample. However, I could

not perform a similar selection in UDS due to the lack of a sufficiently deep X-ray catalogue.

In a departure from the method described in Chapter 3, I choose not to apply the MEx AGN diagnostic (Juneau et al., 2014) on the 3D-*HST* sample. The premise of this study is based on investigating the idea that conditions in star-forming regions become more extreme at high redshift, since Juneau et al. (2014) diagnostic is calibrated with SDSS galaxies, and does account for this possible evolution, we risk removing genuine extreme star-forming galaxies from our sample. Moreover, only N=16/313 galaxies would be classified as AGN via this method, and I have checked that removing galaxies these has no effect on the final results.

In summary, I identify and removed 17 X-ray selected AGN ($\sim$ 5% of original sample). This is comparable to, but slightly lower than, previous studies at similar redshifts (e.g. Stott et al., 2013; Zahid et al., 2014a) which find $\sim$ 8% AGN contamination. Therefore, I cannot rule out residual AGN contamination in our final sample of 313 galaxies due to insufficient line diagnostic tools and lack of sufficiently deep X-ray catalogue in UDS. However, any residual contamination would be expected to be on the order of a few %. In addition, I am able to account for this residual AGN contamination in our stacked spectra via a bootstrapping technique described below.

Bootstrapping Stack Spectra

Most of the science results in this Chapter are derived by stacking the 3D-*HST* spectra in bins of mass and or redshift. To improve the error estimation of the line fluxes in the stacked spectra I used the bootstrapping technique. Bootstrapping gives a better representation of the intrinsic scatter of line fluxes within each stack compared to, for example, propagating the errors of the individual spectra which mainly represents data quality (e.g. Zahid et al., 2014a). Any large scatter in line fluxes induced by AGN contamination will also be accounted for by bootstrapping. As mentioned before, previous studies of emission line galaxies at $z \sim 1-2$ estimate an AGN contamination fraction of $\sim 5-15\%$ (e.g. Stott et al., 2013; Zahid et al., 2014a) therefore, though we have removed some X-ray selected AGN we can assume a contamination of up to $\sim$ 10% per stack. For each redshift and/or mass bin I randomly select N galaxies, with replacement, where N is the number of galaxies in the bin. I then stack the spectra and measure

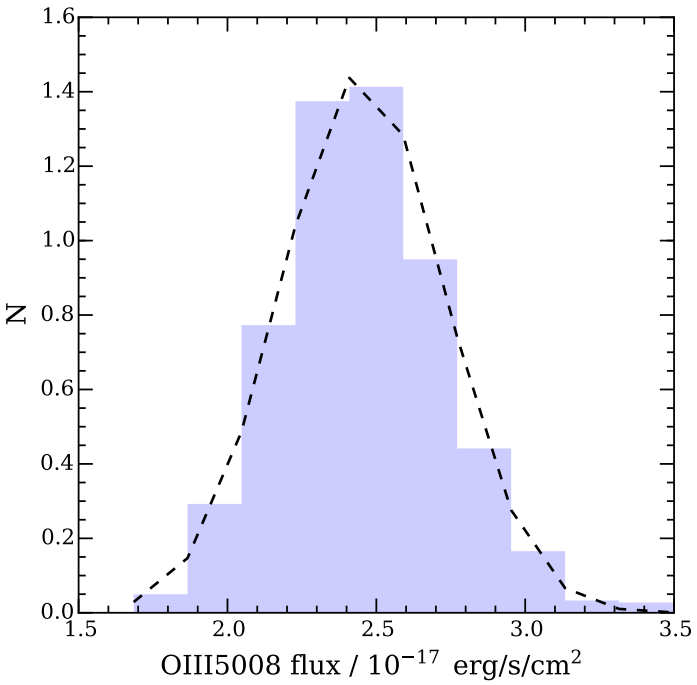

Figure 4.3 *Illustrating the bootstrapping method for measuring fluxes of stacked spectra described in the text. The blue histogram shows the flux distribution for the [OIII]λ5007 line resulting and the black dotted line shows the best-fitting Gaussian function to this distribution. The line flux is taken as the centre of the Gaussian and the error as the standard deviation σ.*

the line fluxes as described above. This process is repeated 10^3 times and final value and error on the line flux is taken as the mean and standard deviation of the Gaussian fit to this distribution.. In this way any increased variance in the line ratios due to AGN contamination will be accounted for in the error on the measurement. An illustration of this technique is given in Fig. 4.3, the figure shows a normalized distribution of [OIII]λ5007 fluxes.

4.2.2 SDSS

For the local galaxy sample I use a Sloan Digital Sky Survey (SDSS) catalogue containing 51,262 star-forming galaxies from Zahid et al. (2013), this sample of star-forming galaxies is selected in the redshift range $0.02 < z < 0.12$, with an aperture covering fraction $\gtrsim 20$ % to minimize aperture effects and with AGN removed using the Kewley et al. (2006) optical classification scheme. The emission line fluxes in this catalogue are taken from the JHU/MPA catalogues[1], these line fluxes have been corrected for underlying stellar absorption. Stellar masses are calculated from the SDSS *ugriz* photometry as described in Zahid et al. (2013).

4.2.3 DEEP2

The Deep Extragalactic Evolutionary Probe 2 (DEEP2) survey consists of $\sim 50,000$ galaxies in the redshift range $0.7 < z < 1.4$. The sample I use here is selected from the mass-metallicity study of Zahid et al. (2012). This DEEP2 sample was selected for blue galaxies following Willmer et al. (2006) and the selection criteria has been shown to remove the majority of AGN with a residual contamination of $\sim 1\%$ (Weiner et al., 2007). A further 17 X-ray selected AGN have been removed using the XDEEP2 catalogue (Goulding et al., 2012). Galaxies are selected between $0.75 < z < 0.82$ with a $> 3\sigma$ detection in the [OIII]/Hβ, Hβ and [OII] emission lines. The final sample contains 1252 star-forming galaxies.

The latest publicly available DEEP2 spectra (Data Release 4; Newman et al. 2013) are not flux calibrated which means line ratios are determined from ratios of equivalent widths as opposed to line fluxes. As will be explained in the relevant sections, the lack of flux calibration means the DEEP2 galaxies can only be studied in Section 4.6 of this chapter. Zahid et al. (2011) have also determined a

[1]http://www.mpa-garching.mpg.de/SDSS/DR7/

mass-dependent Hβ absorption correction for the DEEP2 spectra by stacking the spectra into bins of stellar mass, this correction is then applied to each individual galaxy. Stellar masses for the sample are derived from BRI-band photometry and additional Ks-band photometry (50%) as described in Zahid et al. (2012).

4.2.4 AMAZE/LSD

I utilize a sample of star-forming galaxies at $3 < z < 4$ (median $z = 3.4$) taken from Troncoso et al. (2014). The data compiled in Troncoso et al. (2014) were taken as part of the AMAZE (Maiolino et al., 2008) and LSD (Mannucci et al., 2009) surveys undertaken with the SINFONI instrument at the VLT. The galaxies were selected to exclude AGN based either their UV spectra, X-ray data or MIPS $24\mu m$ flux (see Maiolino et al. (2008) for details). I select galaxies from the Troncoso et al. (2014) catalogue with a 3σ detection in [OIII]λ5007. The final sample contains 33 galaxies.

Troncoso et al. (2014) do not perform a correction for underlying Hβ absorption concluding the correction would be negligible due to the non-detection of a continuum in the majority of sources. Stellar masses for this sample were derived from either 14-band UV - *Spitzer*-IRAC photometry or optical photometric data (U, G, R, I) plus *Spitzer* IRAC and MIPS bands. This is the only sample with stellar masses derived using a Salpeter IMF so we convert the quoted values to a Chabrier IMF for consistency across all datasets.

4.2.5 Holden et al. (2014)

The Holden et al. (2014) dataset consists of 18 Lyman-break selected star-forming galaxies at $z \sim 3.2 - 3.7$ with [OIII]/Hβ ratios measured using the MOSFIRE instrument on the Keck-I telescope. AGN contamination is ruled out based on the rest-frame UV spectra and X-ray data. Again no correction has been made for the underlying Hβ absorption but again no spectra have reliably detected continua and thus, as argued by Troncoso et al. (2014), the correction would most likely be negligible. I select galaxies from the Holden et al. (2014) catalogue with a 3σ detection in [OIII]λ5007. The final sample contains 15 galaxies. In combination with the AMAZE/LSD galaxies this gives a total of 48 galaxies at $z > 3$.

4.3 Completeness Issues

As has been recently pointed out by Juneau et al. (2014), any observed evolution of the [OIII]/Hβ ratio could be a result of incompleteness effects and biases in the high redshift data. Cosmological flux dimming will cause the minimum observable [OIII] luminosity to increase with redshift, and if [OIII]/Hβ correlates with [OIII] luminosity, an evolution to a higher ratio with redshift could be an artifact the increasing [OIII] luminosity detection threshold.

[OIII] luminosity: evolution compared to SDSS

I first explore how this affects any observed evolution compared to galaxies in the local Universe. This issue has been investigated in Juneau et al. (2014). These authors find, using an SDSS sample of 300,000 star-forming galaxies, that by imposing a minimum line luminosity to [OIII] and Hα they can produce sub-samples in the SDSS data that mimic the BPT evolution observed at $z > 1$. For the purposes of our results the implication is that as the line detection luminosity threshold is increased, an artificial evolution towards higher [OIII]/Hβ is observed. I investigate whether the luminosity of [OIII] correlates with [OIII]/Hβ in our SDSS sample in Figure 4.4. I find, in agreement with Juneau et al. (2014), that the [OIII]/Hβ increases with [OIII] luminosity. The best fitting linear relationship, shown by the red dashed line in Fig. 4.4 is given by:

$$\log([\mathrm{OIII}]/\mathrm{H}\beta) = 0.39\log(\mathrm{L}_{\mathrm{OIII}}) - 16.14 \tag{4.1}$$

Also plotted in Figure 4.4 are the position of three redshift stacks from the 3D-*HST* sample both corrected (filled symbols), and uncorrected (open symbols), for dust. The dust attenuation for the stack is taken as the median of the $E(B-V)$ values for each individual galaxy in the stack. It can be seen from Figure 4.4 that, even in the case of no dust correction, our sample lies at the extreme end of the SDSS sample in terms of $\mathrm{L}_{[OIII]}$ and [OIII]/Hβ.

Figure 4.4 indicates that a comparison of the 3D-*HST* sample to the total SDSS star-forming sample will be biased by the luminosity detection limit of 3D-*HST*. Any observed [OIII]/Hβ evolution in this case could simply be an artifact of the clear correlation between $\mathrm{L}_{[OIII]}$ and [OIII]/Hβ. Instead, I must take care to select galaxies from SDSS with the comparable ($\mathrm{L}_{[OIII]}$) in order to compare galaxies

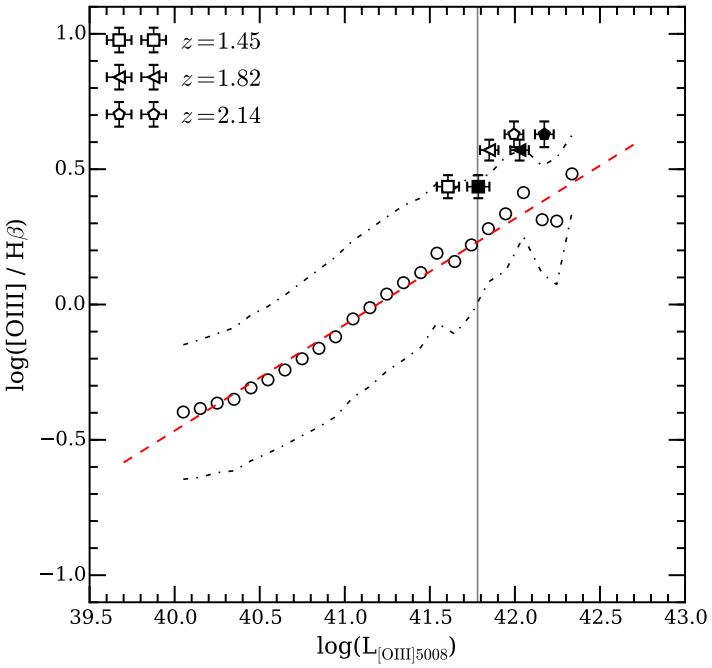

Figure 4.4 *Showing the relationship between [OIII]/Hβ and $L_{[OIII]}$ for the SDSS sample compared to 3D-HST galaxies. The small open circles show the averages of SDSS galaxies binned in 0.05 dex wide bins of log($L_{[OIII]}$), with the dot-dashed lines showing the $\pm 1\sigma$ scatter. The red dashed lines shows a simple linear fit to the SDSS galaxies. The large square, triangle and circle symbols show the position of the stacked spectra from the 3D-HST sample in increasing bins of redshift. The open symbols show the positions of the stacks without applying a dust correction to $L_{[OIII]}$, while the filled symbols show the same stacks after applying a dust correction using the median $E(B-V)$ of the individual galaxies within the stack. The solid vertical black lines shows the log($L_{[OIII]}$) completeness limit of the 3D-HST sample as described in Sec. 4.3.*

with similar properties across cosmic time. To establish the detection limit in [OIII] luminosity in the 3D-*HST* sample I performed extensive simulations described below.

3D-*HST* simulations

Given the flux limit of the 3D-*HST* survey, the minimum observable [OIII] luminosity is of course a function of redshift. Therefore, I consider the highest redshift galaxies in my 3D-*HST* sample ($z > 2$) to determine the [OIII] luminosity threshold. By using only galaxies with $L_{[OIII]}$ above this level it guarantees that no completeness biases are introduced when comparing data at different redshifts. To determine this minimum [OIII] luminosity I run a set of simulations using the software package `aXeSIM`, a dedicated simulation package for *HST* grism data. I created synthetic emission line spectra at $z = 2.15$ (median redshift of the $z > 2$ galaxies) spanning [OIII] luminosities in the range $40.0 < log(L_{[OIII]}) < 43.0$. These spectra were created with [OIII]/Hβ= 5, which is approximately the average ratio for the stacked galaxy spectra at $z > 2$ and were then injected into a simulated G141 grism image with noise properties governed by the input exposure time to the simulation[2].

Once the synthetic grism images were created, they were then fed through the same `aXe` pipeline used for reducing the real data, and 1D spectra extracted in the same way. These spectra were visually inspected and either recovered or rejected in an identical way to the real data, as described in Chapter 2. From this I estimated the recovery fraction as a function of $\log(L_{[OIII]})$ and this is shown as the black solid line in Figure 4.5. From the fit to the recovery fraction shown in Figure 4.5, I infer 90%, 75%, 50% completeness limits at $z > 2$ of, respectively, $\log(L_{[OIII]}) = 41.87$, 41.77 and 41.70.

Also shown in Figure 4.5 are the $\log(L_{[OIII]})$ distributions for the $z \geq 2$ (purple hatched histogram) and $z < 2$ (orange filled histogram) galaxies in the sample normalized to a peak value of 1. It can be seen that a significant fraction of galaxies at $z < 2$ fall below the detection threshold at $z \geq 2$. Given the correlation between [OIII]/Hβ and $L_{[OIII]}$ in SDSS galaxies, any observed evolution even within the 3D-*HST* data could simply be an artifact of the increase in the average

[2]We found the background levels when inputting the exposure times of the 3D-*HST* data in `aXeSIM` under-predicted the actual background levels observed. Therefore we experimented with the input exposure time until the background level matched the average background level of the real 3D-*HST* data across all fields.

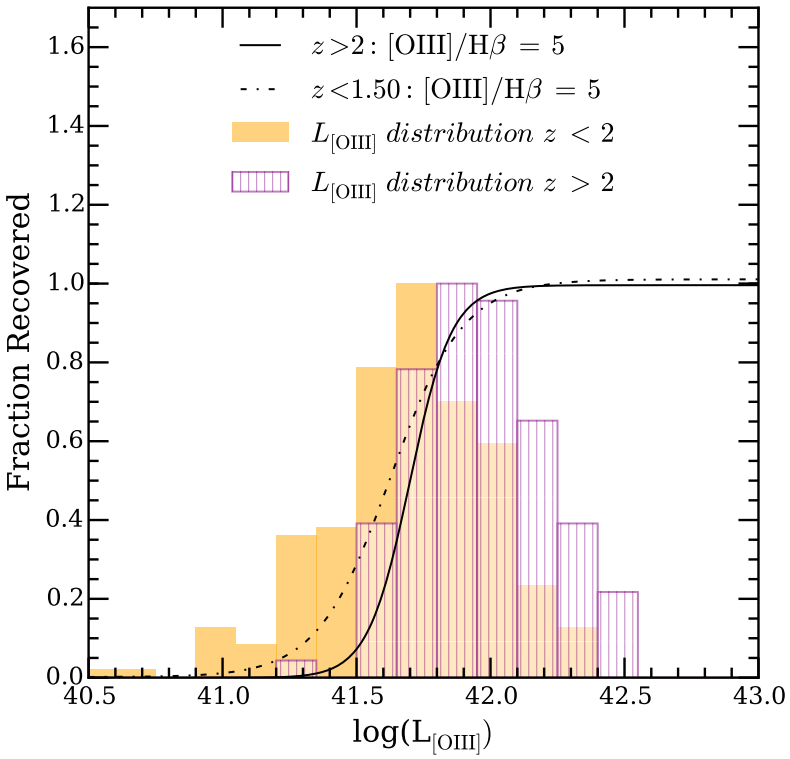

Figure 4.5 *Results of the aXeSIM simulations used to determine the completeness limits in log($L_{[OIII]}$) at $z > 2$. The black solid line is the best fitting logistic function to simulation recovery fraction. The filled orange histogram shows the log($L_{[OIII]}$) distribution for the galaxies in the 3D-HST sample at $z < 2$ and the purple histogram shows the distribution for galaxies at $z \geq 2$. The black dot-dashed line shows the simulated recovery fraction of $z < 1.5$ galaxies with high [OIII]/Hβ ratios (see text for explanation).*

$L_{[OIII]}$ of the samples due to this selection effect. Therefore, for investigating the evolution of [OIII]/Hβ with redshift, I limit all samples to include only galaxies at [OIII] luminosities brighter than the above completeness limits. Clearly, all results will be most robust for the 90% completeness cut, but it is also interesting to investigate how different completeness limits will affect the measurements.

Finally, another possible bias that could be introduced into our data is the non-selection of galaxies with high [OIII]/Hβ ratios at the lowest redshifts in the 3D-*HST* sample. Such a bias could artificially lower the average [OIII]/Hβ at lower redshifts and could arise because the sensitivity of the G141 grism falls off at shorter wavelengths. For any given redshift, at a large enough [OIII]/Hβ ratio, the Hβ line will not be visible in the spectrum below a given [OIII] flux. Due to the decreased sensitivity at short wavelengths this flux limit will be lower at lower redshift. Without a visible Hβ it becomes less likely the galaxy will be visually selected based on the single line detection of [OIII]. I ran a further set of simulations to check whether galaxies with [OIII]/Hβ = 5, typical of our $z > 2$ galaxies, would be visually selected at $z < 1.5$. The recovery fraction as a function of $\log(L_{[OIII]})$ is shown by the black dot-dashed line in Fig. 4.5. I find that above the completeness limit for $z > 2$ galaxies discussed above, we are also complete in galaxies with high [OIII]/Hβ ratios at the lowest redshifts in our sample.

To summarize, I ran simulations to account for two sources of bias in the 3D-*HST* sample: (i) an increasing lower limit to $L_{[OIII]}$ as a function of redshift; (ii) possible non-detection of high [OIII]/Hβ ratio galaxies at the lowest redshifts. To mitigate this effect I have calculated the $L_{[OIII]}$ limit at $z > 2$ and will apply this cut-off to all data for the remainder of this Chapter. I have also confirmed that, above the $L_{[OIII]}$ limit imposed by this cut, the 3D-*HST* sample is still complete for large [OIII]/Hβ ratios at the lowest redshifts.

4.4 Theoretical Models

The other key element of this chapter is the comparison of the data described above with the predictions of theoretical models. In this section I will describe the model based on the theoretical prescriptions of HII regions described in Kewley et al. (2013a,b). As discussed in the introduction three main factors affect the ratio of various emission lines in HII regions: (i) gas-phase metallicity, (ii)

strength of the ionizing radiation field and (iii) electron density (or equivalently ISM pressure). The evolution of the [OIII]/Hβ ratio in star-forming galaxies with redshift tracks the evolution in these parameters. By making theoretical predictions for the evolution of these parameters, we can use the observed redshift evolution of the [OIII]/Hβ ratio to constrain the physical conditions in HII regions across time. Below I will discuss how the redshift evolution of each physical parameter is defined in the models. Firstly, however, I will describe how the local reference values of these parameters are defined by matching the models to the star-forming abundance sequence of SDSS galaxies.

4.4.1 The Local Abundance Sequence

The star-forming abundance sequence model described here is taken from the work of Kewley et al. (2013a). Generating theoretical line ratios for HII regions is essentially a two step process: (i) generate an incident stellar radiation field and (ii) propagate that radiation field through a simulated ISM. Below I will describe how each of these steps is achieved.

STARBURST99

The ionizing stellar radiation spectrum is generated with the `STARBURST99` code (see e.g. Levesque et al., 2010; Nicholls et al., 2012) assuming a Salpeter IMF (Salpeter, 1955)[3]. For investigating the ionization of metallic species in star-forming regions, the dominant wavelength regime is the high-energy FUV. The light at these wavelength is dominated by high-mass ($> 40M_*$) stars with short (< 5Myr) lifetimes, and therefore the fraction of ionizing photons incident on a HII region is a strong function of age, particularly at high metallicities (e.g. Levesque et al., 2010). Other uncertain age-dependent effects such as the mass-loss from high-mass stars will also affect the FUV output (Maeder & Conti, 1994). In this analysis, the models are generated assuming a zero-age instantaneous burst of star-formation, and as such these age dependent effects do not affect the output FUV radiation field. The zero-age model is clearly an approximation since it is unlikely all observed HII regions are produced by instantaneous star-bursts, however this approximation has been found to best reproduce the line ratios of

[3]Kewley et al. (2013a) note the choice of IMF does not significantly affect the emission line ratios output in the models

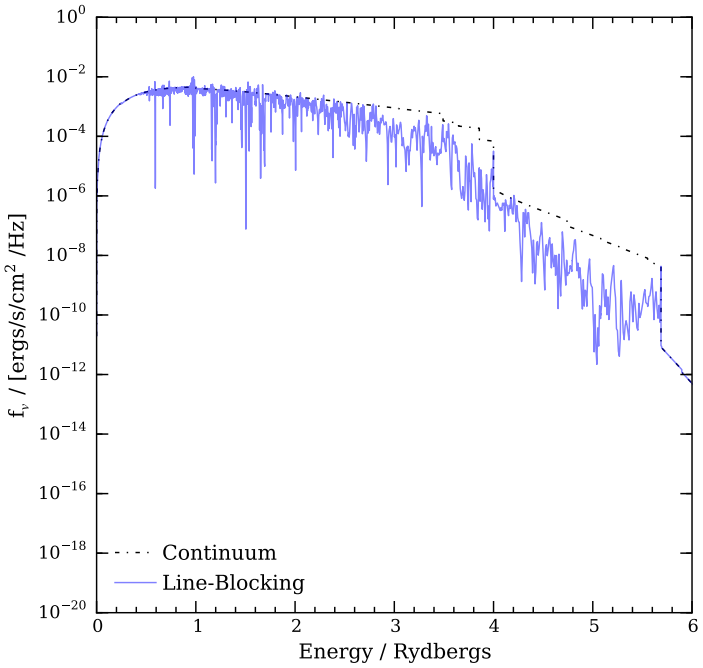

Figure 4.6 *An example of the FUV spectrum emitted from a hot, high-mass star ($T_{\rm eff}$ = 45000K) including the effects of metal line opacity from the Pauldrach et al. (2001) stellar atmosphere models. The black dotted line represents the continuum emission from the star, the solid blue line shows the emitted spectrum after passing through the stellar atmosphere. The absorption of photons due to metal opacity is clearly discernible.*

the SDSS abundance sequence (Dopita et al., 2013).

Metal opacities of the stellar atmospheres are accounted for using the Pauldrach/Hiller models (Hillier & Miller, 1998; Pauldrach et al., 2001). Metals in stellar atmospheres are ionized by the stellar FUV radiation, and act to 'block' a fraction of the energy in the stars spectrum, thus softening the radiation incident on HII regions (Snijders et al., 2007). This effect is sometimes referred to as line-blanketing, or line-blocking. Fig. 4.6 shows an example of a FUV spectrum of a high-mass, hot-star ($T_{eff} = 45000$K) from the Pauldrach et al. (2001) models where this effect is clearly visible. The inclusion of more sophisticated modeling of stellar atmosphere effects is one of the major improvements that have been made in the decade since the first detailed photoionization models of star-forming regions were computed (e.g. in Kewley et al., 2001).

MAPPINGS IV

The gas surrounding the ionizing radiation field is modeled using the photoionization code Mappings IV (Binette et al., 1985; Dopita et al., 2013). The physical properties of the gas are defined by the element abundance, dust depletion factors, geometry, density structure and electron temperature distribution. At solar metallicity the element relative abundances ratios are taken from Asplund et al. (2005) and all non-solar metallicities are defined relative to this abundance set. With the exception of helium and nitrogen, all α elements are assumed to scale linearly with metallicity. Helium abundance in the ISM is enhanced due to the effects stellar yields as in Pagel et al. (1992) (possibly due to increased mass loss during the hydrogen/helium burning phase of stellar evolution), and the nitrogen abundance follows the primary-secondary abundance phases as measured by Mouhcine & Lançon (2002) and Kennicutt et al. (2003). Some fraction of a given element can be locked up in dust grains in the ISM and thus the measured abundance would be an underestimation of the total abundance, to correct for this the models use the dust depletion factors taken from Groves et al. (2004).

A spherical nebular geometry is assumed with an electron temperature of $\sim 10^4$K, or equivalently an electron density of 10-30 cm^{-3}. The electron temperature distribution is modeled as a kappa function (as opposed to Stefan-Boltzmann) as this has been recently found to be a more realistic representation of the distribution in astrophysical environments (Nicholls et al., 2012). The code propagates the input ionizing radiation field through this simulated ISM and

calculates the photoionization, recombination and collisional excitations at small steps through the nebula until the point at which the Hydrogen gas is recombined, finally outputting an optical spectrum from which the emission line ratios can be calculated.

With this set of input parameters, the star-forming abundance sequence of SDSS galaxies can be recovered (see Fig. 1 of Kewley et al. (2013a)). This abundance sequence serves as the zero-point for the physical parameters of the star-forming population, from this abundance sequence one can estimate the typical metallicity, ionization parameter and ISM pressure of star-forming galaxies in the local Universe. Below I will describe how the redshift-evolution of these parameters is parameterized in the models.

4.4.2 Gas-Phase Metallicity Evolution

To account for the evolution of the gas-phase chemical abundance a prescription is taken from the cosmological hydrodynamic simulations of Dave et al. (2011b,a) using the GADGET-2 code (Springel, 2005b) in a ΛCDM cosmology. These simulations take into account gas inflows and outflows, cooling and heating, and star-formation processes between z = 3 and z = 0 for galaxies with $M_* > 10^9$ $M_\odot$. Outflows in the simulations are driven by star-formation and a variable mass-loading factor, referred to as momentum-driven winds. Kewley et al. (2013a) fit a 3rd order polynomial to the change in chemical abundance (Δlog(O/H)) from the Dave et al. (2011b,a) models between z = 0 and an arbitrary redshift z given by:

$$\Delta\log(\mathrm{O/H}) = -0.0013 - 0.2287z + 0.0627z^2 - 0.0070z^3 \tag{4.2}$$

This equation clearly assumes a mass-invariant metallicity change for galaxies with $M_* > 10^9$ $M_\odot$, and this may be a simplistic assumption. However in Fig. 4.7 I show that this evolution is a reasonable parameterization of the global metallicity evolution from z = 0 to z = 2. In this figure I take three samples: the SHELS (N $\sim$ 25,000 galaxies) and DEEP-2 (N $\sim$ 50,000 galaxies) samples using publicly released data from Zahid et al. (2013) at z = 0.3 and z = 0.8 respectively, and the z $\gtrsim$ 2 3D-*HST* sample from the previous chapter (and Cullen et al., 2014). For each sample the metallicity is measured using the Kobulnicky

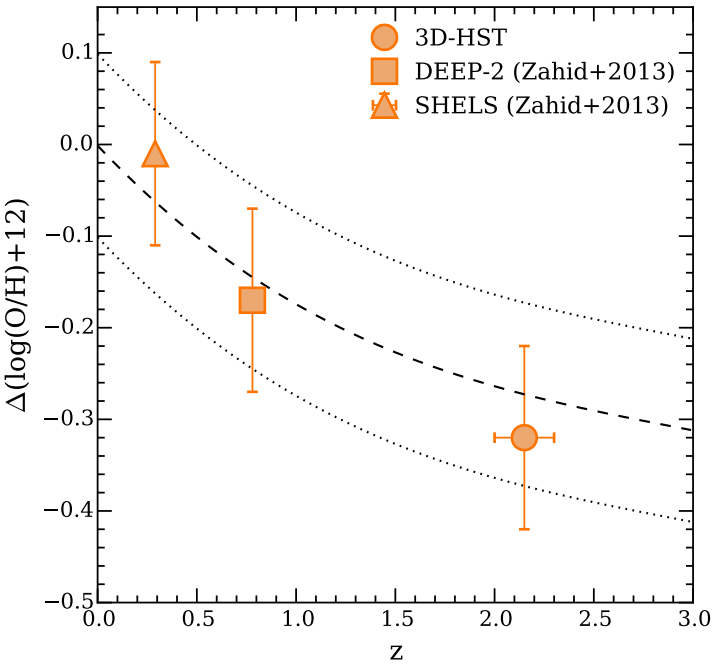

Figure 4.7 *Plot showing the assumed redshift evolution of the oxygen abundance used in the [OIII]/Hβ evolution models as described in the text. This evolution is taken from the cosmological hydrodynamic simulations of Dave et al. (2011b,a) and is shown as the black dashed line, with the dotted line representing the ∼ 0.1 dex error. The three data points are from observations (triangle - SHELS data from Zahid et al. (2013); square - DEEP2 data from Zahid et al. (2013); circle - 3D-HST data from Cullen et al. (2014)) with metallicities measured using the Kobulnicky & Kewley (2004) calibration.*

& Kewley (2004) calibration[4] (KK04) and all samples are cut to contain only galaxies with $M_* > 10^9\ M_\odot$. The z = 0 reference is taken as the average of the metallicity of the SDSS sample described above. Each point shows the average and standard deviation of the metallicity difference across the full sample and these agree with the parameterization from Dave et al. (2011b,a) within the errors. Therefore, I conclude that equation 4.2 gives a reasonable prescription for the global metallicity evolution up to z = 3. A similar conclusion is also reached by Yuan et al. (2013).

4.4.3 Ionization Parameter and ISM Pressure Evolution

The evolution of the ISM pressure is parameterized by:

$$P/k = 2.518\,\mathrm{x}\,10^6(z - 0.07) + (P/k)_{z=0}. \tag{4.3}$$

Where P is the mean ISM pressure and k is the Boltzmann constant. In HII regions the electron temperature of the ionized gas is $\sim 10^4$K (see Dopita et al., 2006, for a discussion) and the ISM pressure is a direct proxy for the electron density via $n_e = \frac{P}{T_e k}$. Therefore, local HII regions have a typical ISM pressure of log(P/k) = 5.0 and this equation 4.6 represents an approximate two order of magnitude increase from the ISM pressure at $z = 0.07$ (mean redshift of the SDSS) to $z = 4$. Two orders of magnitude is perhaps an extreme increase in ISM pressure and realistically provides an upper limit to the ISM pressure evolution with redshift. Indeed, in a recent work Shirazi et al. (2014b) find evidence for a median factor ~ 10 increase in ISM pressure between z = 0 and z = 3.

The evolution of the ionization parameter is modeled by an order of magnitude increase in the same redshift range, parameterized by:

$$\log(U) = 0.254(z\ -\ 0.069) - \log(U)_{z=0}. \tag{4.4}$$

Because the ionization parameter is decoupled from the electron density and separately constrained in these models, it can be thought of as the number of hydrogen ionizing photons incident on a unit area of the ISM per second. Such increases in the ionization parameter with redshift have been hinted at by previous studies (e.g. Nakajima & Ouchi, 2014).

[4]A detailed description of this method is given in Sec. 4.6.

In the above equations, the terms $\log(U)_{z=0}$ and $(P/k)_{z=0}$ are, respectively, the ionization parameter and ISM pressure at $z = 0$ measured from SDSS galaxies. As discussed in Section 4.5, line luminosity completeness limits must be accounted for to ensure an accurate comparison of different datasets spanning a large redshift range. Therefore, the models can be run assuming different luminosity thresholds for the [OIII] and/or Hβ emission lines; $\log(U)_{z=0}$ and $(P/k)_{z=0}$ are then calculated from the SDSS sample for the subset of galaxies that adhere to a given luminosity threshold.

To explore the evolution of the [OIII]/Hβ line ratios with redshift four different scenarios are envisaged: (1) constant ISM pressure or ionization parameter (i.e. purely chemical abundance evolution), (2) the ISM pressure only evolves with redshift, (3) the ionization parameter only evolves with redshift, (4) the ISM pressure and ionization parameter evolve with redshift[5].

4.5 Redshift Evolution of [OIII]/Hβ

I now compare the observed redshift evolution of the [OIII]/Hβ ratio to the theoretical models described above in each of the four scenarios. The models are run for [OIII] luminosity limits of $\log(L_{[OIII]}) \geq 41.87$, 41.77 and 41.70 as discussed above. In the four main datasets I utilize in the comparison (SDSS, 3D-*HST*, AMAZE/LSD, Holden et al. (2014)), I have selected the subset of each sample which adheres to the luminosity threshold discussed above to ensure consistency. As mentioned in Section 5.2, because it is not flux-calibrated, I cannot include the DEEP2 sample here because I cannot apply a cut in line luminosity. Figure 4.8 shows the [OIII]/Hβ vs. redshift relation for the four samples which, when combined, span the redshift range $0 < z < 4$. The SDSS data points are not explicitly shown in Fig. 4.8 but can be inferred from the $z = 0$ origin of all the models.

Each panel in Fig. 4.8 shows the results for each of the different luminosity cut in [OIII]. In each panel the four model scenarios are plotted where the initial ionization parameter (log(U)) and ISM pressure (P/k) has been calculated for the subset of SDSS galaxies which adhere to the stated luminosity threshold. The 3D-*HST*, AMZAZE/LSD and H14 data are also cut to the given luminosity threshold. For the 3D-*HST* data I measure the [OIII]/Hβ ratio from both an

[5]All models contain metallicity evolution according to equation 4.2.

average and median stack in three redshift bins; for the AMAZE/LSD and H14 data I simply plot the average and median values of the [OIII]/Hβ ratios at the median redshift of the remaining sample. All averages are shown as filled symbols and all medians are shown as open symbols.

The first thing to note is that all data rule out the model in which ionization parameter and ISM pressure remain constant (solid black curve), with only the metallicity of HII regions evolving with redshift. Therefore, an important result of this work is that the evolution of the [OIII]/Hβ line ratio, for the luminosity thresholds applied, cannot be accounted for purely by the evolution of metallicity. The observed line ratios at high redshift are affected by the evolution in other physical parameters in HII regions, and this will have a profound effect on measuring metallicities at high redshift (see Sec. 4.7 for a thorough discussion of this issue). Again we note that this result relies on assuming metallicity evolution according to the models of Dave et al. (2011b,a). However, as illustrated in Fig. 4.7 the metallicity defined by these models is comparable with metallicity measurements made using the KK04 calibration (see also the results of Chapter 5).

The data also strongly disfavour the model in which ISM pressure evolves and ionization parameter remains constant (pink dashed curve). For the most robust scenario (90% completeness) only one data point is within 1σ of this model, and across all panels the data are consistently in better agreement with either of the two remaining models. Overall, P/k evolution model is not sufficient to explain the majority of measured line ratios and, despite some measurements being formally consistent within 1σ, all are consistently systemically higher than the P/k evolution model prediction.

The remaining two models - ionization parameter only evolution (blue dot-dashed curve) and ionization parameter + ISM pressure evolution (yellow dotted curve) - are both strongly favoured but are difficult to distinguish with the quality of data currently available. However this still permits us to conclude from the models that, at a minimum, the ionization parameter of HII regions is evolving with redshift, where to recall, the ionization is defined as the number of hydrogen ionizing photons incident on a unit area of the ISM per second. It is not, at present, possible to conclusively say whether this is accompanied by an increase in the ISM pressure. Particularly, in the redshift range $1.5 < z < 2.5$ covered by the 3D-*HST* data, the two models are indistinguishable given the size of the uncertainties. At $z > 3$ the models are more separated and, over all

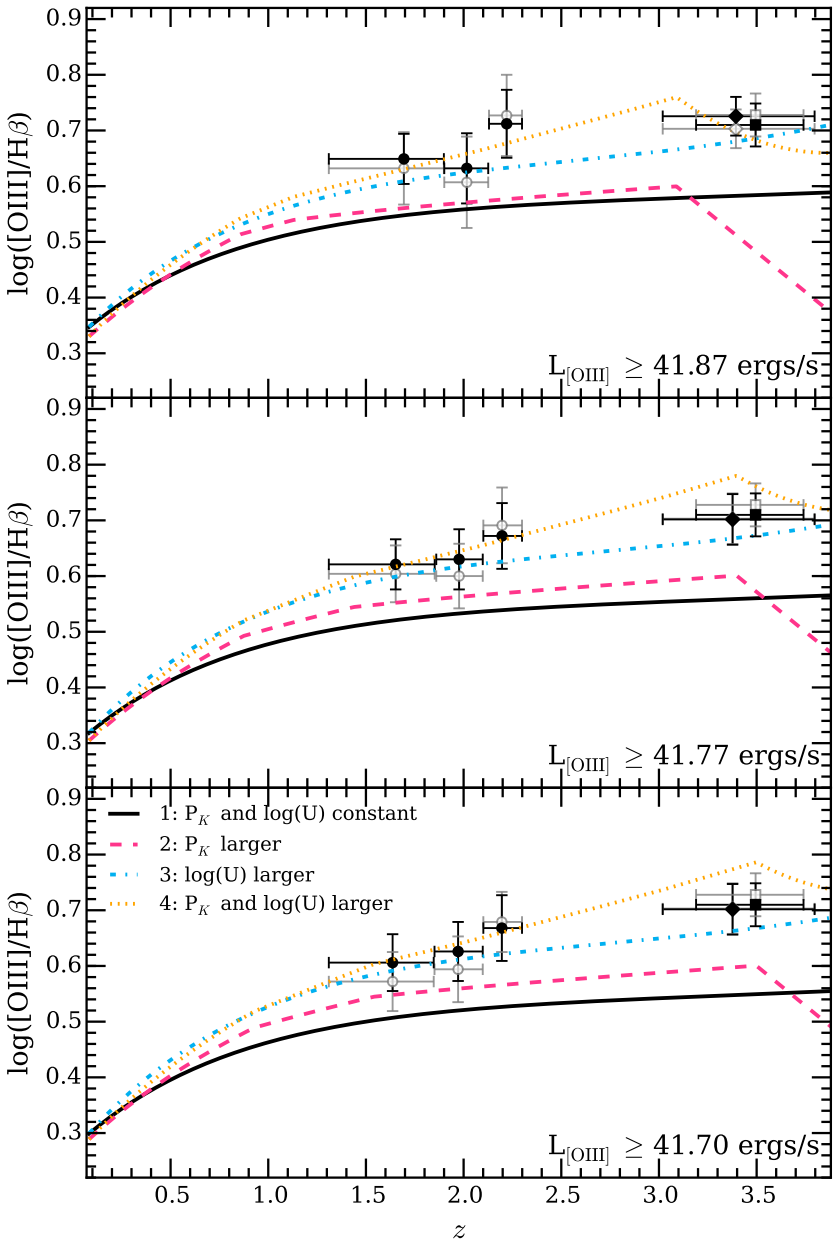

Figure 4.8 *Showing the comparison between the observed evolution of the [OIII]/Hβ ratio as a function of redshift and the theoretical models described briefly in Sec. 4.4. The circles represent the 3D-HST sample, the diamonds the AMAZE/LDS data and the squares the Holden et al. (2014) sample. The open and filled symbols correspond to an average and median stack, respectively (see text for details).*

luminosity limits, the AMAZE/LSD and Holden et al. (2014) data appear to favour ionization parameter only evolution, although at $L_{[OIII]} > 41.87$ the models are again indistinguishable. In Sec. 4.7 I will discuss ways in which this situation can be improved with future observations.

To summarize, the data rule out the scenario in which the evolution of the [OIII]/Hβ line ratio is purely driven by metallicity evolution. Instead it requires, in addition, an evolution in the ionization parameter to higher values with redshift, and potentially an increase in ISM pressure at the same time.

4.6 Scatter in the [OIII]/Hβ vs. Redshift Relation

I have also investigated the scatter about the overall [OIII]/Hβ vs. redshift relation. Naively one would expect to see some scatter about the relation as, at any given redshift, a distribution of metallicity, ionization parameter and ISM pressure around the population average should cause a distribution in [OIII]/Hβ. In this section we explore the distribution of [OIII]/Hβ values in SDSS, DEEP2, 3D-*HST*. The AMAZE/LSD and Holden et al. (2014) data are excluded from this analysis due to the small sample sizes. I revert to using the full samples in this section as I am no longer comparing evolution as a function of redshift and therefore do not have to worry about redshift selection effects.

Figure 4.9 shows the mass-metallicity and mass-ionization parameter relationships for the full SDSS sample in the mass range $9.0 < \log(M/M_{\odot}) < 11.0$. The values of metallicity and ionization parameter were calculated using the calibration of Kobulnicky & Kewley (2004) (KK04). The calibration is based on the theoretical models of Kewley & Dopita (2002) and uses the following two emission line ratios:

$$R23 = \frac{[OII]\lambda 3727 + [OIII]\lambda 4959,5007}{H\beta}, \tag{4.5}$$

$$O32 = \frac{[OIII]\lambda 4959,5007}{[OII]\lambda 3727}. \tag{4.6}$$

R23 and O32 are both dependent on metallicity and ionization parameter; R23 is the more metallicity sensitive ratio while O32 is more sensitive to ionization parameter. The main advantage of using R23 to measure oxygen abundance is that it incorporates both ionization stages of oxygen and is therefore a relatively direct probe of the O/H ratio, this is in contrast to, for example, the [NII]/Hα

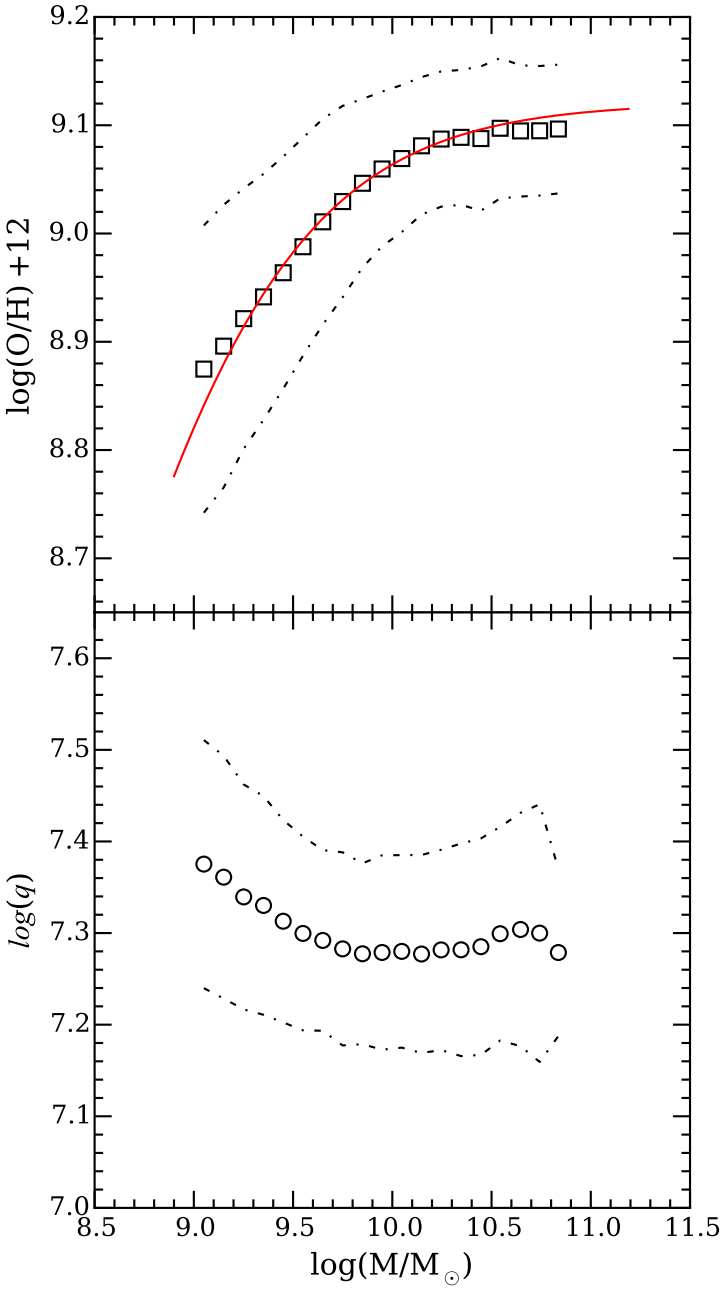

Figure 4.9 *Plot showing the mass-metallicity relation (top panel) and mass-ionization parameter relation (bottom panel) for the SDSS sample using the Kobulnicky & Kewley (2004) calibration in* $\Delta\log(\mathrm{M}/\mathrm{M}_\odot) = 0.1$ *mass bins. The red line in the top panel shows the fit to the SDSS mass-metallicity relation from Zahid et al. (2013).*

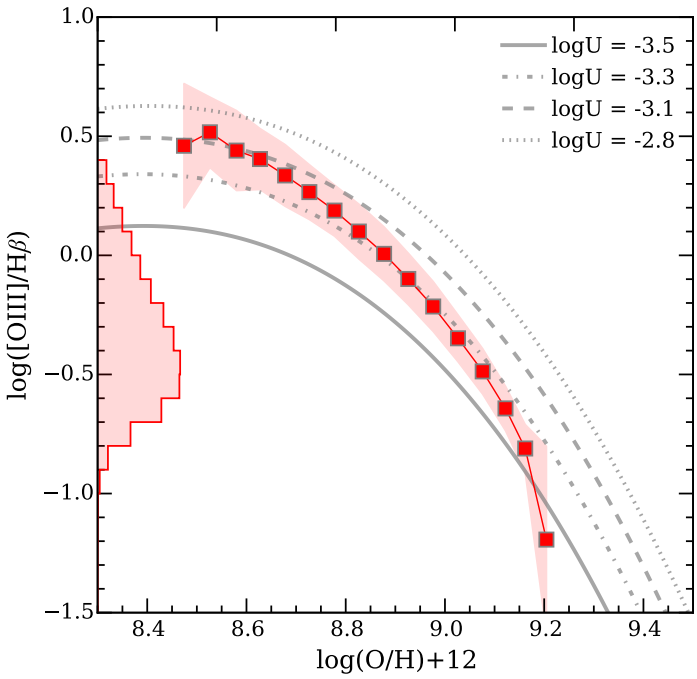

Figure 4.10 *The relationship between metallicity and [OIII]/Hβ ratio for SDSS galaxies. The red squares show the mean value of [OIII]/Hβ in 0.05 dex wide bins of metallicity, the shaded region encloses ±1 standard deviation in the bins. The histogram on the y-axis shows the distribution of the individual [OIII]/Hβ ratios. The grey lines show models of the [OIII]/Hβ vs metallicity relation for different values of ionization parameter (U) based on the MAPPINGS IV photoionization models (Lisa Kewley private communication).*

diagnostic which is sensitive to uncertainties on the N/O vs O/H relation (Pérez-Montero & Contini, 2009). The main disadvantages of the R23 ratio is its sensitivity to the dust attenuation due to the large wavelength spread of the lines involved, and the stellar absorption correction of the Hβ line. R23 is also double-valued with respect to metallicity and therefore there are two possible solutions: the 'lower' metallicity branch and the 'higher' metallicity branch. In practice one must choose from which branch a galaxy is most likely on. Here I have followed the method of Kewley & Ellison (2008) by using the [NII]/[OII] ratio to discriminate between branches, with all galaxies having [NII]/[OII]> -1.2 being upper branch and vice versa.

The KK04 calibration is given by the following equations:

$$12 + \log(\mathrm{O/H})_{\mathrm{lower}} = 9.40 + 4.65x - 3.17x^2 - \log(q)(0.272 + 0.547x - 0.513x^2), \tag{4.7}$$

and

$$\begin{aligned} 12 + \log(\mathrm{O/H})_{\mathrm{upper}} = 9.72 - 0.777x - 0.951x^2 - 0.072x^3 - 0.811x^4 \\ -\log(q)(0.0737 - 0.0713 - 0.141x^2 + 0.0373x^3 - 0.058x^4), \end{aligned} \tag{4.8}$$

where $x \equiv$R23. The ionization parameter q is given by:

$$\begin{aligned} log(q) = 32.18 - 1.153y^2 + z(-3.396 - 0.025y + 0.1444y^2) \\ x[4.603 - 0.3119y - 0.163y^2 + z(-0.48 + 0.0271y - 0.02037y^2)]^{-1}, \end{aligned} \tag{4.9}$$

where $x \equiv$O32 and $z \equiv$12+log(O/H). Thus, by combining both the R23 and O32 ratios, the KK04 calibration allows one to iteratively solve for the metallicity and ionization parameter of a galaxy. I note that here, unlike in the models discussed in this chapter, the ionization parameter takes it more conventional form of the ratio of number density of H-ionizing photons to that H atoms (or equivalently free electrons assuming a fully H-ionized nebula). In a future work it may be worth exploring this parameter further.

In Fig. 4.9 I have applied the KK04 calibration to the SDSS galaxy sample and show both the metallicity and ionization parameter as a function of stellar mass. These correlations have been noted by many previous studies (e.g. the well-known SDSS mass-metallicity relationship from Tremonti et al. (2004)) and are shown here only to illustrate the distribution in the parameters across the SDSS sample. The top panel of Fig. 4.9 also shows the fit to the SDSS MZR (using the KK04 calibration) from Zahid et al. (2013), clearly in excellent agreement with

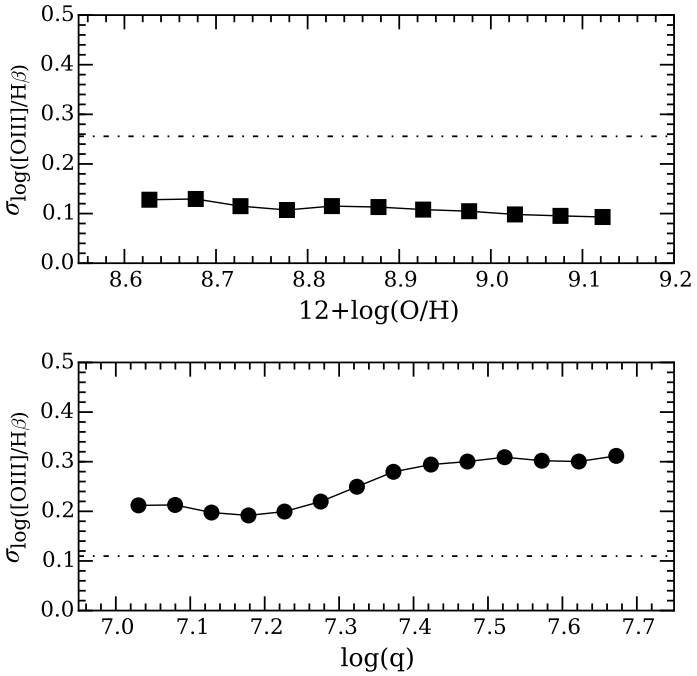

Figure 4.11 *Standard deviation in the [OIII]/Hβ ratio as a function of metallicity (top panel) and ionization parameter (bottom panel). The dot-dashed line in each panel represents the mean value of the standard deviation from the other panel.*

my results. The figure illustrates that variations in metallicity and ionization parameter as a function of mass are both evident. Consequently these parameter distributions will result in a distribution in the [OIII]/Hβ ratio.

Fig. 4.10 illustrates how metallicity affects the [OIII]/Hβ ratio. A correlation is clearly evident, with [OIII]/Hβ decreasing towards higher metallicity due to the increased cooling efficiency of metal-rich nebula leaving fewer hot electrons capable of collisionally exciting oxygen ions. Over the $\sim$ 1 dex range in metallicity the [OIII]/Hβ ratios span a $\sim$ 1.5 dex range of values. Also plotted in Fig. 4.10 is the [OIII]/Hβ vs metallicity relationship as a function of ionization parameter from the latest MAPPINGS IV photo-ionization models (Lisa Kewley private communication), here the ionization parameter is given in its dimensionless form ($U \equiv q/c$) and from the figure it can be seen that the SDSS galaxies are roughly contained within the range of values previously reported for local galaxies and HII regions (-3.2 $<$ log U $<$ -2.9; Dopita et al., 2013; Moustakas et al., 2010).

Similarly one could create an [OIII]/Hβ vs. ionization parameter plot. Since

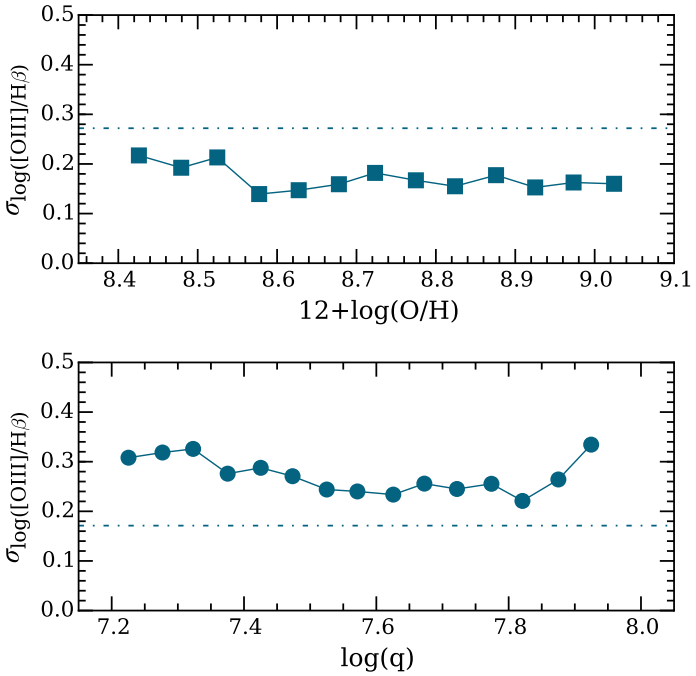

Figure 4.12 *Same as Fig. 4.11 but using the DEEP2 galaxy sample at* $z = 0.78$.

both metallicity and ionization parameter both vary across the SDSS sample, and independently affect the [OIII]/Hβ ratio, the final [OIII]/Hβ distribution will be linked to the distribution of both parameters. However, it is not immediately obvious which of the two is the main driver of this final distribution. I investigated this using the observed scatter in the [OIII]/Hβ ratio as a function of both metallicity and ionization parameter, as illustrated in Fig. 4.11. In each case I have binned the SDSS galaxies in 0.05 dex width-bins of each parameter, and plotted the standard deviation of the [OIII]/Hβ ratio in each bin. The figure illustrates that the scatter in [OIII]/Hβ ratios as a function of ionization parameter is greater than the scatter as a function of metallicity, by ~ 0.15 dex (or equivalently a factor 1.4). This is evidence that, though both metallicity and ionization parameter independently affect the range of [OIII]/Hβ values observed, the distribution is affected more strongly by the range in metallicities of the SDSS sample, rather than the range of ionization parameters.

4.6.1 DEEP2 Sample

I applied the sample technique to the DEEP2 galaxy sample at $z = 0.78$. For the DEEP2 sample the R23 and O32 line ratios are determined from ratios of equivalent widths as opposed to line fluxes. However, as mentioned previously. Zahid et al. (2011) have shown that these equivalent width ratios are consistent with line flux ratios for a sample of 102 galaxies from the Nearby Field Galaxy Survey (NFGS; Jansen et al., 2000). Fig. 4.12 is the same as Fig. 4.11 using the DEEP2 dataset, and the same trend is apparent: the scatter in the [OIII]/Hβ ratio is larger at fixed ionization parameter, suggesting that the [OIII]/Hβ distribution is again governed for the main part by the distribution in metallicities.

The combination of the SDSS and DEEP2 data suggest a scenario in which the evolution of the [OIII]/Hβ with redshift is driven by an evolution towards more extreme ionization conditions, whereas at any given redshift, the distribution of [OIII]/Hβ ratios throughout the population is driven primarily by the spread in metallicity across galaxies.

4.6.2 3D-*HST* Sample

Though a similar analysis is not possible with the 3D-*HST* data due to the low S/N of the individual spectra, hints towards a similar trend can be found by splitting the sample into stellar mass bins at a given redshift, and measuring the [OIII]/Hβ ratio of the stacked spectra. Under the assumption that the mass-metallicity relationship holds at $1.3 < z < 2.3$, and assuming from the SDSS and DEEP2 analysis that the [OIII]/Hβ scatter is more metallicity-dependent, then a stellar mass split will be equivalent to a metallicity split and higher mass galaxies will have correspondingly lower [OIII]/Hβ ratios.

In Fig. 4.13 I have split the full 3D-*HST* sample into three bins of stellar mass and then, in each stellar mass bin, split into two redshift bins. I have then stacked the spectra in each of the six bins and measured the [OIII]/Hβ as described above. As can be seen from the figure there is indeed a trend, in both redshift bins, for a decrease in the [OIII]/Hβ ratio at larger stellar masses indicating a lower metallicity (see Fig. 4.10). I have checked that this observation is not biased by an evolution in [OIII] luminosity across the mass bins, which as illustrated in Fig.

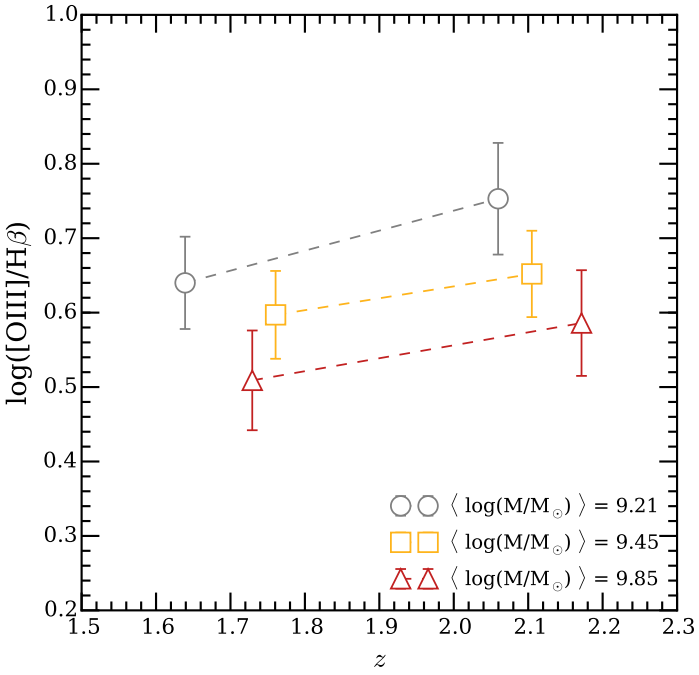

Figure 4.13 *Showing the scatter in [OIII]/Hβ ratios as a function of stellar mass in two redshift bins for the 3D-HST data.*

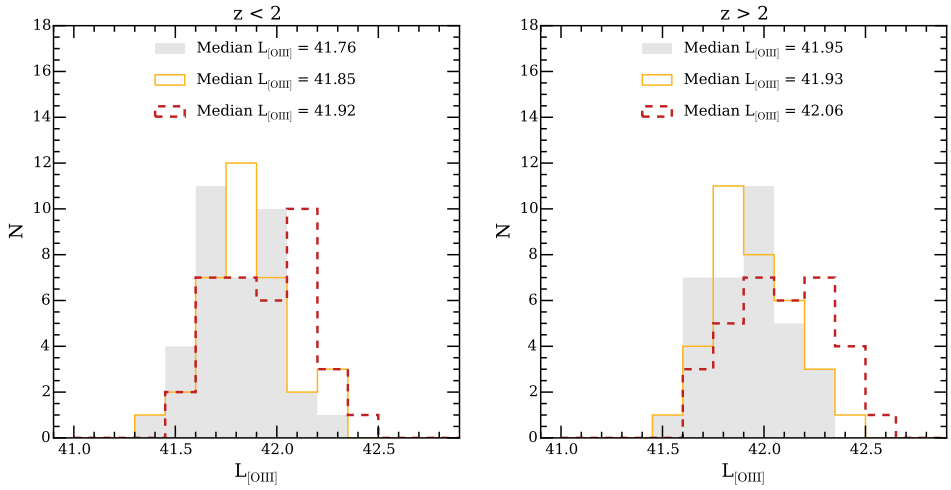

Figure 4.14 *Distributions of [OIII] luminosity in the three stellar mass bins and two redshift bins from Fig. 4.13. The left panel shows $z < 2$ galaxies while the right panel shows $z > 2$ galaxies. The colors representing the different masses correspond to the colors used in Fig. 4.13.*

4.4, could result in an artifical evolution in [OIII]/Hβ. Fig. 4.14 compares the distribution of [OIII] luminosities in each mass bins for the two different redshifts. It is clear that the variation in [OIII]/Hβ ratios with stellar mass is not driven by [OIII] luminosities. Firstly, the difference in median [OIII] luminosities translates into a Δ[OIII]/Hβ of $\sim$ 0.05 dex from equation 4.1, whereas the range in Fig. 4.13 is of the order 0.15 - 0.2 dex. Secondly, the highest mass bins at both redshift have higher median [OIII] luminosities whilst having lower [OIII]/Hβ, therefore the spread in [OIII]/Hβ with mass is underestimated if anything. However, more detailed analysis of the [OIII]/Hβ scatter at $z > 1.3$ will have to wait until deeper, high-S/N data becomes available.

4.7 Discussion

In this section I will discuss some of the practical and theoretical implications of the results presented here, as well as how our results compare with the recent literature. If the evolution in ionization parameter and/or ISM parameter in star-forming regions at high redshift is real, this will have important consequences both for how strong-line ratios are applied in high redshift galaxies to measure physical parameters and, perhaps more fundamentally, on our theoretical understanding of the nature of HII regions and the stars that power them. I will also relate this discussion to the results presented in Chapter 3.

4.7.1 Implications for metallicity calibrations

As discussed in the introduction, at high redshift the strong line ratios (e.g. [NII]/Hα, [OIII]/Hβ, R_{23}) are used as a proxy for galaxy metallicity since, in most cases, only these lines are detected given the signal-to-noise ratio of typical observations. Direct methods for measuring metallicities, based on measuring the temperature of star-forming regions (T_e method see e.g. Andrews & Martini, 2013), are extremely challenging at high redshift because of the low luminosity of the required emission lines (e.g. the auroral [OIII]λ4363 line).

Therefore, to use strong line ratios as metallicity diagnostics one must first calibrate them against a true measure of the metallicity. This can be done using either the T_e method (e.g. Pettini & Pagel, 2004), detailed photoionization modeling (e.g. Kobulnicky & Kewley, 2004), or a mixture of both (e.g. Maiolino

et al., 2008). The result of the process is most often a functional fit to the observed relationship between a given line ratio and metallicity which can be applied to high-z galaxies. I focus our discussion here on the empirical metallicity calibrations, which I define as being based in some part on the spectra of local galaxies.[6] These calibrations implicitly assume the physical conditions (e.g. ionization parameter, ISM pressure) typical of star-forming galaxies at $z \sim 0$, and it is important to understand how an evolution of these parameters at high-z, as implied in Section 4.5, could bias such calibrations.

I take as my example the Maiolino et al. (2008) (M08) calibration since relates to the previous chapter investigating the FMR, and is commonly applied to high redshift samples. However, the results should in general apply to any empirically based metallicity calibration. Indeed, see Steidel et al. (2014) for a similar discussion using the Pettini & Pagel (2004) (PP04) calibration to compare metallicities derived from the [NII]/Hα ratio, to those derived from the ([NII]/Hα)/([OIII]/Hβ) ratio. It is possible to illustrate a similar offset for the M08 calibration (Figure 4.15) by utilizing the recent KBSS-MOSFIRE dataset of galaxies at $2.0 \leq z \leq 2.6$ presented in Steidel et al. (2014)[7]. Figure 4.15 shows a similar trend to that observed by Steidel et al. (2014): metallicities measured from O/H are systematically offset to lower values than metallicities measured from N/H. The best-fitting line to the data in Figure 4.15 implies an offset of 0.35 dex for the KBSS-MOSFIRE sample.

This results relates directly back to the observations from Chapter 3 where I found a $\sim$ 0.3 dex offset between the 3D-*HST* metallicities (based on O/H measurements) and the Erb et al. (2006b) measurements (based on N/H measurements), in the sense that metallicities inferred from O/H are systematically offset to lower values. Indeed, if the 3D-*HST* O/H-based metallicities in Chapter 3 where increased by 0.35 dex this would bring them into much better agreement with the Erb et al. (2006b) data and also the FMR predictions. However, given that this offset is driven by changes in ionization conditions in high redshift galaxies, and both ratios are sensitive to these ionization conditions, it is not sufficient to simply correct one or the other for an offset in this way, since the intrinsic values for metallicities derived from

[6]The discussion does not in principal apply to purely theoretical metallicity calibrations (e.g. Kewley & Dopita, 2002; Kobulnicky & Kewley, 2004), unless these theoretical models assume values of ionization parameter and ISM pressure typical of $z \sim 0$ star-forming galaxies.

[7]This figure is essentially a re-production of Figure 6 from Steidel et al. (2014) but using a different metallicity calibration (M08 as opposed to PP04) and slightly different line-ratio diagnostics.

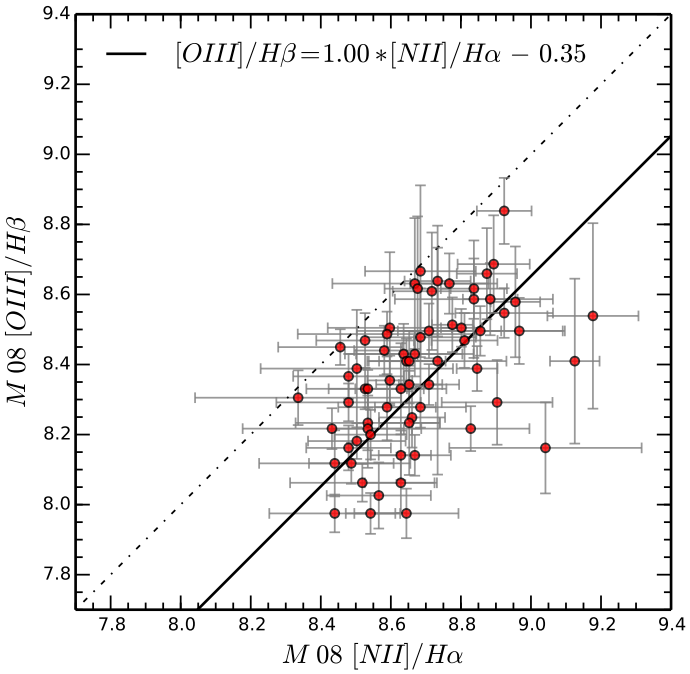

Figure 4.15 *A comparison of the inferred metallicity from the Maiolino et al. (2008) metallicity calibration using the [OIII]/Hβ and [NII]/Hα line ratio diagnostics. The red data points are taken from the KBSS-MOSFIRE sample of Steidel et al. (2014). The black dash-dot line shows the 1:1 relation. The black solid line shows the best-fitting linear equation to the data, the equation of this line is given in the legend in the top left of the figure.*

both ratios is likely to be incorrect. Instead, one must solve for both ionization state and metallicity simultaneously in order to get an un-biased measurement metallicity measurement. This is possible using the KK04 calibration describe above, and I will explore this issue in much greater detail in Chapter 5. Finally, it is worth pointing out that this results implies that it is not possible to make any reliable inferences about the FMR at high redshift using local empirical calibrations.

In Figure 4.16 I show how this metallicity diagnostic offset is directly related to the offset the KBSS-MOSFIRE galaxies in the BPT diagram. As mentioned in the introduction this BPT offset is a commonly observed feature of high redshift sample. The dashed black line is the relationship between [OIII]/Hβ and [NII]/Hα inferred from the M08 calibration which, by design, follows the star-forming galaxy population sequence of SDSS galaxies since these galaxies were used to build the calibration. The solid black line shows this relationship when applying the conversion equation shown in Figure 4.15 to the M08 calibration, this line is clearly offset from the BPT $z \sim 0$ sequence and is consistent with the position of the KBSS-MOSFIRE sample (grey points with error-bars, best-fitting relationship shown by orange dot-dashed line). This figure illustrates how the offset of $z \sim 2.3$ galaxies in the BPT diagram, and the offset metallicities inferred from different line diagnostics using locally metallicity calibrations, are directly related.

Example: the impact of ionization parameter metallicities inferred from [OIII]/Hβ

I now investigate directly how an evolution in the ionization parameter only would theoretically affect the measured metallicity using the [OIII]/Hβ line ratio. I note the [OIII]/Hβ ratio is not a commonly used on its own to infer metallicity, however the ratio is often used in combination with other line ratios (e.g. [NII]/Hα) or is contained within other diagnostics (e.g. $R23$). The discussion here is mainly to illustrate how not accounting for the ionization parameter can affect measurements of metallicities from line ratios.

The left panel of Figure 4.17 shows an [OIII]/Hβ metallicity diagnostic (as discussed in Section 4.6) for four different values of the ionization parameter. It can be seen that depending on the value of the ionization parameter adopted, the metallicity solution for a given [OIII]/Hβ ratio can be significantly different.

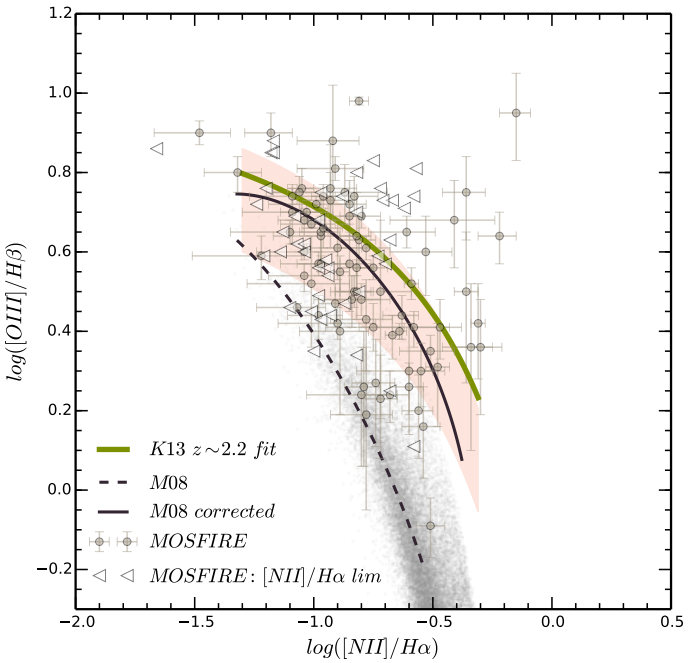

Figure 4.16 *Comparing the position of the KBSS-MOSFIRE sample (Steidel et al., 2014) in the BPT diagram with various model predictions. The grey points with error-bars show the KBSS-MOSFIRE sample with detection in all emission lines, the grey triangles show the galaxies in this sample with only a lower limit on the [NII]/Hα ratio. The black dashed line shows the predicted position of galaxies in this plane using the M08 metallicity calibration, this is consistent with the population of $z \sim 0$ star-forming galaxies (black points). The black solid line shows the same line when applying the transformation given the Figure 4.15 to the M08 calibration. The shaded orange region shows the $\pm 1\sigma$ intrinsic dispersion of the best-fitting BPT sequence to the KBSS-MOSFIRE data. The olive solid line shows the theoretical upper-limit of the BPT sequence at $z \sim 2.3$ from the Kewley et al. (2013a) models.*

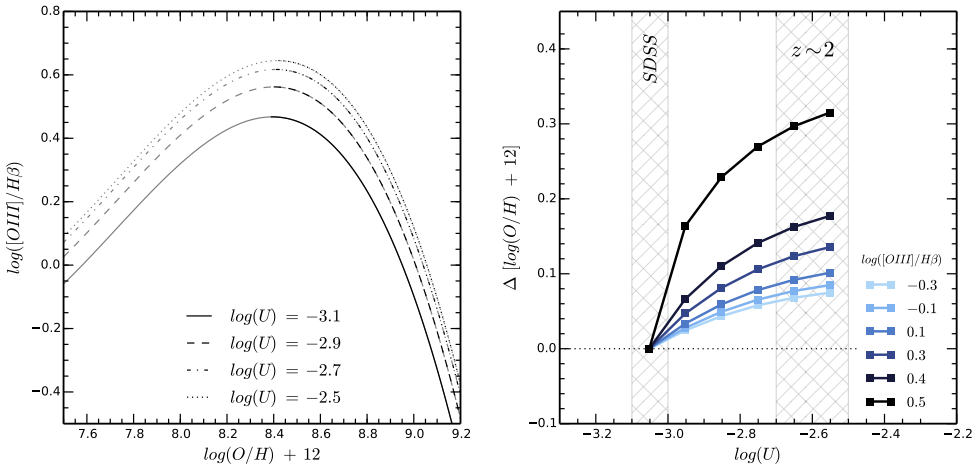

Figure 4.17 *Showing the difference in inferred metallicity, as a function to ionization parameter and [OIII]/Hβ ratio, for the Maiolino et al. (2008) [OIII]/Hβ metallicity calibration and a calibration which takes into account the effect of metallicity and ionization parameter on the [OIII]/Hβ ratio. (Kewley et al. in prep.). The blue shaded lines show different values of the [OIII]/Hβ ratio, these values are listed in the legend in the bottom right. The grey shaded regions show values of the ionization parameter typical of our SDSS sample and our $z \gtrsim 2$ sample from 3D-HST.*

This is illustrated in the right-hand panel of Fig. 4.17 where I show the difference in inferred metallicity as a function of ionization parameter for the [OIII]/Hβ diagnostic. The difference is measured relative to a reference value of $log(U) = -3.05$ (median value inferred for the SDSS sample in Section 4.6) and is only calculated for the upper branch solutions ($log(O/H) + 12 \gtrsim 8.4$). The maximum ionization parameter ($log(U) \sim -2.6$) is typical of current measurements of $z \sim 2$ galaxies both from the 3D-*HST* spectra at $z > 2$, and the $z \sim 2 - 3$ LBGS from Nakajima & Ouchi (2014). Across the range of [OIII]/Hβ ratios shown in the figure, the inferred metallicity for a given ratio increases with increasing ionization parameter. The difference is particularly pronounced for the largest [OIII]/Hβ ratios, with an offset of up to ~ 0.3 dex for $log([\text{OIII}]/\text{H}\beta) = 0.5$

Fig. 4.17 illustrates clearly that not accounting for the ionization parameter of a galaxy can have a large impact on the inferred metallicity from the [OIII]/Hβ ratio. It suggests that calibrating future metallicity diagnostics for ionization conditions will be crucial for determining un-biased measurements of galaxy metallicities at high redshift.

Improving the model constraints at high redshift

As discussed in Sec. 4.5, with the data currently available at high redshift it is not possible to robustly distinguish between the models for ionization parameter only evolution and ionization parameter + ISM pressure evolution. It is worth illustrating how this situation can be improved with future observations. As previously discussed, the theoretical curves are dependent on the luminosity thresholds applied to the SDSS data, as this determines the reference values of ISM pressure and ionization parameter used as input to the models. Fig. 4.18 shows the model evolution from z = 0 to z = 4 for four cases; the top three panels show the luminosity thresholds applied in this chapter and the bottom panel shows the model evolution when the full SDSS sample is used to calculate the initial values of the physical parameters (corresponding to a lower limit of $\log(L_{[OIII]}) \sim 40.2$ ergs/s.

It can be easily seen from Fig. 4.18 that raising the luminosity threshold makes it increasingly more difficult to distinguish between the models. There is a much larger [OIII]/Hβ separation between the models when the lower luminosity threshold of full SDSS sample is used. The figure illustrates clearly how deeper spectroscopic observation will allow a robust distinction between the two currently indistinguishable scenarios. These observations should be possible with current near-IR facilities such as KMOS and MOSFIRE and in the future with deep $z > 1$ near-IR surveys with MOONS.

4.7.2 Theoretical Implications

I now briefly discuss some of the possible theoretical explanations of the results presented here. Since our data favour models in which at least the ionization parameter increases with redshift, but cannot distinguish whether this is also accompanied by a simultaneous increase in ISM pressure, we limit our discussion to the possible causes of a higher ionization parameter.

An increased ionization parameter requires, from the models, an increased number of ionizing photons per unit area per unit time incident on the ISM. One way of achieving this is to scale the ionizing radiation field by raising the star-formation rate within a given ISM volume. It is known that the average star-formation rate of galaxies increases out to $z \sim 2$ and beyond (e.g. Pannella et al., 2014; Whitaker et al., 2012, and many more), if these stars form in similar volumes

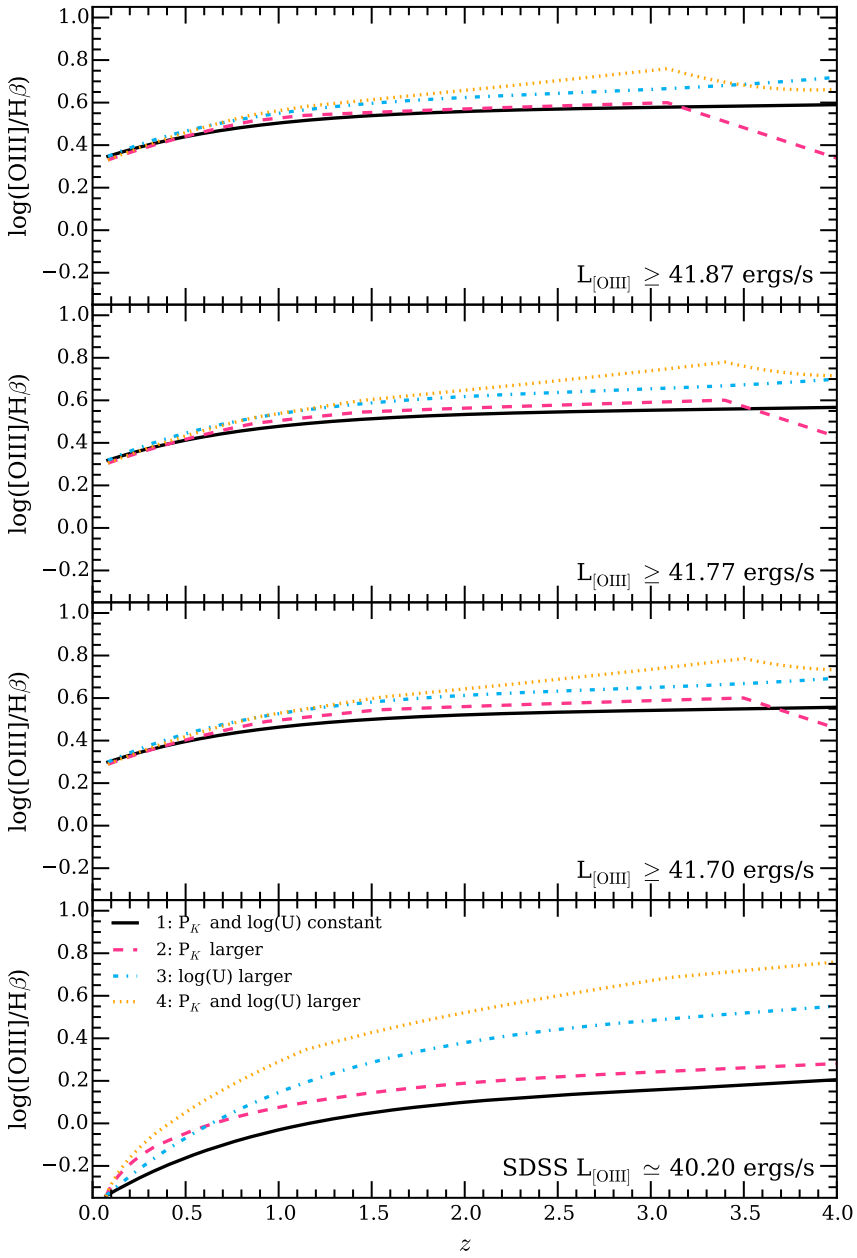

Figure 4.18 *Illustrating how the [OIII] luminosity thresholds affect the theoretical curves. In each panel the models are plotted as in Fig. 4.8. The top three panels show the various luminosity cuts applied to the data used in this chapter and the bottom panel shows the case for the lower luminosity limit of the full SDSS sample (log($L_{[OIII]}$) ∼ 40.2 ergs/s). It is clear from the figure how deeper observations will be better able to differentiate between models at all redshifts.*

to local galaxies there will be an excess of ionizing photons at high redshift and consequently a higher ionization parameter. This can be thought of as an increase in the 'volume-averaged' star-formation (or star-formation density) in galactic HII regions with redshift. Such dense star-forming clusters are commonly referred to as 'super star clusters', they have been theoretically investigated (see e.g. Elmegreen, 1998; Hopkins et al., 2013) and have been observed in local dwarf galaxies and galaxy mergers (e.g. Shioya et al., 2001; Wofford et al., 2014). However to date no comprehensive statistical study of the ionization parameter in these clusters has been made, nor any detailed investigation into their prevalence at high redshift.

An elevated ionization parameter may also be the result of a lower metallicity environment at high redshift. For example, the opacity of the stellar wind decreases with stellar metallicity and hence absorbs less ionizing photons. More photons are then available to ionize the surrounding HII region resulting in an increased ionization parameter (see Dopita et al., 2006, for a discussion).

The effective ionization parameter is also affected by the geometrical distribution of the gas in HII regions, for example clumpy HII regions allow more ionizing photons to escape and hence lower the effective ionization parameter (Nakajima & Ouchi, 2014). The difference between a radiation bounded HII region (where the nebula ends where hydrogen is completely recombined) and a density bounded HII region (where the entire nebula is ionized by the stars) is also important. In a density bounded HII region the [OIII] zone (closest to the star) will likely remain unaffected but the Hydrogen recombination zone (which extends to larger radii) could be shortened, thus resulting in an increase in the [OIII]/Hβ ratio. Some evidence exists for density bounded HII regions at high-z (see Kewley et al., 2013a, for a detailed discussion of the geometrical effects).

Finally differences in the IMF in high redshift galaxies will also affect the ionization parameter. For example a top-heavy IMF, with a greater proportion of high-mass stars, will increase the number of ionizing photons impacting on a nebula. However there is a present little evidence for a drastic evolution of the IMF across $0 < z < 4$.

4.8 Summary and Conclusions

I have investigated the [OIII]/Hβ vs redshift relation for a sample galaxies in the redshift range $0 < z < 4$ by combining data from SDSS, 3D-*HST*, AMAZE/LSD and Holden et al. (2014). I have compared the [OIII]/Hβ evolution to the theoretical models described in Kewley et al. (2013a), which account for the effects of an evolving ionization parameter and ISM pressure, in order to understand the evolution in the physical conditions of star-forming galaxies over the last ~ 11 billion years of cosmic time. I have explored how line luminosity selection limits can affect any observed trends and carefully accounted for these selection biases in all datasets. I have finally investigated the scatter about the overall [OIII]/Hβ vs. redshift trend in the SDSS, DEEP2 and 3D-*HST* datasets and discussed some of the practical and theoretical implications of the findings. Below is a summary of the results.

- I first show, using the SDSS sample, that there is a positive correlation between [OIII]/Hβ ratio and [OIII] luminosity, as pointed out by Juneau et al. (2014). This relationship could potentially bias any results since the observed evolution of the [OIII]/Hβ ratio could simply be an artifact of the increasing line luminosity threshold with redshift. Therefore I conclude that the luminosity detection limit of all samples must be carefully accounted for when comparing to models of line ratio evolution.

- I correct for any biases introduced from an [OIII] luminosity detection limit by restricting all samples to galaxies with $\log(L_{[OIII]}) > 41.87$, 41.77 and 41.70, corresponding to completeness limits in the 3D-*HST* sample of, respectively, 90%, 75% and 50%. I show that, after applying these luminosity thresholds, the 3D-*HST* stacks consistently show an increase in the [OIII]/Hβ ratio across the redshift range $1.3 < z < 2.3$. Therefore I conclude this evolution is real and unaffected by the luminosity detection bias highlighted in Juneau et al. (2014).

- I compare the [OIII]/Hβ redshift evolution to theoretical models described in Sec. 4.4 based on the models of Kewley et al. (2013a). From these models I rule out the possibility that the line ratio increase is a results of metallicity evolution or ISM pressure evolution with redshift. I conclude the line ratio evolution is best accounted by, at least, an increase in the

ionization parameter with redshift. Unfortunately the data cannot yet distinguish whether this ionization parameter increase is also accompanied by an increase in ISM pressure, though the prospects for improving this situation in the future are good. These conclusions are independent of the line luminosity limits imposed.

- I investigate the scatter about the overall [OIII]/Hβ vs. redshift relation and show that for the SDSS and DEEP2 data the distribution of [OIII]/Hβ values is driven mainly by the distribution of galaxy metallicities at these redshifts. I conclude that, though the redshift evolution is driven mainly by other physical parameters, the scatter at a given redshift is primarily metallicity dependent. For the 3D-*HST* data I show that there is a mass dependence on the [OIII]/Hβ ratio in two independent redshift bins and conclude that this is also most likely due to a metallicity distribution.

- Finally I discuss how, assuming an increase in ionization parameter and ISM pressure at high redshift, locally calibrated metallicity diagnostics will be biased when applied to high redshift galaxies. This also explains the offset in Chapter 3 observed between the O/H-based metallicities of 3D-*HST* and the N/H-based metallicities of Erb et al. (2006b). This highlights the need for the proper treatment of other physical parameters (and certainly the ionization parameter) when estimating the metallicity of high redshift galaxies.

Chapter 5

The $z \gtrsim 2$ Mass-Metallicity Relationship Revisited

5.1 Introduction

From the evidence presented so far in this thesis, and a growing number of literature sources, it seems that measurements of gas-phase metallicities at high redshift are being biased in some way which is not observed in measurements of local galaxies. Specifically there is a definite discrepancy between O/H abundances determined from the strong-line ratio N^+/H (e.g. [NII]/Hα) and others determined from the O^+/H, O^{++}/H or $(O^+ + O^{++})/H$ ratios (e.g. [OIII]/Hβ, R23). This discrepancy is observed in all current measurements of galaxies at $z > 2$, but not in the majority of the star-forming population at z = 0 (see e.g. Cullen et al., 2014; Steidel et al., 2014). The current interpretation of this systematic discrepancy is that it is due to some evolution in the conditions of HII regions in these galaxies.

To briefly review, these evolving conditions include an increase in the number of ionizing photons incident on HII regions at high redshift, often referred to as an increase in the 'hardness' of the incident radiation field. This hardness may be the result of, for example, lower metallicity massive stars which can reach high effective temperatures and are less efficient at line-blanketing FUV photons in the stellar photosphere, dense 'super-star clusters', or a more top-heavy IMF (Kewley et al., 2013a). In Chapter 4 I presented evidence for an increase in the

number of ionizing photons incident on HII regions for galaxies at $z > 1.3$ by tracking the evolution of the [OIII]/Hβ ratio in a sample of galaxies selected by [OIII]λ5007 luminosity. In addition, some evidence also exists for an increase in the electron density, or equivalently ISM pressure, at high redshift, such that stars are forming in significantly denser regions. Shirazi et al. (2014b) estimate a factor ~ 7 increase in the electron density from z = 0 to z = 3.3, and the models presented in Chapter 4, while not formally requiring it, do not rule out some evolution to high electron densities. Stated crudely, these results mean that metallicity calibrations built using local Universe galaxies will not be reliable at high redshift. For example, an [OIII]/Hβ - O/H calibration derived using a given sample of galaxies should strictly only be applied to other galaxies with similar ionization parameters and election densities (see e.g. Moustakas et al., 2010, for a detailed discussion of this problem). To properly correct for the ionization parameter when calculating metallicities one must explicitly solve for it, and the same applies to the ISM pressure.

Another complication which may be important for measuring metallicities at high redshift is variations in the N/O ratio at fixed O/H abundance. This applies in particular to O/H abundances derived using the [NII]/Hα ratio, where a relation between N/O and O/H must be assumed in order to make the conversion[1]. In the local Universe this relationship has been extensively studied by many authors (e.g. Andrews & Martini, 2013; Pilyugin et al., 2012; van Zee et al., 1998). Fig. 5.1 illustrates this relation using the parameterization from Pilyugin et al. (2012)[2]. Below a certain threshold metallicity (12+log(O/H) = 8.14 in Fig. 5.1) the N/O ratio is a constant as both nitrogen and oxygen have a primary origin (i.e. are produced from helium fusion in massive stars), and above this threshold there is an excess in nitrogen enrichment from a secondary production via the CNO cycle (Alloin et al., 1979; Edmunds & Pagel, 1978). Both empirical and theoretical metallicity calibrations have this local Universe relationship built-in and thus any evolution in high redshift galaxies will independently bias metallicities derived from the [NII]/Hα ratio.

Recently, a number of studies have suggested that some observations of line ratio evolution, and metallicity discrepancies, at high redshift can be explained by an evolution of N/O at fixed O/H (e.g. Masters et al., 2014; Shapley et al., 2015; Steidel et al., 2014). Steidel et al. (2014) suggest the stellar population

[1]To date, the majority of metallicities at $z > 2$ have been measured using the [NII]/Hα ratio via the Pettini & Pagel (2004) calibration.

[2]The metallicity scale in Fig. 5.1 will of course depend on the metallicity calibration adopted.

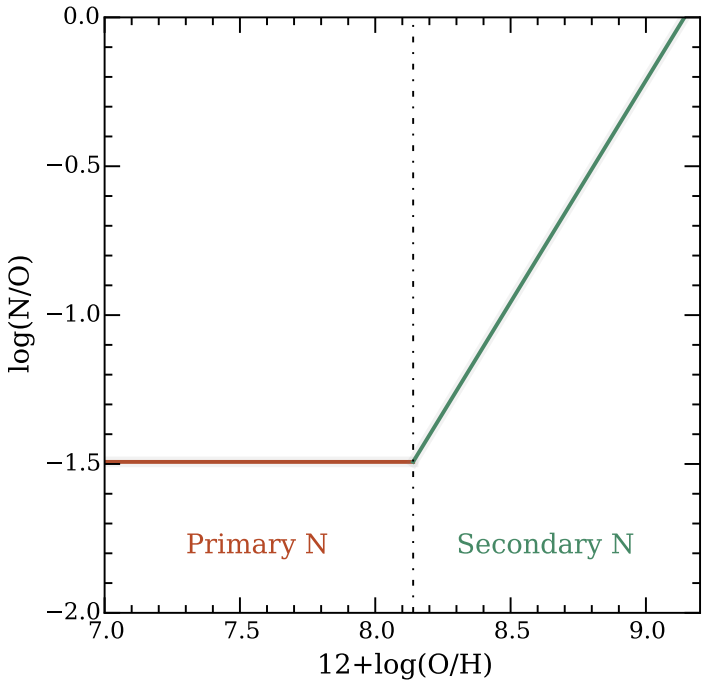

Figure 5.1 *The evolution of the N/O ratio as a function of O/H as inferred from models in the low redshift Universe. The empirical relationship shown here is taken from Pilyugin et al. (2012) but many other similar examples exist in the literature. The current understanding of this relationship is described in the text.*

synthesis models including the effects the rapid rotation of massive stars and binary evolution can account for an increase in primary nitrogen production in the main sequence, however it is not currently clear why such features of a stellar population would be preferentially seen at high redshift. Moreover, no direct measurement of the N/O ratio has yet been possible at high redshift. Nevertheless, this remains an important open question which needs to be resolved.

In this chapter, in light of these issues affecting the measurements of metallicities at high redshift, I revisit the metallicity evolution of galaxies at $z > 2$ with the purely theoretical metallicity calibration of Kobulnicky & Kewley (2004) (KK04). Since at present all of the literature metallicities at $z > 2$ have been made using local empirical calibrations (Cullen et al., 2014; Erb et al., 2006b; Maiolino et al., 2008; Steidel et al., 2014; Troncoso et al., 2014, e.g.), it is of interest to investigate the inferred evolution in metallicity from z = 0 to z = 4 using a self-consistent calibration which accounts for redshift-dependent ionization parameter evolution. In this chapter we neglect evolution in ISM pressure since (i) our results from Chapter 4 do not conclusively support this scenario, and (ii) no metallicity calibration currently exists which simultaneously solves for ionization parameter and ISM pressure. In future, this work can be extended to include ISM pressure evolution. In Sections 5.2 and 5.3 I describe the dataset used in this chapter and how metallicities are derived from the KK04 calibration. In Section 5.4 I revisit the metallicities evolution of galaxies from z = 2 to z = 3 using this calibration and in Section 5.5 explore the properties of analogue galaxies in SDSS including a discussion of evidence for N/O evolution. Finally, in Section 5.6 I explore how using these SDSS analogues it may be possible to reconcile metallicities at z = 2 based on the [NII]/Hα ratio with those based on the oxygen and Hβ lines, directly addressing the problem identified in Chapter 3.

5.2 Data

The data used in this chapter are detailed below.

5.2.1 SDSS

I create a new custom sample of SDSS galaxies in this chapter to use as the $z \sim 0$ reference sample. I use the SDSS DR7 catalogues from the JHU/MPA

group as before, the initial sample consists of $\sim$ 900,000 galaxies with emission line measurements for all the strong emission lines corrected for underlying stellar absorption[3]. I select galaxies at $z < 0.12$ to maximize the redshift completeness of the sample and require a 5σ detection in the relevant optical emission lines used in this chapter (Hα, Hβ, [OII], [OIII]λ4958, [OIII]λ5007 and [NII]). I reject AGN using the Kewley et al. (2006) prescription. Stellar masses are taken from the JHU/MPA catalogues, measured from the *ugriz* photometry. I use the JHU/MPA star-formation rates corrected from aperture to total following the method described in Salim et al. (2007). The final sample contains $\sim$ 81,000 galaxies

5.2.2 3D-*HST*

The 3D-*HST* dataset comprises galaxies in the redshift range $2.0 < z < 2.3$ identical to that presented in Chapter 3. These galaxies are visually selected from the 3D-*HST* catalogue described in Chapter 2 and, as described in Chapter 4, are 90% complete down to a luminosity limit in [OIII] of $L_{[OIII]} = 41.87$ ergs/s. The sample has been cross-matched with X-ray catalogues to remove AGNs. Due to the low S/N of the spectra, for the purposes of most of the science in this chapter, the individual spectra are stacked together and the fluxes measured from the stacked spectra using the bootstrapping technique as described in Chapter 4. Stellar masses are determined as described in Chapter 3, however throughout this chapter I use the instantaneous mass in stars rather than total mass in stars formed so do not apply the additional conversion described in Chapter 3.

5.2.3 AMAZE/LSD

I utilise a sample of star-forming galaxies a at $3 < z < 4$ (median $z = 3.4$) as part of the AMAZE/LSD survey as described in previous chapters (Maiolino et al., 2008; Mannucci et al., 2009; Troncoso et al., 2014).

Additionally, in Section 5.6 I use some additional $z \gtrsim 2$ datasets which are described in that section.

[3]http://www.mpa-garching.mpg.de/SDSS/DR7/

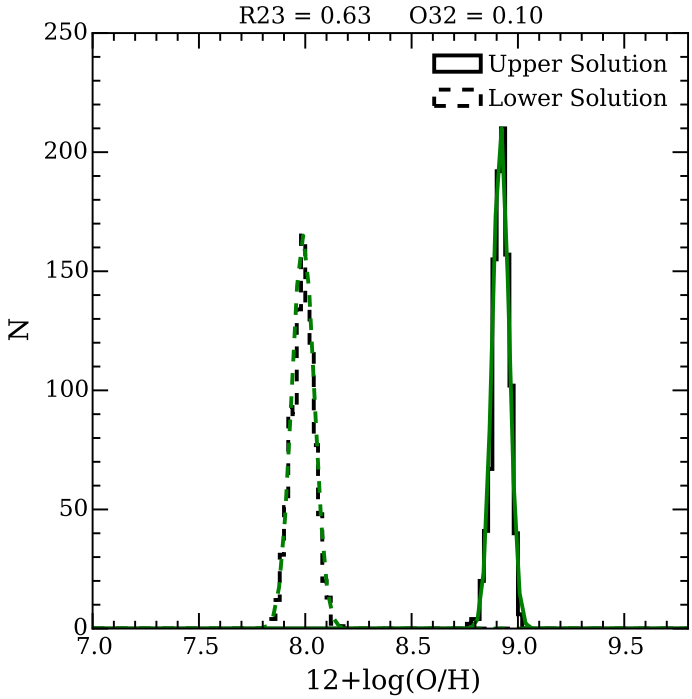

Figure 5.2 *Example of the Monte Carlo method outlined in the text for measuring metallicities from the KK04 calibration. This example illustrates the procedure for one of the galaxies from the AMAZE/LSD sample where the measured ratios give a clear distinction between upper (solid histogram) and lower (dashed histogram) branch metallicity solution. Once the choice has been made between upper and lower branch solutions, the value for metallicity and 1σ error are given by the mean and width of the fitted gaussian profile (green curves).*

5.3 Measuring KK04 Metallicities

From the evidence presented in Chapters 3 and 4 it appears that using local empirical calibrations (e.g. Maiolino et al., 2008; Pettini & Pagel, 2004) to measure metallicities at high redshift, and especially to compare metallicities at different redshifts, is biased by the evolution of ionization conditions in star-forming galaxies with redshift. Therefore, as mentioned in the introduction, I employ a new technique for solving the metallicity and ionization parameter of galaxies simultaneously using the KK04 calibration. The KK04 calibration was introduced briefly in Chapter 4, but here I will describe in detail the method I employ for measuring KK04 metallicities following Moustakas et al. (2010).

First the measured R23 and O32 ratios are perturbed by their measured errors

assuming a Gaussian distribution and the metallicity and ionization parameter solved from the KK04 calibration in an iterative manner as described in the previous chapter. I initially solve for both the upper and lower branch metallicity solutions, which is double valued because the the O/H versus R23 relation turns over above a threshold metallicity (see e.g. Kobulnicky & Kewley, 2004). At low metallicities R23 increases with O/H as the HII region becomes more oxygen enriched, however once the metallicity reaches a certain threshold value, the metals are able to efficiently cool the HII region, thus decreasing the likelihood of collisional excitations, and lowering the R23 ratio. This process of perturbing the line ratios and solving the KK04 equations is repeated 10^3 times so that a Monte Carlo distribution is built up for each parameter: $12+\log(\mathrm{O/H})_{\mathrm{upper}}$, $12+\log(\mathrm{O/H})_{\mathrm{lower}}$ and $\log(q)$.

An example of this process is shown in Fig. 5.2 for one galaxy in the AMAZE/LSD sample. In this case there is an unambiguous separation between the upper and lower branch solutions (the solid and dashed histograms in Fig. 5.2 respectively) and a choice must be made between the two. It is worth noting here that, unlike with the Maiolino et al. (2008) calibration described in Chapter 3, which uses the O32 ratio to distinguish between the upper and lower branches of double valued indices, there is no such 'built-in' way to make this distinction using KK04, instead an independent method must be used to make this distinction. For the SDSS sample the branch is chosen, as described in Chapter 4, by using the [NII]/[OII] ratio, with all galaxies having [NII]/[OII]> -1.2 being upper branch and vice versa (Kewley & Ellison, 2008). For the high redshift samples, since it is not possible to measure the [NII]/[OII] ratio, the situation is more nuanced and will be described separately below. However, once the upper or lower branch has been decided on, the final value of the metallicity and 1σ uncertainty are given by the centre and width of the gaussian fit to the distribution (see Fig. 5.2). A similar distribution is also built up for the ionization parameter, $\log(U)$, and its value and error determined in the same way.

Fig. 5.3 shows another common case which occurs at large values of R23 near the turn-over between the upper and lower branches. In this region the formal upper-branch solution given by the gaussian fit to the histogram can be at lower metallicity than the lower-branch solution and this is clearly an unphysical situation. In this case, if the central values of each branch are within $\pm 1\sigma$ of each other, I select the subset of case where the upper solution is greater than the lower solution (the grey shaded region in Fig. 5.3) and fit a gaussian to this

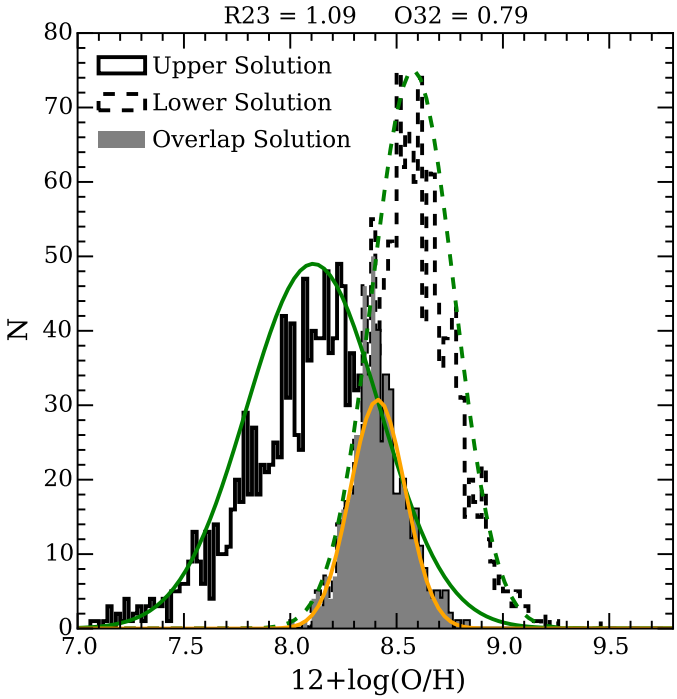

Figure 5.3 *Illustrating a case where the metallicity solution is ambiguous due to a high value of R23 near the metallicity turnover. Here the upper-branch solution is formally less than the lower-branch solution so a subset of the values where* $(O/H)_{\rm upper} > (O/H)_{\rm lower}$ *is used to derive the final value.*

distribution (yellow curve), the centre and width of this gaussian are taken as the metallicity solution and 1σ uncertainty. If the central values of each branch are $> 1\sigma$ apart then the galaxy has no formal metallicity solution, physically this means that the R23 values observed cannot be reproduced by the assumed stellar ionizing field in the Kewley & Dopita (2002) models that form the basis of KK04. Possible explanations for this scenario are that the observed spectrum is being ionized by an AGN rather than HII regions, the models are underestimating the ionizing spectra from massive stars, or perhaps simply that an over-correction for dust has boosted the [OII] flux relative to Hβ artificially enhancing the R23 ratio. One major disadvantage of the R23 calibration is its sensitivity to dust extinction due to the long wavelength baseline between the [OII]and [OIII] line.

These ambiguous situations are particularly relevant to high redshift galaxies, which are commonly observed to have R23 ratios in this region. Fig. 5.4 illustrates this by showing the R23-O/H relation from the KK04 calibration at

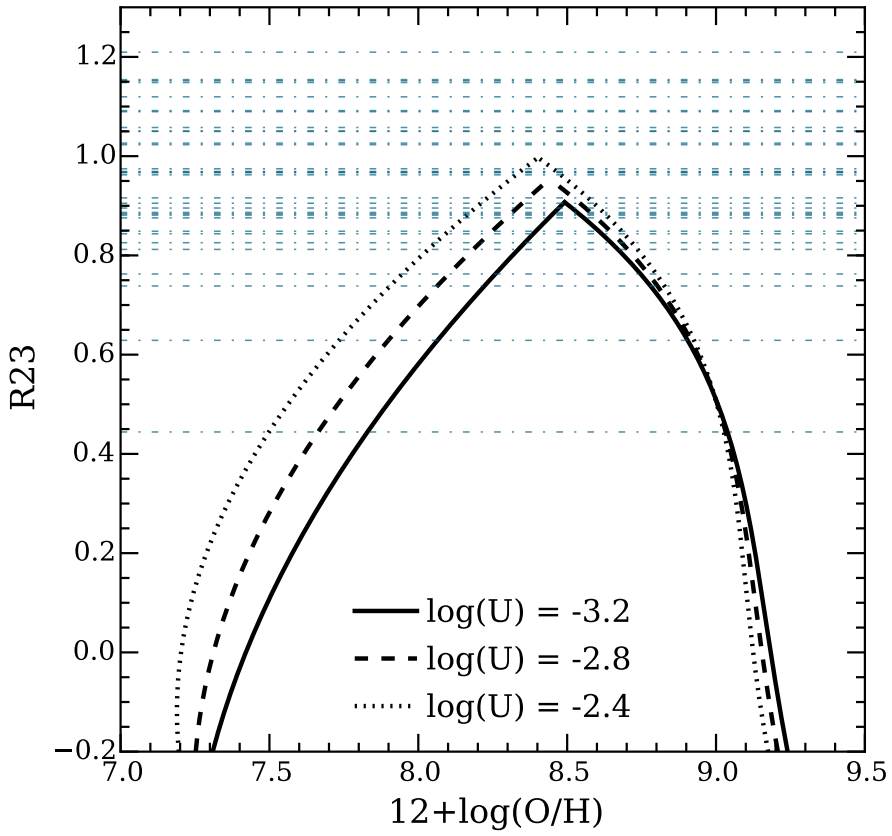

Figure 5.4 *Showing the R23-O/H relation from the KK04 calibration at three values of the ionization parameter, logU. The horizontal blue dashed lines show the measured R23 values of the $z > 3$ galaxies from the AMAZE/LSD sample from which it can be seen many lie above the theoretical curves.*

different values of the ionization parameter, log(U)[4]. The theoretical maximum of the relation at all values of the ionization parameter is R23 $\simeq$ 1. Also plotted as dashed horizontal lines in Fig. 5.4 are the R23 ratios measured for the AMAZE/LSD sample used in the chapter and it is clear that most ratios fall around the peak of the R23-O/H relation, while some with R23 $\gg$ 1 are simply 'off' the KK04 calibration. For the AMAZE/LSD sample N=7/32 galaxies have no formal KK04 metallicity solution and are removed from the sample.

[4]log(U) = q/c

5.3.1 Upper or Lower Branch at High Redshift?

For the high redshift galaxy samples no good independent line ratio is available (e.g. [NII]/[OII]) to decide whether a given galaxy is on the upper or lower branch of the KK04 calibration. Fortunately it is possible to make a reliable inference based on the fact that most galaxies at $z > 2$ lie around the peak of the KK04 calibration (see Fig. 5.4) at the point where there is a $< 1\sigma$ separation between the two solutions, and the upper and lower branch are essentially equivalent within the errors. Moreover these galaxies are generally the lowest mass galaxies of the respective samples, and galaxies for which a distinction between upper and lower solution is required (i.e. lower R23 values) have higher mass. Therefore, under the reasonable assumption that the mass-metallicity relationship exists at these redshifts these high mass, low-R23 galaxies should lie on the upper branch and all the high redshift galaxies in this chapter are assumed to lie on the upper branch. Nevertheless, a key way in which KK04 metallicity determinations at $z > 2$ can be improved is to incorporate a more robust distinction between the upper and lower branch solutions.

5.4 MZR at z = 2 and z =3

With these KK04-measured metallicities it is now possible to compare the evolution of the MZR between $z = 2$ and $z = 3$ while accounting for the evolution in ionization parameter with redshift. In Fig. 5.5 I show the MZR across the full redshift range of the combined samples. The 3D-*HST* data is shown as stacks in four bins of stellar mass (turquoise squares) whereas the AMAZE/LSD sample is shown as individual galaxies (orange circles). Also shown in the figure are the best-fitting MZR curves from Zahid et al. (2013), measured with KK04, for three galaxy samples at z = 0.08 (SDSS), z = 0.27 (SHELS) and z = 0.87 (DEEP2)[5].

A fit to the 3D-*HST* data is shown by the turquoise curve in Fig. 5.5, the functional form of this fit is given by:

$$12 + \log(\mathrm{O/H}) = Z_o - \log[1 + (\tfrac{M_*}{M_o})^{-\gamma}] \tag{5.1}$$

[5]The best-fitting SDSS curve is fully consistent with my SDSS data but I elect not to show the data points here for clarity as these low redshift curves are plotted purely to provide a visual reference to the z = 2 and z = 3 metallicity data.

This function was first proposed by Moustakas et al. (2011) and encapsulates much of our physical intuition with regard to the form of the relation. For example, whereas previous polynomial fits (Kewley & Ellison, 2008; Tremonti et al., 2004, e.g.) could turn over high stellar mass leading to a decrease in metallicity with increasing stellar mass, Eq. 5.1 increases monotonically with stellar mass, and in the high mass limit asymptotes to Z_o. This flattening of the MZR at high mass is a commonly observed feature for all statistically comprehensive studies at $z < 1$ (e.g. Kewley & Ellison, 2008; Tremonti et al., 2004; Zahid et al., 2013; **?**). In the context of equation 5.1, the parameter M_o is the characteristic mass at which the MZR begins to flatten and γ is the power law slope for $M_* \ll M_o$, γ also determines the rate at which the slope flattens above M_o.

It can be seen from Fig. 5.5 that, despite the small number of data points, the 3D-*HST* data is well described by Eq. 5.1. Unfortunately, due to the low numbers and relatively large uncertainties on the $z > 3$ data it is not possible to perform a similar fit. However it is still apparent that a large fraction of AMAZE/LSD have metallicities fully consistent with the $z \gtrsim 2$ curve, I will revisit this observation in more detail in Sec 5.6. In summary, this new analysis provides the first insight into the metallicity evolution between $z = 0-2$ to and $z = 2-3$ using a metallicity calibration that accounts for the evolution in ionization parameter with redshift. Unfortunately, the results are clearly hindered by low number statistics. However, there are a growing number of galaxies at $z \gtrsim 2$ with measured [NII]/Hα ratio and, if a reliable way could be found to convert between [NII]/Hα and KK04-measured O/H, a more accurate determination of the MZR at $z \gtrsim 2$ could be made. In Section 5.5 below, I will seek derive a reliable [NII]/Hα - O/H conversion for high redshift galaxies by utilizing analogues of these galaxies in the SDSS dataset, and in Section 5.6 I will revisit this measurement with a much improved $z \gtrsim 2$ sample.

5.5 SDSS Analogue Sample

To investigate the properties of high redshift star-forming galaxies it is useful to consider local Universe analogues. Though on average the properties of high redshift samples may differ from the overall population locally, there nevertheless exist $z = 0$ galaxies with broadly similar properties. For this purpose, I generate two sub-samples from the full SDSS catalogue which mimic some of the key

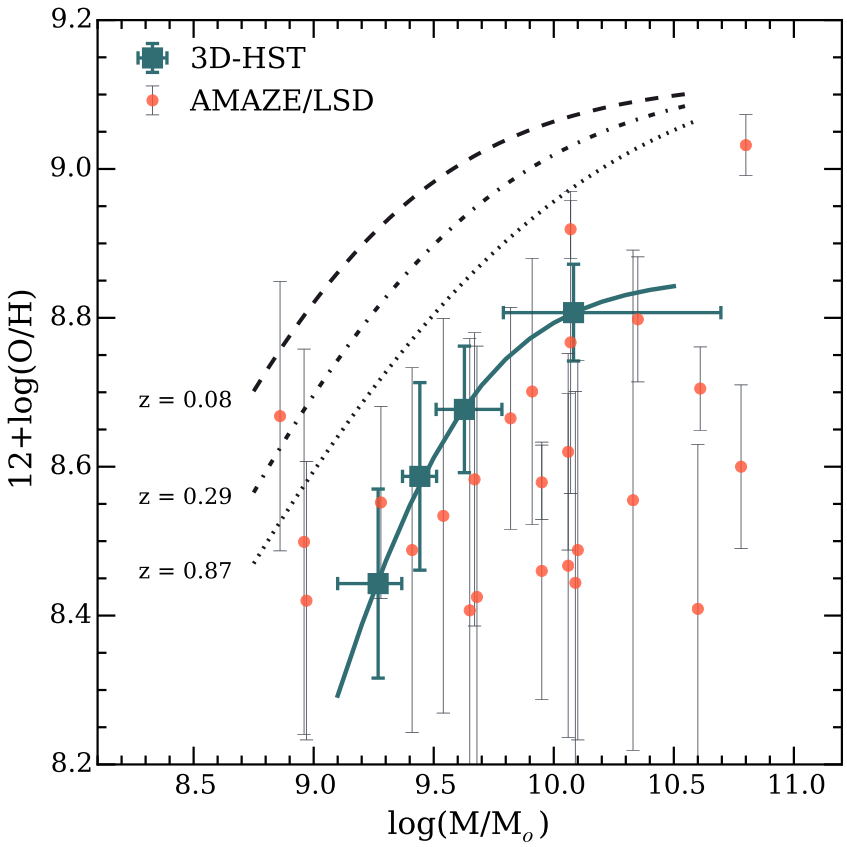

Figure 5.5 *Showing the mass-metallicity relation from SDSS ($z = 0.08$) up to $z \sim 3.5$ (AMAZE/LSD) with the KK04 metallicity calibration. The turquoise squares show the four stacked spectra from the 3D-HST sample and the turquoise curve shows the functional fit to these data as described in the text. The orange circles show individual galaxies from the AMAZE/LSD survey. The errors represent measurement uncertainties and do not include the uncertainty in the KK04 calibration. The three black curves show fits to the MZR from Zahid et al. (2013) at $z = 0.08$, 0.27 and 0.87 as labeled. The $z = 0.08$ SDSS curve is fully consistent with our full SDSS sample (see figure from previous chapter).*

observables of galaxies at $z > 2$. These two sub-samples were chosen to satisfy, respectively, the following criteria:

1. [OIII]λ5007/[OII] > 0.0;
2. $L_{[OIII]\lambda5007} > 41.87$.

The first criterion mimics the high O32 ratios commonly observed at $z > 2$ (e.g. Cullen et al., 2014; Nakajima & Ouchi, 2014; Shapley et al., 2015). To first order, this criterion selects galaxies with high ionization parameters and low metallicities. Fig. 5.6 illustrates this by showing the positions of a number of different galaxy samples in the O32 vs. R23 plane. The majority of $z > 2$ samples (illustrated here with the 3D-*HST* and AMAZE/LSD) lie at O32 > 0 in the high-R23 (low-metallicity) tail of the SDSS distribution (see also e.g. Shapley et al., 2015, Fig. 3). Within the full SDSS sample there are N=574 galaxies which satisfy this criterion. It can be seen that there is good agreement between the position of the O32 > 0 galaxies and the $z > 2$ samples. Therefore, we argue from Fig. 5.6, that though O32 > 0 is an empirical and somewhat arbitrary selection criterion, it is nevertheless plausibly representative of the population of high excitation, low metallicity galaxies observed so far at high redshift. I refer to this SDSS sub-sample as HES (High-Excitation SDSS) sample throughout the rest of this section.

The second criterion mimics the selection effects which apply to the $z > 2$ emission line selected samples. At higher redshift, due to the greater distances, the minimum observed line luminosity increases dramatically. In this chapter, as in Chapter 4, we select an SDSS sub-sample which is based purely on [OIII]λ5007 luminosity. Furthermore, Juneau et al. (2014) show that their results remain largely unchanged for a pure Hα, pure [OIII]λ5007, or combined Hα+[OIII]λ5007 luminosity selection. In the previous chapter I show that at $z > 2$ the 3D-*HST* sample is 90% complete to $L_{[OIII]\lambda5007} = 41.87$ ergs/s, and therefore we select SDSS galaxies above this threshold. There are N=132 galaxies within the full SDSS sample which satisfy this criterion. We refer to this SDSS sub-sample as HLS (High-Luminosity SDSS) sample throughout the rest of this section. In total there are N=87 galaxies in common to both catalogues, we discuss and compare some of their global properties below.

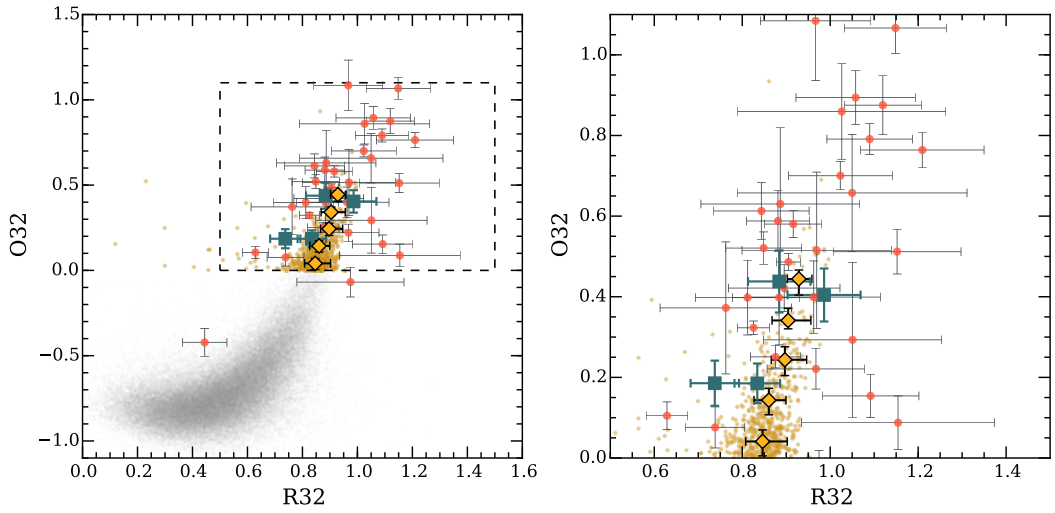

Figure 5.6 *Illustrating the positions of SDSS and $z > 2$ galaxies in the R23 vs. O32 plane.* Left panel: *Black points show the full SDSS sample with a median O32 of -0.71 dex. The small yellow diamonds show the SDSS sample selected to have O32 > 0.0 and the large yellow diamonds show the running medians in bins of O32. The blue squares show the $z > 2$ galaxy stacks from the 3D-HST sample and the orange circles show the individual $z > 3$ galaxies from the AMAZE/LSD sample.* Right panel: *Showing a zoom-in of the left-hand panel as indicated by the dashed box.*

5.5.1 Global Properties of Samples

It is instructive to investigate how the global properties of the various SDSS samples compare with each other, and with the $z > 2$ population. Fig. 5.7 compares the mass, SFR, SFR surface density ($\Sigma_{\rm SFR}$), and metallicity distributions of the HES and HLS to the combined 3D-*HST* and AMAZE/LSD data at $z > 2$. To measure $\Sigma_{\rm SFR}$ for the $z > 2$ galaxies I used the $H_{\rm F160W}$-band catalogues of van der Wel et al. (2012), where the galaxy size is defined as the semi-major axis of the ellipse containing 50% of the total light in the best fitting model. For SDSS galaxies I use the sizes provided in the JHU/MPA catalogues which are defined as the radius contained 50% of the total light in a Petrosian aperture (Petrosian, 1976). At $z > 2$ the central wavelength of the $H_{\rm F160W}$ filter is best matched with the SDSS r-band filter so all SDSS sizes are taken in the r-band. The distributions of physical properties are presented in Fig.5.7 are outlined in Table 5.1. There are a number of interesting points to note from this comparison.

Firstly, the high-excitation, low metallicity galaxies selected via the O32 ratio have, unsurprisingly, a median metallicity 0.36 dex lower that the overall SDSS sample, and, as expected from the mass-metallicity relation, a significantly lower median mass. The HES sample has a slightly larger median metallicity than the $z > 2$ galaxies and a mass distribution offset to lower masses, with a median mass 0.2 dex lower, this may be a consequence of cosmic metallicity evolution (i.e. lower metallicity systems moving to higher mass galaxies at higher redshift). Interestingly the SFR distribution of the HES sample, though 0.22 dex greater than the total SDSS sample, is shifted to lower SFRs than both the HLS and $z > 2$ samples by ~ 0.5 dex. This would imply that this sample contains large proportion of low-SFR galaxies not commonly observed at $z > 2$, at least down to the mass limit of our samples ($\log(\rm M/M_{\odot}) \simeq 9.0$). Finally, the $\Sigma_{\rm SFR}$ distribution is also offset to significantly lower values implying, perhaps surprisingly, that high excitation conditions are not necessarily associated with compact star-forming regions. That being said, the median $\Sigma_{\rm SFR}$ of the HES sample is still $\sim 4\times$ larger than the median of the total population. Overall, the HES sample mimics the $z > 2$ galaxies in terms of mass and metallicity, but exhibits a significantly different SFR and $\Sigma_{\rm SFR}$ distributions, offset to the lower values. From the growing evidence of elevated SFRs at high redshift, it seems reasonable to assume that this subset of low-SFR HES galaxies is not fully representative of the $z > 2$ population.

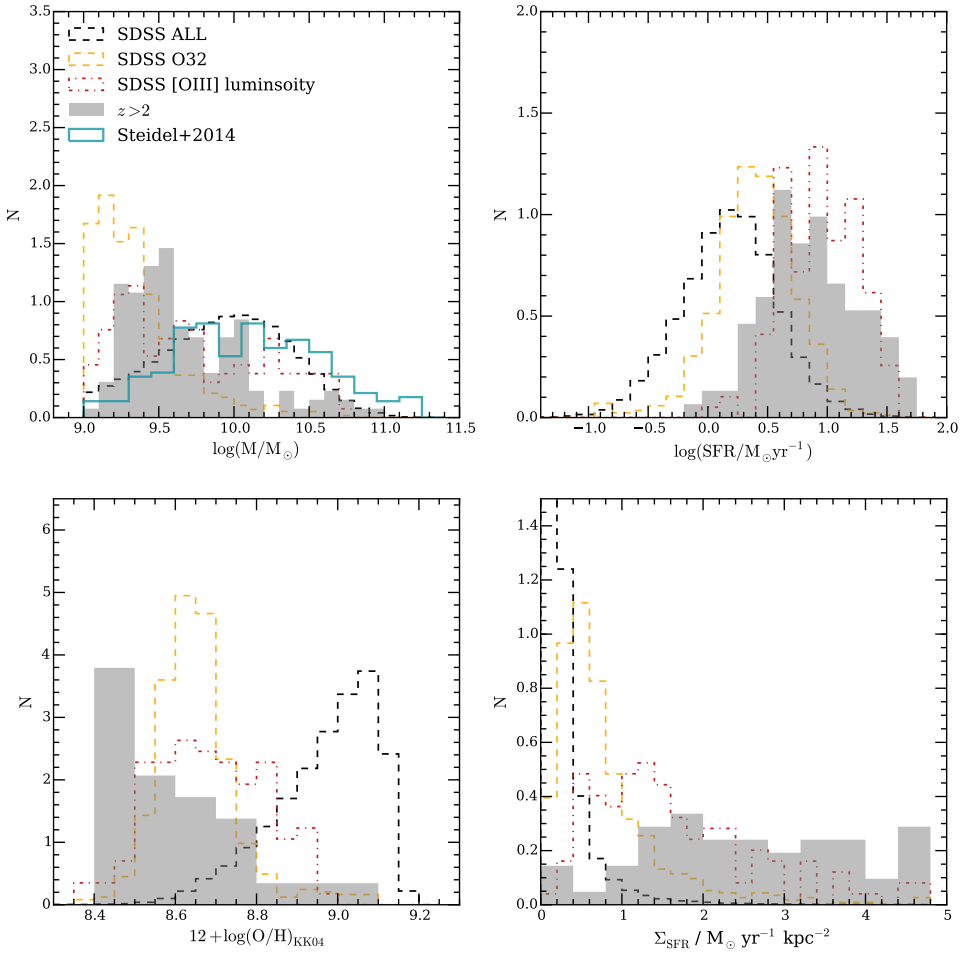

Figure 5.7 *Comparing the distribution of global properties of the various galaxy samples used in this chapter. In each panel the black dashed histogram shows the full SDSS sample, red dot-dash histogram shows the HLS, the yellow dot-dashed histogram shows the HES. The filled grey histogram shows the 3D-HST and AMAZE/LSD data at $z > 2$. The solid blue histogram in the mass panel (upper left) shows the mass distribution of the $z \gtrsim 2$ sample from Steidel et al. (2014).*

Table 5.1 *A comparison of the properties of SDSS, HES and HLS samples. The first two columns list the name and sizes of the different samples. Columns 3, 4, and 5 list the median and standard deviation of, respectively, the stellar mass, star-formation rate, and metallicity of each sample.*

Sample	N	$\log(M/M_\odot)$	$\log(SFR\ /\ M_\odot\ yr^{-1})^a$	$12 + \log(O/H)$	$\Sigma_{SFR}\ /\ M_\odot\ yr^{-1}\ pc^{-2}$
SDSS	80,789	9.94 ± 0.42	0.18 ± 0.64	8.97 ± 0.12	0.28 ± 0.49
HES	547	9.35 ± 0.29	0.40 ± 0.36	8.66 ± 0.10	0.89 ± 1.34
HLS	132	9.73 ± 0.47	0.95 ± 0.32	8.69 ± 0.14	2.20 ± 2.29
$z > 2$	117	9.66 ± 0.43	0.88 ± 0.43	8.60 ± 0.16	3.66 ± 2.53

[a] For the $z > 2$ samples the SFR is taken from the best fitting SED SFR.

The HLS sample, on the other hand, selects higher masses and significantly higher SFRs than the HES sample. The HLS SFRs are more representative of the high redshift star-forming population and in contrast to the HES sample, HLS is most similar to the $z > 2$ sample in terms of the SFR and $\Sigma_{\rm SFR}$ distributions. This suggests that the HLS sample is picking up similarly compact highly star-forming galaxies to those observed at high-redshift. The mass and metallicity distributions of the HLS sample are broader than for the $z > 2$ galaxies, and offset to higher values of both parameters. However, such broad mass and metallicity distributions are a feature of other $z > 2$ studies, for example the UV selected KBSS-MOSFIRE star-forming galaxy sample from Steidel et al. (2014) (see the stellar mass panel in Fig. 5.7). The lack of high mass, high metallicity galaxies in 3D-*HST* and AMAZE/LSD being due to selection effects biasing both samples. As discussed in the introduction (see Fig 1.25) optical emission line selections are biased to galaxies with lower masses and higher SFRs, and rest-UV selections will are insensitive to heavily dust reddened galaxies which are more common at higher mass. Moreover, due to the relatively small sample sizes and survey areas both samples will be further biased towards galaxies with masses below the characteristic mass of the stellar mass function at these redshifts (see e.g. Muzzin et al., 2013). It seems reasonable to assume that the higher masses and metallicities of the HLS galaxies represent a plausible extensions of the 3D-*HST* and AMAZE/LSD samples, and that such galaxies plausibly exist at $z > 2$ as evidenced by the Steidel et al. (2014) sample.

Moreover N=87/132 (66%) of the HLS sample overlaps with the HES sample, therefore the majority of [OIII] luminosity selected galaxies are compatible with the high-excitation. Of the remaining N=45/132 galaxies with O32 < 0, the median value of the O32 ratio is -0.27, still significantly elevated from the bulk of the SDSS star-forming population (see Fig. 5.6). I therefore conclude that the HLS sample gives the most reasonable representation of the currently observed $z > 2$ galaxy population. For the rest of this chapter I will refer to these galaxies as the SDSS analogue sample.

5.5.2 Reproducing High Redshift Observations

In this section, I compare the SDSS analogue galaxies with some of the other key observational properties of $z > 2$ galaxies.

BPT Diagram

As discussed throughout this thesis, one of the most interesting, and debated, results to have emerged in the study of $z > 2$ galaxies is the offset in the BPT diagram, of which the most up-to-date and convincing examples are given in Steidel et al. (2014) and Shapley et al. (2015). This offset, which is sensitive to the chemical abundance, ionization state, and density of HII region gas, is also responsible for the discrepancy between oxygen-based and nitrogen-based metallicity calibrations observed at $z > 2$ as discussed in Chapters 3 and 4 (see also Cullen et al., 2014; Steidel et al., 2014). Various, albeit generally broadly similar, theoretical interpretations have been advanced to explain these observations (see e.g. Kewley et al. (2013a) and Steidel et al. (2014)). As previously discussed, these include a decrease in metallicity with a corresponding increase in the ionization parameter at high redshift, an increase in density of HII regions, as well as the possible evolution of the N/O abundance ratio with redshift (e.g. Masters et al., 2014; Shapley et al., 2015; Steidel et al., 2014).

Fig. 5.8 shows the position of the SDSS analogue galaxies in the BPT diagram. Unfortunately, since neither the 3D-*HST* or AMAZE/LSD samples have measurements of the [NII]/Hα ratio, they cannot be included in the figure. Instead I show the sample of 126 galaxies with $\langle 2.34 \rangle \pm 0.16$ from the KBSS-MOSFIRE survey from Steidel et al. (2014) along with the best-fitting abundance sequence to their data (green dotted line). Also shown by the green solid line is the best-fitting abundance sequence to the recent study of 53 $z \sim 2.3$ galaxies from the MOSDEF survey from Shapley et al. (2015). It can been seen this sequence is offset to lower [OIII]/Hβ at fixed [NII]/Hα compared to the Steidel et al. (2014) sequence, and is closer to the abundance sequence of the full SDSS sample (green dashed line). As discussed in Shapley et al. (2015) though the median stellar mass of the two samples are similar ($\log(\mathrm{M}/M_{\odot}) \sim 10$), the Steidel et al. (2014) sample spans a wider range in stellar mass and, at the lowest masses ($\log(\mathrm{M}/M_{\odot}) = 9.5$), has elevated SFRs. Therefore, this difference could be due to biases introduced by the different selection criteria of both samples as discussed in the introduction. A quick comparison to Table. 5.1 reveals that the median mass and SFR of the Steidel et al. (2014) sample are also much higher than the 3D-*HST*+AMAZE/LSD and SDSS analogue samples used in this chapter, as the majority of the galaxies come from the rest-frame optical 3D-*HST* selection. It is therefore perhaps not surprising that the SDSS analogue sample shown in the figure is in better agreement with the abundance sequence of Shapley et al.

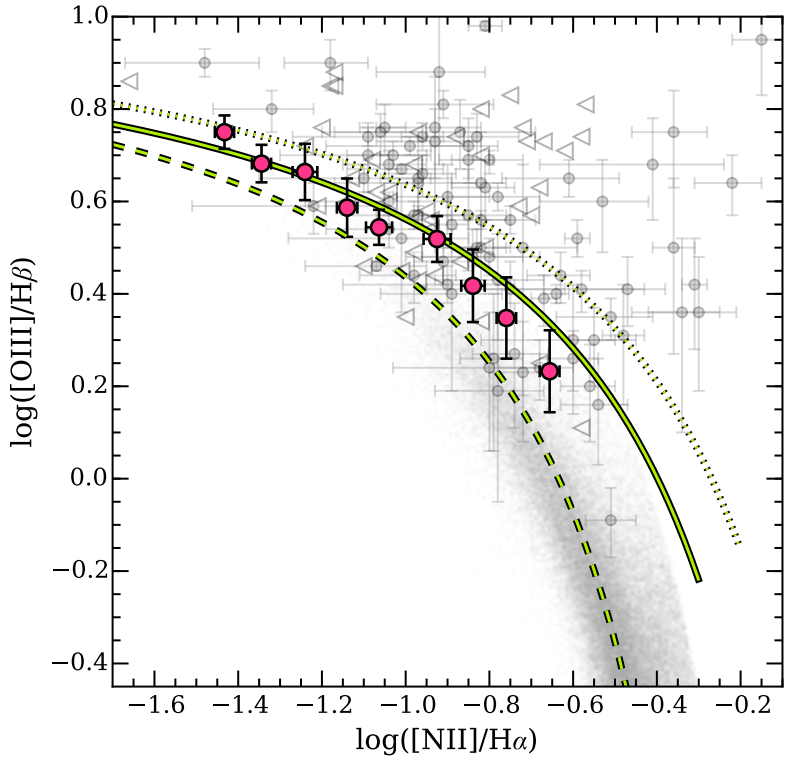

Figure 5.8 *The BPT diagram for the SDSS analogue sample (pink) compared with the recent* $2 < z < 2.6$ *observations from Steidel et al. (2014) (grey). The left-pointing triangles show galaxies from the Steidel et al. (2014) sample with only upper limits on the [NII]/H*α *ratio. The locus of faded grey points shows the SDSS sample. The green dashed line shows the* $z = 0$ *fit to the star-forming galaxy sequence in the BPT plane from Kewley et al. (2013a), while the green solid line and green dotted line shows the best fit to the* $z > 2$ *samples of Shapley et al. (2015) and Steidel et al. (2014) respectively.*

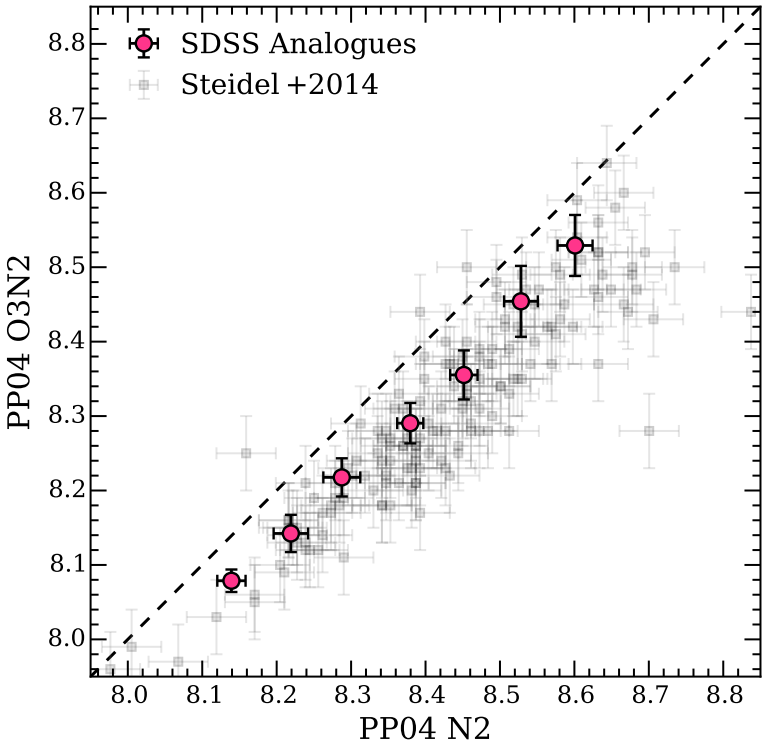

Figure 5.9 *N2-derived versus O3N2-derived metallicities for the SDSS analogue galaxies (pink) compared with the recent $\langle z \rangle = 2.3$ observations from Steidel et al. (2014) (grey). The dashed line shows the 1:1 relation between the two metallicity indicators.*

(2015).

Nevertheless, most importantly, the SDSS analogue sample is consistent with the observation that $z > 2$ galaxies are offset from SDSS abundance sequence in the BPT diagram. Taken at face value, this offset can be attributed to the high-excitation, low metallicity properties of these galaxies.

N/H vs O/H Metallicity Offset

Another intriguing property of high redshift galaxies is the offset observed between oxygen-based and nitrogen-based metallicity calibrations (see e.g. Cullen et al., 2014; Steidel et al., 2014; Zahid et al., 2013). Here we illustrate this with the routinely applied Pettini & Pagel (2004) calibration (PP04). However, as previously discussed PP04 is only one of many metallicity calibrations that can be applied at high redshift.

Briefly, the PP04 calibration relates the gas-phase oxygen abundance (O/H) to both the N2 and O3N2 emission line index's, where:

$$\mathrm{N2} \equiv \log([\mathrm{NII}]/\mathrm{H}\alpha), \tag{5.2}$$

$$\mathrm{O3N2} \equiv \log([\mathrm{OIII}]/H\beta) - \log([\mathrm{NII}]/\mathrm{H}\alpha). \tag{5.3}$$

The calibration is based on a fit to N=187 extragalactic HII regions compiled from a variety of literature sources where each HII region in the dataset has a measurement of the [NII]/Hα ratio, [OIII]/Hβ ratio, and a reliable measurement oxygen abundance (O/H) based on either a direct measurement of the electron temperature (T_e method, N=181), or detailed photoionization modeling (N=6). PP04 is an example of an 'empirical' calibration in which a given line ratio is calibrated against a more robust determination of the oxygen abundance. Pettini & Pagel (2004) derive both a linear fit and marginally better fitting third order polynomial to the relation between N2 and (O/H), given by the following equations:

$$12 + \log(\mathrm{O/H}) = 8.90 + 0.57 \times \mathrm{N2}, \tag{5.4}$$

$$12 + \log(\mathrm{O/H}) = 9.37 + 2.03\mathrm{N2} + 1.26\mathrm{N2}^2 + 0.32\mathrm{N2}^3, \tag{5.5}$$

valid in the range $-2.5 < \mathrm{N2} < -0.3$. Of these two, equation 5.4 is more commonly used in the literature and I adopt it here. Similarly PP04 provides a linear relation between the O3N2 and (O/H) given by:

$$12 + \log(\mathrm{O/H}) = 8.73 - 0.32 \times \mathrm{O3N2}, \tag{5.6}$$

valid in the range $-1 < \mathrm{O3N2} < 1.9$. Combining equations 5.4 and 5.6 with their respective limits, it follows that the approximate range in metallicity over which both calibrations can be reliably applied is $8.1 < 12+\log(\mathrm{O/H}) < 8.7$.

In Fig. 5.9, I plot the offset between the N2 and O3N2 derived metallicities for the SDSS analogue sample compared to the KBSS-MOSFIRE sample from Steidel et al. (2014). It is clear from Fig. 5.9 that for the SDSS analogue and Steidel et al. (2014) samples, the O3N2 metallicity solution, for a given N2 solution, is *systematically* lower than the 1:1 relation. The mean and standard deviation of the offset between the O3N2 and N2 solutions across the full sample for the SDSS and Steidel et al. (2014) galaxies respectively is -0.08 $\pm$ 0.01 and -0.12 $\pm$ 0.06. Again, our SDSS analogue samples are consistent with the metallicity calibration offsets observed at high redshift. This is similar to the offsets observed with the

Maiolino et al. (2008) calibration discussed in Chapters 3 and 4.

Mass-Metallicity Relation

Though it has already been established that the SDSS analogue sample has a similar mass and metallicity distribution to the high redshift population, this topic is worth discussing further. In Fig. 5.10 I show the position of the SDSS analogue sample in the mass-metallicity plane compared to the position of the 3D-*HST* and AMAZE/LSD galaxies. Unsurprisingly, the SDSS analogues galaxies are consistent with the position of the $z > 2$ samples in the mass-metallicity plane. An obvious implication being that in the local Universe there exist galaxies with similar O/H abundances as $z > 2$ galaxies at the same stellar mass. Therefore, as pointed out by Juneau et al. (2014), when exploring the MZR evolution one must be wary of the various line luminosity selection effects applicable to the samples being compared.

This observation also raises the question of whether, at high redshift, we are only sensitive to a similarly extreme population of star-forming galaxies? If this were the case it would have profound implications for our understanding of the evolution of the MZR. However, the SDSS analogue sample accounts for only N=132/80,789 galaxies in the star-forming population of the local Universe ($\sim$ 0.16% of the total). It seems unlikely, given the relatively small volumes and large numbers of $z > 2$ emission line galaxies visible in the 3D-*HST* survey, that this would be the case at high redshift. To perform a quick sanity check I use the 3D-*HST* galaxies to estimate the fraction of the $2 < z < 2.5$ star-forming population contained in this sample. The 3D-*HST* galaxies are selected from 88, 123 x 136 arcsec^2, WFC pointings equating to a co-moving volume within this redshift interval of 6.8 x 10^5 Mpc^3. Muzzin et al. (2013), from a determination of the stellar mass function, estimate the number density of star-forming galaxies with $\log(\mathrm{M}/\mathrm{M}_\odot) > 9.0$ in the redshift interval $2 < z < 2.5$ to be $5.9^{+1.9}_{-4.1}$ x 10^{-4} Mpc^{-3}, and from this is can be easily determined that the 96 galaxies in the 3D-*HST* survey represent $\simeq 24^{+55}_{-6}$ % of the star-forming population in this redshift interval and co-moving volume. Clearly this estimate is highly uncertain due to the difficulty in estimating the stellar mass function at high redshifts, however it rules out at $> 3\sigma$ the extremely low population fraction of the SDSS analogue galaxies. Moreover, the estimation can be thought of a lower limit since the number density is determined for galaxies at $2 < z < 2.5$, while the 3D-*HST*

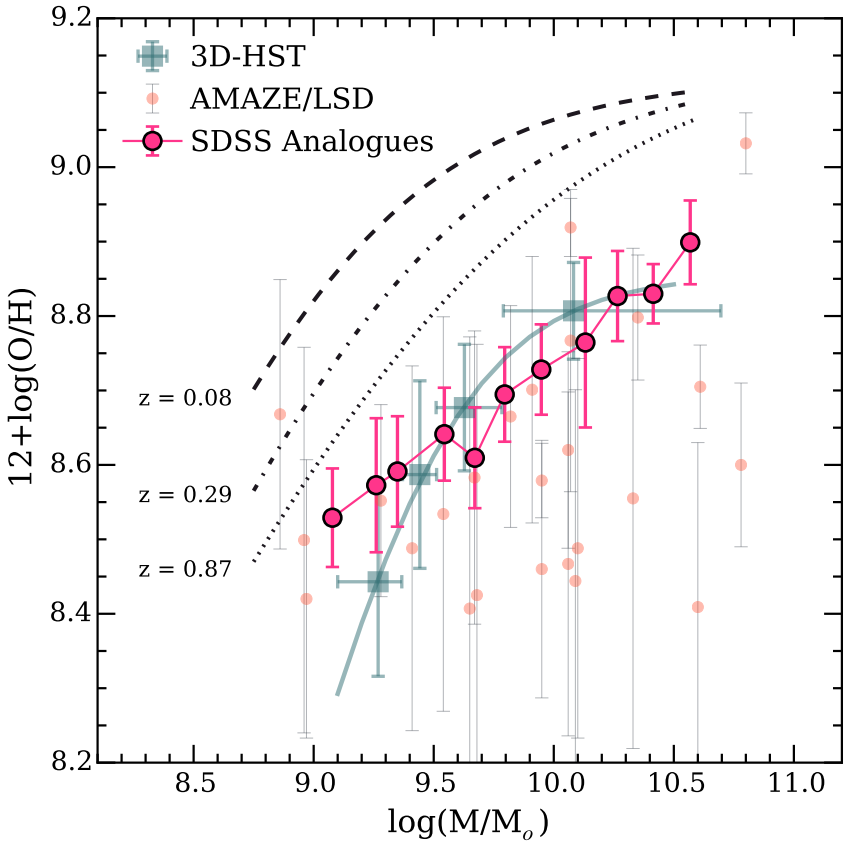

Figure 5.10 *Reproduction of the mass-metallicity plane from Fig. 5.5 with the addition of the 87 galaxies from SDSS analogue sample (pink circles) shown as running medians in 0.15 dex mass bins. The errors on the SDSS points show the standard deviation in each bin.*

galaxies are only observed in the interval $2 < z < 2.3$. It seems reasonable to conclude that the 3D-*HST* sample constitutes a much higher percentage of all star-forming galaxies at $z \gtrsim 2$ with a rough lower limit of $\simeq 20\%$. Therefore, in the context of the MZR, there is still a genuine evolution in metallicity since the low metallicities observed at $z \gtrsim 2$ represent a much larger percentage of the overall star-forming population. This population fraction argument can also be extended to all the other observations presented in this sections i.e., the observed effects (BPT offset, metallicity discrepancies etc ..) are applicable to a much larger fraction of the star-forming galaxies at $z > 2$.

N/O vs. O/H

A number of recent studies have suggested that variations in the N/O abundance ratio may be responsible for some of the observed properties of $z > 2$ galaxies (e.g. Masters et al., 2014; Shapley et al., 2015; Steidel et al., 2014). As discussed in Steidel et al. (2014), the issue is of particular importance when mapping measurements of the nitrogen abundance (N/H, e.g using [NII]/Hα) to the oxygen abundance (O/H), as is commonly done when measuring gas-phase metallicities. Pérez-Montero & Contini (2009) (PMC09) have shown, using the direct T_e method to derived the N/O and O/H abundances, that for samples of HII regions from the Milky Way and Magellanic clouds, and local HII galaxies, there is a large dispersion in the N/O ratio at fixed metallicity. However, this in itself simply implies a scatter in the [NII]/Hα vs. (O/H) relation which would propagate into the uncertainties in a given metallicity calibration. The question at high redshift is whether there is a systematic offset in N/O at fixed metallicity in high redshift samples, due to either a physical evolution in the ratio or some kind of selection effect?

In the top panel of Fig. 5.11 I plot the N/O abundance, derived using the [NII]/[OII] ratio using the Pérez-Montero & Contini (2009) prescription, as a function of the KK04 O/H abundance for the SDSS analogue and full samples. It is worth reiterating that the KK04 method ensures the O/H measurement is not biased by any N/O variations as the method utilises only the oxygen lines and Hβ. The full SDSS sample is plotted as the median N/O in 0.05 dex wide bins of O/H. A second order polynomial fit through this data shows a qualitatively similar relation as described in the introduction and shown in Fig. 5.1 with a pl analogue samples.

The median N/O of the SDSS analogue sample is plotted in the top panel of Fig. 5.11 using the same O/H bins as above, and the difference in N/O between the overlapping bins is plotted in the bottom panel. It can be seen that, at low O/H, the N/O of the SDSS analogue sample is fully consistent, with the N/O of the full sample. At log(O/H) > 8.7 the SDSS analogue sample does appear for have systematically larger N/O by ~ 0.1 dex but these galaxies are still only $\sim 1\sigma$ outliers and there is no clear evidence for a large systematic offset for these galaxies nor any deviation from the basic form of the N/O vs. O/H relation. This is in contrast to some studies which have inferred a shift to higher N/O at fixed O/H, especially for low metallicities, for $z > 2$ galaxies. Steidel et al.

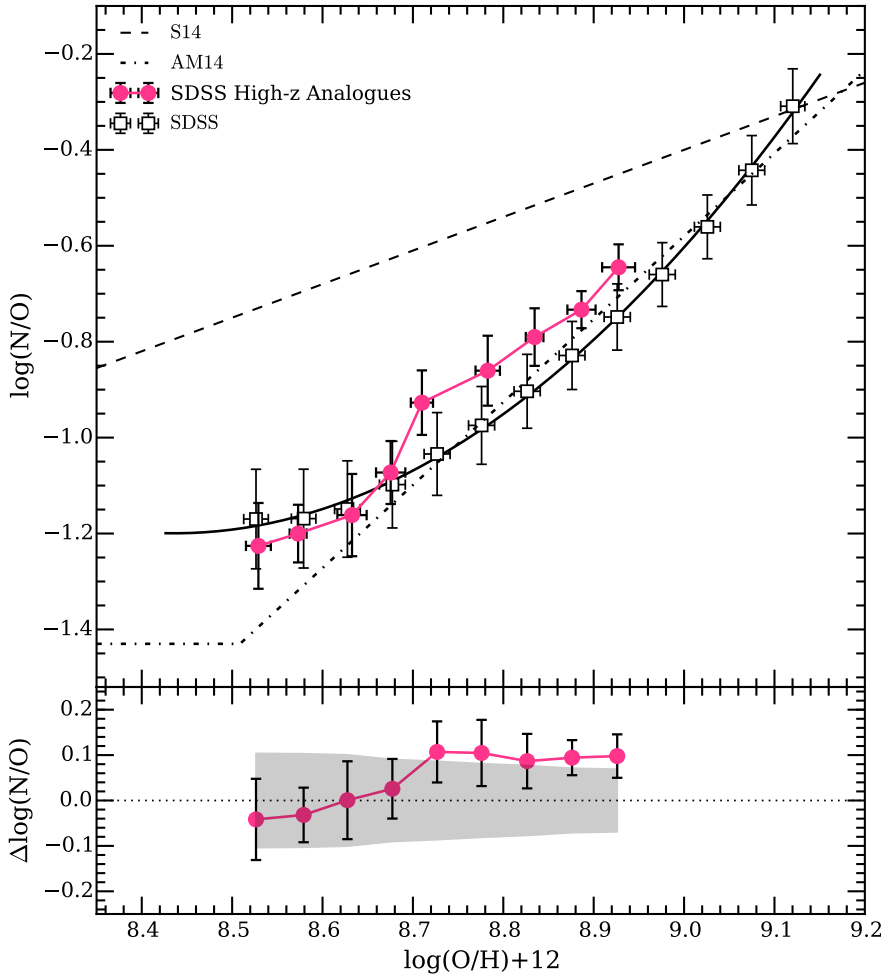

Figure 5.11 *Top panel: N/O versus O/H for the SDSS analogue sample (pink circles) and full SDSS sample (black open squares). N/O is measured following the Pérez-Montero & Contini (2009) prescription and O/H measured from the Kobulnicky & Kewley (2004) calibration. The error-bars represent measurement errors only and do not include uncertainties in the calibrations. The dot-dashed black line (AM14) shows the (N/O) vs. (O/H) relation for stacked SDSS spectra from Andrews & Martini (2013) where both quantities have been measured using the direct T_e method. The dashed black line (S14) is a relation presented in Steidel et al. (2014) inferred from their $\langle z \rangle = 2.3$ data and data presented in Pérez-Montero & Contini (2009). Bottom panel: Showing the difference in N/O between the SDSS analogue and full SDSS samples, the grey shaded region shows the standard deviation of the full sample.*

(2014) suggest the position of $z > 2$ galaxies in the BPT diagram can be best reproduced assuming a shallower N/O versus O/H relation (shown in Fig. 5.11), they argue that there is little evidence for the N/O plateau at low metallicities in their sample. However, Kewley et al. (2013b) have shown that the evolution of the abundance sequence can be achieved without assuming any systematic shift in the N/O versus O/H relation, moreover the Kewley et al. (2013b) models include a more sophisticated treatment of the stellar ionizing radiation field. Shapley et al. (2015) infer an evolution in N/O by matching their MOSDEF sample to SDSS galaxies with similar excitation properties and plotting their positions in the BPT diagram. They find the low mass galaxies in their sample are offset to higher [NII]/Hα at fixed [OIII]/Hβ ratio implying a shift to higher N/O at fixed O/H. However it is not clear that the low [NII]/Hα galaxies are simply not detected in their sample due to line luminosity limits. [NII] is the weakest of the strong emission lines, and since they only include galaxies with significant measurements in all lines, their sample will be biased against galaxies with low [NII]/Hα. Importantly no actual measurement of the N/O vs. O/H relation has been made at $z > 2$, and so far all conclusions are based on inferences from other observations.

In summary, the SDSS analogue galaxies presented here mimic all observed properties of $z > 2$ galaxies in terms of their excitation properties, mass, metallicities, and occupy a similar region in the BPT diagram. However, there is no evidence that these galaxies have a large systematic offset in N/O at fixed O/H, nor show any deviation from the overall form of the relation. I therefore argue that the observed properties of high redshift galaxies can be accounted for without invoking systematically higher values of the N/O ratio at fixed O/H as a result of a shallower N/O versus O/H relation.

5.5.3 A Robust [NII]/Hα - O/H Conversion

In light of all the evidence presented above, it seems reasonable to assume that the SDSS analogue sample closely resembles all known properties of $z > 2$ galaxies. Also, assuming the high redshift galaxies do not follow a significantly different N/O versus O/H relation, it should be possible to use the SDSS analogue sample to define an accurate calibration for converting between [NII]/Hα and O/H for the KK04 calibration. This calibration would, unlike current empirical [NII]/Hα calibrations, account for the changes in ionization conditions with redshift. Such

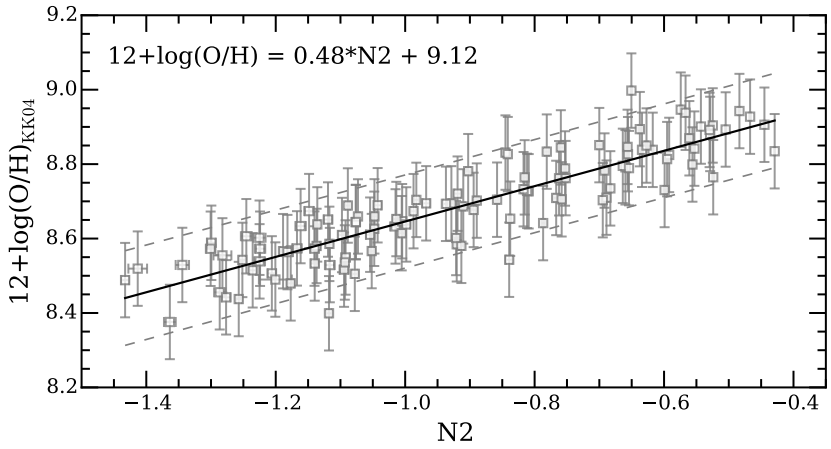

Figure 5.12 *KK04 oxygen abundance versus N2 index for the SDSS analogue sample. The errors on the oxygen abundances are dominated by the calibration error estimated at 0.1 dex (Kobulnicky & Kewley, 2004). The solid line is the best-fitting linear relationship as given in the top corner of the plot. The dashed lines encompass 95% of the measurements and correspond to a range in* $\Delta log(O/H) = \pm$ *0.12 dex.*

a calibration would therefore allow the growing number of $z \sim 2$ galaxies with [NII]/Hα measurements to be compared robustly with metallicities from the KK04 calibration, overcoming the issue that was raised in Chapter 3 of this thesis.

Fig. 5.12 shows the best-fitting linear relation between $12+\log(\mathrm{O/H})_{\mathrm{KK04}}$ and the N2 index for the SDSS analogue galaxies given by the equation:

$$12 + \log(\mathrm{O/H})_{\mathrm{KK04}} = 9.12 + 0.48 \times \mathrm{N2}, \tag{5.7}$$

valid in the range $-1.45 < \mathrm{N2} < -0.4$. The lower limit in N2 corresponds to the fact that the equation in only valid for galaxies on the upper branch of the KK04 metallicity calibration. The upper limit in N2 is a result of the upper metallicity limit of the SDSS analogue sample. It is not advisable to extrapolate the relation at $\mathrm{N2} > -0.4$, since it is know that the N2 vs O/H relation saturates at high metallicity (see Figs. 1.22 and 1.23 in the introduction). Moreover, the relation is only strictly applicable to galaxies with similar physical properties to the SDSS analogue sample, which is a selection based purely on [OIII] luminosity. However, if it is not possible to measure [OIII] luminosity, Fig. 5.7 illustrates how matching samples by mass, SFR or Σ_{SFR} is a viable alternative. This equation has both a shallower gradient and lower intercept than the commonly used Pettini & Pagel

(2004) N2 calibration (see equation 5.4). The 2σ limits on the best fitting line are given as dashed line in Fig. 5.12 corresponding to $\Delta\log(\mathrm{O/H}) = \pm\ 0.12$ dex, I therefore conclude this calibration is able to estimate the oxygen abundance within ~ 0.1 dex at the 95% confidence level.

5.6 Reconciling $z = 2$ metallicities

Using this new calibration I can compare the growing number of $z > 2$ galaxies with measured N2 index to the KK04 metallicities derived directly for the 3D-*HST* and AMAZE/LSD galaxies and re-examine, with an increased sample size, the mass metallicity relation at $z = 2 - 3$. Firstly, I will give a brief overview of each of the datasets which are analysedp in Fig. 5.13:

Steidel et al. (2014): The St14 sample consists of N=195 UV-selected galaxies at 2.0< z <2.6 from the KBSS-MOSFIRE survey with a measurement of the N2 index. These galaxies have stellar masses in the range $8.6 < \log(\mathrm{M/M_\odot}) < 11.4$ and Hα based SFRs in the range $2 < \mathrm{SFR_{H\alpha}} < 500\ \mathrm{M_\odot yr^{-1}}$. Of these N=195 galaxies, N=192 satisfy the requisite N2>-1.4 dex condition for using the new calibration. O/H was calculated for each individual galaxies using equation 5.7 and for the purposes of clarity I take the median O/H ratio in 0.2 dex wide bins of stellar mass. Errors in each bin are given by the standard deviation. Masses were derived using a Chabrier IMF so no conversion was required for consistency with our data.

Erb et al. (2006b): The E06 sample consists of N=87 UV-selected galaxies stacked into six bins of stellar mass at $\langle z \rangle = 2.26$. The N2 index is measured on the stacked spectra which cover the stellar mass range $9.1 < \log(\mathrm{M/M_\odot}) < 10.7$. As discussed in Chapter 3, the stellar masses in E06 are quoted as total mass in stars formed rather than the more conventional current stellar mass, to correct for this I have decreased the E06 masses by 0.18 dex. The O/H abundances were calculated from equation 5.7 using the N2 index measurements quoted in the paper.

Sanders et al. (2015): The Sa14 sample consists of N=88 optically-selected galaxies from the MOSDEF survey (Kriek et al., 2015) in the redshift range 2.08< z <2.61. I use N2 index measurements from the stacked galaxy spectra in four stellar mass bins covering the mass range $9.15 < \log(\mathrm{M/M_\odot}) < 11.1$. Sa14

use a Chabrier IMF so no mass conversion is necessary.

Wuyts et al. (2014): The W14 sample consists of N=113 optically-selected galaxies as part of the LUCI, SINS/zC-SINF and KMOS^{3D} surveys at $\langle z \rangle = 2.3$. The W14 galaxies span the stellar mass range $9.50 < \log(M/M_{\odot}) < 10.87$ and the N2 index is measured from stacked spectra in 4 stellar mass bins. Again, W14 use a Chabrier IMF so no mass conversion is necessary

In total, therefore, the full sample at $z \sim 2.3$ consists of N=576 galaxies from various different surveys. The N2 index has in the majority of cases been measured from stacked galaxy spectra (E06, Sa14, W14), and for the St14 data I have taken running medians of the O/H abundance in stellar mass bins to mimic the rest of the measurements. As mentioned above, given the line-luminosity dependence on metallicity (see e.g. Juneau et al., 2014, Chapter 4) ideally one would like a homogeneous dataset for which a luminosity limit could be quantitatively defined. The $L_{[OIII]\lambda 5007} > 41.87$ ergs/s 3D-HST selection defined in this Chapter may not be strictly representative of all other datasets, indeed parts of the Sa14 KBSS/MOSFIRE dataset goes substantially deeper (down to $L_{[OIII]\lambda 5007} > 41.0$ ergs/s for the longest integration times). I have checked that such a difference in luminosity threshold does not significantly affect the N2 - O/H conversion defined by equation 5.7.. Also, since the SFR distributions of the samples, which are a good proxy for [OIII] luminoisity (Fig. 5.7), are similar, I assume the Eq. 5.7 applies to all datasets.

I plot the mass-metallicity relationship for the combined $z \gtrsim 2$ samples in Fig. 5.13. This figure is a direct reproduction of Fig. 5.5 with the new additional datasets. The first point to note is that all the $z \gtrsim 2$ measurements which have been converted to O/H from the N2 index are consistent with the 3D-*HST* data, this is in contrast to the 0.2 - 0.3 dex offset observed in Chapter 3 between the 3D-HST and E06 datasets using the Maiolino et al. (2008) calibration. This implies that, by accounting for the evolution in ionization conditions (demonstrated in Chapter 4), one can reconcile all measurements of the oxygen abundance at high redshift without having to invoke variations in measured SFR, as will be discussed below. I also note that this agreement has also been achieved without invoking any strong evolution in the N/O ratio.

The form for the best-fitting relation, as discussed in Section 5.4 is given by:

$$12 + \log(\mathrm{O/H}) = Z_o - \log[1 + (\tfrac{M_*}{M_o})^{-\gamma}]. \tag{5.8}$$

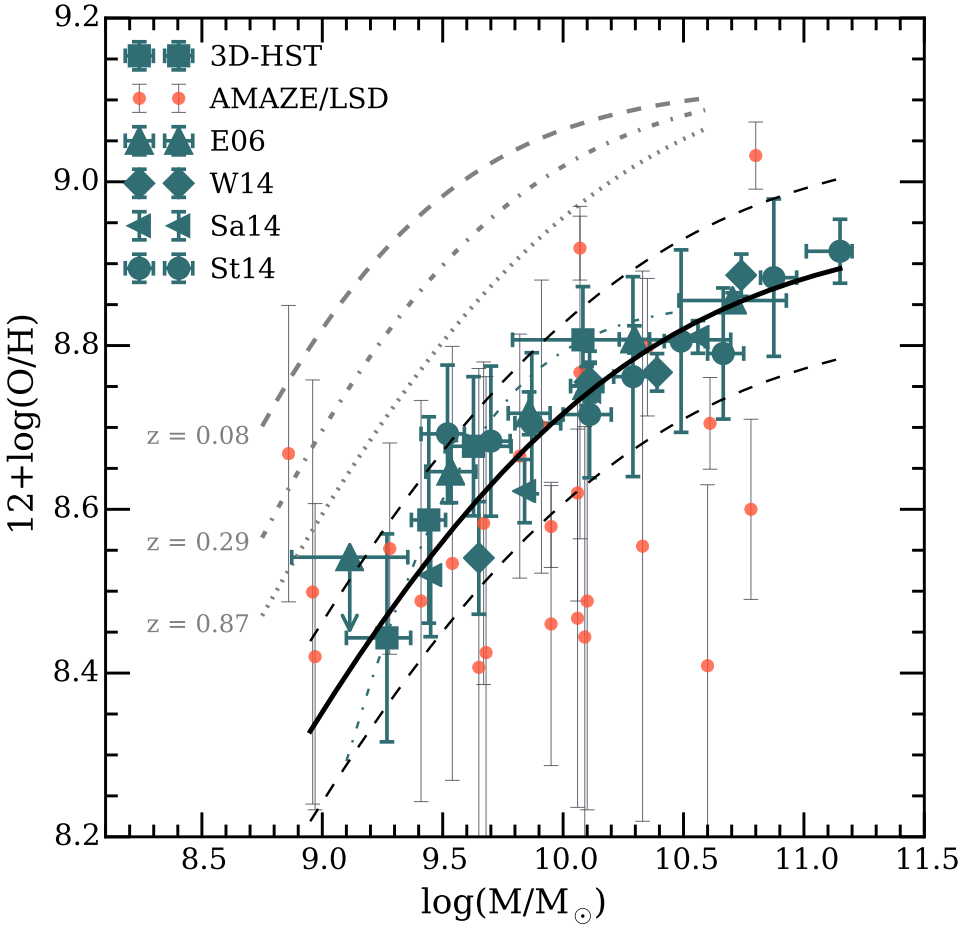

Figure 5.13 *A reproduction of the mass-metallicity data shown in Fig. 5.5 but for the combined $z \gtrsim 2$ samples described in Section 5.6. The solid black line shows new best-fitting function form of the MZR as defined by equation 5.1. All datasets at $z \gtrsim 2$ are in turquoise which symbols described in the legend, while the sample at $z > 3$ (AMAZE/LSD) is in orange.*

The best-fitting parameters for the combined $z \gtrsim 2$ datasets are: $Z_o = 8.85 \pm 0.01$, $\log(M_o/M_\odot) = 9.77 \pm 0.16$ and $\gamma = 0.61 \pm 0.18$. 95% (68%) of all measurements of log(O/H) lie within ± 0.11 (± 0.04) of the best-fitting line; the 95% confidence intervals are how as the dashed lines in Fig. 5.13.

5.6.1 $z = 2 - 3$ Metallicity Evolution

It is potentially instructive to explore how the $z > 3$ metallicities compare to the fitted form of the relation at $z = 2$. Fig. 5.14 illustrates this by showing the metallicity difference as a function of stellar mass between each AMAZE/LSD data point and the $z = 2$ fit. The median metallicity difference (shown as the horizontal orange dashed line) is 0.05 dex with a median absolute deviation (σ_{MAD}) of 0.15 dex, yielding a standard deviation of 0.22 dex ($\sigma \approx 1.4826 \times \sigma_{MAD}$). Also shown in Fig. 5.14 is the metallicity difference between z = 2 and z = 3 taken from the function fits to the AMAZE/LSD and Erb et al. (2006b) data from Maiolino et al. (2008) and Troncoso et al. (2014), it can be seen that here the increase is both mass dependent[6] and on average larger with a median value of 0.37 dex across the mass range visible in the figure. These original AMAZE/LSD studies, in contrast to the measurements presented here, use the Maiolino et al. (2008) metallicity calibration and also compare the N/H-based oxygen abundances of (Erb et al., 2006b) to their direct O/H-based abundances, so in the light of all results presented so far in this thesis it is perhaps not surprising that there is a disagreement.

In Fig. 5.5 I also compare the observations to the metallicity evolution predicted by two current state-of-the-art cosmological hydrodynamic simulations: the Dv2011 model (Dave et al., 2011b,a), and the Ma2015 model (Ma et al., 2015). These two models were chosen to represent two general classes of theoretical model. Dv2011 employs "sub-grid" physics recipes which include empirical prescriptions for various physical phenomena (e.g. galactic winds) while modeling large cosmological volumes. Ma2015, on the other hand, fully resolve the physics of the ISM without the need for pre-determined parameterizations by running "zoom-in" simulations tracking individual dark matter halos across cosmic time. Below I will give a more detailed analysis of each approach and describe how the predictions compare to the observed evolution between $z = 2$ and $z = 3$.

[6]My 0.05 dex offset is not mass dependent simply because it is not possible to fit an MZR to the $z = 3$ data, in reality there is likely to be some mass dependence to the MZR evolution.

Other recent models can be found in, for example, Lu et al. (2014) and Torrey et al. (2014) however these papers do not include parameterizations that can be directly compared to observations.

Dv2011

The Dv2011 models are a suite of cosmological hydrodynamical simulations run with `GADGET-2` (Springel, 2005b) for a boxsize of $48h^{-1}$Mpc, which employ different prescriptions for galaxy scale outflows. Four separate wind recipes are employed in the simulations (no winds, constant winds, slow winds, momentum-conserving winds) and Dv2011 conclude that measurements of the $z = 0$ MZR and its evolution are best matched by outflows driven by momentum-conserving winds, where the wind velocity is proportional to the velocity dispersion of a galaxy, and inflows which become more metal enriched with time. The equation for the metallicity evolution predicted from these models was introduced in Chapter 4 and is described by a 3rd order polynomial giving the change in metallicity (Δlog(O/H)) between $z = 0$ and an arbitrary redshift z as:

$$\Delta\log(\mathrm{O/H}) = -0.0013 - 0.2287z + 0.0627z^2 - 0.0070z^3. \tag{5.9}$$

The equation is formally valid for galaxies with $\log(\mathrm{M/M_\odot}) > 9.0$ and taken from Kewley et al. (2013a). Using this equation, the metallicity evolution between the median redshifts of the 3D-*HST* and AMAZE/LSD samples (2.15 and 3.40 respectively), is 0.06 $\pm$ 0.1 dex and is shown by the solid black line in Fig. 5.5. This is, within the uncertainties, consistent with the data presented here using the KK04 calibration but at odds with the stronger evolution predicted from Troncoso et al. (2014), becoming increasingly discrepant with increasing stellar mass.

Ma2015

The Ma et al. (2015) models are based on the `GIZMO` code developed as part of the Feedback in Realistic Environment (FIRE) project (Hopkins et al., 2014). The FIRE project is a series of high-resolution cosmological "zoom-in" simulations which track individual halos from high redshift down to $z = 0$ covering (final) stellar masses in the range $10^4 - 10^{11} M_\odot$. The simulated galaxies presented in Ma2015 cover a wide range of masses and merger histories. Crucially, by

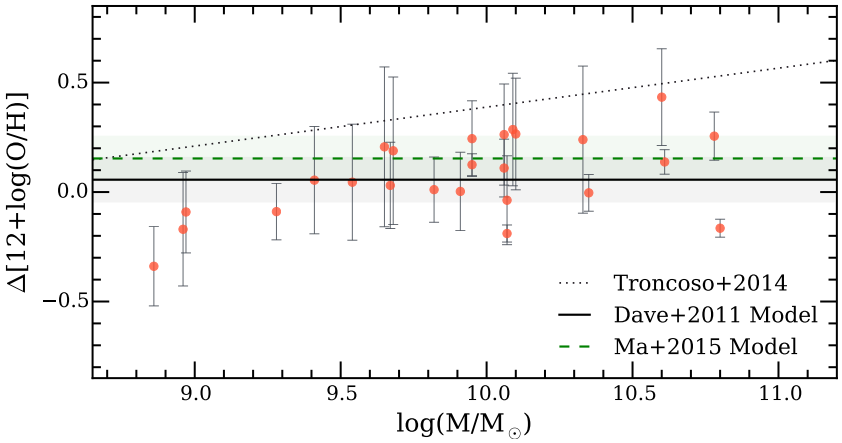

Figure 5.14 *Illustrating the difference in metallicity as a function of stellar mass from $z = 2$ to $z = 3$ using the new best-fitting MZR given by equation 5.8. The orange points show the metallicity difference between the best-fitting $z \gtrsim 2$ MZR and the metallicity of each AMAZE/LSD galaxy. The orange dashed line shows the median value of this difference (0.05 dex). The dotted black line shows the $z = 2$- 3 metallicity difference as a function of mass taken from Troncoso et al. (2014) as described in Sec 5.4. The black solid line shows the evolution from the Dave et al. (2011b,a) models as described in the text with the grey shaded region representing the estimated 0.1 dex uncertainty. The green dashed line shows the evolution from the Ma et al. (2015) models as described in the text with the shaded region again showing a representative ± 0.1 dex uncertainty.*

decreasing the cosmological volume these zoom-in simulations, Ma2015 can implement a full set of realistic physics for the multi-phase ISM, star-formation and feedback, without employing empirical prescriptions.

Ma2015 conclude that the form and evolution of the MZR is driven by (i) efficient metal recycling within galaxies whereby most metals produced are unable to escape the halo even at low stellar masses ($\sim 10^6 M_\odot$) and (ii) the gas/stellar mass fraction evolution with redshift whereby gas fractions are higher at higher redshift. Ma2015 fit a universal linear form of the MZR at all redshifts and derive its evolution between $z = 0 - 6$ as:

$$\log(\mathrm{O/H}) = 9.0 + 0.35[\log(\mathrm{M_*/M_\odot}) - 10] + 0.93\mathrm{e}^{-0.43z} - 1.05. \quad (5.10)$$

Using this equation, the metallicity evolution between the median redshifts of the 3D-*HST* and AMAZE/LSD samples (2.15 and 3.40 respectively), is 0.15 $\pm$ 0.1 dex and is shown by the green dashed line in Fig. 5.5. Again this is, within the uncertainties, consistent with the data presented here using the KK04 calibration but at odds with the stronger evolution predicted from Troncoso et al. (2014), becoming increasingly discrepant with increasing stellar mass. There is also reasonable consistency between the Ma2015 and Dv2011 models (within $\sim$ 0.1 dex) at these redshifts, and it is not possible from the data to clearly distinguish them.

Theoretical Implications

The overall implication of Fig. 5.14 is that correcting metallicity measurements at high redshift for changes in ISM conditions brings the observed metallicity evolution between $z = 2$ and $z = 3$ into better agreement with the both Dv2011 and Ma2015 theoretical models. Therefore, the observations are broadly consistent with a scenario with momentum driven winds ejecting metals for galaxies balanced by the efficient re-accretion of the ejected metal enriched gas. However, better data will be required to constrain in detail the physics driving the MZR and its evolution. More generally, from an observational viewpoint, this work implies that the metallicity evolution between $z = 2$ and $z = 3$ may not be as extreme as currently reported in the literature.

5.7 Revisiting the Fundamental Metallicity Relation

The original motivation for investigating the evolution in ionizing conditions in star-forming galaxies in Chapter 4, and hence revisiting the mass-metallicity relation with the KK04 calibration here, was the observation, presented in in Chapter 3, of a discrepancy between the 3D-*HST* and E06 datasets when measuring the $z \gtrsim 2$ 'fundamental metallicity relation' (FMR). Here I revisit the FMR with the new $z \gtrsim 2$ data and determine whether the redshift evolution of the MZR presented in Fig. 5.13 has a SFR dependence. Also, my improved method of estimating metallicities may elucidate the reason for the $z \gtrsim 2$ discrepancy and determine the nature of the FMR at high redshift.

However, it is first necessary to establish whether, using the KK04 calibration, a FMR exists within the SDSS sample. The original FMR was built using the Maiolino et al. (2008) metallicity calibration, which does not correct for the ionization parameter. Since SFR affects ionization parameter by increasing the number of ionizing photons incident on the ISM of a galaxy, when the metallicity is corrected for the ionization parameter using the KK04 calibration, the form of the FMR is likely to be affected. Also, the SDSS sample presented here is not identical to the Mannucci et al. (2010) sample, and different methods of selection may additionally affect the local form of the FMR (Salim et al., 2014). Therefore, when using a different metallicity calibration and selection method, one must first establish the form, or existence, of the FMR for that calibration.

The most direct way of determining the presence of a FMR, as introduced in Mannucci et al. (2010), is to consider how the scatter of metallicity reduces when plotted against a linear combination of mass and SFR, rather than mass directly. Following Mannucci et al. (2010), the FMR is defined by

$$12 + \log(\mathrm{O/H}) \propto \mu_\alpha \equiv \log(\mathrm{M_*}) - \alpha \log(\mathrm{SFR}) \tag{5.11}$$

Where α is the constant which minimizes the scatter in the 12+log(O/H) vs. μ_α plane. If $\alpha = 0$, the scatter is minimized in the regular mass-metallicity plane and this implies no extra SFR dependence to the MZR. Mannucci et al. (2010) found that the scatter is minimized when $\alpha = 0.32$. The application of this method to the original parameterization of the FMR by Mannucci et al. (2010) is shown

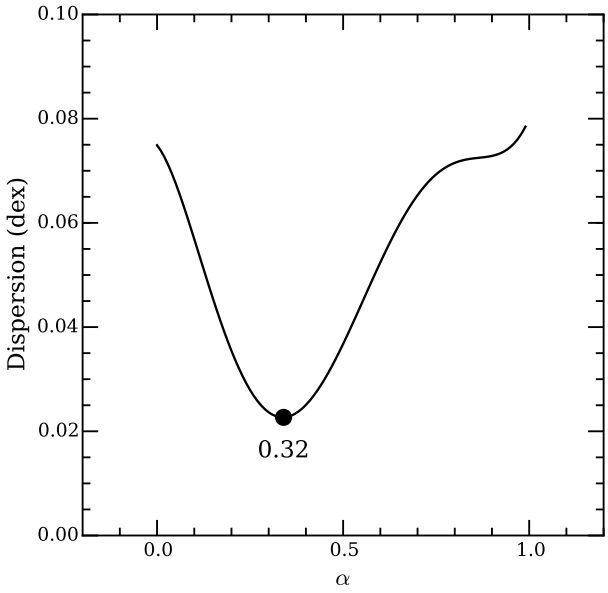

Figure 5.15 *Illustrating the value of α which minimizes the dispersion of 12+log(O/H) at fixed μ_α for the original parameterization of the FMR from Mannucci et al. (2010). The solid lines shows a polynomial fit to the mean value of the scatter in 0.1 dex bins in μ_α which has a minimum dispersion of 0.023 dex at $\alpha = 0.32$.*

in Fig. 5.15 for purely illustrative purposes. To make this plot I generated a synthetic dataset using equation 1 of Mannucci et al. (2010) and measured the mean scatter in 12+log(O/H) in 0.1 dex bins of μ_α. Fig. 5.15 shows a polynomial fit to the mean dispersion as a function of α in the range $\alpha = 0$ - 1, which has a minimum, as expected, at $\alpha = 0.32$.

Using the same method I measured α for the SDSS dataset presented in this chapter with the KK04 calibration. In this case, the scatter of the relation is minimized for $\alpha = 0$, and progressively increases out to $\alpha = 1$ (Fig. 5.16). This implies no SFR dependence, and hence no FMR, of the form proposed by Mannucci et al. (2010). An obvious implication of this result is that it is not possible to revisit the observation in chapter 3, and investigate the nature of the FMR for the sample of $z \gtrsim 2$ galaxies. However, it raises an important question about the true nature of the SFR dependence of the MZR, and how this is affected by different metallicity calibrations and selection effects.

Such an investigation is beyond the scope of this thesis. However, the issue has recently been addressed in Salim et al. (2014), who find that when carefully accounting for sample selection effects and considering a variety of different

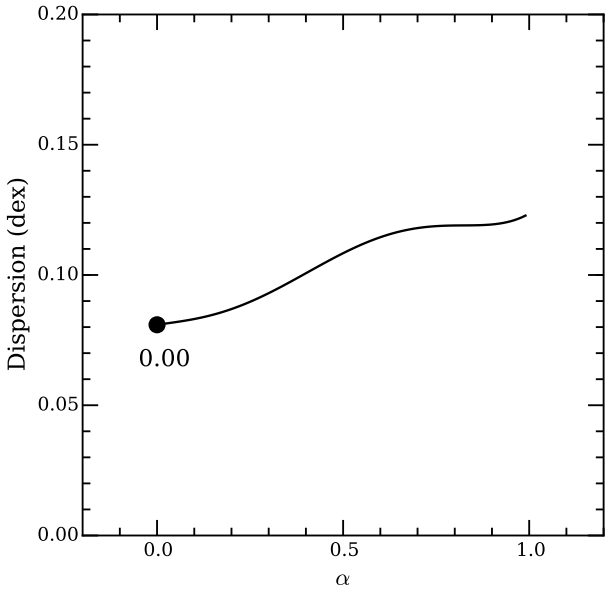

Figure 5.16 *Illustrating the value of α which minimizes the dispersion of 12+log(O/H) at fixed μ_α for the SDSS presented in this chapter using the KK04 calibration. The solid lines shows a polynomial fit to the mean value of the scatter in 0.1 dex bins in μ_α which has a minimum dispersion of 0.081 dex at $\alpha = 0$*

metallicity calibrations, the inclusion of SFR as a third parameter in the MZR (following Mannucci et al. (2010)) does not greatly reduce the scatter in metallicity. Instead they advocate a non-parametric framework for studying the M-Z-SFR relation and find that, in narrow bins of mass, the scatter is more directly related to the relative specific-SFR (sSFR). Clearly, there is still a lot of work to be done to properly understand the true nature of the scatter in the MZR, its relation to SFR, and its redshift evolution.

5.8 Summary and Conclusions

Using a sample of high redshift galaxies I have revisited the evolution of the mass-metallicity relation in the redshift range z = 2 - 3. In order to collate as large as possible a sample of $z \gtrsim 2$ galaxies I have investigated the properties of high redshift analogue galaxies within the local SDSS star-forming galaxy catalogue. In doing so I have been able to create a new conversion between the N2 index and O/H abundance accounting for the increase in ionization parameter with redshift. Below is a summary of the results.

- By directly using the KK04 metallicity calibration on the 3D-*HST* and AMAZE/LSD datasets I provide the first direct measurements of the $z \gtrsim 2$ and $z \gtrsim 3$ MZR's with a calibration accounting for the evolution in ionization conditions with redshift.

- To alleviate this problem of low number statistics I use the SDSS star-forming catalogue to find local analogues of high redshift galaxies. Using these local analogues it is in theory possible to find a conversion between N2 index and KK04-measured O/H which would allow the large number of galaxies at $z \gtrsim 2$ with measured N2 to be robustly compared to the 3D-*HST* and AMAZE/LSD data.

- To do this I select SDSS galaxies which mimic the properties of the 3D-*HST* and AMAZE/LSD sample. I find, following a similar method outlined in Chapter 4 and Juneau et al. (2014), that a line luminosity selection is the best way to find analogues of the high redshift galaxy population. The [OIII] > 41.87 ergs/s luminosity selection I employ broadly mimics $z > 2$ galaxies in terms of the mass, metallicity and SFR distributions, with the exception that there are a lack galaxies in SDSS with the extremely high SFR tail of high redshift population ($\gtrsim 10$ $M_{\odot}yr^{-1}$). This [OIII] line luminosity limit is based on the 90% completeness threshold of the 3D-*HST* sample for $z > 2$ galaxies as derived in Chapter 4.

- I show that it is possible to reproduce other important high redshift observations using these SDSS analogue galaxies. These observations include the offset in the BPT diagram, the offset between N2 and O3N2 metallicity diagnostics using the Pettini & Pagel (2004) calibration, and the position in the mass-metallicity plane and R23 vs. O32 diagram. I also show that there is no evidence for a large increase in the N/O ratio at fixed O/H ratio for these galaxies and therefore elevated N/O ratios are not necessarily needed to explain the high redshift observations.

- Assuming the SDSS analogue galaxies are truly local examples of the high redshift population I use this sample to create a calibration between N2 index and KK04 O/H abundance which by design accounts for the evolution in ionization conditions with redshift. This new calibration can then be used to convert measured $z \gtrsim 2$ N2 index's into an O/H abundance that can be robustly compared to the 3D-*HST* and AMAZE/LSD data. This calibration assumes no strong N/O evolution and that the [OIII] > 41.87 ergs/s luminosity selection is reasonably representative of other $z \gtrsim 2$ data.

- I apply the new N2 - O/H conversion to a sample of N=576 $z \gtrsim 2$ galaxies taken from five separate studies to give a more robust determination of the MZR at this redshift, over a larger range in stellar mass. This new best-fitting MZR is more extensive than any other currently published and is unique in that it is based on a calibration which accounts for the evolution in the ionization parameter of galaxies. I find evidence that the evolution in metallicity at a given mass between z = 2 and z = 3 may not be as large as inferred from current observations made using the Maiolino et al. (2008) calibration. The evolution observed using KK04 is in better agreement with the cosmological hydrodynamic simulations of Dave et al. (2011b,a) and Ma et al. (2015).

- Finally, I revisit the FMR with the new SDSS sample using the KK04 calibration. I find that including the SFR as a third parameter in the MZR, via the original parameterization of the FMR in Mannucci et al. (2010), does not reduce the scatter in metallicity. This may be due to the correction for ionization parameter in the KK04 calibration or the the difference between my SDSS sample and that used in Mannucci et al. (2010). Investigating this issue further, at both low and high redshift, will be and important avenue of future research.

Chapter 6

Conclusion and Future Work

For the research presented in this thesis I have utilized near-IR grism spectroscopic observations of a uniquely large sample of galaxies within the redshift range $1 < z < 3$. The aim has been to study the physical properties of these galaxies using their rest-frame optical emission lines and gain insight into the evolution of the physical conditions in star-forming galaxies across cosmic time. The conclusion of this work will be reviewed in Sec. 6.3 below. First, however, I will outline how I will use the expertise I have gained in near-IR observations of high-redshift galaxies, and in the use of strong optical emission lines for diagnosing physical conditions in star-forming galaxies, to pursue further avenues of research in the future. Specifically I will detail work I have begun using the ground-based near-IR multi-object spectrograph KMOS to extend the study emission lines galaxies presented here to $z > 3$, and how using my near-IR grism reduction expertise I plan to reduce data from the recently begun FIGS survey to search for Lyα emitting galaxies during the epoch of reionization ($z \gtrsim 6$).

6.1 KMOS Deep Survey: Emission lines galaxies at $z > 3$

The K-band Multi Object Spectrograph (KMOS) is a new second-generation near-IR instrument which was commissioned for operation on the VLT in 2012 (Sharples et al., 2013). I am involved as part of a team undertaking observations with KMOS as part of the KMOS Deep Survey (KDS). The survey aims to collect

Table 6.1 *Wavelength coverage and resolution of KMOS gratings*

Grating	Wavelength Coverage (μm)	Resolution (R)
IZ	0.779 - 1.079	3400
YJ	1.025 - 1.344	3600
H	1.456 - 1.846	4000
K	1.924 - 2.460	4200
HK	1.484 - 2.442	2000

a large sample of very deep near-IR observations of star-forming galaxies at $z > 3$ to unveil the physical processes that shape their evolution over the first ~ 4 billion years of cosmic time. Below I will give an overview of the KMOS instrument and survey design as well as detailing my contribution so far to the early observations and data reduction.

6.1.1 Instrument Details

KMOS is a near-IR spectrograph capable of measuring the spectra of astrophysical objects in the wavelength range 0.8 - 2.5μm. The wavelength coverage is, however, not simultaneous and consists of five separate gratings (IZ, YJ, H, K, HK) each with a different wavelength passband and resolution as detailed in Table 6.1. Perhaps the key feature of the KMOS instrument, which distinguishes it from first-generation near-IR ground-based spectrographs (e.g. SINFONI), is its multi-object capabilities, allowing it to observe simultaneously 24 targets as opposed to one object at a time. KMOS has 24 pickoff arms each of which can be positioned on a separate target within a 7.2 arcmin diameter patrol field as illustrated in Fig. 6.1. Each pickoff arm collects the light from a given target, with a square field of view (FOV) of 2.8 x 2.8 arcsec, which is then fed through to an integral field unit (IFU)

The IFU capability represents another unique aspect of the KMOS instrument. Integral field spectroscopy allows us to obtain simultaneously spectra of every spatial element (commonly referred as 'spaxel') within a two-dimensional area of the image plane. There are various techniques to perform integral field spectroscopy, and in KMOS this is performed by using image slicers. With this technique the image is dissected in 14 x 14 slices, providing a spatial resolution of 0.2 x 0.2 arcsec per spaxel The IFU capability of KMOS distinguishes it from the more traditional method of slit spectroscopy where a slit is placed over the object of interest and only light falling within the slit mask is dispersed.

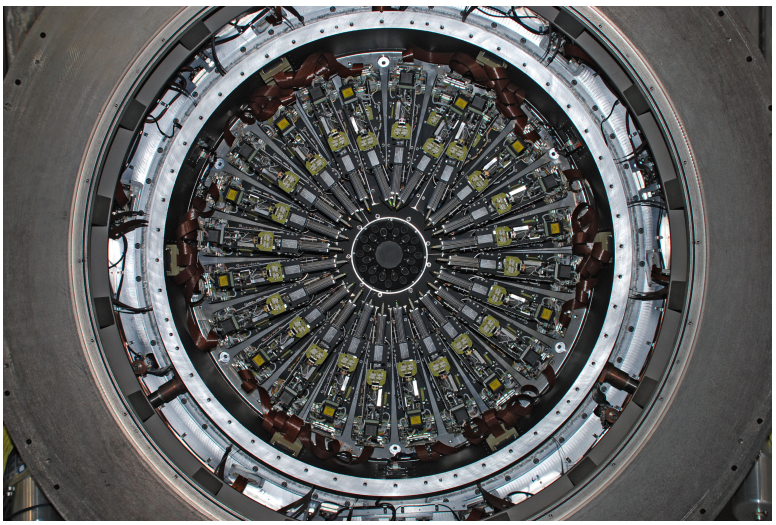

Figure 6.1 *Showing a face-on view of the 24 pickoff arms on the KMOS instrument surrounding the 7.2 arcmin diameter patrol field over which the arms can be positioned when taking observations. The light collected through each pickoff arm is then fed to an individual IFU. The square field of view of each IFU is 2.8 x 2.8 arcsec.*

This slit spectroscopy method is adopted by the other second generation near-IR spectrograph MOSFIRE on the Keck-I telescope (McLean et al., 2012). With slit spectroscopy, one must be careful to account for slit loss corrections arising because the slit mask only covers a portion of the object of interest. A major advantage of the IFU method is that, assuming the object of interest fits within the 2.8 x 2.8 arcsec FOV (as will be the case for high redshift galaxies), all light from the object will be collected across all spaxels and the total integrated spectrum of the galaxy can be found be summing the spaxels. Moreover, using an IFU one can measure spatial trends within a galaxy, for example tracing kinematics and gradients of metallicity and star-formation.

KMOS has two major advantages over the current state of the art space-based near-IR spectroscopy taken with the WFC3 grisms on *HST* as presented in this thesis. Firstly, the wavelength coverage is much broader (0.8 - 2.5μm compared to 1.1 - 1.7μm), in particular the extension in to the K-band allows us to study of emission line galaxies out to much higher redshifts with KMOS (e.g Hα out to $z \sim 2.8$ and [OII] out to $z \sim 5.7$). Secondly, the spectral resolution is improved with respect to the G141 grism by a factor ~ 30 meaning that the issue of line blending encountered in grism spectra is removed. However, the crucial drawback of any ground based near-IR observations is the strong sky background which must be carefully accounted for in any observation, as will be discussed in more detail below. First, however, I will give a brief overview of the science I will help

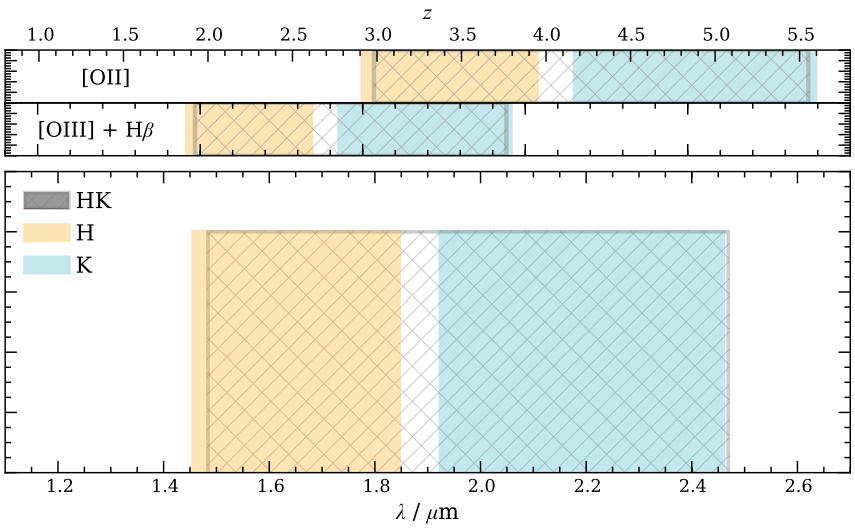

Figure 6.2 *Showing the redshift intervals in which the [OIII], Hβ and [OII] lines are visible in the H, K and HK KMOS gratings. The bottom channel shows the wavelength coverage of the three gratings approximating the transmission curve as a perfect top-hat for convenience. The upper two panels show, for each of the filters plotted, the redshift intervals in which the [OIII]+Hβ, and [OII] lines are visible.*

carry out with the KMOS instrument as part of the KDS survey.

6.1.2 KDS Overview

The three main science objectives of the KDS are:

- Spectroscopically follow-up more that 100 Lyman-break galaxies at $z > 7.5$ and unveil the physics of cosmic re-ionization.
- Measure spatially resolved SFR, metallicity and kinematics for ~ 200 star-forming galaxies at $z > 3$ in a wide range of stellar masses and SFR, to determine fundamental scaling relations and whether galaxies are formed inside-out, via mergers and/or the fast accretion of cold gas via cooling.
- Establish the star-formation history and dynamics of about 50 passive/quiescent galaxies at $1.5 < z < 2.5$.
- Tentative detection of [CIII] and HeII in > 50 galaxies at $z > 5$.

The interesting spectral features and estimated final sample sizes are given in Table 6.2. Following on the research I have done during my Ph.D., and described

Table 6.2 *Summary of KMOS Science Objectives*

Science Objective	Spectral Features	KDS Sample
$z > 7$	Lyα	> 200
$3 < z < 5.5$	[OIII], [OII], Hβ	~ 200 100
$z \simeq 2$	$4000\AA$ break, Hδ, Hγ	~ 50
$z \sim 5$	[CIII]	~ 50

in this thesis, the study of the chemical abundance in galaxies at $z > 3$ with KMOS is the natural extension. It is hoped that the KDS will be able to measure strong nebular emission lines in > 200 galaxies in the redshift range $3 < z < 5.5$, with several possible science outcomes. As highlighted in Chapter 5, there is at present a lack of galaxies with gas phase metallicities measured at $z > 3$ (N $\simeq$ 30) making it difficult to make any strong inferences on the form of the mass-metallicity relation at these redshifts. As can be seen from Fig. 6.2 the [OIII], Hβ and [OII] lines fall simultaneously within the KMOS HK filter in the redshift range $3.0 < z < 3.8$. As demonstrated at various points throughout this thesis, with these lines it is possible to measure simultaneously the metallicity and ionization parameter of galaxies with the Kobulnicky & Kewley (2004) R23 + O32 calibration, and the large KDS sample will enable me to extend my work at $z \gtrsim 2$ to a statistically significant sample of galaxies at $z > 3$. Uniquely, I will also be able to measure the spatially resolved metallicities of these galaxies with the IFU capabilities of KMOS; despite their high redshifts, it has been shown from *HST* imaging that a substantial fraction of these galaxies have half-light radii of a several kpc (e.g. Bruce et al., 2012) so spatially resolved spectroscopy is still possible as has been demonstrated by the AMAZE/LSD survey (Maiolino et al., 2008; Mannucci et al., 2009; Troncoso et al., 2014). Furthermore, Maiolino et al. (2008) and Troncoso et al. (2014) have shown that it is possible to detect the [NeIII]λ3869 emission line in $z > 3$ galaxies, this line can serve as an additional tracer of the ionization state of the gas (Levesque & Richardson, 2014), and has recently been observed to be unusually strong in stacked spectra of $z \gtrsim 2$ galaxies making it a potentially useful diagnostic for the changing physical conditions in HII regions at high redshift (Zeimann et al., 2015). In addition I will also be able to measure spatially resolved SFRs with Hβ and [OII] and kinematics via the velocity shifts of [OIII] or [OII]. As can be seen from Fig. 6.2, these SFR and kinematics measurements can be extended out to $z \simeq 5.5$ with the [OII] line.

In total, the combination of all these measurements will provide the first detailed picture of the chemical, structural and dynamical build up of star-forming galaxies

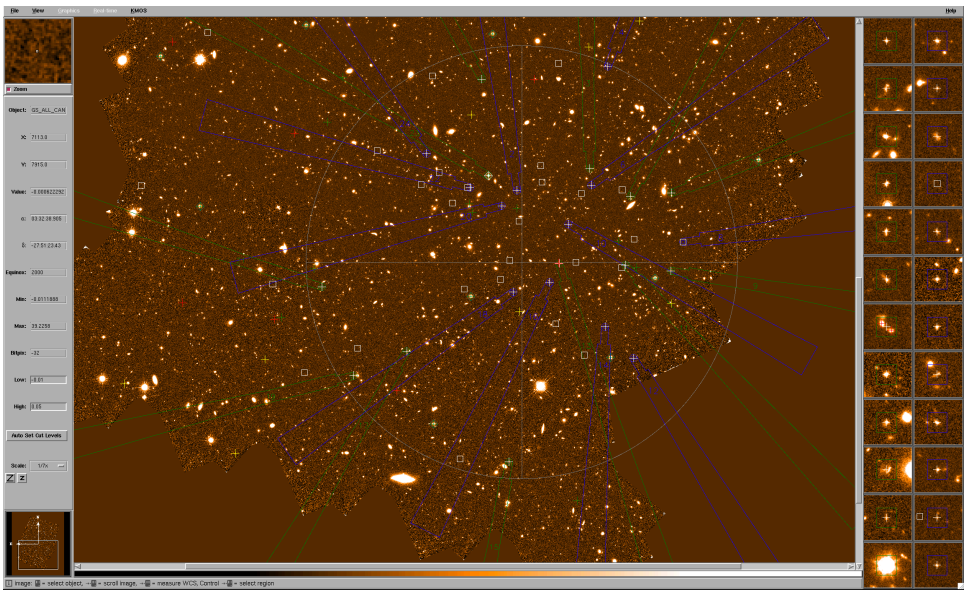

Figure 6.3 *Illustrating the KMOS Arm Allocator (KARMA) software used to prepare KMOS observations. The central panel shows a CANDELS mosaic with the large circle representing the KMOS patrol field with the green and blue KMOS arms situated within it. The right hand image thumbnails show zoom-ins of each of the 24 allocated targets.*

over the first $\sim$ 2 Gyr of cosmic time, revealing in unprecedented detail the mechanisms by which the precursors of todays massive galaxy population were forming in the early Universe. I have been involved in two observing runs and some of the early data reduction as part of the KDS survey team as will be described below.

6.1.3 Observations

Preparation of Observations

I have been involved in both target selection and observation preparation as well as taking part in two of the runs out at the VLT in Paranal, Chile. As discussed above, one of the most unique aspects of the KMOS instrument is the multiplex capability, with the 24 pick-off arms which allow one to take spectroscopy of multiple objects in the patrol field simultaneously. However, this unique feature also adds a extra dimension of complexity when preparing observations, as one must be careful when attempting to assign each of the arms within a given field-of-view to targets with different priorities. This can be particularly troublesome with high redshift observations when targets can be spread over a wide sky area.

I have been involved in preparing KMOS observations with the KMOS Arm Allocator (KARMA) software. As shown in Fig. 6.3, KARMA allows the user to input a target list with a given set of priorities and has some in-built algorithms to optimally position the arms, for a given patrol field position provided by the user, such that the maximum number of top priority targets are allocated. For the KDS survey of $3 < z < 5.5$ galaxies we base our priority (from high to low) by objects with a previous measured spectroscopic measurement with the Lyα line, spectra with [OII] line visible in the 3D-*HST* spectra with a good photometric redshift solution at $z > 3$, and objects with a secure photometric redshift at $z > 3$ with evidence for on-going star-formation in the rest-frame UV. In addition, reference stars must be provided to allow KMOS to accurately acquire the faint high redshift targets and a nearby guide star must be found (defined by having R-band magnitude $8 < \mathrm{R_{Vega}} < 12$) to allow the telescope track during observations.

Sky Subtraction

An important aspect of ground-based near-IR spectroscopy which must be taken into account when preparing observations is the sky line emission. The sky emits in the near-IR across essentially the whole of the 0.8 - 2.5μm wavelength range of the KMOS gratings, and dealing with this sky emission is one of the most difficult aspects of near-IR spectroscopy. Fig. 6.4 shows an example of this sky emission across the HK grating, with a model spectrum of a $z = 3.3$ galaxies over-plotted for reference. Moreover, this sky emission is time varying and therefore it is not possible to use any kind of 'master' sky background as is used with the 3D-*HST* space-based observations (see Chapter 2). Instead, the time dependent variation of the sky emission must be measured during the observation in order to accurately remove sky lines from the final spectra.

To achieve this we adopt a 'nod-to-sky' strategy whereby the instrument intersperses object exposures with pure sky exposures according to a user specified pattern. The positions of the KMOS arms for the sky exposures is configured manually by the user when preparing the observations with KARMA. For high redshift galaxies (because they are very faint) it is recommended that a sky frame is taken for every one, two or four object frames to achieve optimal sky subtraction (i.e either the sequence AB AB, ABA ABA or AABAA AABAA where A is an object frame and B is a sky frame). Once a given sky sequence has been

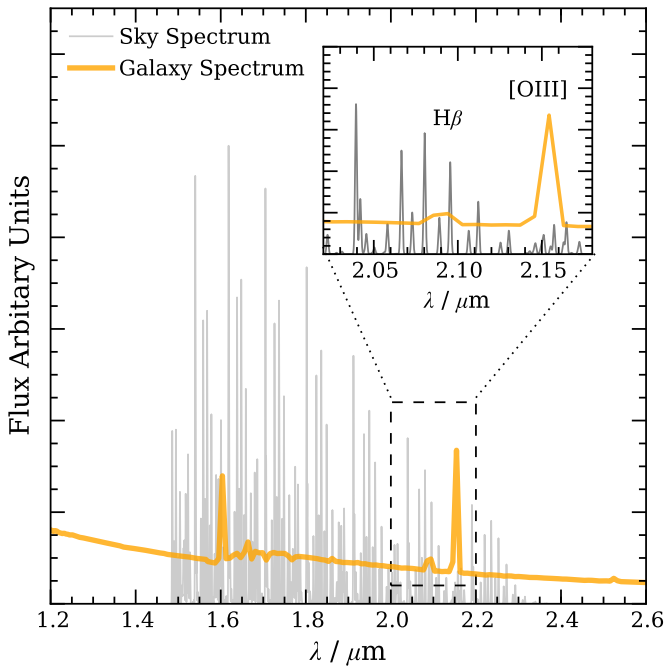

Figure 6.4 *Example of the sky spectrum across the KMOS HK grating. The grey curve shows the sky lines which cover the full extent of the wavelength range, over-plotted in orange is an example spectrum of a star-forming galaxy at $z = 3.3$. The inset axis shows a zoom-in over the [OIII] and Hβ lines showing the fine structure of the sky lines.*

decided upon, the KMOS data pipeline (see below) automatically deals with the sky subtraction by using the closet sky frame to a given observation frame as the assumed sky background. For the early KDS science observations we have experimented with the two or four sky frames strategy depending on the science goal.

6.1.4 Data Reduction

I have also been involved in some of the early data reduction for the KDS survey using the ESO provided data reduction pipeline[1]. The pipeline provides a complete set of recipes for reducing the raw instrument data into final 3D data products, i.e. a spectra for every 0.2 x 0.2 arcsec pixel of a given object. At present I have simply used the pipeline in its fully automated mode, though in future I plan to modify some of the pipeline recipes to optimize the pipeline for extremely faint high redshift targets. A detailed description of this fully automated pipeline is given in Davies et al. (2013) but for completeness I will give a brief summary of the steps here.

Firstly, all observations must be properly calibrated; this includes a flat field correction to account for pixel-to-pixel variations in detector gain, a master dark to correct for bad ('hot') pixels, and a wavelength calibration. The flat-field, dark and wavelength calibrations are updated daily for the instrument. Once the raw data have been corrected for these effects, the data from a given set of observations can be combined. For each IFU, the pipeline selects object-sky pairs, choosing the closest in time sky frame for a given object frame (given the chosen sequence a sky frame may be used for multiple object frames). The object frames are sky-subtracted, telluric corrected (flux calibration using spectrum of a standard star) and finally combined into the final data cube which consists of a spectrum for each spatial pixel in the IFU. The number of spatial pixels can be increased from the standard 14 x 14 by combining dithered observations in a similar way to described in Chapter 2 with reference to increasing the resolution of *HST* images.

An example of the final products of the KMOS pipeline are shown in Figs. 6.5 and 6.6, taken from K-band observations of a galaxy at $z = 3.41$. Fig 6.5 shows the final IFU cube images at the wavelength of the [OIII]λ5007 line; each pixel

[1]http://www.eso.org/sci/software/pipelines/

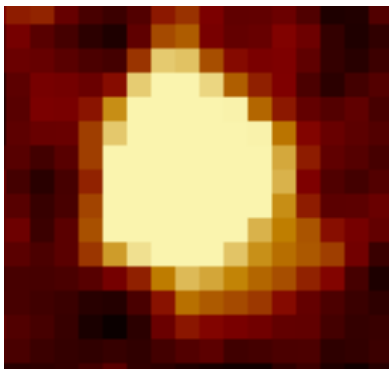

Figure 6.5 *An example image of the $z = 3.41$ galaxy shown in Fig. 6.6 generated by collapsing the 3D data-cube at the wavelength of the [OIII]λ5007 line. Each pixel in this image has its own spectrum allowing spatial variations of emission line features to be investigated.*

visible in the image has a full K-band spectrum and therefore this image can be created at any desired wavelength. Fig. 6.6 shows the collapsed 2D and 1D spectrum obtained by placing a 'pseudo-slit' across the IFU, analogous to conventional 2D slit spectroscopy, with the advantage that the pseudo-slit can be defined to guarantee that all light from the galaxy is contained within it. In both the 1D and 2D spectrum the [OIII] and Hβ lines are clearly visible and the increased resolution compared to the 3D-*HST* data is clearly apparent (e.g. see with Fig. 3.3 in Chapter 3 to compare with grism spectra).

These two examples illustrate the quality of the data it is possible to obtain out to $z > 3$ with KMOS but are only a very basic examples of how the data can be used. With the fully reduced data it will be possible to trace spatial gradients in line fluxes and ratios, investigate the dynamics and kinematics of these galaxies, however, all this will be the subject of my future work.

6.2 FIGS: Lyα emitters at $z \gtrsim 6$

The Faint Infrared Grism Survey (FIGS) is a cycle 22 *HST* programme (Proposal ID: 13779, P.I. Malhotra) which aims to use the WFC3 G102 grism in four separate pointings to measure the observed-frame near-IR spectra of an estimated $\sim$ 6,000 galaxies down to a continuum limit of J = 26.5 (AB), and a line flux limit of 4 x 10^{-18} ergs/cm^2/s. With this unprecedented depth, the FIGS survey will be able to probe the spectra of galaxies during the reionization epoch at $5.5 < z < 8.5$ and place useful constraints on whether these early galaxies were

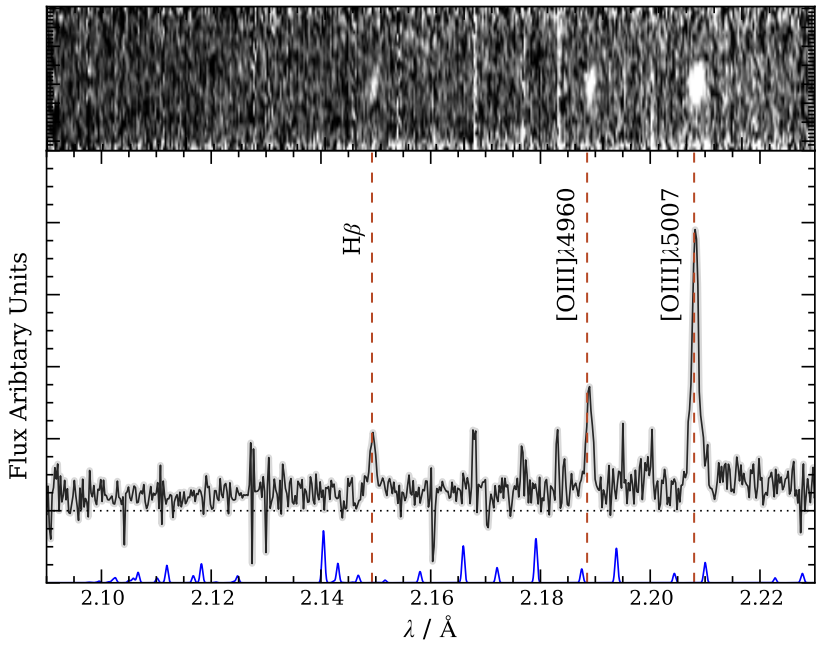

Figure 6.6 *Showing an example of a $z = 3.41$ galaxy spectrum taken as part of the KDS survey. The bottom panel shows the 1D spectrum with the [OIII]λ4958, [OIII]λ5007, and Hβ emission lines labeled. The top panel shows a 2D spectrum generated by collapsing the 3D data cube into a 2D 'pseudo-slit'. An example sky spectrum is shown, offset from the 1D spectrum, in blue*

responsible for re-ionizing the Universe. Below I will give an overview of the technical aspects and science goals of the survey and briefly describe the work I have conducted to date.

6.2.1 Survey Overview

FIGS will cover four pointings with the WFC3 G102 grism in two of the CANDELS survey fields, two pointings in GOODS-S (one being the Hubble Ultra Deep Field) and two pointings in GOODS-N. Each pointing will be observed at five separate roll angles to enable a more accurate estimation of the contamination of a given spectrum, and increasing the likelihood that a spectrum will be observed contamination-free in at least one of the orientations. Each orientation will get two full *HST* orbits equating to a total exposure time of $\sim$ 1.92 x 10^4s per roll angle, and hence a combined total exposure of $\sim$ 9.6 x 10^4s for each of the four pointings. Compared to the 3D-*HST* survey I have used throughout this thesis, which consists of $\sim$ 150 separate pointings each with a total exposure time of $\sim$ 5000s, it is clear that the FIGS survey is an attempt to go much deeper over a significantly smaller area. The factor $\sim$ 20 increase in exposure time gives a factor $\sim$ 4.5 increase in the S/N noise. Also, crucially, FIGS will use the shorter wavelength G102 grism as opposed to the G141 grism, the reasons for this choice will be made clear in the science goals described below.

FIGS observations began in October 2014 and, to date, data for each of the four fields has been taken at one roll angle. The full survey is estimated to be completed by January 2016, therefore this will be a project that is ongoing over the next 1 - 2 years. Below I will outline the main science goals of the survey and describe some of the preliminary work I have conducted.

6.2.2 Science Objectives

The principal science objective of the FIGS survey is to obtain deep space-based spectroscopy of very high redshift galaxies during the first $\simeq$ 1 Gyr of cosmic time (i.e. $z \gtrsim 6$). The study of these early galaxies represents a vast area of research which is to a large extent distinct from the work I have presented in this thesis. For this reason, I will give a brief description of this topic in the context of the FIGS survey, but for a detailed overview see Dunlop (2013).

Exploring the $z \gtrsim 6$ galaxy population is an important astrophysical observation for a variety of different reasons. Firstly, and fairly obviously, in order to test our understanding of the formation and evolution of the first galaxies, it is always useful to push our observations of the Universe as far back in cosmic time as possible with the available instrumentation. Secondly, by measuring the global population statistics such as the UV luminosity function (LF) can help us constrain the star-formation rate density and thus how quickly galaxies are building up their stellar mass at these early epochs. Thirdly, and perhaps more intriguingly, at $z \gtrsim 6$ we are observing a population of galaxies close to the epoch of reionization, the transitional period between the neutral intra-galactic medium (IGM) after recombination ($\sim$ 370,000 years after the Big Bang), and the fully ionized IGM that exists today. Tracing the UV output from these early star-forming galaxies will help us understand how, and over what timescale, reionization proceeded.

Fortunately, with good quality observations, finding these early galaxies is relatively straight-forward. Since the original pioneering work of Steidel et al. (1995), the Lyman-break or 'dropout' technique for photometrically identifying high redshift galaxies has proved extremely successful (e.g. Bouwens et al., 2007; Schenker et al., 2013). This method is based on the fact that neutral hydrogen along the line-of-sight between us and a given galaxy, as well as the neutral hydrogen within the galaxy itself, will almost completely absorb its emitted light blue-ward of the $\lambda_{\rm rest} = 912$Å Lyman-limit, creating a sharp break in the SED (Fan et al., 2006; Mortlock et al., 2011). At $z > 6$ this break is in the near-IR, therefore these galaxies will be invisible to optical telescopes but detectable in near-IR images. More recently, this technique has been refined by using full stellar population synthesis fitting on the observed photometry, essentially using the same photometric redshift technique as described in Chapter 2. This full photometric redshift fitting method (Fig. 6.7) is, unlike the original dropout technique, better able to quantify sample contamination by low redshift galaxies or cool brown dwarf stars, and also provides a direct way to estimate the redshift probability distribution (e.g. Bowler et al., 2014; McLure et al., 2013). With the advent of the WFC3 near-IR camera on *HST* this technique has been employed to identify hundreds of $z > 6$ galaxy candidates, with the deepest photometric sample to date obtained as part of the Hubble Deep Field (HUDF) 2012 campaign (Ellis et al., 2013).

While these photometric observations have allowed us to develop a good

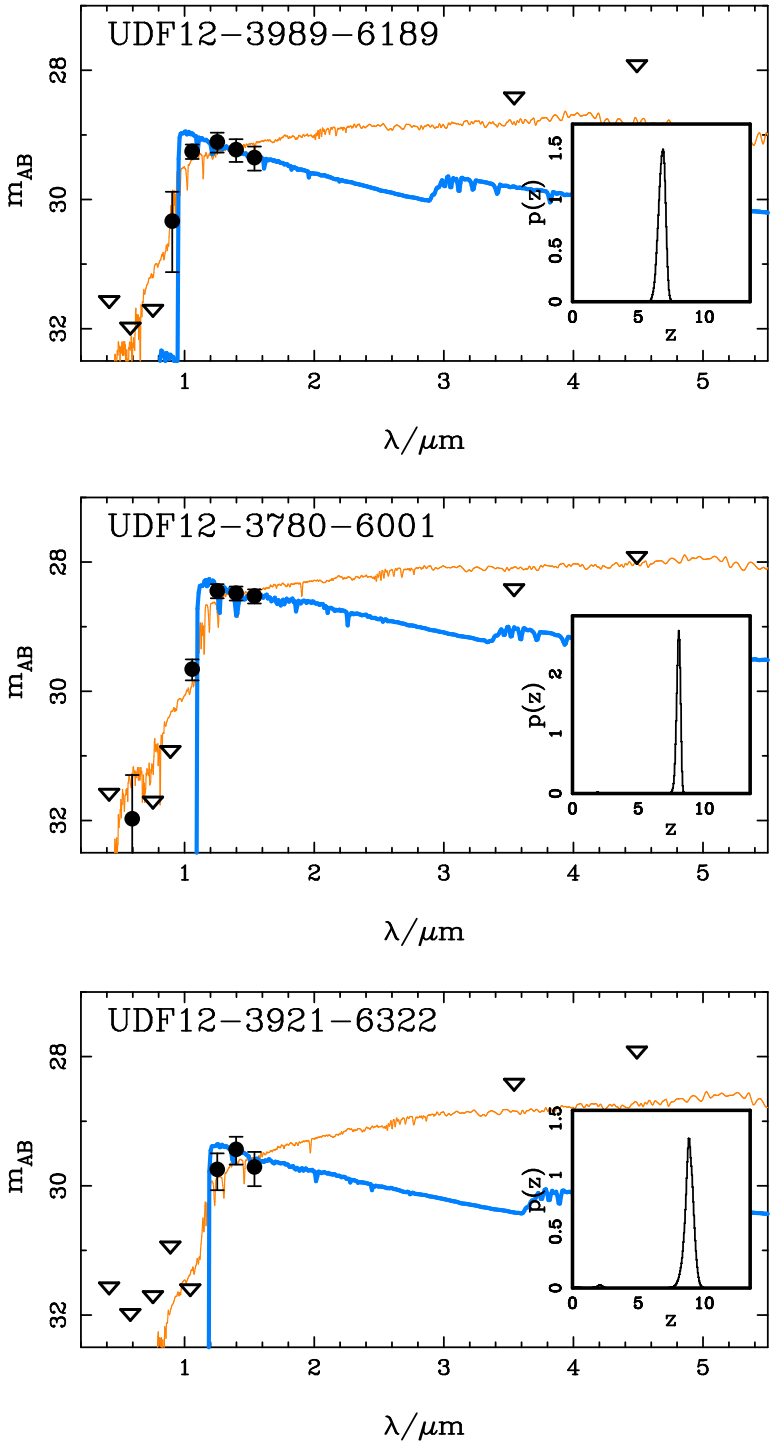

Figure 6.7 *Examples of the photometric redshift technique used for selecting $z \gtrsim 6$ galaxies (taken from McLure et al. (2013)). In each panel the black points show the observed photometry with upper limit shown as downward pointing arrows. The blue curve shows the best-fitting high redshift solution and the orange curve shows the alternative low redshift solution, the inset panel shows the final redshift probability distribution $p(z)$ from this analysis.*

knowledge of the population statistics at these redshifts, most notably through the measurement of the UV luminosity function, getting a more detailed insight into the $z > 6$ population requires spectroscopic observations, particularly for investigating the reionization epoch. At these redshifts, spectroscopic follow-up is for the time-being limited to detection and measurement of the Lyα emission line. Firstly, and most mundanely, detecting Lyα provides a confirmation of the photometric selection technique and a much more robust measurement of the galaxy redshift. Additionally, the detection or non-detection of Lyα can inform us about the ionization state of the IGM, which is expected to vary as a function of redshift during reionization. There is, at present, tentative evidence for a decline in the fraction of Lyα emitting galaxies at $z \simeq 7$ compared to $z \simeq 6$ (Caruana et al., 2014; Ono et al., 2012; Pentericci et al., 2011; Schenker et al., 2012). This result, in addition to the observed increase of the Lyα emitter fraction from $z = 0$ to $z \simeq 6$ (possibly due to a decreasing dust content in galaxies with redshift), is intriguing evidence for an increasing fraction of neutral hydrogen in the IGM at $z > 6$. If confirmed, it would be a tantalising sign that we are beginning to probe normal star-forming galaxies at the frontier of the reionization epoch. It is in this field in particular that spectra obtained through the FIGS survey will play an important role.

As illustrated in Fig. 6.8, the Lyα emission line should be visible in the G012 grism from $z \simeq 5.5$ to $z \simeq 8.5$. Moreover the FIGS survey covers the GOODS-S and GOODS-N field where deep photometric data is available down to $M_{UV} \simeq -17$, and many photometrically selected $z > 5.5$ galaxies have been found. Therefore I intend, over the next couple of years, to use the FIGS survey to investigate the Lyα emitter population fraction at $5.5 < z < 8.5$. This deep, small area survey, will complement other ground based efforts to measure Lyα emission over wider areas with the added benefit of being free from atmospheric sky-line contamination.

6.2.3 Work to date

To date I have begun preliminary work in reducing the currently available FIGS data, this has involved slightly modifying the pipeline described in Chapter 2 to be compatible with the G102 grism (this mainly involves changing certain configuration files). The current reduction does not include a careful treatment of the background as described in Chapter 2, for this I will need to generate a

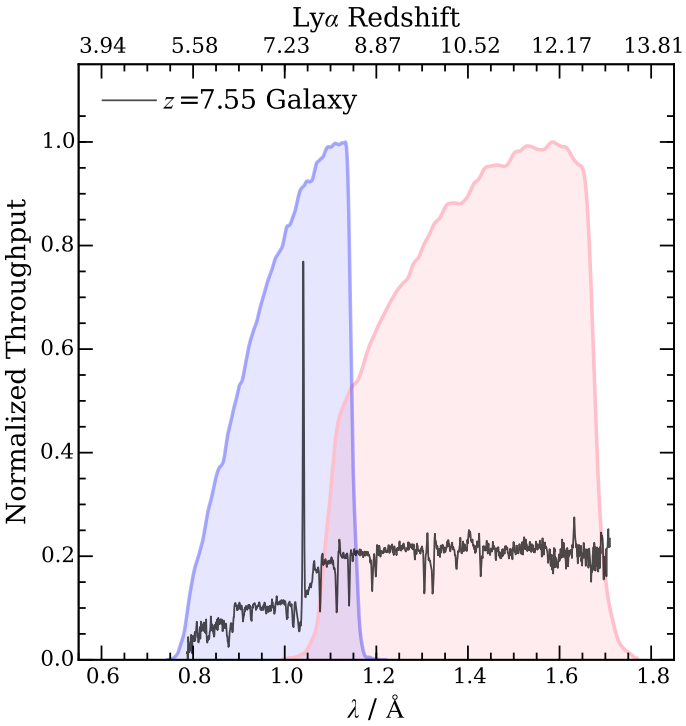

Figure 6.8 *Showing the normalized sensitivity curves (for the 1st order spectra) of the G102 (blue) and G141 (pink) grisms. Also shown for reference is a composite spectrum of a $z \sim 3$ Lyα emitting galaxy (Shapley et al., 2003) redshifted to $z = 7.55$. The top axis shows the Lyα redshift corresponding to a line detection at the wavelength shown on the bottom axis.*

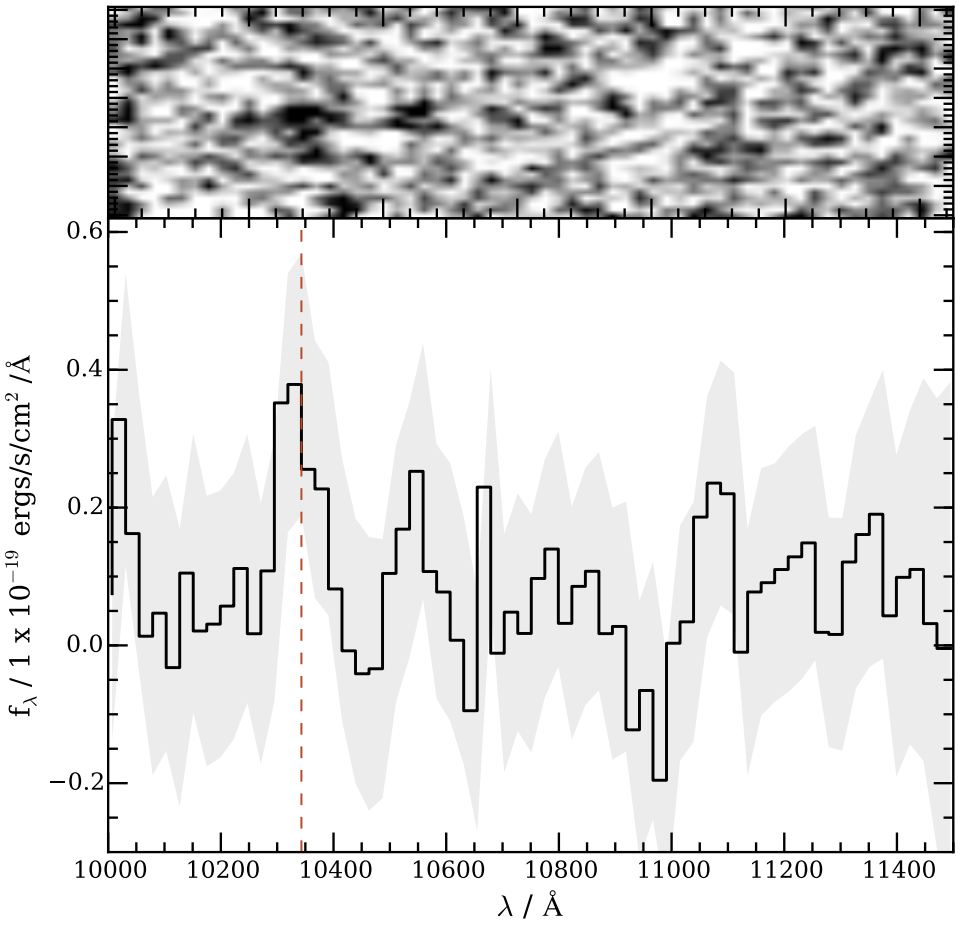

Figure 6.9 *An example of a spectrum from a preliminary reduction of data from the FIGS survey. The bottom panel shows the 1D spectrum of the claimed Lyα emitting galaxy at $z = 7.51$ from Finkelstein et al. (2013). The spectrum is shown as the black stepped curve with the grey shaded area showing the $\pm 1\sigma$ error. The orange dashed line shows the wavelength of the Lyα line detected in the MOSFIRE spectrum from Finkelstein et al. (2013). The upper panel shows the 2D spectrum.*

more representative set of 'master' G102 sky backgrounds than the default sky background provided by the aXe pipeline. Also all preliminary runs so far have not included the full quantitative contamination modeling.

Nevertheless, in Fig. 6.9 I show an example spectrum from these preliminary FIGS runs. The figure shows the G102 spectrum of the claimed $z = 7.51$ galaxy from Finkelstein et al. (2013), who detected a prominent emission line at $\lambda = 10343$Å from ground-based MOSFIRE observations, which, based on the photometric redshift solution and other considerations, they concluded was the Lyα emission line making it one of the highest redshift galaxies with Lyα detection observed to date. As can be seen from Fig. 6.9 the preliminary reduction does indeed shows sign of emission at $\lambda = 10343$Å. However, at this stage, due to the lack of robust contamination modelling and background subtraction it is too early to make any firm conclusions based on the FIGS spectrum. Nevertheless, this will clearly be an interesting early observation to make with the FIGS survey. The main advantage of the FIGS data being the lack of contaminating sky lines which contribute the major source of uncertainty in the Finkelstein et al. (2013) detection.

Over the next few years I will investigate the spectra of photometrically selected $5.5 < z < 8.5$ galaxy to simultaneously assess the quality of the photometric selection and estimate the Lyα emission fraction across the redshift range. This will represent a second branch of my research independent of the metallicities and ionization parameter investigations of galaxies at $2 < z < 5$.

6.3 Thesis Conclusions

In this thesis I have studied the rest-frame optical emission of star-forming galaxies at the peak epoch of cosmic star-formation ($1 \leq z \leq 3$), comparing the properties of these galaxies to star-forming galaxies in the local Universe. The majority of the observations presented here have been taken from a custom reduction of the 3D-*HST* near-IR grism spectroscopic survey. The 3D-*HST* survey represents, at present, the largest homogeneous collection of near-IR spectra at $z > 1$, and in Chapter 2 I give a detailed description of the 3D-*HST* data reduction pipeline I developed as part of my thesis work. In Chapter 3, I use a subset of the 3D-*HST* spectra, in the redshift range $2.0 < z < 2.3$, to measure galaxy metallicities with the [OII], [OIII] and Hβ emission lines in

order to investigate the mass-metallicity and fundamental metallicity relations. In Chapter 4, motivated by the results to Chapter 3, I have explored the physical conditions of star-forming regions in the redshift range $0 < z < 4$ through the evolution of the [OIII]/Hβ line ratio, using the 3D-*HST* spectra to place crucial constraints on the evolution in the redshift range $1.3 < z < 2.3$. Finally in Chapter 5 I have explored how more extreme ionization conditions at high-redshift can affect the measurement of metallicities.

To conclude this thesis, I now present a final review of all the most important results from each chapter.

- Using the Maiolino et al. (2008) empirical metallicity calibration, I show that the mass-metallicity relationship is observed in a sample of N=93 3D-*HST* galaxies at $2.0 < z < 2.3$. For the first time, with a statistical sample of galaxies at this redshift, I derive the O/H abundance ratio directly from measurements of the oxygen and hydrogen lines.

- Strangely the mass-metallicity relationship I measure is offset to lower metallicities at a given stellar mass compared to the z $\gtrsim$ 2 MZR of Erb et al. (2006b). Crucially, the metallicities in the Erb et al. (2006b) study are based on converting a measured N/H ratio to O/H abundance. This observation hints at a potential systematic issue when measuring high-redshift metallicities.

- I also show that, contrary to previous claims, $z \gtrsim 2$ galaxies are not necessarily consistent with the locally defined fundamental metallicity relation (FMR), and that different conclusions can be reached depending on the method for measuring metallicity. Specifically, the N/H-based metallicities of Erb et al. (2006b) are FMR-compatible, whereas the 3D-*HST* O/H-based metallicities are not.

- Based on the strange discrepancy between metallicity measurements I use the line ratio evolution of the [OIII]/Hβ ratio to probe the physical conditions in star-forming galaxies across cosmic time. I first demonstrate how, when trying to measure the [OIII]/Hβ line ratio evolution, one must be careful to select [OIII] luminosity complete samples, due to correlations between $L_{[OIII]}$ and [OIII]/Hβ.

- Once these completeness effects have been accounted for I am able to show that there is a genuine evolution in the [OIII]/Hβ ratio from $z = 0$ to $z = 4$.

- Comparing this evolution to stellar spectral synthesis and photoionization modeling I conclude that this evolution cannot be accounted for purely by a model in which the metallicity of star-forming regions decreases with time. Instead it requires an increase on the amount of hydrogen ionizing photons incident on unit area of the ISM per second. Moreover, the data cannot rule out a model in which the ISM pressure, or equivalently electron density, of HII regions simultaneously increases with redshift.

- Based on these model predictions, I discuss how this evolution in physical conditions can bias locally calibrated metallicity calibrations such as those of Maiolino et al. (2008) and Pettini & Pagel (2004). I show how evolving ionization conditions can neatly explain the offset observed between the O/H-based metallicities of 3D-*HST* and the N/H-based metallicities of Erb et al. (2006b) at $z \gtrsim 2$, thus emphasizing the need for the proper treatment of other physical parameters when estimating the metallicity of high-redshift galaxies.

- On account of this result, I revisit the $z \gtrsim 2$ mass-metallicity using the theoretical metallicity calibration of Kobulnicky & Kewley (2004) (KK04). KK04 simultaneously solves for metallicity and ionization parameter and is thus capable of accounting for an evolution in ionization conditions with redshift. I provide the first direct, ionization parameter sensitive measurement of the $z \gtrsim 2$ MZR with the 3D-*HST* data.

- In an attempt to increase the sample size with which to measure the $z \gtrsim 2$ MZR, I use SDSS analogues of high-redshift star-forming galaxies to create a robust N/H-O/H conversion applicable to high-redshift galaxies. I show that by selecting SDSS galaxies above the [OIII] luminosity completeness of the 3D-*HST* $z > 2$ sample, one can find a subset of local galaxies which best mimics the global properties of high-redshift galaxies in terms of mass, star-formation rate and metallicity.

- These SDSS analogue galaxies also mimic other crucial observational traits of $z > 2$ galaxies, for example the offset in the BPT diagram and the discrepancy between N/H-based and O/H-based metallicities. I find that there is no evidence for a large increase in the N/O ratio at fixed O/H ratio for the SDSS analogue galaxies and therefore elevated N/O ratios are not necessarily needed to explain the high-redshift observations.

- Using the SDSS analogue galaxies I fit a N/H - O/H conversion relationship

which can be applied to high-redshift galaxies. With this new conversion I compile a new measurement of the $z \gtrsim 2$ MZR with a combined sample of N=576 galaxies from the literature which is unique in that it explicitly accounts for the evolution in the ionization parameter of high-redshift galaxies.

- I find evidence that the evolution in metallicity at a given mass between z = 2 and z = 3 may not be as large as inferred from current observations made using the Maiolino et al. (2008) calibration. This smaller metallicity evolution is in better agreement with the cosmological hydrodynamic simulations of Dave et al. (2011b,a) and Ma et al. (2015) implying momentum driven wind outflows from galaxies and efficient reclycing of the metal-enriched ejected gas.

6.3.1 Concluding Remarks

In summary, the work presented in this thesis has focused on how the emission line properties of star-forming galaxies are evolving with redshift, and how this evolution must be carefully accounted for and understood when attempting to derive metallicity measurements at high redshift. These results have an important impact on how we understand the evolution galaxies with cosmic time. Firstly, by iterating towards more accurate ways of measuring galaxy metallicities, we will be able to place tighter constraints on the star-formation histories of galaxies, and the roles that gas inflows and outflows play in galaxy evolution. This will enable us to begin answering questions such as what are the physical processes by which gas is driven out of galaxies? How efficiently and over what time scales are the metal-enriched outflows recycled into the ISM of a galaxy? How are all these effects dependent on the stellar mass of a galaxy? A robust measurement of the form and redshift evolution MZR, along with the stellar mass function and cosmic star-formation history, constitutes one of the key observables that should be matched by any large-scale cosmological hydrodynamical galaxy simulation. In terms of the overall emission line properties, and the evolution to more 'extreme' ISM conditions with redshift, many interesting theories can be explored in our attempt to understand exactly what this means. We already know more stars are being formed in high redshift galaxies, but is that star-formation occurring within smaller physical volumes than typical of local galaxies? How is the evolution in star-formation, and the properties of the stellar emission, linked to the metallicity

of the stars? In the authors speculative opinion, which will undoubtedly be proved incorrect, we are observing the effects of star-formation from massive condensed metal-poor gas clouds in which the stars form in denser clusters. This increased 'star-formation density', along with the increased overall rate of star-formation and the harder stellar SEDS produced by lower metallicity stars, causes an excess in high energy UV photons impinging on the ISM at high redshift, resulting in the extreme emission lines observed. The good news is that in the immediate future all the observations presented here will be expanded and improved upon with state-of-the-art ground based instrumentation such as KMOS and MOSFIRE, followed in a decade or so by next generation instruments such as the E-ELT and *James Webb Space Telescope*.

Bibliography

Aguirre A., Dow Hygelund C., Schaye J., Theuns T., 2008, ApJ, 689, 851

Allen M. G., Groves B. A., Dopita M. A., Sutherland R. S., Kewley L. J., 2008, ApJS, 178, 20

Alloin D., Collin-Souffrin S., Joly M., Vigroux L., 1979, A&A, 78, 200

Anderson L. et al., 2014, MNRAS, 441, 24

Andrews B. H., Martini P., 2013, ApJ, 765, 140

Asplund M., Grevesse N., Sauval A. J., 2005, 336, 25

Atek H. et al., 2010, ApJ, 723, 104

Baldry I. K., Glazebrook K., Brinkmann J., Ivezić Ž., Lupton R. H., Nichol R. C., Szalay A. S., 2004, ApJ, 600, 681

Baldwin J. A., Phillips M. M., Terlevich R., 1981, PASP, 93, 5

Balestra I. et al., 2010, A&A, 512, A12

Belli S., Jones T., Ellis R. S., Richard J., 2013, ApJ, 772, 141

Benson A. J., 2010, PhysR, 495, 33

Bertin E., Arnouts S., 1996, A&AS, 117, 393

Binette L., Dopita M. A., Tuohy I. R., 1985, ApJ, 297, 476

Blanton M. R., 2006, ApJ, 648, 268

Blanton M. R., Roweis S., 2007, AJ, 133, 734

Bouwens R. J., Illingworth G. D., Franx M., Ford H., 2007, ApJ, 670, 928

Bowler R. A. A. et al., 2012, MNRAS, 426, 2772

Bowler R. A. A. et al., 2014, MNRAS, 440, 2810

Brammer G. B., van Dokkum P. G., Coppi P., 2008, ApJ, 686, 1503

Brammer G. B. et al., 2012, ApJS, 200, 13

Brammer G. B. et al., 2011, ApJ, 739, 24

Brammer G. B. et al., 2009, ApJ, 706, L173

Brinchmann J., Pettini M., Charlot S., 2008, MNRAS, 385, 769

Bromm V., Yoshida N., Hernquist L., McKee C. F., 2009, Nature, 459, 49

Bruce V. A. et al., 2012, MNRAS, 427, 1666

Bruzual G., Charlot S., 2003, MNRAS, 344, 1000

Calura F., Pipino A., Chiappini C., Matteucci F., Maiolino R., 2009, A&A, 504, 373

Calzetti D., Armus L., Bohlin R. C., Kinney A. L., Koornneef J., Storchi-Bergmann T., 2000, ApJ, 533, 682

Caruana J., Bunker A. J., Wilkins S. M., Stanway E. R., Lorenzoni S., Jarvis M. J., Ebert H., 2014, MNRAS, 443, 2831

Chabrier G., 2003, PASP, 115, 763

Cirasuolo M. et al., 2007, MNRAS, 380, 585

Civano F. et al., 2012, ApJS, 201, 30

Cole S., Lacey C. G., Baugh C. M., Frenk C. S., 2002, MNRAS, 319, 168

Collaboration P. et al., 2015, arXiv

Colless M. et al., 2001, MNRAS, 328, 1039

Conroy C., 2013, A&AR, 51, 393

Cooke R. J., Pettini M., Jorgenson R. A., Murphy M. T., Steidel C. C., 2014, ApJ, 781, 31

Cowie L. L., Barger A. J., 2008, ApJ, 686, 72

Cowie L. L., Songaila A., Hu E. M., Cohen J. G., 1996, AJ, 112, 839

Cresci G., Mannucci F., Sommariva V., Maiolino R., Marconi A., Brusa M., 2012, MNRAS, 421, 262

Cullen F., Cirasuolo M., McLure R. J., Dunlop J. S., Bowler R. A. A., 2014, MNRAS, 440, 2300

da Cunha E., Charlot S., Elbaz D., 2008, MNRAS, 388, 1595

Daddi E., Cimatti A., Renzini A., Fontana A., Mignoli M., Pozzetti L., Tozzi P., Zamorani G., 2004, ApJ, 617, 746

Daddi E. et al., 2007, ApJ, 670, 156

Dave R., Finlator K., Oppenheimer B. D., 2011b, MNRAS, 416, 1354

Dave R., Oppenheimer B. D., Finlator K., 2011a, MNRAS, 415, 11

Davies R. I. et al., 2013, A&A, 558, A56

Dayal P., Ferrara A., Dunlop J. S., 2013, MNRAS, 430, 2891

De Lucia G., Blaizot J., 2007, MNRAS, 375, 2

De Marchi G. et al., 2011, ApJ, 739, 27

Dekel A., Sari R., Ceverino D., 2009, ApJ, 703, 785

Diaz A. I., Pérez-Montero E., 2000, MNRAS, 312, 130

Domínguez A. et al., 2013, ApJ, 763, 145

Dopita M. A. et al., 2006, ApJ, 647, 244

Dopita M. A., Kewley L. J., Heisler C. A., Sutherland R. S., 2000, ApJ, 542, 224

Dopita M. A., Sutherland R. S., Nicholls D. C., Kewley L. J., Vogt F. P. A., 2013, ApJS, 208, 10

Dunlop J. S., 2013, 396, 223

Edmunds M. G., Pagel B. E. J., 1978, MNRAS, 185, 77P

Eisenstein D. J. et al., 2005, ApJ, 633, 560

Eldridge J. J., Stanway E. R., 2012, MNRAS, 419, 479

Ellis R. S. et al., 2013, ApJL, 763, L7

Ellison S. L., Patton D. R., Simard L., McConnachie A. W., 2008, ApJ, 672, L107

Elmegreen B. G., 1998, ASPC, 148, 150

Erb D. K., Shapley A. E., Pettini M., Steidel C. C., Reddy N. A., Adelberger K. L., 2006b, ApJ, 644, 813

Erb D. K., Steidel C. C., Shapley A. E., Pettini M., Reddy N. A., Adelberger K. L., 2006a, ApJ, 647, 128

Esteban C., Peimbert M., García-Rojas J., Ruiz M. T., Peimbert A., Rodríguez M., 2004, MNRAS, 355, 229

Fan X. et al., 2006, AJ, 132, 117

Ferland G. J., Korista K. T., Verner D. A., Ferguson J. W., Kingdon J. B., Verner E. M., 1998, PASP, 110, 761

Finkelstein S. L. et al., 2013, Nature, 502, 524

Finlator K., Davé R., 2008, MNRAS, 385, 2181

Fioc M., Rocca-Volmerange B., 1997, A&A, 326, 950

Förster Schreiber N. M. et al., 2009, ApJ, 706, 1364

Fruchter A. S., Hook R. N., 2002, PASP, 114, 144

Galametz A. et al., 2013, ApJS, 206, 10

Gamow G., 1946, PhysR, 70, 572

Garn T., Best P. N., 2010, MNRAS, 409, 421

Goulding A. D. et al., 2012, ApJS, 202, 6

Grogin N. A. et al., 2011, ApJS, 197, 35

Groves B. A., Dopita M. A., Sutherland R. S., 2004, ApJS, 153, 9

Guo Y. et al., 2013, ApJS, 207, 24

Guth A. H., 1981, PRD, 23, 347

Hainline K. N., Shapley A. E., Kornei K. A., Pettini M., Buckley-Geer E., Allam S. S., Tucker D. L., 2009, ApJ, 701, 52

Henry A., Martin C. L., Finlator K., Dressler A., 2013a, ApJ, 769, 148

Henry A. et al., 2013b, ApJ, 776, L27

Hillier D. J., Miller D. L., 1998, ApJ, 496, 407

Ho I. T. et al., 2014, MNRAS, 444, 3894

Holden B. P. et al., 2014, preprint (arXiv:1401.5490)

Hopkins A. M., Beacom J. F., 2006, ApJ, 651, 142

Hopkins P. F., Cox T. J., Hernquist L., Narayanan D., Hayward C. C., Murray N., 2013, MNRAS, 430, 1901

Hopkins P. F., Kerev s D., Onorbe J., Faucher-Giguere C.-A., Quataert E., Murray N., Bullock J. S., 2014, MNRAS, 445, 581

Hopkins P. F., Richards G. T., Hernquist L., 2007, ApJ, 654, 731

Horne K., 1986, PASP, 98, 609

Hubble E., 1929, PNAS, 15, 168

Ilbert O. et al., 2006, A&A, 457, 841

Ilbert O. et al., 2008, ApJ, 690, 1236

Ilbert O. et al., 2010a, ApJ, 709, 644

Ilbert O. et al., 2010b, ApJ, 709, 644

Izotov Y. I., Thuan T. X., 2010, ApJ, 710, L67

Jansen R. A., Fabricant D., Franx M., Caldwell N., 2000, ApJS, 126, 331

Juneau S. et al., 2014, ApJ, 788, 88

Juneau S., Dickinson M., Alexander D. M., Salim S., 2011, ApJ, 736, 104

Kashino D. et al., 2013, ApJ, 777, L8

Kauffmann G. et al., 2003a, MNRAS, 346, 1055

Kauffmann G., White S. D. M., Guiderdoni B., 1993, MNRAS, 264, 201

Kennicutt R. C., Evans N. J., 2012, A&ARv, 50, 531

Kennicutt, Jr. R. C., Bresolin F., Garnett D. R., 2003, ApJ, 591, 801

Kennicutt R. C. J., 1998, A&ARv, 36, 189

Kewley L. J., Dopita M. A., 2002, ApJS, 142, 35

Kewley L. J., Dopita M. A., Leitherer C., Davé R., Yuan T., Allen M., Groves B., Sutherland R., 2013a, ApJ, 774, 100

Kewley L. J., Dopita M. A., Sutherland R. S., Heisler C. A., Trevena J., 2001, ApJ, 556, 121

Kewley L. J., Ellison S. L., 2008, ApJ, 681, 1183

Kewley L. J., Groves B., Kauffmann G., Heckman T., 2006, MNRAS, 372, 961

Kewley L. J., Maier C., Yabe K., Ohta K., Akiyama M., Dopita M. A., Yuan T., 2013b, ApJ, 774, L10

Kobayashi C., Springel V., White S. D. M., 2007, MNRAS, 376, 1465

Kobulnicky H. A., Kewley L. J., 2004, ApJ, 617, 240

Koekemoer A. M. et al., 2011, ApJS, 197, 36

Koppen J., Weidner C., Kroupa P., 2007, MNRAS, 375, 673

Kriek M. et al., 2015, ApJS, 218, 15

Kulas K. R. et al., 2013, ApJ, 774, 130

Kümmel M., Walsh J. R., Pirzkal N., Kuntschner H., Pasquali A., 2009, PASP, 121, 59

Kuntschner H., Kümmel M., Walsh J. R., 2013

Lacey C., Cole S., 1993, MNRAS, 262, 672

Lara-Lopez M. A. et al., 2010, A&A, 521, L53

Lara-López M. A., López-Sánchez Á. R., Hopkins A. M., 2013, ApJ, 764, 178

Le Fèvre O. et al., 2005, A&A, 439, 845

Lehnert M. D., Nesvadba N. P. H., Le Tiran L., Di Matteo P., van Driel W., Douglas L. S., Chemin L., Bournaud F., 2009, ApJ, 699, 1660

Leitherer C., Ekström S., Meynet G., Schaerer D., Agienko K. B., Levesque E. M., 2014, ApJS, 212, 14

Leitherer C., Ortiz Otálvaro P. A., Bresolin F., Kudritzki R.-P., Lo Faro B., Pauldrach A. W. A., Pettini M., Rix S. A., 2010, ApJS, 189, 309

Leitherer C. et al., 1999, ApJS, 123, 3

Lemaître G., 1932, ASSB

Lenz D. D., Ayres T. R., 1992, PASP, 104, 1104

Lequeux J., Peimbert M., Rayo J. F., Serrano A., Torres-Peimbert S., 1979, A&A, 80, 155

Levesque E. M., Kewley L. J., Larson K. L., 2010, ApJ, 139, 712

Levesque E. M., Richardson M. L. A., 2014, ApJ, 780, 100

Liang Y. C., Hammer F., Yin S. Y., Flores H., Rodrigues M., Yang Y. B., 2007, A&A, 473, 411

Lilly S. J., Carollo C. M., Stockton A. N., 2003, ApJ, 597, 730

Lilly S. J., Le Fevre O., Hammer F., Crampton D., 1996, ApJL, 460, L1

Liu X., Shapley A. E., Coil A. L., Brinchmann J., Ma C.-P., 2008, ApJ, 678, 758

Lu Y. et al., 2014, ApJ, 795, 123

Ly C., Malkan M. A., Nagao T., Kashikawa N., Shimasaku K., Hayashi M., 2014, ApJ, 780, 122

Ma X., Hopkins P. F., Faucher-Giguere C.-A., Zolman N., Muratov A. L., Keres D., Quataert E., 2015, arXiv

Madau P., Dickinson M., 2014, A&ARv, 52, 415

Madau P., Pozzetti L., Dickinson M., 1998, ApJ, 498, 106

Maeder A., Conti P. S., 1994, A&ARv, 32, 227

Maiolino R. et al., 2008, A&A, 488, 463

Mannucci F., Cresci G., Maiolino R., Marconi A., Gnerucci A., 2010, MNRAS, 408, 2115

Mannucci F. et al., 2009, MNRAS, 398, 1915

Mannucci F., Salvaterra R., Campisi M. A., 2011, MNRAS, 414, 1263

Maraston C., 2005, MNRAS, 362, 799

Marchesini D., van Dokkum P. G., Förster Schreiber N. M., Franx M., Labbé I., Wuyts S., 2009, ApJ, 701, 1765

Masters D. et al., 2014, ApJ, 785, 153

McCracken H. J. et al., 2012, A&A, 544, A156

McLean I. S. et al., 2012, SPIE, 8446, 0

McLure R. J. et al., 2013, MNRAS, 432, 2696

Mignoli M. et al., 2005, A&A, 437, 883

Mortlock D. J. et al., 2011, Nature, 474, 616

Mouhcine M., Lançon A., 2002, A&A, 393, 149

Moustakas J. et al., 2013, ApJ, 767, 50

Moustakas J., Kennicutt R. C., Tremonti C. A., Dale D. A., Smith J.-D. T., Calzetti D., 2010, ApJS, 190, 233

Moustakas J. et al., 2011, arXiv

Muzzin A. et al., 2013, ApJ, 777, 18

Nagao T., Maiolino R., Marconi A., 2006, A&A, 459, 85

Nakajima K., Ouchi M., 2014, MNRAS, 442, 900

Newman J. A. et al., 2013a, ApJS, 208, 5

Newman S. F. et al., 2013b, ApJ, 781, 21

Nicholls D. C., Dopita M. A., Sutherland R. S., 2012, ApJ, 752, 148

Niino Y., 2012, ApJ, 761, 126

Ono Y. et al., 2012, ApJ, 744, 83

Osterbrock D. E., 1989, Astrophysics of Gaseous Nebulae and Active Galactic Nuclei

Osterbrock D. E., Pogge R. W., 1985, ApJ, 297, 166

Pagel B. E. J., Simonson E. A., Terlevich R. J., Edmunds M. G., 1992, MNRAS, 255, 325

Pannella M. et al., 2014, preeprint (arXiv:1407.5072)

Panter B., Jimenez R., Heavens A. F., Charlot S., 2008, MNRAS, 391, 1117

Pauldrach A. W. A., Hoffmann T. L., Lennon M., 2001, A&A, 375, 161

Peacock J. A. et al., 2001, Nature, Volume 410, Issue 6825, pp. 169-173 (2001).

Peebles P. J. E., 1965, ApJ, 142, 1317

Peebles P. J. E., 1980, The large-scale structure of the universe

Pentericci L. et al., 2011, ApJ, 743, 132

Penzias A. A., Wilson R. W., 1965, ApJ, 142, 419

Pérez-Montero E., Contini T., 2009, MNRAS, 398, 949

Perlmutter S. et al., 1999, ApJ, 517, 565

Petrosian V., 1976, ApJL, 209, L1

Pettini M., Pagel B. E. J., 2004, MNRAS, 348, L59

Pettini M., Steidel C. C., Adelberger K. L., Dickinson M., Giavalisco M., 2000, ApJ, 528, 96

Pforr J., Maraston C., Tonini C., 2012, MNRAS, 422, 3285

Pilbratt G. L. et al., 2010, A&A, 518, L1

Pilyugin L. S., Thuan T. X., 2005, ApJ, 631, 231

Pilyugin L. S., Vílchez J. M., Mattsson L., Thuan T. X., 2012, MNRAS, 421, 1624

Pirzkal N. et al., 2013, ApJ, 772, 48

Press W. H., Schechter P., 1974, ApJ, 187, 425

Price S. H. et al., 2014, ApJ, 788, 86

Rich J. A., Dopita M. A., Kewley L. J., Rupke D. S. N., 2010, ApJ, 721, 505

Richard J., Jones T., Ellis R., Stark D. P., Livermore R., Swinbank M., 2011, MNRAS, 413, 643

Riess A. G. et al., 1998, AJ, 116, 1009

Rodrigues M. et al., 2008, A&A, 492, 371

Rodríguez-Pascual P. M., González-Riestra R., Schartel N., Wamsteker W., 1999, A&AS, 139, 183

Roseboom I. G. et al., 2012, MNRAS, 426, 1782

Salim S., Lee J. C., Ly C., Brinchmann J., Davé R., Dickinson M., Salzer J. J., Charlot S., 2014, ApJ, 797, 126

Salim S. et al., 2007, ApJS, 173, 267

Salmon B. et al., 2015, ApJ, 799, 183

Salpeter E. E., 1955, ApJ, 121, 161

Sanders R. L. et al., 2015, ApJ, 799, 138

Savaglio S. et al., 2005, ApJ, 635, 260

Schaye J. et al., 2015, MNRAS, 446, 521

Schenker M. A. et al., 2013, ApJ, 768, 196

Schenker M. A., Stark D. P., Ellis R. S., Robertson B. E., Dunlop J. S., McLure R. J., Kneib J.-P., Richard J., 2012, ApJ, 744, 179

Shapley A. E., Coil A. L., Ma C.-P., Bundy K., 2005, ApJ, 635, 1006

Shapley A. E. et al., 2015, ApJ, 801, 88

Shapley A. E., Steidel C. C., Pettini M., Adelberger K. L., 2003, ApJ, 588, 65

Sharples R. et al., 2013, Messenger, 151, 21

Shioya Y., Taniguchi Y., Trentham N., 2001, MNRAS, 321, 11

Shirazi M., Brinchmann J., Rahmati A., 2014b, ApJ, 787, 120

Shirazi M., Vegetti S., Nesvadba N., Allam S., Brinchmann J., Tucker D., 2014a, MNRAS, 440, 2201

Shull J. M., Stevans M., Danforth C. W., 2012, ApJ, 752, 162

Simcoe R. A., 2011, ApJ, 738, 159

Slipher V. M., 1916, PAPS

Snijders L., Kewley L. J., van der Werf P. P., 2007, ApJ, 669, 269

Sobral D., Smail I., Best P. N., Geach J. E., Matsuda Y., Stott J. P., Cirasuolo M., Kurk J., 2013, MNRAS, 428, 1128

Somerville R. S., Hopkins P. F., Cox T. J., Robertson B. E., Hernquist L., 2008, MNRAS, 391, 481

Somerville R. S., Primack J. R., 1999, MNRAS, 310, 1087

Sommariva V., Mannucci F., Cresci G., Maiolino R., Marconi A., Nagao T., Baroni A., Grazian A., 2012, A&A, 539, A136

Springel V., 2005b, MNRAS, 364, 1105

Springel V., 2010, MNRAS, 401, 791

Springel V. et al., 2005a, Nature, 435, 629

Stasinska G., 2005, A&A, 434, 507

Steidel C. C., Adelberger K. L., Shapley A. E., Pettini M., Dickinson M., Giavalisco M., 2003, ApJ, 592, 728

Steidel C. C., Pettini M., Hamilton D., 1995, ApJ, 110, 2519

Steidel C. C. et al., 2014, ApJ, 795, 165

Steidel C. C., Shapley A. E., Pettini M., Adelberger K. L., Erb D. K., Reddy N. A., Hunt M. P., 2004, ApJ, 604, 534

Storey P. J., Zeippen C. J., 2000, MNRAS, 312, 813

Stott J. P. et al., 2013, MNRAS, 436, 1130

Sutherland R. S., Dopita M. A., 1993, ApJS, 88, 253

Torrey P., Vogelsberger M., Genel S., Sijacki D., Springel V., Hernquist L., 2014, MNRAS, 438, 1985

Tremonti C. A. et al., 2004, ApJ, 613, 898

Troncoso P. et al., 2014, A&A, 563, A58

Trump J. R. et al., 2013, ApJL, 763, L6

van der Wel A. et al., 2012, ApJS, 203, 24

van Zee L., Salzer J. J., Haynes M. P., 1998, ApJL, 497, L1

Vanzella E. et al., 2008, A&A, 478, 83

Vanzella E. et al., 2006, A&A, 454, 423

Veilleux S., Osterbrock D. E., 1987, ApJS, 63, 295

Weiner B. J. et al., 2007, ApJ, 660, L39

Whitaker K. E., van Dokkum P. G., Brammer G., Franx M., 2012, ApJL, 754, L29

White S. D. M., Frenk C. S., 1991, ApJ, 379, 52

Williams R. J., Quadri R. F., Franx M., van Dokkum P., Labbé I., 2009, ApJ, 691, 1879

Willmer C. N. A. et al., 2006, ApJ, 647, 853

Wofford A., Leitherer C., Chandar R., Bouret J.-C., 2014, ApJ, 781, 122

Worthey G., 1994, ApJS, 95, 107

Wuyts E. et al., 2014, ApJ, 789, L40

Wuyts S. et al., 2011, ApJ, 738, 106

Wuyts S. et al., 2013, ApJ, 779, 135

Xue Y. Q. et al., 2011, ApJS, 195, 10

Yabe K. et al., 2012, PASJ, 64, 60

Yates R. M., Kauffmann G., Guo Q., 2012, MNRAS, 422, 215

Yeh S. C. C., Matzner C. D., 2012, ApJ, 757, 108

York D. G. et al., 2000, ApJ, 120, 1579

Yuan T. T., Kewley L. J., Richard J., 2013, ApJ, 763, 9

Zahid H. J., Bresolin F., Kewley L. J., Coil A. L., Davé R., 2012, ApJ, 750, 120

Zahid H. J., Dima G. I., Kudritzki R.-P., Kewley L. J., Geller M. J., Hwang H. S., Silverman J. D., Kashino D., 2014b, ApJ, 791, 130

Zahid H. J., Geller M. J., Kewley L. J., Hwang H. S., Fabricant D. G., Kurtz M. J., 2013, ApJ, 771, L19

Zahid H. J. et al., 2014a, ApJ, 792, 75

Zahid H. J., Kewley L. J., Bresolin F., 2011, ApJ, 730, 137

Zeimann G. R. et al., 2015, ApJ, 798, 29